Geordnete poröse Nanostrukturen

ein Baukastensysten für die Photonik

Habilitationsschrift

zur Erlangung des akademischen Grades

Dr. rer. nat. habil.

vorgelegt der

Mathematisch-Naturwissenschaftlich-Technische Fakultät
(mathematisch-naturwissenschaftlicher Bereich)
der Martin-Luther-Universität Halle-Wittenberg

von Herrn Dr. rer. nat. Ralf Boris Wehrspohn
geb.: 17.08.1970 in: Lübeck

Gutachter:

1. Prof. U. Gösele, MPI für Mikrostrukturphysik, Halle
2. Prof. R. Höche, Martin-Luther-Universität Halle-Wittenberg
3. Prof. A. Scherer, California Institute of Technology, Pasadena, USA

Halle (Saale), verteidigt am 6.6.2003, Probevorlesung am 11.7.2003

Inhaltsverzeichnis

1 Einleitung

1.1 Kristalle

"A crystal is any solid material in which the component atoms are arranged in a definite pattern and whose surface irregularity reflects its internal symmetry", definiert die Encyclopedia Britannica. Es ist also ein Körper, der in einer, zwei oder drei Dimensionen des Raumes eine periodische Anordnung von Teilchen aufweist. Entsprechend werden die Körper als 1D–, 2D– oder 3D–Kristalle bezeichnet. Besitzt die Anordnung der Teilchen keine Periodizität, so wird die Anordnung als amorph bezeichnet. Haben die Teilchen Einfluss auf die Propagation von Wellen, so werden die Teilchen als Streuer bezeichnet.

Die Natur ist überwiegend aus Festkörpern aufgebaut, die entweder keine Periodizität oder eine 3D–Periodizität an Streuern haben. Die elektronischen Eigenschaften von 3D–Festkörperkristallen sind vor allem durch die Interferenz von Elektronenwellen unter Berücksichtigung der Coulombschen Wechselwirkung und des Pauli-Prinzips bestimmt. Die Streuer der Elektronenwellen sind die Atomrümpfe und die Rumpfelektronen. In der modernen Festkörperphysik versucht man die vorgegebene 3D–Periodizität der Materie zu reduzieren, um neue Effekte zu untersuchen. Dünne Schichten, die Dicken kleiner als die Koherenzlänge der Elektronenwellen aufweisen, zeigen Quanteneffekte in einer Dimension. Man bezeichnet Sie als Quantenschichten oder 2D-Nanostrukturen. Neuere Nanostrukturierungsmethoden erlauben auch die Herstellung von 1D–Nanostrukturen (Quantendrähte) wie auch OD–Strukturen (Quantenpunkte). In letzteren spürt die Elektronenwelle die endliche Struktur in allen drei Raumrichtungen und es gibt keine ausgedehnte Periodizität mehr.

Im Vergleich zur Festkörperphysik vollzieht sich in der Optik ein entgegengesetzter Trend. Elektromagnetische Strukturen mit 3D–Periodizität im Bereich der Wellenlänge des Lichtes waren bislang kaum herstellbar. Die Natur ist für elektromagnetische Wellen überwiegend isotrop. Es gibt Reflexion und Transmission an isotropen Strukturen, aber Interferenzerscheinungen von elektromagnetischen Wellen aufgrund einer Strukturierung im Bereich der Wellenlänge sind die Ausnahme.

Die ersten "Nanostrukturen" in der Optik sind ca. 50 Jahre alt und würden heutzutage als eindimensionale Kristalle bezeichnet werden, traditionell aber als dielektrische Spiegel. In diesen Strukturen wird das Streupotential für elektromagnetische Wellen, d.h. der Brechungsindex, in einer Dimension variiert. Dabei muss der Abstand der Streuer im Bereich der Wellenlänge des Lichtes liegen. Vor ca. 15 Jahren wurde dieses Konzept theoretisch auf zwei und drei Dimensionen ausgedehnt, der Begriff des Photonischen Kristalls wurde geprägt [1, 2].

Ähnliche Konzepte wurden in den letzten Jahren auch für akustische und elastische Wellen, magnetische Vielteilchenanregungen (Spinwellen) und elektronische Vielteilchenanregungen (Plasmonen) entwickelt. Die entsprechenden Kristalle werden als Akustische Kristalle [3], Magnonische Kristalle [4] und Plasmonische Kristalle [5] bezeichnet. Abbildung 1.1 zeigt Bilder von zweidimensionalen Photonischen, Akustischen und Magnetischen Kristallen, die am Max-Planck-Institut für Mikrostrukturphysik in Halle hergestellt worden sind.

1.2 Das hexagonale zweidimensionale Gitter

Die grundlegenden Eigenschaften von Interferenzeffekten in periodischen Medien lassen sich mit 1D-Strukturen, d.h. Strukturen mit räumlicher Periodizität in einer Richtung, charakterisieren. Allerdings eröffnen erst 2D– bzw. 3D–Strukturen einen zusätzlichen Parameter, der mit Schichtsystemen nicht

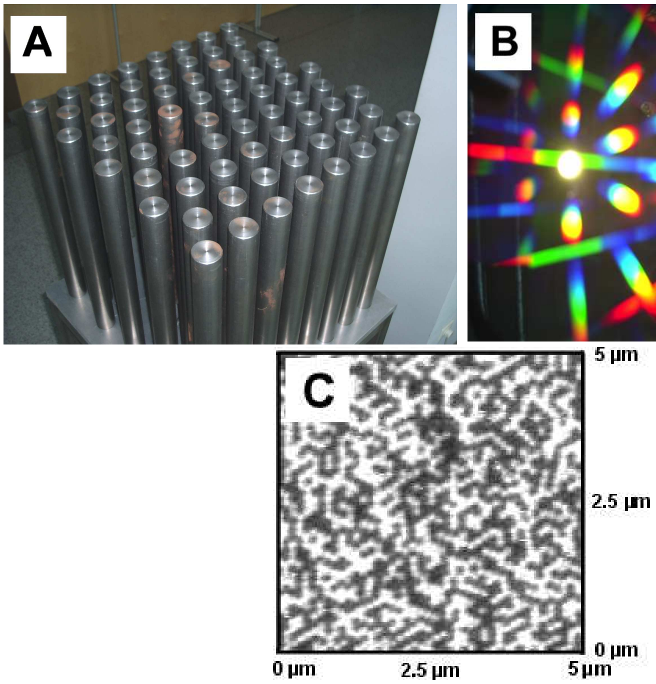

Abbildung 1.1: (a) Photographie eines hexagonalen 2D–Akustischen Kristalls (gebaut nach [6]). Es existiert eine Interferenztotalreflexion für Schallwellen bei $\lambda \approx$ 1,5 kHz; (b) Photographie eines 2D–Photonischen Kristalls mit Beleuchtung [7]. Der Photonische Kristall hat eine hexagonale Periodizität, welche zu einer Interferenztotalreflexion bei $\lambda \approx$ 3,5 μm führt. Die spektral aufgelösten Reflexe stammen von dem hexagonalen 2D–Gitter an der Oberfläche; (c) Magnetische Rasterkraftmikroskopische-Aufnahme eines 2D–Magnetischen Kristalls (Ni-Nanostabensemble mit a = 100 nm und r = 20 nm im entmagnetisierten Zustand [8])

.

zugänglich ist: die Symmetrie der Anordnung der Streuer im Raum. Die einfachsten Symmetrien in 2D–Strukturen sind das quadratische und das hexagonale Gitter. Es besteht darüberhinaus die Möglichkeit einer Symmetriereduzierung innerhalb des Kristalls unter Beibehaltung der Periodizität. Zum Beispiel wird in geraden Wellenleitern in 2D–Kristallen die 2D–Periodizität auf eine 1D–Periodizität reduziert.

Welche Symmetrie ist die optimale bezüglich Interferenzerscheinungen? Dies ist allgemein schwer zu beantworten und hängt von den physikalischen Effekten ab, die man studieren möchte. Die 2D–hexagonale Struktur besitzt die größte photonische Bandlücke, weil Sie sich einem Kreis im Fourierraum am Besten annähert und damit die Interferenzbedingungen in alle Richtungen die gleiche sind. Zweidimensionale hexagonale Strukturen treten zu Hauf in unserem täglichen Leben auf: gestapelte Holzstämme, dicht gepackte Strohhalme in einem Glas oder auch die Kapillaren in den Borsten der Seemaus [9]. Die relevanten Kräfte sind die Graviationskraft, äußere mechanische Kräfte oder biologische Wachstumsprozesse. Allen zu Grunde liegt, dass die hexagonale Struktur die höchste Packungsdichte in zwei Dimensionen besitzt.

Der entscheidene Parameter für das Zustandekommen einer Interferenzerscheinung ist die Periodizität. Für Akustische Kristalle liegt diese im cm- bis m-Bereich, für Photonische Kristalle im sichtbaren und infraroten Spektralbereich zwischen einigen 100 nm und einigen Mikrometern, für Magnonische Kristalle im Bereich der Streufeldwechselwirkung, d.h., im Submikrometerbereich, sowie für Plasmonische Kristalle im Bereich des evaneszierenden Feldes, d.h. ca. 10 nm. Für alle Strukturen außer den Akustischen Kristallen sind aufgrund der kleinen Abmessungen neuartige Verfahren zu entwickeln, um 2D–*nano*strukturierte Materialien herzustellen. Hierbei ist *nano* zu verstehen als alle Abmessungen, die sich bequem in Einheiten von Nanometern beschreiben lassen.

1.3 Aufbau

Diese Habilitationsschrift ist kummulativ. Sie besteht aus zwei Kapiteln, die die wichtigsten Ergebnisse meiner Arbeiten zusammenfassen. Im Anhang sind ausgewählte Veröffentlichungen enthalten. Das erste Kapitel beschreibt die Materialsysteme, die wir während meiner Habilitation verwendet und weiterentwickelt haben, um geordnete poröse Nanostrukturen zu erzeugen. Dies beinhaltet das Materialsystem Makroporöses Silizium sowie das Materialsystem der porösen Ventilmetalloxide [1], im Speziellen, poröses Aluminiumoxid. Desweiteren werden Replikationsverfahren zur Herstellung metallischer Nanostabensembles sowie Polymer- und Polymerkomposit-Nanoröhrchen beschrieben.

Das zweite Kapitel meiner Habilitationsschrift beschreibt die Charakterisierung von Photonischen Kristallen, deren Durchstimmbarkeit und potentielle Anwendungsmöglichkeiten. Ein kurzer Ausblick beschäftigt sich mit Magnonischen und Plasmonischen Kristallen. Die Zusammenfassung schließt mit einer Danksagung ab.

---

[1] Ventilmetalloxide sind metallische Oxide, die Wechselspannungen gleichrichten und daher auf elektrische Ströme wie eine Diode oder Ventil wirken [10].

2 Materialien

2.1 Einleitung

Zur Herstellung von geordneten porösen Nanostrukturen kann man prinzipiell zwei Herstellungsstrategien anwenden: einerseits moderne Strukturierungsverfahren bestehend aus Lithographie und plasmachemischem Ätzen, andererseits Selbstordnungsphänomene. Allerdings haben beide Strategien als solche Nachteile. Plasmachemische Nanostrukturierungsverfahren erlauben keine sehr hohen Aspektverhältnisse, d.h. Quotient von Porenlänge h zu Porendurchmesser $2r$. Sie liegen bei den modernsten Niederdruck-Plasmaverfahren wie zum Beispiel induktiv-gespeisten Plasmen (ICP) oder Zyklotron-Plasmen (ECR) bei 30 bis 40. Andererseits haben Prozesse, die ausschließlich auf Selbstordnung basieren wie z.B. im Falle von poröses Aluminiumoxid den Nachteil, dass keine langreichweitige Ordnung zugänglich ist und Korngrenzen sowie Punktdefekte auftreten. Mein Ziel war es durch eine Kombination von Lithographie und elektrochemischer Selbstordnung perfekt geordnete poröse Nanostrukturen zu erzeugen. Dies ist uns sowohl für makroporöse Siliziumstrukturen wie auch poröse Aluminiumoxidstrukturen gelungen.

In der Literatur sind viele elektrochemische Porenstrukturen bekannt. Halbleiter aus den Gruppen IV, III-V und II-VI zeigen Porenstrukturen unter bestimmten elektrochemischen Wachstumsbedingen [11]. Eine andere Gruppe sind die Ventilmetalle, die bei elektrochemischer Oxidation unter bestimmten Umständen Poren aufweisen [10]. Die heutzutage am Besten studiertesten Systeme sind Silizium und Aluminiumoxid. Im Folgenden wird kurz zusammengefasst, welche Beiträge zum Verständnis des Porenwachstums während meiner Habilitation hinzugekommen sind und wo wir heute stehen. Darüberhinaus wurden Replika-Prozesse entwickelt, die das vollständige Füllen der Nanoporen mit Metallen wie Nickel, Kobalt, Silber und Gold erlauben. Außerdem konnte ein universelles Verfahren zu Herstellung von Polymer-Nanoröhrchen entwickelt werden, das auf der Ausnutzung kinetischer Phänomene während der Benetzung der Porenwände mit flüssigen Polymeren basiert.

2.2 Silizium

2.2.1 Einführung in die Silizium-Elektrochemie

Die elektrochemische Auflösung von Silizium ist aufgrund der Stabilität seines Oxides in wässerigen Lösungen nur in fluorhaltiger Säure (HF) möglich. Da zur elektrochemischen Auflösung von Silizium postive Ladungsträger (Löcher) notwendig sind, wurden die anfänglichen elektrochemischen Prozesse ausschließlich mit p-typ Silizium durchgeführt, in dem die positiven Ladungsträger Majoritätsladungsträger sind. Mikroporenbildung in p-typ Si ist seit ca. 50 Jahren bekannt [12]. Erst 1997 wurde von mir gezeigt, dass es unter den gleichen Bedingung auch Makroporen in p-typ Silizium geben kann [13]. Sie enstehen nach sehr langen Anodisationszeiten unter einer Schicht von Mikroporen. Für n-typ Silizium müssen die positiven Ladungsträger entweder durch Beleuchtung (Photoelektrochemie) oder durch Avalanche-Effekte in der Raumladungszone erzeugt werden. Es ist auch möglich, mittels stromloser, autokatalytischer elektrochemischer Verfahren Silizium aufzulösen. Hierbei werden lokal positive Ladungsträger mittels einer Reduktion generiert. Ein sehr gut untersuchtes System sind HF/HNO_3-Elektrolyten [14].

Um das Porenwachstum, d.h. die lokale Auflösung von Silizium, zu verstehen, muss man die physiko-chemischen Prozesse an der Grenzfläche Silizium/HF unter Stromfluß untersuchen. Diese hängen wesentlich von der Dotierung des Siliziumwafers und damit von den Eigenschaften der Raumladungszone an der Grenzfläche ab. Insofern ist es notwendig drei Fälle zu unterscheiden: (a) moderat p-dotiertes Silizium, (b) moderat n-dotiertes Silizium und (c) hochdotiertes Silizium. Hochdotiertes Silizium wurde im Rahmen meiner Habilitation nicht untersucht, da in diesem Fall die Porendurchmesser und die Porenabstände sehr klein sind (typischerweise in der Größenordnung von 50 nm) und keine Selbstsordnung existiert [15]. Porenabstände im Bereich einiger Mikrometer lassen sich mit p-typ Silizium wie auch n-typ Silizium moderater Dotierung herstellen. Daher werden beide Systeme im Folgenden genauer untersucht.

2.2.2 p-typ Silizium

Der Transport über die Si/HF Grenzfläche in p-typ Si lässt sich am Besten mittels einer I-U-Kennlinie (Voltammogram) experimentell bestimmen. Abbildung 2.1a zeigt ein typisches Voltammogram für p-typ Silizium. Im Bereich zwischen 0 und 0,5 V (gegen Ag/AgCl-Referenzelektrode) steigt der Strom sehr steil bis zum ersten Strommaximum bei dem Potential $U = U_{PS}$ an. Der elektronische Transport ist limitert durch den Transport über die Raumladunszone und die chemische Reaktionsgeschwindigkeit. In diesem Spannungsbereich entsteht poröses Silizium. Für Potentiale größer U_{PS} wird der Siliziumwafer elektropoliert. Der Transport ist limitiert durch die chemische Auflösegeschwindigkeit von anodischem SiO_2. Eine Seitenansicht von porösem Silizium nach sehr langen Anodisationszeiten ist in Abbildung 2.1b gezeigt. Dies ist ein typisches Bild von porösem p-typ Silizium in HF. Ich konnte während meiner Doktorarbeit zeigen, dass zuerst Mikroporen für einige Mikrometer entstehen und dann Makroporen, welche mit Mikroporen gefüllt sind [13, 16]. Dies ist von vielen anderen Gruppen bestätigt worden [17, 18, 19]. Abbildung 2.1c zeigt ein rasterelektronenmikroskopisches Bild einer ähnlichen Probe wie in Abb. 2.1b, die unter einem Winkel von 1/8 radian poliert worden ist. Eine Bildauswertung des Porendurchmessers sowie der Wanddicke ist in Abb. 2.1d sehen. Es scheint, dass Mikro- und Makroporenbildung ein und denselben Urspung haben. Dies haben wir theoretisch mittels einer linearen Stabilitätsanalyse nachweisen können [20, 21].

Im Bereich der Mikro- und Makroporenbildung ist der Stromtransport in p-typ Silizium limitiert durch die Raumladungszone und die chemische Reaktionsgeschwindigkeit. Eine schematische Darstellung des Potentialverlaufs über die p-typ Si/HF Grenzfläche ist in Abb. 2.2a gezeigt.

Im Folgenden wird kurz das Modell der linearen Stabilitätsanalyse im Falle von zwei isotropen Medien vorgestellt werden. Dann werden die Ergebnisse der Modellierungen der letzten acht Jahre für einen realistischen Potentialverlauf dargestellt und mit Experimenten verglichen [21].

2.2.2.1 Lineare Stabilitätsanalyse für die Grenzfläche zwischen zwei isotropen Medien

Der Stabilitätskoeffizient $\alpha(q)$ für die Wachstumsfromt zwischen einem Halbleiter mit dem spezifischen Widerstand ρ_s und einem Elektrolyten mit dem spezifischen Widerstand ρ_e wurde von uns in [23] hergeleitet. Dabei bedeuten positive Werte von $\alpha(q)$, dass die Wachstumsgrenzfläche für eine bestimmte Fluktuationswellenlänge λ, welche durch den Wellenvektor q (=$2\pi/\lambda$) beschrieben werden kann, instabil ist, d.h. es bilden sich Poren. Negative Werte von $\alpha(q)$ können als stabile Wachstumsgrenzfläche gedeutet werden. Der absolute Wert von $\alpha(q)$ kann als inverse Schichtdicke $\Delta = (\alpha(q))^{-1}$ betrachtet werden, bei der eine bestimmte Fluktuationswellenlänge in Erscheinung tritt. $\alpha(q)$ ist bestimmt worden, indem das Potenzial $\Phi(x,y)$ in eine Form gebracht wurde, die die Laplace-Gleichung in beiden Medien erfüllt:

$$\text{poröse Schicht + Elektrolyt}(y < y_B) : \Phi(x,y) = \rho_e J_0 y + \delta\Phi_e \exp(qy)\cos(qx) \qquad (2.1)$$

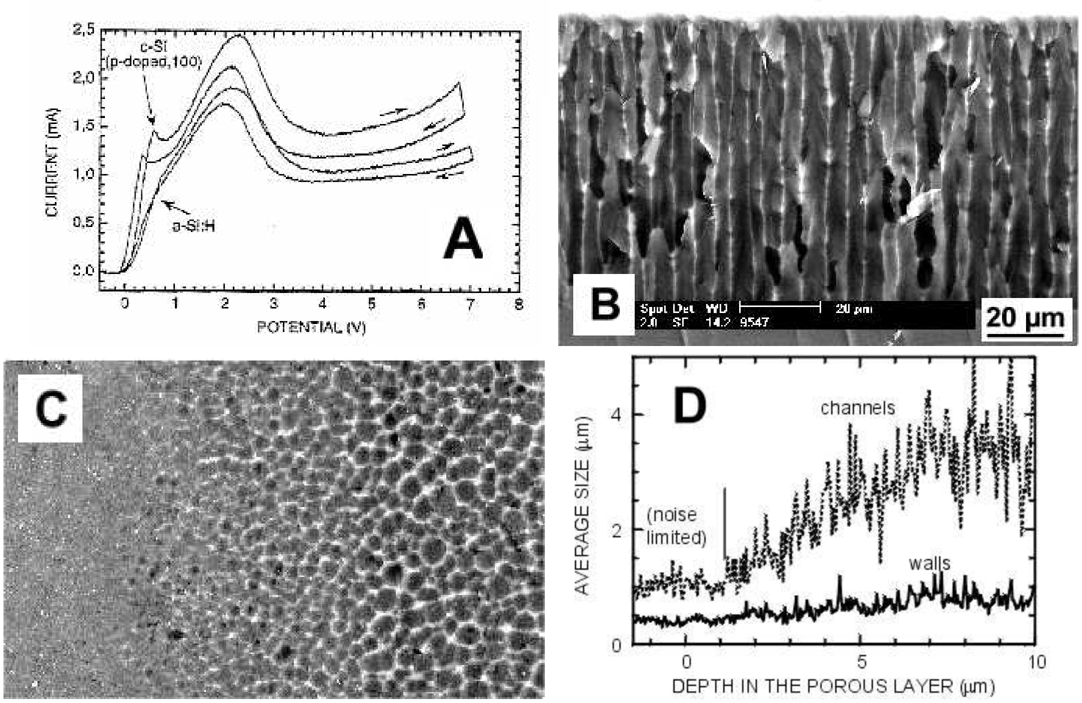

Abbildung 2.1: (a) Zyklisches Voltammogram von kristallinem und amorphem Si in HF (Potential gegen Ag/AgCl-Referenzelektrode) [22]; (b) Rasterelektronenmikroskopische Querschnitts-Aufnahme von porösem p-typ Silizium nach einer Stunde Anodisation. Herstellungsbedingungen: p-Si, 100 Ωcm, 35% HF in EtOH, 20 mA/cm^2. KOH-Behandlung zum Entfernen der mikroporösen Schicht [13]; (c) Rasterlektronenmikroskopische Aufnahme eines Schliffes einer ähnlichen Probe wie in (b) [11]; (d) Numerische Auswertung des Schliffes aus (c). Gepunkte Kurve entspricht Porendurchmessern, die durchgezogenen Linie den Porenwänden [11].

$$\text{Halbleiter}(y > y_B) : \Phi(x,y) = \rho_s J_0 y + \delta\Phi_s \exp(-qy)\cos(qx), \tag{2.2}$$

wobei J_0 die mittlere Stromdichte ist und $\delta\Phi_e$ und $\delta\Phi_s$ zwei über die Randbedingungen zu bestimmende Parameter sind. Die Lösungen des Potentials und der Stromdichte sind an der Grenzfläche $y_B = \delta_y cos(qx)$ von Halbleiter und Elektrolyte stetig (siehe Abb. 2.2b). Entwicklung nach δ_y liefert in erster Ordnung von δ_y die beiden Randbedigungen

$$\rho_e J_0 \delta_y + \delta\Phi_e = \rho_s J_0 \delta_y + \delta\Phi_s \ \text{ und} \tag{2.3}$$

$$\delta J = q\delta\Phi_e/\rho_e = -q\delta\Phi_s/\rho_s. \tag{2.4}$$

Die Stromdichte an der Grenzfläche ist von der Gestalt $J_0 + \delta J cos(qx)$, wobei δJ proportional zu δ_y ist (hierbei sind J_0 und δJ postiv im Sinne von anodisch). Der Stabilitätskoeffizient $\alpha(q)$ entspricht dann $\delta J/(J_0\delta y)$. Die elektrochemische Kinetik kann in dieser einfachen Behandlung des Problems in Form eines Grenzflächenwiderstandes R_i inkooperiert werden (in Einheiten von Ωcm^2). Dies führt zu einem zusätzlichem Term in Gl. (2.3), welcher das Grenzflächenpotential $R_i\delta J$ beschreibt. Als Lösung von $\alpha(q)$ ergibt sich [11, 20]

$$\alpha(q) = \frac{\rho_s - \rho_e}{\rho_s + \rho_e + qR_i} q. \tag{2.5}$$

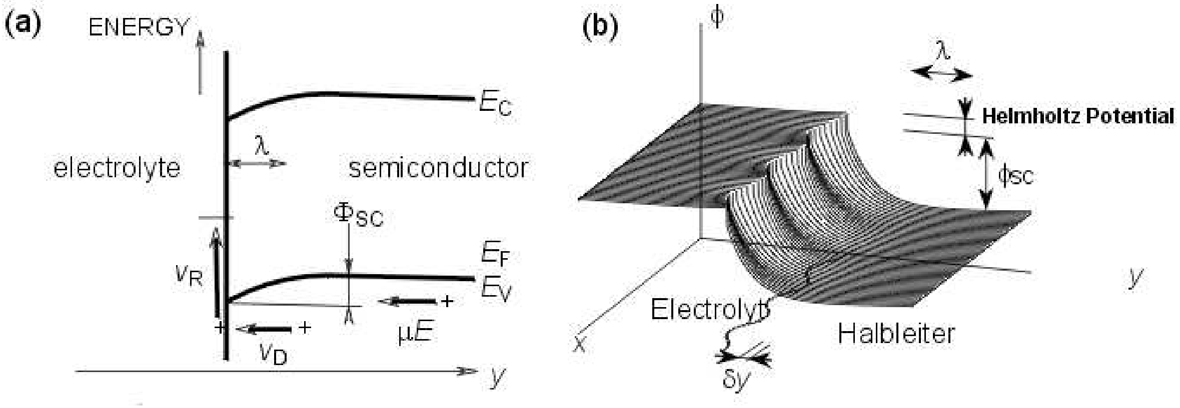

Abbildung 2.2: (a) Potentialverlauf über die p-typ Si/HF-Grenzfläche. Die Auflöserate von p-typ Silizium ist limitiert durch den Transport eines Loches durch die Raumladungszone λ_{RLZ} (bestimmt durch die Geschwindigkeit v_D) und durch die Reaktion an der Grenzfläche (bestimmt durch die Geschwindigkeit v_R). Bei hochresistiem Silizium limitiert außerdem die Beweglichkeit der Löcher im Silizium (bestimmt durch die Elektronendrift μE); (b) Schematisches Modell für die lineare Stabilitätsanalyse. Der Potentialprofil hat an der Si/HF-Grenzfläche einen sinusförmigen Verlauf bestimmt durch die Wellenzahl q [21].

Das Vorzeichen von α ist ausschließlich durch die beiden spezifischen Widerstände ρ_e and ρ_s bestimmt. In diesem Sinne kann die Grenzfläche Si/HF nur instabil werden, wenn der Elektrolyt einen höheren spezifischen Widerstand hat als Silizium.

2.2.2.2 Lineare Stabilitätsanalyse für Poren in p-typ Silizium

Dies ist natürlich die einfachste Beschreibung unter Vernachlässigung des Transportes über die Raumladungszone, der exakten chemischen Reaktionssgeschwindigkeit, des Potentialabfalls in der Helmholtzschicht und des anisotropen Verlaufs der Potentiallinien in porösem Silizium. Daher ist die Lösung von α in Gl. (2.5) im Allgemeinen falsch. Nimmt man alle diese Faktoren mit in die lineare Stabilitätsanalyse, so ergibt sich für α ein wesentlich komplizierterer Term, der von der Schichtdicke der porösen Schicht abhängt. Ein schematischer Aufbau des Potentialverlaufs für eine solche Rechnung ist in Abb. 2.2b zu sehen. Für den stabilisierten Porenabstand $1/q_c$ für Makroporen in p-typ Silizium unter einer Schicht von Mikroporen (siehe z.B. Abb 2.1c und d) ergibt sich [21]:

$$\frac{1}{q_c} = \left(\lambda_{\mathrm{RLZ}}^3 S^3 \frac{kT}{eJ_0\rho_e}\right)^{1/4} . \tag{2.6}$$

Diese Abhängigkeit kann relativ einfach überprüft werden, indem die Raumladungszone λ_{RLZ}, d.h. die Dotierung, die Stromstärke J_0 oder der Widerstand des Elektrolyten ρ_e variiert werden. Die experimentellen Ergebnisse zusammen mit den theoretischen Vorhersagen basierend auf Gl. (2.6) sind in Abb. 2.3 dargestellt. Es ist eine hervorragende Übereinstimmung über weite Parameterbereiche zu erkennen. Dabei ist zu berücksichtigen, dass die Porenwandstärke immer ungefähr der zweifachen Raumladungszone entspricht. Dies ist anschaulich zu verstehen, da die Wände zwischen den Poren komplett an elektronischen Löchern verarmt sein müssen, da sich ansonsten die Wände auflösen würden. Warum bei sehr hohen Dotierungen keine Makroporen mehr entstehen, kann man mit diesem Modell nicht verstehen. Allerdings konnten wir zeigen, dass die Schottky-Näherung einer Raumladungszone für Dotierungen größer als 10^{16} cm^{-3} nicht mehr korrekt ist und die Raumladungszone ihren isolierenden Charakter verliert [21].

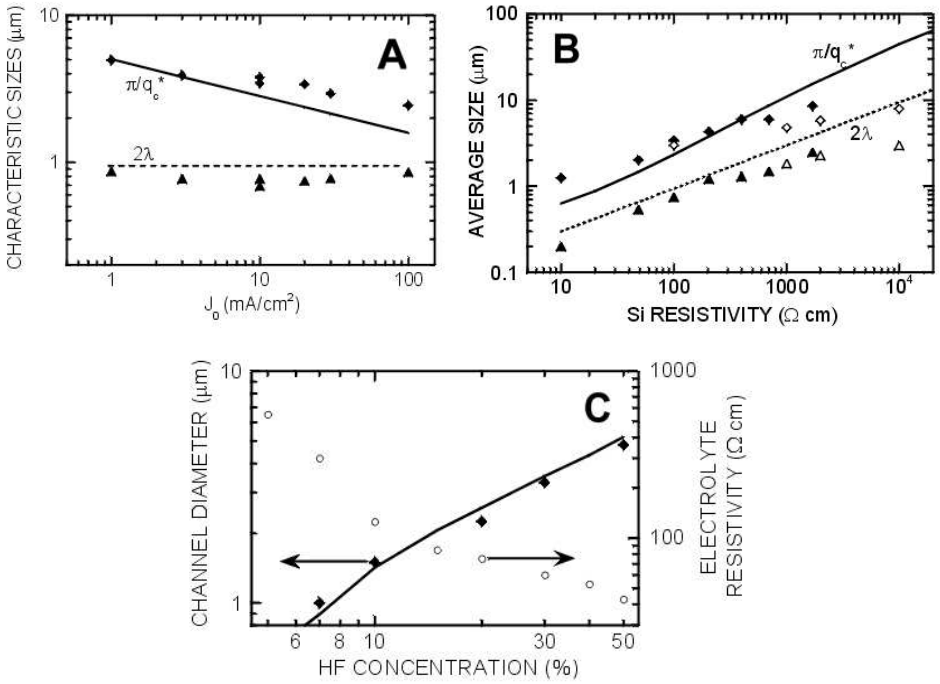

Abbildung 2.3: (a) Einfluß der Variation von J_0 auf die Dimensionen der Makroporen in p-typ Silizium. Mittlere Wandstärke (Theorie: gestrichelte Linie; Experiment: ▲) und mittlerer Porendurchmesser (Theorie: durchgezogene Linie; Experiment: ♦). Parameter: p-Si 100 Ωcm, 35% HF in EtoH. Die theoretischen Kurven wurden für Φ_{SC} = 0,1 eV, λ_{RLZ} = 0,47 μm, $v_R = 10^5$ cm/s, ρ_e = 4 Ωcm berechnet. (b) Einfluß der Variation des spezifischen Widerstandes von Silizium auf die Dimensionen der Makroporen. Durchschnittliche Wandstärke (Theorie: gestrichelte Linie; Experiment: ▲) und durchschnittlicher Porendurchmesser (Theorie: durchgezogene Linie; Experiment: ♦). Parameter: 35% HF in EtOH ($\Diamond, \triangle$: 25%), ρ_e = 4 Ωcm, J_0 = 10 mA/cm^2, Φ_{SC} = 0,1 eV, $\lambda_{\mathrm{RLZ}}/(\rho_s)^{1/2}$ [μm $(\Omega cm)^{-1/2}$] = 0,047, $v_R = 10^5$ cm/s. (c) Einfluß der Variation des spezifischen Widerstandes des Elektrolyten auf die Dimensionen der Makroporen. Durchschnittlicher Porendurchmesser (Theorie: durchgezogene Linie; Experiment: ♦). Parameter: p-Si 1500 Ωcm, J_0 = 10 mA/cm^2, der Elektrolyt ist 50% wässerige HF gemischt mit Ethylenglykol in unterschiedlichen Konzentrationen. Rechts: Spezifischer Widerstand des Elektrolyten (o). Die theoretischen Kurven wurden für Φ_{SC} = 0,1 eV, λ_{RLZ} = 1 μm and v_R (cm/s) = $3 \cdot 10^3 \times$HF% berechnet [21].

2.2.2.3 Geordnete Makroporenarrays in p-typ Silizium

Durch geeignete Kombination von Selbstordnung zum nächsten Nachbarn nach Gl. (2.6) und Photolithographie lassen sich langreichweitig geordnete Makroporenarrays erzeugen. Ich habe dies im Rahmen meiner Habilitation nicht weiter verfolgt. Die prinzipielle Machbarkeit ist aber in mehreren Veröffentlichungen gezeigt worden [17, 18, 24].

Der Nachteil von p-typ Silizium ist, dass die Wandstärke immer die zweifache Raumladungszone beträgt und somit direkt zum Porenabstand über Gl. (2.6) korreliert ist. Ein unabhängiges Einstellen von Wandstärke und Porenabstand ist mit diesem Material nicht möglich. Es ist allerdings mit n-typ Silizium möglich, welches von uns zur Herstellung von Photonischen Kristallen ausschließlich benutzt wird.

2.2.3 n-typ Silizium

Betrachtet man den Fall der unbeleuchteten n-typ Siliziumelektrode, ergibt sich das umgekehrte Strom-Spannungs-Verhalten im Vergleich zu p-typ Silizium. Im kathodischen Bereich kommt es zu einem exponentiellen Anstieg des Stroms, da in diesem Fall der Si/HF Schottky-Kontakt in Durchlassrichtung gepolt ist. Es kommt zur Wasserstoffbildung. Wird die n-typ Siliziumelektrode dagegen anodisch gepolt, ist die Si/HF-Schottkydiode in Sperrrichtung gepolt und nur ein geringer Dunkelstrom fliesst. Erst bei höheren Spannungen, die die Durchbruchsspannung U_{Durch} übersteigen, kommt es zum Durchbruch. Die Stromdichte steigt steil an. Es entstehen Mesoporen im Falle von hochdotierten Siliziumwafern [15].

Wird der Siliziumwafer von der Rückseite beleuchtet, können positive Ladungsträger (Löcher) im Inneren des Siliziumwafers erzeugt werden. Für anodische Potentiale sammeln sich die Löcher an der Grenzfläche Si/HF. Es fliesst ein Photostrom in Sperrrichtung der Diode. Die Strom-Spannungs-Kennlinie zeigt bei hohen Beleuchtungsstärken I_{light} denselben Verlauf wie im Falle des p-typ Siliziums, allerdings um die Differenz der Quasi-Ferminiveaus kathodisch verschoben. Diese Verschiebung führt auch zu einem Ätzstrom ohne äußeres Potential (U_{oc}). Ähnlich wie im Falle des p-typ Siliziums können auch für Potentiale zwischen U_{oc} und dem Elektropoliturpotential U_{PS} Mikroporen erzeugt werden.

Für niedrige Beleuchtungsstärken I_{light} bleibt der Photostrom nach kurzem Anstieg entlang der Kennlinie auf einem konstanten Wert. Aufgrund der Entkopplung von angelegtem Potential und angelegtem Strom, welcher durch die Rückseitenbeleuchtung gegeben ist, ist das Strom-Spannungs-Verhalten nicht mehr ein-eindeutig. Es kann durch geeignete Wahl des Potentials und des Stroms der gesamte Bereich unterhalb der I-U-Kennlinie abgedeckt werden. Damit ergibt sich z.B. auch die Möglichkeit, das Potential größer als das Elektropoliturpotential zu wählen, den Strom allerdings zu begrenzen. Diese Variante soll im Weiteren noch genauer diskutiert werden.

Es ist 1990 von Lehmann und Föll gezeigt worden [25], dass für Ströme $J < J(U_{PS}) = J_{PS}$ und Potentiale $U > U_{PS}$ mit $U < U_{Durch}$ stabile Makroporen wachsen. Die Porosität P folgt der einfachen Relation:

$$P = J/J_{PS} \propto I_{\mathrm{light}} \; . \tag{2.7}$$

Sie besagt, dass am Porenboden immer Elektropolitur herrscht und daher die Porosität limitiert ist durch die Fläche, auf der mit einem vorgegebenen Strom elektropoliert werden kann. Dies ist eine Näherung und genauere Untersuchungen zeigen, dass bei einer halbkugelförmigen Porenform der Elektropoliturstrom nicht überall gleich ist. Einfache geometrische Betrachtungen zeigen, dass an den Porenrändern $J < J_{PS}$ ist und sich daher mikroporöses Silizium bildet (Abb. 2.4).

Da Makroporen in n-typ Si also vor allem durch chemische Elektropolitur-Prozesse entstehen, dominieren diese auch die Kinetik. Das Porenwachstum ist in diesem Fall nicht durch den Stromtransport über eine Barriere wie im Falle des p-typ Siliziums limitiert sondern ausschließlich durch die chemische Auflösungsgeschwindigkeit der gebildeteten anodischen Oxidschicht. Diese hängt von der Temperatur T und der Konzentration der Flußsäure c ab. Experimentell ist für wässerige Elektrolyten folgende Abhängigkeit gefunden worden [26]:

$$J_{PS} = 3300 c^{3/2} \exp\left(\frac{-0,345eV}{kT}\right) \; [A/cm^2] \; . \tag{2.8}$$

Ähnlich wie p-typ Si Makroporen zeigen auch n-typ Makroporen keine langreichweitige Ordnung. Der nächste Nachbar ist definiert über Gl. (2.7) und die Breite der Raumladungszone (Abb. 2.4b). Die minimale Wanddicke ist bei ungeordneten Makroporen ungefähr das Doppelte der Raumladungszonenbreite. Allerdings kann im Gegensatz zu p-typ Silizium der Abstand zwischen zwei Poren bis zum zehnfachen der Raumladungszone betragen, wenn Ätzkeime lithographisch vorgegeben werden [28]. Bei noch größeren Abstanden gibt es eine signifikante Diffusion von Ladungsträger in die Porenwandbereiche. Die Porenwände werden auch seitlich photoelektrochemisch geätzt. Dies führt zu einer Aufrauhung der Porenwände und konischen Poren [28].

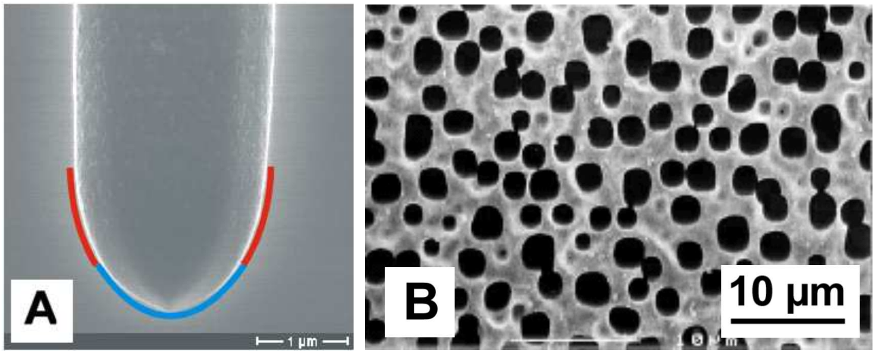

Abbildung 2.4: (a) REM-Detailaufnahme eines Porenbodens einer Makropore in n-typ Si. Der blau markierte Bereich der äußersten Porenspitze erscheint sehr glatt. Hier tritt während des Ätzprozesses Elektropolieren auf ($J = J_{PS}$). Der rot markierte Bereich erscheint rauh und besitzt eine mikroporöse Siliziumschicht an der Porenwand. Es gilt $J < J_{PS}$ [27]. (b) REM-Aufnahme eines ungeordneten Makroporenarrays.

2.2.3.1 Geordnete Makroporenarrays in n-typ Silizium

Eine langreichweitige Ordnung der Makoporen kann erzwungen werden, indem Nukleationskeime der Poren von vornherein vorgegeben werden. Im Gegensatz zu p-typ Silizium, kann das Muster und der Abstand relativ frei vorgegeben werden. Der Radius der Makroporen hängt hingegen von der mittleren Stromdichte J ab. Da die Porosität nach Gl. (2.7) definiert ist, folgt für das hexagonale Gitter :

$$r = a\sqrt{\frac{\sqrt{3}J}{2\pi J_{PS}}}\ . \tag{2.9}$$

Hohe Beleuchtungsstärken ergeben nach Gl. (2.7) hohe Ströme und damit nach Gl. (2.9) weite Poren. Damit lässt sich der Radius der Poren während der Ätzens einstellen. Dies ist eine wichtige Möglichkeit, Diffusionsprozesse in tiefen Poren, die die Ätzgeschwindigkeit nach Gl. (2.8) verändern, zu kompensieren. Sie erlauben auch bei starken Variationen der Belechtungsstärke den Porendurchmesser mit der Tiefe zu modulieren (siehe Abschnitt 2.2.3.2). Angefangen mit Arbeiten von Grüning und Lehmann wurden hexagonale Porenarrays mit Gitterkonstanten a von 8 μm [29] und 3 μm [30] hergestellt. A. Birner reduzierte die Gitterkonstante auf 1,5 μm [31]. Wir haben in den letzten Jahren Porenarrays mit Gitterkonstanten von a = 1; 0,7 und 0,5 μm hergestellt [27, 7]. Die 0,5 μm Porenarrays mit einer Tiefe von 100 μm sind in Abb. 2.5 gezeigt.

Zu beachten ist, dass bei kleineren Gitterkonstanten a die Wände immer dünner werden. Sie besitzen aber einen minimalen Durchmesser, der der zweifachen Raumladungszonebreite λ_{RLZ} entspricht. Diese ist definiert als

$$\lambda_{\mathrm{RLZ}} = \sqrt{\frac{2\varepsilon_{Si}\varepsilon_0(U + \Phi_{\mathrm{SC}})}{qN_D}}\ . \tag{2.10}$$

Um kleinere Porenwände erzeugen zu können, muss die Dotierung erhöht werden, da die angelegte Spannung mit $U > U_{PS}$ festgelegt ist. Typischerweise erlauben Dotierungen von 0,5 Ωcm (λ_{RLZ} = 360 nm für $U + \Phi_{\mathrm{SC}}$ = 1 V), Gitterkonstanten bis ca. 1 μm. Für kleinere Strukturen müssen Dotierungen von 0,1 Ωcm (λ_{RLZ} = 115 nm für $U + \Phi_{\mathrm{SC}}$ = 1 V) benutzt werden. Mit den höheren Dotierungen treten zwei Probleme auf. (a) Die Diffusionslängen für elektronische Löcher im Silizium werden auf Grund des Einbaus von Störstellen und durch erhöhte Rekombination immer schlechter. Die Qualität des Siliziumswafer ist somit von entscheidender Bedeutung. (b) Das Durchbruchspotential der Raumladungszone reduziert sich. Für eine ebene Grenzfläche ergibt sich für das Durchbruchspotential U_{Durch}

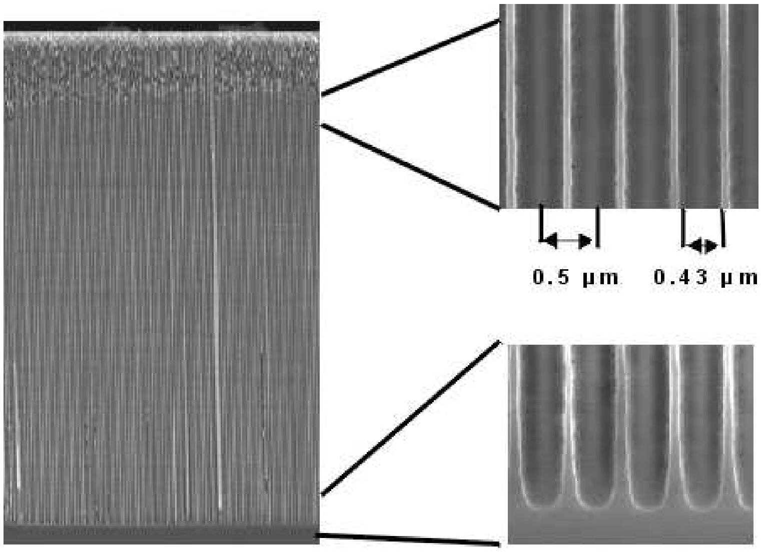

Abbildung 2.5: REM-Detailaufnahme eines hexagonalen Silizium-Makroporenarrays mit 0,5 μm Gitterkonstante und 100 μm Tiefe. Der Porendurchmesser ist 430 nm [7].

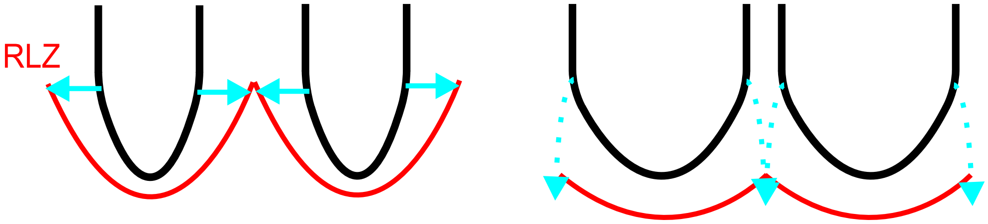

Abbildung 2.6: Reduzierung der Bildung von Mesoporen durch größere Porendurchmesser. Links: Kleine Porendurchmesser. Die Raumladungszone λ_{RLZ} im Bereich der Flanken des Porenbodens ist dünn und die Feldstärke daher hoch. Durchbrüche entstehen (blaue Pfeile). Rechts: Durch einen größeren Porendurchmesser ist die Krümmung geringer. Die Überlappung der Raumladungszonen führt zu geringen Feldstärken im Bereich der Flanken der Porenböden. Dadurch wird die Durchbruchsfeldstärke erheblich erhöht [27].

$$U_{\text{Durch}} = \frac{E_{\text{Durch}} w}{2} \,, \tag{2.11}$$

wobei die Durchbruchsfeldstärke von Silizium $E_{\text{Durch}} = 3 \cdot 10^5$ V/cm beträgt. Durch selbstkonsistenten Lösen von Gln. (2.10) und (2.11), ergibt sich für eine ebene Grenzfläche $U_{\text{Durch}} \sim$ 3,5 V für n-typ Siliziumwafer mit einem spez. Widerstand von 0.1 Ωcm. Da aber die Poren am Porenboden stark gekrümmt sind, muss die Poisson-Gleichung dreidimensional gelöst werden. Für sphärische Krümmungsradien von 160 nm ergeben sich Durchbruchsspannungen von $U_{\text{Durch}} \approx 2$ V [32]. Andererseits ist für stabiles Makroporenwachstum mindestens $U > U_{PS}$ nötig. Um die Entstehung von Durchbrüchen, die zu Mesoporen führen zu verhindern, haben wir folgende Strategie gewählt (Abb. 2.6): Durch größere Beleuchtungsstärken während des Ätzens kommt es zu einem vergrößerten Porendurchmesser. Dadurch wird die Krümmung der Raumladungszone und damit die Durchbruchsfeldstärke lokal reduziert.

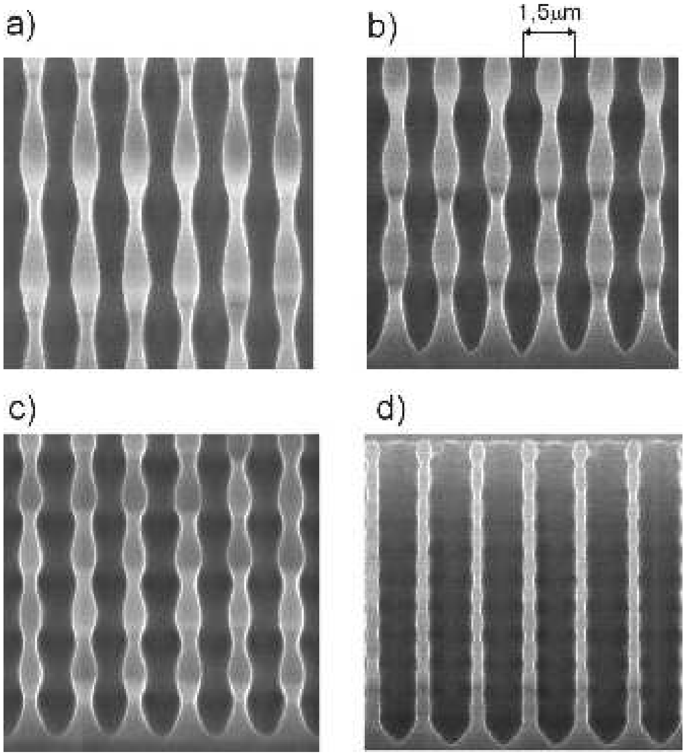

Abbildung 2.7: REM-Bilder von Längsschnitten modulierter Poren mit unterschiedlichen Modulationsperioden bei gleicher Gitterkonstante $a = 1,5\mu m$. Vorgegebene Modulationsperioden: 1;2;3 und 4 μm. Gemessene Perioden: 0,84; 1,73; 2,62; 3,59 μm [27].

2.2.3.2 Modulierte Makroporenarrays

Eine einzigartige Möglichkeit der dreidimensionalen Strukturierung ergibt sich aus Gl. (2.7). Da der Porendurchmesser durch die aktuelle Stromdichte definiert ist, welche wiederum durch die Beleuchtungsintensität bestimmt ist, lässt sich der Porendurchmesser mit der Tiefe beliebig verändern. Jörg Schilling zeigte in seiner Dissertation, dass ein parabolisches Sägezahnprofil in der Beleuchtungsintensität, und damit lineares Sägezahnprofil im Radius, zu sinusförmig modulierten Poren führt [27]. Wird das Sägezahnprofil außerdem noch bezüglich der veränderten Wachstumsgeschwindigkeit mit der Tiefe kompensiert, können perfekt modulierte Poren hergestellt werden, die einen dreidimensionalen Photonischen Kristall erzeugen. Abbildung 2.7 zeigt mehrere Profile für unterschiedliche Perioden des Sägezahnprofils bei gleicher Gitterkonstante a. Es ist allerdings eine leichte Verschmierung des Profils zu erkennen sowie eine Verkürzung der sinusförmigen Periode im Vergleich zur Periode des Sägezahnprofils. Dies ist auf zwei Faktoren zurückzuführen:

(a) Die Ätzgeschwindigkeit ist durch die chemische Auflösungsgeschwindigkeit des anodischen SiO_2 bestimmt. Werden große Mengen an positiven Ladungsträgern angeboten, so diffundieren diese in die Porenwände und vergrößern schon geätzte Bereiche. Dies führt zu einer Verschmierung des Sägezahnprofils und einem reduzierten Modulationshub. Analytische Abschätzungen und Zufalls-Läufer-Modelle (*DLA*) bestätigen diese Annahme. Diese Verschmierung kann reduziert werden, indem das Verhältnis der vorgegebenen Modulationsperiode τ_{mod} und der chemischen Auflöserate $1/\tau_{\text{chem}}$des anodischen Oxides $\tau_{\text{mod}}/\tau_{\text{chem}} \approx 1$ wird. Dies kann entweder durch eine Reduzierung der Modulationsperiode $1/\tau_{\text{mod}}$ erzielt werden (siehe Abb. 2.7) oder durch eine Erhöhung der chemischen Auflöserate $1/\tau_{\text{chem}}$ des anodischen SiO_2. Die letztere Möglichkeit ist in wässrigen Elektrolyten über kleine Bereiche über die HF-Konzentration und die Temperatur zu erzielen [Gl. (2.8)]. Allerdings ist für organische

HF-Elektrolyte gezeigt worden, dass viel geringere Verschmierungen auftreten [33]. Dies ist auf die schlechte Qualität des anodischen Oxides zurückzuführen und die damit verbundene höhere Auflöserate.

(b) Die Verringerung der Modulationsperiode um einige Prozent ist auf eine kurzfristige Verarmung von F^- zurückzuführen und damit nach Gl. (2.8) einer reduzierten Ätzrate. Dies kann durch langsame Ätzgeschwidigkeiten, d.h. niedrigere Temperaturen, teilweise kompensiert werden.

Zusammengefasst lassen sich mit diesem Verfahren durch die Variation der Beleuchtungsstärke periodische Porendurchmessermodulationen erzeugen. Die besten Ergebnisse wurden für Modulationsperioden $l_z < a$ erzeugt.

2.3 Ventilmetalloxide

2.3.1 Aluminiumoxid

2.3.1.1 Einleitung

Unter Lufteinfluss bildet sich auf der Oberfläche von Aluminium ein natürlicher, homogen geschlossener Oxidfilm von ca. 3 nm Dicke. Der Aluminiumoxidfilm (Al_2O_3) richtet Wechselspannungen gleich und wirkt auf elektrische Ströme wie eine Diode [10]. Wegen dieser physikalischen Eigenschaft wird Aluminium wie auch z.B. Titan und Tantal zur Gruppe der Ventilmetalle gezählt. Durch eine elektrochemische Oxidation kann die Dicke der natürlichen Oxidschicht gesteigert und damit die physikalischen Eigenschaften gezielt manipuliert werden. Die ersten Anwendungen von oxidierten Aluminiumoberflächen waren Kondensatoren und Stromgleichrichter. Bei Kondensatoren wird Al_2O_3 als Dielektrikum verwendet, wobei die Oxiddicke vom Oxidationspotential linear abhängt. Typischerweise können homogene dielektrische Schichten mit Dicken bis max. 1 μm, was einem Potential U = 800 V entspricht, erzeugt werden. Wesentliche Arbeiten auf dem Gebiet des Elektrolytkondensators wurden u.a. von Betz und Günterschulz [34] in den Jahren 1890 bis 1930 geleistet.

Der Prozess der elektrochemischen Oxidation von Aluminium wird im Deutschen eloxieren genannt, und die sich bildende Oxidschicht wird als Eloxal bezeichnet. Poröses Al_2O_3 wurde patentrechtlich das erste mal 1898 erwähnt [35]. Die Schichtdicke ist bei porösem Al_2O_3 nicht mehr von dem Oxidationspotential abhängig, sondern wächst linear mit der Zeit, sodass poröse Oxidschichten mit Dicken von mehr als 100 μm erzeugt werden können. Diese mechanisch widerstandsfähigen Oxidschichten werden vor allem zur Korossionspassivierung von Aluminiumteilen im Flugzeugbau und bei der Veredelung von Haushaltswaren und Möbeln [36] aus Aluminium eingesetzt.

Einen großen Fortschritt bei der Herstellung von porösem Al_2O_3 erzielten Masuda und Fukuda im Jahre 1995 [37]: Unter bestimmten Bedingungen können geordnete Al_2O_3-Porenstrukturen mit perfekt geordneten Domänen im Mikrometerbereich erzeugt werden, die durchgehend gerade Poren in einem hexagonalen Gitter mit einem monodispersen Porendurchmesser $2r$ aufweisen. Aufbauend auf Masudas und Fukudas Entdeckungen wurde es möglich, durch eine lithographische Vorstrukturierung der Aluminiumoberfläche die Poren in eine perfekte hexagonale Ordnung zu zwingen (Monodomäne). Auf Grund der Strukturgrößen im Submikrometer-Bereich wurde dies mittels Elektronenstrahllithographie [38] oder *Imprint*-Lithographie [39] erzielt. Jüngste Arbeiten von Masuda [40] zeigen, dass andere Konfigurationen der Porenanordnung, wie z.B. quadratische Gitter, möglich sind. Diese Konfiguration ist allerdings metastabil, und mit fortschreitendem Porenwachstum ordnen sich die Poren im Grundzustand der hexagonalen Anordnung an.

Im Folgenden wird auf die Grundlagen der elektrochemischen Bildung von Al_2O_3, die Entstehung von porösen Oxidschichten und im Speziellen auf die Bildung hochgeordneter Porenstrukturen eingegangen. Hierzu werden neue experimentelle Ergebnisse zur Herstellung und zum Aufbau der Oxidstruktur gezeigt und das Modell zum geordneten Porenwachstum von Jessensky und Müller [41] weiterentwickelt. Um Photonische Kristalle aus Al_2O_3 herzustellen, ist ein neues *Imprint*-Verfahren entwickelt worden. Perfekt geordnete Strukturen mit a = 500 nm konnten durch Kombination von Selbstordnung und Lithographie hergestellt werden.

2.3.1.2 Ungeordnete Aluminiumoxid-Porenstrukturen

Die Anodisierung von Aluminium in wässrigen Elektrolyten ist bestimmt durch die Drift von Anionen und Kationen im elektrischen Feld und den Ratengleichungen an den beiden Grenzflächen. Die Art des anodischen Oxides hängt von seiner Löslichkeit im Elektrolyten ab und bestimmt damit die dritte Ratengleichung. Man kann daher drei Fälle unterscheiden:

- Wenn das anodische Oxid im Elektrolyten unlöslich ist, entsteht eine einheitliche Oxidschicht deren Dicke D nur von dem angelegten Potential U abhängt :

  $$D \propto \alpha U \ , \tag{2.12}$$

  wobei α zwischen 1,2 und 1,4 nm/V liegt [42]. Elektrolyten mit einer sehr niedrigen Al_2O_3-Löslichkeit sind z.B. Borsäure, Zitronensäure oder Essigsäure.

- Wenn das anodische Oxid sehr schwerlöslich löslich im Elektrolyten ist, entsteht ein poröser anodischer Film, dessen Wachstum detaillierter weiter unten beschrieben wird. Elektrolyten sind Schwefelsäure, Chromsäure, Oxalsäure und Phosphorsäure [42] sowie Derivate der Oxalsäure [43].

- Wenn das anodische Oxid im Elektrolyten gut löslich ist, wird die Aluminiumoberfläche elektropoliert. Elektrolyt ist z.B. Perchlorsäure. Bei einigen Säuren wie Salzsäure können auch Oberflächenrauigkeiten im Aluminiumfilm selbst entstehen, weil das Durchbruchspotential sehr reduziert ist (Pitting).

Das Wachstum von ungeordneten Porenstrukturen wurde in den letzten 40 Jahren ausführlich studiert und es ergibt sich zwischen dem angelegten Potential U und dem mittleren Porenabstand a folgende Relation [42, 44]:

$$a = 2r + 2\alpha U \ . \tag{2.13}$$

Die elektrochemische Anodisation kann entweder potentiostatisch oder galvanostatisch durchgeführt werden. Da der mittlere Porenabstand nach Gl. (2.13) durch das Potential festgelegt ist, wird normalerweise potentiostatisch gearbeitet. Abbildung 2.8 zeigt eine typische Stromtransiente $(I - t)$ von Aluminium in Oxalsäure. Man kann die Entstehung der porösen Schicht in vier Regime einteilen. In Phase I wird ein fast planares Barrierenoxid gebildet, welches mit zunehmender Dicke zu einem stark abklingenden Strom führt. Die maximale Dicke ist durch die Drift von Anionen und Kationen bestimmt und damit durch das angelegte Potential [Gl. (2.12)]. Wenn die Anodisation mit nichtauflösenden Elektrolyten wie z.B. Borsäure durchgeführt wird, bleibt der Strom konstant niedrig bis es schließlich für sehr hohe Potential zum Durchbruch des Oxides kommt. Ist jedoch das anodische Oxid nur ein wenig löslich im Elektrolyten, treten Fluktuationen an der Oberfläche auf (Phase II). Stromlinien verstärken sich an Fluktuationen der Grenzfläche und es gibt eine felderhöhte Auflösung des Oxides [45, 46]. Aufgrund des überhöhten elektrischen Feldes an den konvexgekrümmten Oberflächen, ist die Ionendrift erhöht. Der Strom steigt global (Phase III) und Poren beginnen zu wachsen (Abb. 2.8b). In Phase IV sinkt der Strom auf Grund des Absterbens einiger Poren leicht bis ein stabiler Fluktuationenwellenvektor $2\pi/a$ bzw. eine stabile Porendichte n erreicht ist. Sie ist im hexagonalen Gitter über Gl. (2.13) definiert als $n_{hex} = 2\alpha^{-2}U^{-2}/\sqrt{3}$. Die Phasen I bis III laufen bei Oxalsäure innerhalb von 20 bis 30 min ab. Der Potentialverlauf in Phase IV gibt Aufschluss über geordnetes Wachstum [47] . Die Ähnlichkeiten der Porenentstehung mit der Ausbildung eines stabilen Wellenvektors ähneln sehr denen einer

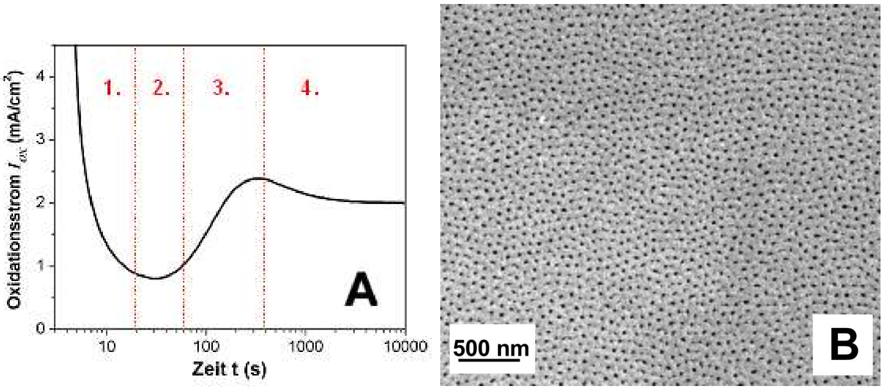

Abbildung 2.8: (a) Stromtransienten während der potentiostatischen Anodisation von Aluminium in Oxalsäure. (b) Rasterelektronenmikroskopische Aufnahme von ungeordnetem porösem Aluminiumoxid [49].

linearen Stabilitätsanalyse (Abschn. 2.2.2.2). Für dieses System lassen sich die Laplace-Gleichungen aufstellen, wie Parkhutik et al. [44] zeigten. Sie vernachlässigten aber die chemische Komponente der feldunterstützten Porenauflösung am Boden in ihren Rechnungen. Realistischere Stabilitätsanalysen wurden kürzlich von Thamida und Chang [48] durchgeführt. Durch Berücksichtigung des pH-Werts am Porenboden konnte neben Gl. (2.13) auch gezeigt werden, dass das r/a-Verhältnis nur durch den pH-Wert bestimmt ist und nicht durch das Potential. Diese theoretische Vorhersage wird im weiteren noch experimentell nachgewiesen und auf das selbstgeordnete Porenwachstum angewandt.

2.3.1.3 Selbstgeordnete Aluminiumoxid-Porenstrukturen

Masuda and Fukuda [37] entdeckten 1995, dass sich nach langen Anodisationszeiten die Poren in porösem Aluminiumoxid im 2D–hexagonalen Gitter anordnen. Dieses Phänomen tritt allerdings nur unter ganz bestimmten Bedingung auf. Es konnten geordnete Strukturen mit a = 65, 100 und 500 nm hergestellt werden (siehe Tab. 2.1). Selbstordnung tritt nur auf, wenn die Art der Säure, die Konzentration, die Temperatur und die Spannung zueinander passen. In Abb. 2.9 ist die Vorder- und Rückseite von porösem Aluminiumoxid, welches unter Selbstordnungsbedingungen hergestellt worden ist, gezeigt. Numerische Auswertungen des Ordnungsgrades zeigen, dass die Größe der geordneten Domänen (in μm^2) mit der Zeit linear wächst. Der maximale Durchmesser der Domäne beträgt typischerweise bis zu 30 a (Abb. 2.9c). Dies entspricht im Falle a = 500 nm (H_3PO_4, 195V) ca. 15μm (Abb.2.9c und 2.10). Dies lässt sich auch mit der Paarverteilungsfunktion, d.h. dem Analogon der radialen Verteilungsfunktion in der Kristallographie, nachweisen [50]. Neben der Verbesserung des Ordnungsgrades erhöht sich auch die Monodispersität des Porendurchmessers. Während bei ungeordneten Strukturen eine typische Standardabweichung der Porendurchmesserverteilung von 25% numerisch ermittelt wurde, ergibt sich für geordnete Strukturen eine Standardabweichung von nur 8% [50, 51].

Jessensky und Müller entwickelten 1998 ein Modell zur Beschreibung des geordneten Porenwachstums [41]. Es basiert auf der Annahme, dass die Umwandlung von Aluminium zu Aluminiumoxid zu einer Verdopplung des Volumens pro Al-Atom führt und somit mechanische Spannungen entstehen. Bei nichtporösen Oxidfilmen führt Volumenausdehnung zu Verspannungen und damit zu einer Verformung des Substrates. Bei porösen Oxidfilmen besitzt das System einen zusätzlichen Freiheitsgrad. Es kann mittels der Porosität die effektive Volumenausdehnung anpassen. Experimentell wurde von Jessenky und Müller mittels gravimetrischer Messungen gezeigt, dass geordnetes Wachstum immer dann entsteht, wenn eine Volumenausdehnung um einen Faktor 1,2 auftritt [41]. Dies ist von uns mittels genauer Messungen der Al-Konzentration im Elektrolyten über Atom-Absorptions-Spektroskopie bestätigt worden. Desweiteren wird vorausgesagt, das bei einer gegebenen Volumenausdehnung um den Fak-

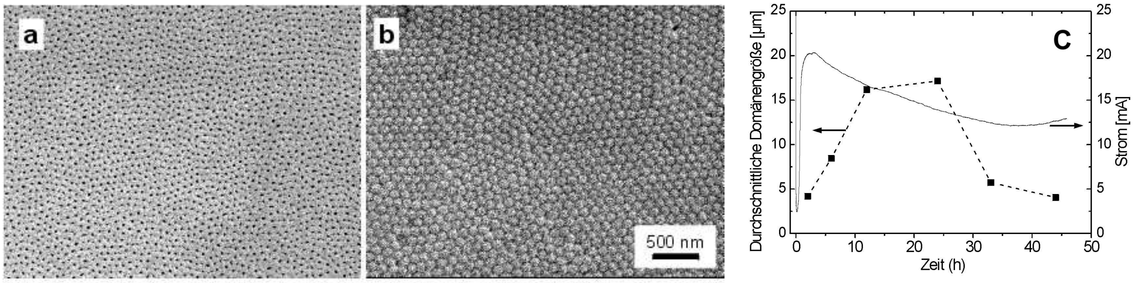

Abbildung 2.9: (a)Vorder- und (b) Rückseite einer porösen Aluminiumoxidstruktur, die unter geordneten Wachstumsbedingungen hergestellt worden ist. (c) Größe der geordneten Domäne als Funktion der Ätzzeit für die Anodisation von Aluminium (195 V in 1 wt % H_3PO_4) [53].

tor 1,2 unabhängig von dem Porendurchmesser bei geordneten Wachstumsregimen immer die gleiche Porosität erhalten wird. Dies wurde anfänglich bezweifelt, da Thompson und Wood unterschiedliche Porositäten für unterschiedliche Säuren bestimmten [52]. Allerdings waren 1981 die Regime geordneten Wachstums noch nicht bekannt. Wir konnten mittels Transmissionselektronenmikroskopie (TEM) zeigen, dass in der Tat für die geordneten Wachstumsregime immer dieselbe Porosität existiert (Abb. 2.11). Sie beträgt ca. 10%. Dies entspricht unter Berücksichtigung der entsprechenden Dichten genau einer Volumenausdehnung von einem Faktor 1,2 [53].

Da die Porosität in den geordneten Wachstumsregimes immer 10% beträgt, lassen sich Voraussagen über neue geordnete Regime treffen. Die Porosität im hexagonalen Gitter ist definiert durch

$$P = \frac{2\pi}{\sqrt{3}} \left(\frac{r}{a}\right)^2 . \tag{2.14}$$

Um den Gitterabstand im geordnetem Wachstum zu variieren, reicht es nicht aus, nur das Potential nach Gl. (2.13) zu verändern. Auch der Radius r muss dementsprechend angepasst werden. Der Porenradius hängt ausschließlich vom dem pH-Wert der Säure ab [48]. Erhöht man den pH-Wert, so erhöht man die Schwellspannung für die feldunterstützte chemische Aluminiumoxidauflösung am Porenboden; reduziert man den pH-Wert, so reduziert sich die Schwellspannung für die Auflösung. Intuitiv kann man sich das folgendermaßen vorstellen: das angelegte Potential fällt bei der Anodisation ausschließlich im Oxid ab. Dabei schwächt es Al-O Bindungen an Orten hoher Feldstärken am stärksten. Da in allen Elektrolyten Aluminiumoxid schwer löslich ist, erhöht sich die Löslichkeit an Orten erhöhter Feldstärke. Die absolute Löslichkeit hängt wiederum vom pH-Wert des Elektrolyten ab. Dieses einfache Modell kann anhand der Messdaten überprüft werden. Erhöht man den pH-Wert eines der Standard-Elektrolyten signifikant, so sollte sich der Porenabstand für geordnetes Wachstum verringern. Dies ist in Tabelle 2.1 deutlich sichtbar für Phosphorsäure und Schwefelsäure. Die Konzentration von Oxalsäure lässt sich in wässerigen Elektrolyten nicht weiter erhöhen. Auch kann man damit das Langzeitverhalten während Anodisationen verstehen. Verändert sich die Konzentration in tiefen Poren, so verändern sich auch die Bedingungen für geordnetes Wachstum und die geordneten Domänen verschwinden (Abb.2.9c) [53].

2.3.1.4 Lithographisch geordnete Aluminiumoxid-Porenstrukturen

Um langreichweitig geordnete Porenstrukturen mit einem perfekten Ordnungsgrad zu bekommen, ist Lithographie notwendig. Elektronenstrahl-Lithographie ist eine Möglichkeit, die u.a. von A.P. Li entwickelt worden ist [38]. Eine andere Möglichkeit ist das Nanoprägeverfahren (*Imprint*-Lithographie). Der große Vorteil der *Imprint*-Lithographie ist, dass der Stempel, welcher mit Elektronenstrahllithographie oder tiefer UV-Lithographie erzeugt wird, mehrmals verwendet werden kann. Dieses Verfahren

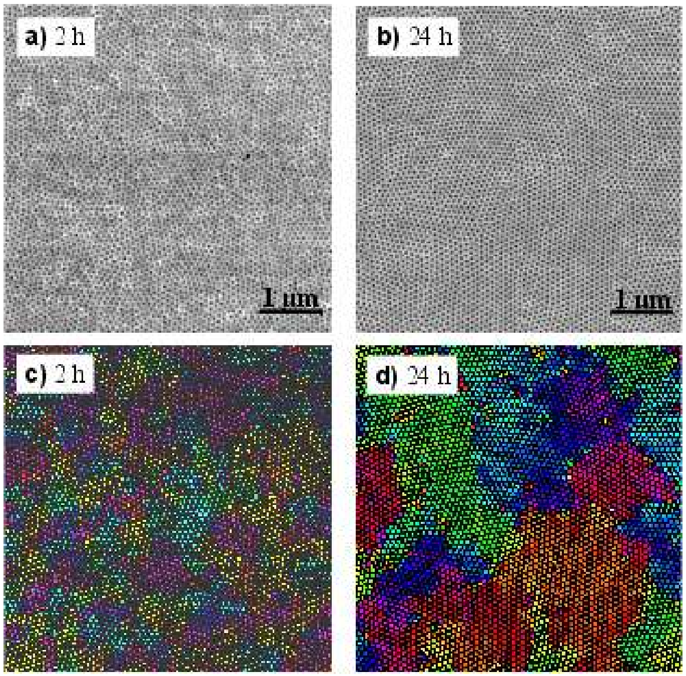

Abbildung 2.10: (a+b) REM-Aufnahme von zwei unterschiedlich stark geordneten Porenstrukturen nach verschiedenen Ätzzeiten (2 h und 24 h mit 195 V in 1 wt % H_3PO_4). (c+d) Numerische Auswertung der Domänen mittels Fehlfarben [53].

wurde erstmals von Masuda et al. [39] angewendet. Wir haben diese Technik weiterentwickelt und optimiert: Unser Stempel aus SiN-Pyramiden kann mit einem ca. 50-fach niedriger Prägedruck arbeiten als der von Masuda, welcher aus quaderförmigen Spitzen besteht [39]. Abbildung 2.12a zeigt den Stempel und damit hergestellte monodomänige Porenarrays mit einem Abstand von 500 nm [54]. Wir haben einen Stempel mit a = 500 nm gewählt, weil für diesen Porenabstand ein selbstgeordnetes Regime existiert. Die Kombination von Lithographie und Selbstordnung führt in diesem Fall zu sehr tiefen, perfekt geordneten Porenarrays, wie sie für photonische Anwendungen erforderlich sind (Abb. 2.12c). Würde man eine Gitterkonstante von z.B. 200 nm nehmen und nur die Spannung entsprechend anpassen, nicht aber den pH-Wert (siehe Kap. 2.3.1.3), so können keine tiefen, perfekt geordneten Porenarrays erzeugt werden. Die Ordnung geht nach einigen Mikrometern in Unordnung über [55]. Das nächste bekannte geordnete Wachstumsregime liegt bei ca. a = 100 nm. Es ist technologisch schwierig *Imprint*-Stempel

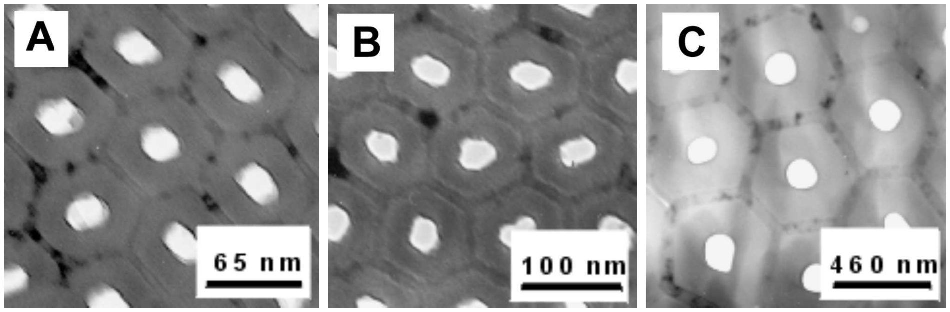

Abbildung 2.11: TEM-Bilder von selbstgeordneten Aluminiumoxid-Porenstrukturen. (a) 25 V in 1,7 wt % H_2SO_4, (b) 40 V in 2,7 wt % $(COOH)_2$, und (c) 195 V in 1 wt % H_3PO_4 [53].

Elektrolyt	Konz.(wt%)	Potential(V)	T (^{o}C)	a (nm)
Schwefelsäure	20	19	1	50
Schwefelsäure	1,7	25	1	65
Oxalsäure	2,7	40	1	100
Phosphorsäure	10	160	1	460
Phosphorsäure	1	195	1	500

Tabelle 2.1: Wachstumsbedingungen für geordnete Aluminiumoxidporenstrukturen.

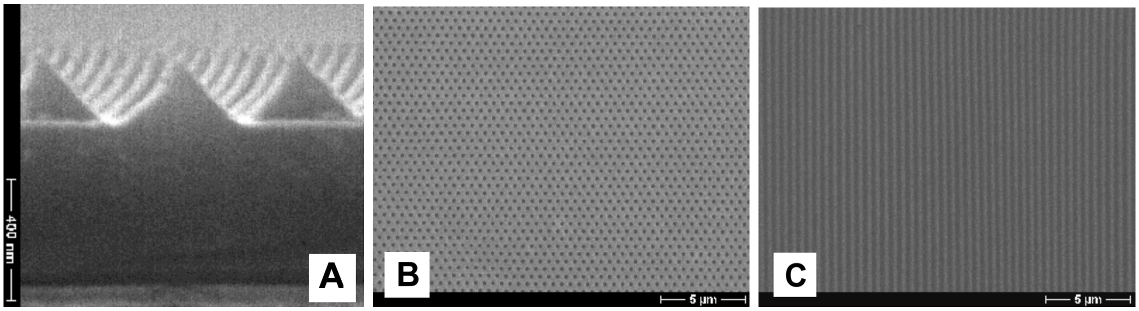

Abbildung 2.12: (a) REM-Seitenansicht unseres *Imprint*-Stempels. Poröses Aluminiumoxid, welches nach dem Abdruck des *Imprint*-Stempels hergestellt worden ist. (b) Draufsicht; (c) Seitenansicht [54].

mit einer solchen Periodizität herzustellen, da die benötigte Auflösung der Lithographie bei ca. 10 nm liegt.

Eine andere Möglichkeit, den Porenabstand im Aluminiumoxid zu reduzieren, ohne die Periodizität des *Imprint*-Stempels zu verändern, ist von uns kürzlich entwickelt worden [54]. Gibt man lithographisch ein Gitter von 500 nm Abstand vor, so können durch geeignete Wahl des Potentials und des Elektrolyten Poren im Zentrum von drei lithographisch definierten Poren erzeugt werden. Der effektive Porenabstand im Aluminiumoxid reduziert sich dadurch um ca. 40%. Wir konnten zeigen, dass über ein solches Verfahren ein Porenabstand von a = 300 nm mit einem *Imprint*-Stempel von a = 500 nm erreicht werden kann (Abb. 2.13). Da a = 300 nm kein selbstgeordnetes Wachstumsregime, bricht die vorgegebene Ordnung nach einigen Mikrometern ab. Der nächste Schritt wäre ein Stempel mit a = 180 nm, so dass man a = 110 nm erzielen kann. Desweiteren haben wir untersucht, wieviele lithographisch definierte Poren nötig sind, damit eine neue Pore in deren Zentrum wächst. Es konnte gezeigt werden, dass zwei nicht reichen, aber drei ausreichend sind, was einer Triangulierung im 2D–Gitter entspricht [54].

2.3.2 Andere Ventilmetalloxide

Neben Aluminiumoxid gibt es noch andere Ventilmetalle, die auch Porenwachstum aufweisen. Es ist allerdings noch keine Selbstordnung in diesen Systemen gezeigt worden. In der Literatur sind Studien über poröses Titanoxid und Tantaloxid beschrieben [10, 56]. Jinsub Choi ist es gelungen, die in der Literatur beschriebenen Ergebnisse in diesem beiden Materialien zu reproduzieren (Abb. 2.14). Allerdings konnten wir kein Porenwachstum entdecken, welches dem von Aluminiumoxid ähnelt. Dies liegt vermutlich an der geringen Durchbruchsfeldstärke E_{Durch} anderer Ventilmetalloxide. TiO_2 sowie Ta_2O_5 haben beide relativ geringe Bandlücken und damit niedrige E_{Durch} [10]. Um aber dicke poröse Oxide zu erhalten, muss die Schwelle für die feldaufgelöste Porenbildung weit unterhalb der Durchbruchsfeldstärke des Oxides liegen. Beide porösen Oxide in Abb. 2.14 entstehen aber weit oberhalb der Durchbruchsfeldstärke und sind Durchbruchsporen, die mit Oxid dekoriert sind. Andere Ventilme-

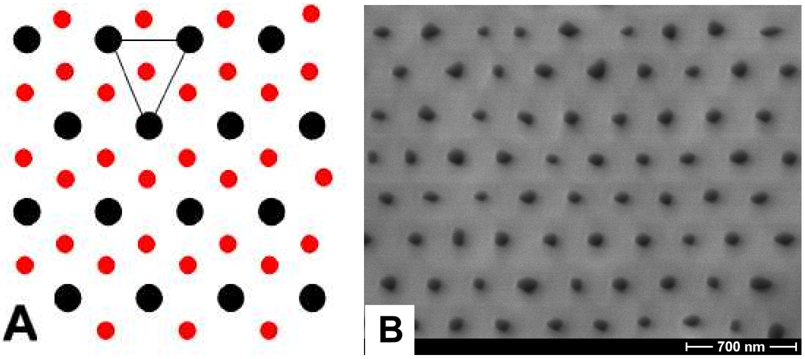

Abbildung 2.13: a) Schematische Darstellung der Strategie neue selbstgeordente Poren in der Mitte von lithographisch definierten Poren wachsen zu lassen. Große Kreise kennzeichnen Poren, die mittels Lithographie definiert worden sind und kleine Kreise kennzeichnen Poren, die aufgrund der Kombination von Selbstordnung und Lithographie entstehen. (b) Realisierung von (a). REM-Draufsicht einer mit a = 500 nm per *Imprint*-Lithographie vorstrukturierten porösen Aluminiumoxidstruktur. Der mittlere Porenabstand beträgt a = 300 nm. Wachstumsbedingungen: 2^oC bei 120V in 1,7 wt% Phosphorsäure [54].

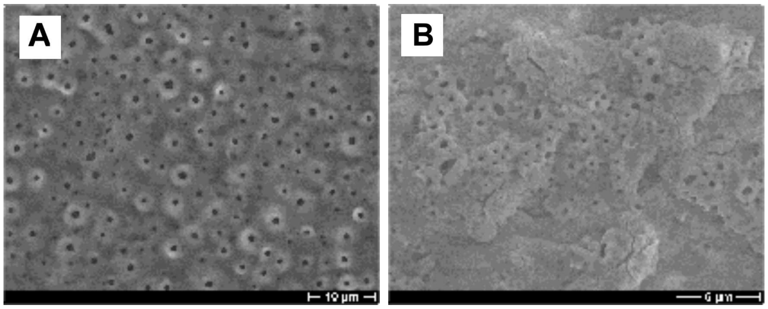

Abbildung 2.14: (a) REM-Draufsicht von porösem Titanoxid (10wt%H_3PO_4, 210V, 60^oC). (b) REM-Draufsicht von porösem Tantaloxid (1 wt% H_2SO_4, 210V, 10^oC).

talle mit größere Bandlücke wie Hafniumoxid ode Zirkoniumoxid mögen daher besser geeignet sein und sind Gegenstand unser aktuellen Forschungsbemühungen. Ein Oxid, welches aber ähnlich hohe Durchbruchsfeldstärken hat wie Al_2O_3, ist Siliziumoxid, welches im nächsten Kapitel diskutiert wird.

2.3.3 Siliziumoxid

Silizium hatten wir im vorigen Kapitel vor allem im Hinblick auf Makroporen im Silizium selbst untersucht (Kap. 2.2.2). Allerdings bildet sich für Potentiale oberhalb des Elektropoliturpotentials U_{PS} in HF ein anodisches Oxid. Dieses ist normalerweise nach Abstellen des Potentials nicht stabil und löst sich sofort auf. Ein Ausweg ist mit extrem niedrigen Konzentrationen bei tiefen Temperaturen zu ätzen, so dass das Oxid stabil bleibt. Ein typisches Voltammogram für das Si/HF System bis ca. 100 V ist in Abb. 2.15 gezeigt. Für den Potentialbereich zwischen 0 und 5 V ist das Voltammogram aus Abb. 2.1a zu erkennen. Ähnlich wie im Aluminiumoxid ist ein Plateau für höhere Potentiale deutlich erkennbar. Die Stromdichten sind etwa eine Größenordnung höher. Es gelang erstmals in diesem Regime, poröses SiO_2 herzustellen [57]. In Abbildung 2.15 ist poröses SiO_2 gezeigt, welches mit einem Potential von 30, 50 und 70 V hergestellt worden ist. Es ist ähnlich wie bei porösem Aluminiumoxid deutlich eine Vergrößerung des Porenabstandes mit dem angelegten Potential erkennbar. Die Porosität beträgt ca. 15%.

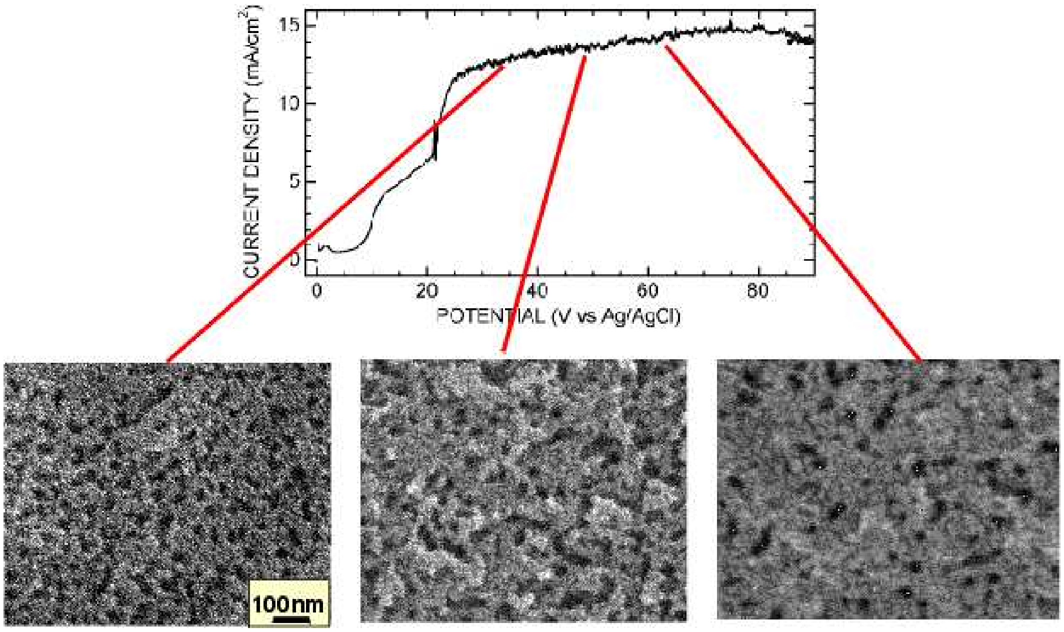

Abbildung 2.15: Voltammogram von 0 bis 100 V von p-Si (111) in HF (c_{HF} = 0,05 M, $pH > 3$, 1 M NH_4Cl + 0,025M NH_4F + 0,025 M HF) und die entsprechenden REM-Bilder von porösem Siliziumoxid, welches bei (a) 35 V, (b) 50 V und (c) 70 V hergestellt worden ist [57].

2.4 Replikate

2.4.1 Einführung

Poröses Aluminiumoxid und Silizium können als Templat zum Wachstum von Nanostäben oder Nanoröhrchen benutzt werden. Wir haben uns in den letzten Jahren intensiv mit der Herstellung von Nanostäben und -röhren aus Metallen und Polymeren beschäftigt.

2.4.2 Metallische Nanostäbe

2.4.2.1 Abscheidemethoden

Die elektrochemische Abscheidung von Metallen auf einer isolierenden Barrierenoxidschicht (D_{ox} = 1 – 1,3 nm/V $\times$ U) erfordert hohe Potentiale. Geordnete Al_2O_3-Porenstrukturen (U = 20-200 V mit D_{ox} = 25-250 nm) weisen ein besonders dickes Barrierenoxid im Vergleich zu ungeordneten Strukturen (U = 10-20 V mit D_{ox} = 10-25 nm) auf. Hohe Potentiale führen zu einer lokalen Zerstörung der Oxidschicht und zu einer unkontrollierten Abscheidung an Defekten.

Um dieses Problem zu umgehen, gibt es zwei in der Literatur beschriebene elektrochemische Abscheideverfahren. Bei der erste Methode wird das Aluminiumsubstrat von der Oxidmatrix entfernt, die Barrierenschicht am Porenboden chemisch aufgelöst und ein Elektrodenkontakt aufgebracht [58]. Damit kann das Metall mit einem Gleichstrom (DC) bei niedrigen Potenzialen abgeschieden werden. Diese Methode ist nur auf freitragende Membranstrukturen anwendbar, die typischerweise >20 μm dick sind und damit stabil genug sind, um mechanisch gehandhabt werden zu können. Das zweite Konzept wurde von Caboni 1936 [59] zum Füllen der Al_2O_3-Poren entwickelt. Dabei verbleibt die poröse Oxidstruktur auf dem Aluminiumsubstrat und das Metall wird unmittelbar auf dem Barrierenoxid abgeschieden. Der gleichrichtende Charakter der Barrierenschicht ermöglicht die Abscheidung mittels einer Wechselspannung (AC). Diese Methode eignet sich besonders für dünne Al_2O_3-Porenstrukturen. Für

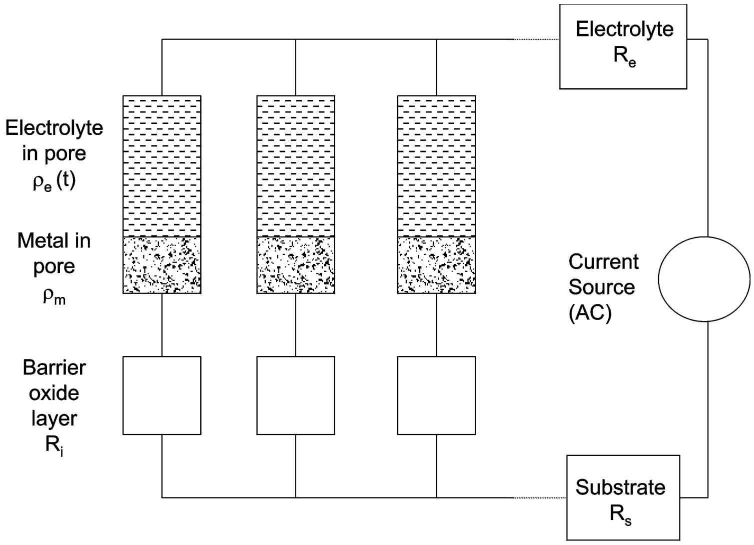

Abbildung 2.16: Ersatzschaltbild während gepulster Abscheidung in Aluminiumoxid-Porenstrukturen [60].

die meisten Anwendungen von Nanostrukturen ist eine Dicke der porösen Al_2O_3-Struktur von wenigen hundert Nanometern erforderlich. Deshalb wurde das Konzept von Caboni von uns im Falle von Al_2O_3-Strukturen benutzt und weiterentwickelt.

Die entscheidenden Weiterentwicklungen, die im Rahmen der Dissertation von K. Nielsch durchgeführt worden sind [49], sind das strombregenzte Abdünnen des Barrierenoxides und die stromgepulste Materialabscheidung, welche zu einer kompletten Füllung der Porenstrukturen führten. Das strombegrenzte Abdünnen reduziert das Abscheidepotential und fördert die Keimbildung in den Poren. Die stromgepulste Abscheidung ermöglicht eine homogenere Materialabscheidung in den Poren und kompensiert den langsamen diffusionsgetriebenen Ionentransport durch die Poren.

Dieses Problem lässt sich ähnlich wie im Falle des Porenwachstums mit elektrostatischen Instabilitäten beschreiben und kann teilweise anhand einer linearen Stabilitätsanalyse analysiert werden [60]. Abbildung 2.16 zeigt schematisch das Ersatzschaltbild während der gepulsten Abscheidung. Beginnend bei der Stromquelle, besteht das System aus dem Widerstand des Aluminiumsubstrates (R_s), danach sind alle Poren parallel geschaltet. Sie bestehen aus einem dünnen Barrierenoxid (R_i), dem abgeschiedenen Metall (ρ_m) und dem Elektrolyten (ρ_e). Am Ende liegt in Serie der Widerstand des Elektrolyten in der Zelle (R_e). Für die Stabilitätsanalyse kann der Potentialabfall im Elektrolyten in der Zelle sowie im Aluminiumsubstrat vernachlässigt werden, da Sie niedrige Serienwiderstände darstellen und daher nicht entscheidend für die Stabilitätsanalyse sind [22]. Es treten nun mehrere Instabilitäten in diesem System auf. Die größte Potentialfluktuation und damit Stromvariation entsteht, wenn das Barrierenoxid in den Poren nicht überall die gleiche Dicke aufweist. Diese Dickenfluktuationen sind durch den elektrochemischen Prozess immer gegeben. Daher sollte, wie schon von Zagiel et al. [61] diskutiert, die Barrierenoxiddicke und damit der Potentialabfall $U = iR_i$ gering sein im Vergleich zum Potentialabfall über ρ_e und ρ_m. Dies ist der Grund für das Abdünnen der Barrierenoxiddicke unterhalb von 10 nm. Jedoch ergeben selbst solch dünne Oxidfilme noch signifikante Potentialabfälle von ~6 V im Vergleich zu einigen 10 meV im Elektrolyten (Tab. 2.2). Deshalb und wegen der gleichrichtenden Eigenschaft des Barrierenoxides haben wir zusätzlich noch mit der gepulsten Abscheidung eine selbstlimitierende Strombegrenzung pro Pore eingebaut, die diese Instabilität kompensiert. Während eines 6 ms langen negativen Pulses werden alle Metallionen in der Pore aufgrund der angelegten hohen Stromdichte abgeschieden. Sind alle Metallionen in einer bestimmten Pore abgeschieden, reduziert sich der lokale Stromfluß und in einer andere Pore mit einem etwas dickerem Barrierenoxid werden alle Ionen abgeschieden. Eine einheitliche Abscheidefront entsteht und der Einfluss der Fluktuationen in R_i ist aufgrund des zeitabhängigen spezifischen Widerstandes ρ_e(t) reduziert.

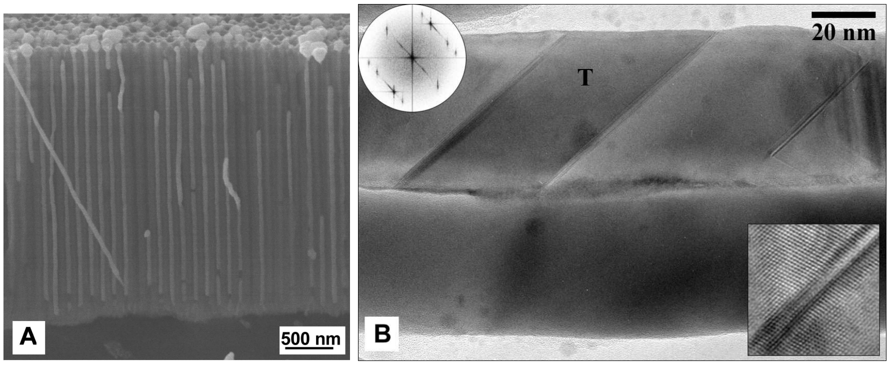

Abbildung 2.17: (a) REM-Bild einer Ag-gefüllten Aluminiumoxidmembran. (b) Höchstauflösendes TEM-Bild von einem Segment zweier nebeneinander liegender Silber-Nanostäbe. Der obere Stab hat drei planare Defekte, welche im Detail in der eingefügten Box zu sehen sind. Das Beugungsbild zeigt die Relation des Gitter zwischen der Zwillingslamelle (T) und der Stabmatrix [60].

Während des nachfolgenden positiven Pulses wird die Kapazität des Barrierenoxides entladen. Desweiteren ist der positive Puls für eine gute Kristallinität des Metalles förderlich. Dobrev et al. [62] stellen fest, dass während des postiven Pulses ein Teil des Stromes zur Widerauflösung des Metalles beiträgt. Dabei wird selektiv das defektreiche Metall aufgelöst und somit epitaktisches Wachstums gefördert. Wir fanden bei Silberstäben einen ähnlichen Effekt [60].

Neben der Instabilität, welche durch eine räumliche Variation von R_i ausgelöst wird, gibt es bei der Abscheidung in parallel geschalteten Poren noch eine viel grundlegendere Instabilität, die zu einem inhomogenen Füllgrad führt. Die Metall-Nanostäbe haben immer einen niedrigeren spezifischen Widerstand als der Elektrolyt ($\rho_e > \rho_m$). Kleine Fluktuationen in der Stablänge werden durch diesen Effekt verstärkt, ähnlich dem Wachstum von Poren in hochresistivem p-typ Silizium [20, 22]. Daher kann Gl. (2.5) angewandt werden und der Koeffizient α lautet in diesem Fall

$$\alpha = \frac{\rho_e - \rho_m}{\rho_e + qR_i + \rho_m} q \; . \tag{2.15}$$

Falls α negativ ist, wachsen die Metallstäbe einheitlich und es gibt einen homogenen Füllgrad. Wenn α positiv ist, ist das Wachstum instabil und der Füllgrad ist < 100%. Da immer $\rho_e > \rho_m$ gilt (Tab. 2.2), ist das Wachstum von Nanostäben immer instabil, ein 100%iger Füllgrad ist theoretisch nicht erreichbar. Dies gilt allerdings nur für unendlich dicke Template. $1/\alpha$ stellt eine typische Länge dar, ab der die Wachstumfront instabil wird und einige Silberstäbe schneller wachsen als andere. Eine Möglichkeit bei endlichen Templatdicken h einen homogen Füllgrad zu bekommen, existiert wenn $1/\alpha \geq h$. Da $\rho_m \ll \rho_e$, vereinfacht sich $1/\alpha$ zu $1/\alpha = 1/q + R_i/\rho_e$. Für $q \approx 10^5 \mathrm{cm}^{-1}$, $R_i \approx 36\ \Omega\mathrm{cm}^2$ bezogen auf eine Stromdichte von I = 15 mA/cm^2 und einer Porosität von 9%, $\rho_e \approx 10\ \Omega\mathrm{cm}$, ist $1/\alpha$ begrenzt durch den Term R_i/ρ_e, d.h. grenzflächen- oder barrierenoxidlimitiert. Damit ist die Barrierenoxiddicke und die Leitfähigkeit des Elektrolyten proportional zu $1/\alpha$. Dies unterstreicht die Bedeutung von hochleitfähigen Elektrolyten wie Wattsbädern für Abscheidungen. Vergleicht man diese Ergebnisse mit empirischen Rezepten aus der Literatur, so benutzen gerade die Gruppen, die einen 100% Füllgrad erreichen, ähnliche Parameter (Tab 2.2) [63, 64]

Elektrochemische Abscheidung von Metallen in Siliziumporen ist komplizierter, da Silizium selbst leitfähig ist. Wir haben daher in diesem Fall ausschließlich autokatalytische Abscheidebäder benutzt, mit denen stromlos abgeschieden werden kann [66].

Material	Spez. Widerstand [Ωcm]
Nickel (bulk)	6,3e-6
Silber (bulk)	1,4e-6
Nickel-Watts-Bad [65]	14
Metzger Co-Bad [63]	77
Xu Ni-Bad [64]	500
Silber-Elektrolyt [60]	5.2

Tabelle 2.2: Spezifische Widerstände einiger Metalle und Elektrolyten, teilweise Rezepte aus der Literatur (gemessen bei 38°C).

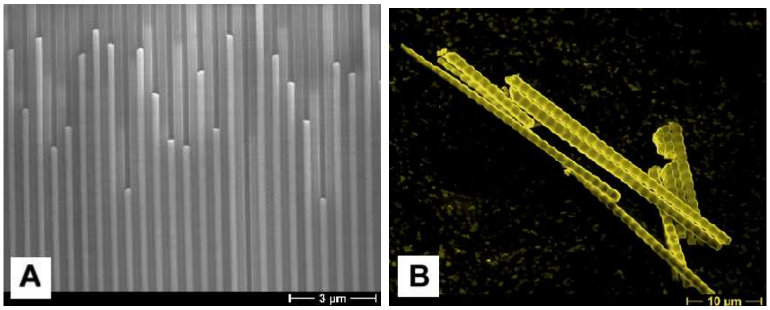

Abbildung 2.18: (a) REM-Seitensicht auf ein Ag-gefülltes, mittels *Imprint*-Lithgrographie hergestelltes, Al_2O_3-Templat (a = 500 nm) [51]. (b) REM-Bild von sinusförmig modulierten Goldmikrostäben [66].

2.4.2.2 Metallische Nanostabensembles

Wir haben uns in den letzten Jahren im Rahmen der Dissertation von K. Nielsch [49] mit der Abscheidung von magnetischen Materialien wie Ni, Co, NiFe und Pt-Legierungen in Al_2O_3-Poren mit einem Durchmesser von 25 bis 70 nm beschäftigt. Das Ziel war, magnetische Nanostabensembles herzustellen und die Wechselwirkung der Nanostabmagneten zueinander zu charakterisieren (Kap. 3.3). Im Rahmen der Dissertation von Guido Sauer erweiterten wir dieses Materialsystem auf Edelmetall-Nanostäbe aus Cu, Ag and Au (Abb. 2.17) [60], um optische Effekte wie Mie-Streuung und oberflächenverstärkten Ramaneffekt an Nanostäben zu untersuchen (Kap. 3.2). Im Rahmen der Dissertation von Jinsub Choi versuchten wir, metallo-dielektrische Photonische Kristalle herzustellen (Kap. 3.2). Dabei müssen die Durchmesser der Metallstäbe in der Größenordnung der Wellenlänge des Lichtes sein. Es ist uns gelungen mittels *Imprint*-Lithographie hergestellte Al_2O_3-Porenstrukturen mit einem Abstand von 500 nm und Porendurchmessern von 180 bis 400 nm mit Silber zu füllen (Abb. 2.18a) [51]. Desweiteren haben wir auch 2D– und 3D–Si-photonische Kristalle mit Edelmetallen repliziert (Abb. 2.18b). Diese sollen in Zukunft als selektive thermische Emitter charakterisiert werden [67]. Außerdem können sie im Bereich der Nanobiotechnologie als z.B. Biomarker eingesetzt werden [66, 68]. Zusammengefaßt haben wir in den letzten Jahren ein Baukastensysten entwickelt, um metallische Mikro- und Nanostäbe mit Durchmessern von einigen Mikrometern bis ca. 25 nm herzustellen, die eine Vielzahl von Studien im Bereich der Grundlagenforschung ermöglichten und ermöglichen werden.

2.4.3 Polymer- und Polymerkomposit-Nanoröhrchen

2.4.3.1 Konzept der Benetzung von Porenstrukturen

Die Funktionalisierung von Porenstrukturen, beispielsweise für durchstimmbare photonische Kristalle oder licht-emmittierende Materialien in den Poren, ist ein weiterer wichtiger Baustein in unserem Bau-

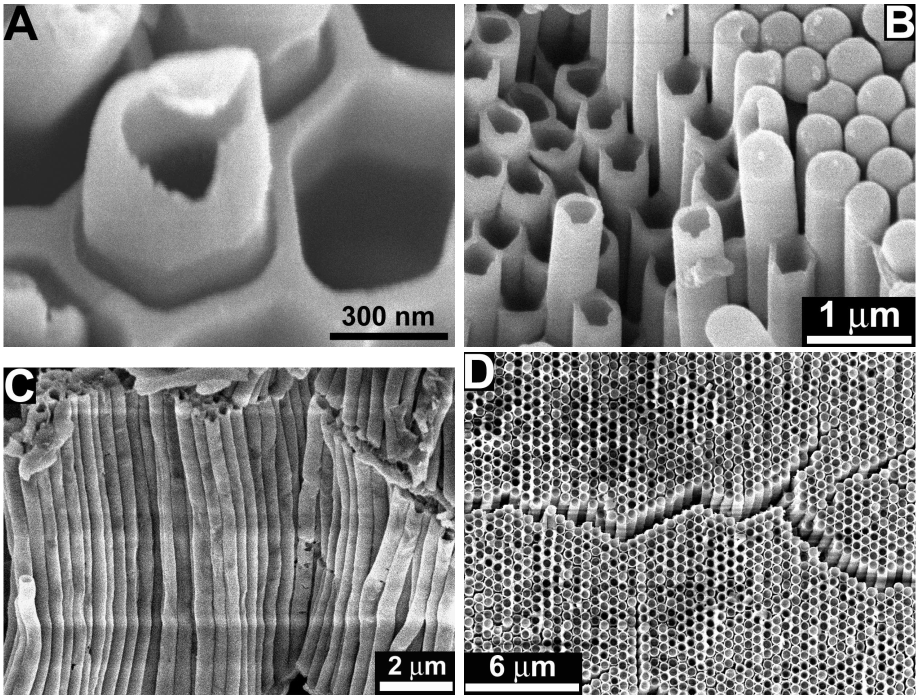

Abbildung 2.19: REM-Aufnahmen von Nanoröhrchen, die mittels Benetzung hergestellt wurden. (A) Beschädigte Spitze einer Polystyrol-Nanoröhre in einer Aluminiumoxid-Porenstruktur (M = 850000 g/mol). (B) Hexagonale Anordnung von Polystyrol-Nanoröhrchen nach selektivem Entfernen des Templates. (C) Anordnung von PTFE (Teflon) Nanoröhrchen. (D) Geordnete Anordnung von PMMA-Nanoröhrchen [73].

kastensystem, den wir in den letzten Jahre eingehend untersucht haben. Während Templatsynthesen zur Herstellung von Nanoröhrchen und Nanostäben seit langem bekannt und in der Literatur ausführlich beschrieben sind [69], enwickelten wir ein Verfahren, welches auf der Benetzung von Oberflächen mit hoher Oberflächenenrgie basiert[1]. Spreitet ein Tropfen einer organischen Flüssigkeit auf einem flachen Substrat mit hoher Oberflächenenergie, benetzt die Flüssigkeit die Hochenergieoberfläche. Der Kontaktwinkel ist null. Unter diesen Bedingungen kann sich ein Vorläuferfilm (engl. precursor film) bilden [70, 71, 72]. Dieser breitet sich vom Fuß des makroskopischen Tropfens aus auf dem Substrat aus, wobei seine Dicke von ca. 100 nm bis zu einer molekularen Monolage reichen kann. Die laterale Ausdehnung eines solchen Vorläuferfilmes kann die des makroskopischen Tropfens um ein Vielfaches überschreiten. Dies wurde insbesondere bei viskosen, nicht flüchtigen Flüssigkeiten wie Polydimethylsiloxan oder Polystyrol beobachtet.

Es ist zu erwarten, dass ähnliche Benetzungsphänomene auftreten, wenn Polymere enthaltene Flüssigkeiten wie Polymerschmelzen oder -lösungen in Kontakt mit Makroporösem Silizium[2] oder porösem Aluminiumoxid gebracht werden. Dies ist der Tat der Fall, und erlaubt die Herstellung von Nanoröhrchen (Abb. 2.19) [73]. Das zugrunde liegende Prinzip ist schematisch in Abb. 2.20 dargestellt. Wenn die Polymere enthaltende Flüssigkeit in Kontakt mit einer porösen Struktur gebracht wird (Abb. 2.20a), benetzt aufgrund der Adhäsion zuerst ein dünner Vorläuferfilm die Porenwände innerhalb einer Zeitspanne, die bis hinunter in den Bereich einiger Sekunden reichen kann (Abb. 2.20b). Bei den zugrundeliegenden Wechselwirkungen dürfte sich es hauptsächlich um van der Waals-Kräfte handeln, wenngleich bei einzelnen Materialsystemen auch Chemisorption in Betracht zu ziehen ist.

---

[1] Nimmt man Wasser als Referenz, so entspricht einer hohen Oberflächenenergie Hydrophobie und einer niedrigen Oberflächenenergie Hydrophilie.

[2] Während Silizium eine Niedrigenergieoberfäche ist, sind die Porenwände von Makroporösem Si von einer hochenergetischen SiO_2-Schicht bedeckt.

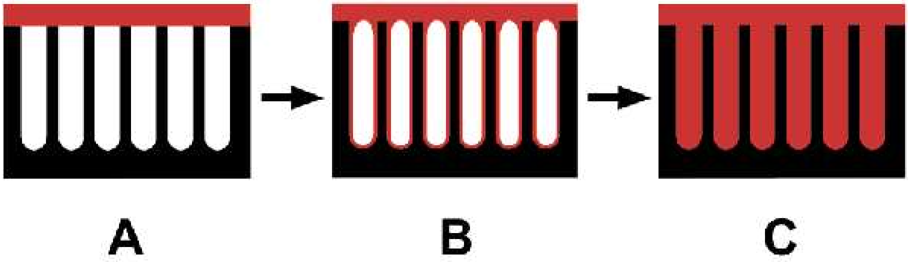

Abbildung 2.20: Schematische Darstellung der Kinetik von Flüssigkeiten in Mikro- und Nanoporen. (A) Das Polymer wird in Kontakt mit der Porenstruktur gebracht. (B) Wenn das Polymer thermisch verflüssigt wird, benetzen die Porenwände mit einem dünnen Polymerfilm sehr schnell. (C) Im Gleichgewicht ist die Pore komplett befüllt. Die Befüllung tritt aber erst nach sehr langen Zeiten auf und hängt von der Viskosität des Polymers ab.

Während ein flaches Substrat als unendlich betrachtet werden kann, ist die zu benetzende Fläche einer Pore endlich. Wenn an allen Adsorptionsplätzen der Porenwand Polymerkettensegmente adsorbiert sind, bildet sich ein kinetisch stabiler stationärer Zustand aus. Kohäsion ist die Triebkraft für die komplette Befüllung des Porenvolumens (Abb. 2.20c). Diese läuft allerdings auf einer wesentlich langsameren Zeitskala ab als die Benetzung der Wände. Nach Ausbildung des benetztenden Films kann der Prozess eingefroren werden, indem durch Abkühlen oder Verdampfen eines Lösungsmittels zumindest eine polymere Komponente den Glasübergang durchläuft oder kristallisiert. Man erhält so Nanoröhrchen mit einer Wandstärke in der Größenordnung von etwa 20 nm, wobei die als Templat fungierende Porenstruktur selektiv entfernt werden kann. Durch Aufschmelzen verschiedener Strukturpolymere wie Polymethylmethacrylat oder Polystyrol wurden Nanoröhrchen aus diesen Materialien als Pulver oder hochgeordnete Anordnung präpariert (Abb. 2.19). Ersmals gelang die Herstellung von Polytetrafluorethylen (PTFE)-Nanoröhrchen auch aus PTFE mit hohen Molekulargewichten (Abb. 2.19c). Das hier vorgestellte Konzept ist universell: auch Polymere enthaltende Mehrkomponentensysteme können die Poren benetzten. Auf diese Weise ist es möglich, anorganische Materialien in die Poren einzubringen. Die Nanoröhrchen können durch Induzieren von Entmischungsprozessen, selektives Entfernen einzelner Komponenten oder chemische Umwandlungen weiter funktionalisiert werden. Beispiele sind in den folgenden Abschnitten beschrieben.

2.4.3.2 Funktionalisierung von Polymernanoröhrchen

Die Benetzungmethode kann relativ einfach modifiziert werden, um anorganische Nanoröhrchen bzw. Polymerkomposit-Nanoröhrchen herzustellen. Werden polymere Komponenten mit anorganischen Materialien vermischt, sind diese mit in den Wänden der Nanoröhrchen enthalten. Weitere Funktionalisierung kann chemisch oder physikalisch erfolgen. Ein Beispiel hierfür sind Palladium-Nanoröhrchen mit definierter Wand-Morphologie [74]. Zunächst wird das Templat mit einer Lösung, die Polylactid (PLA) und Palladiumacetat ($Pd(OAc)_2$) enthält, benetzt. Durch Verdampfen des Lösungsmittels tritt eine Entmischung beider Materialien ein. Bei 200^oC wird $Pd(OAc)_2$ zersetzt und Palladium zum Metall reduziert. Durch Tempern bei 200^oC kann die Größe der Palladium-Nanokristallite, die ein zusammenhängendes Netzwerk bilden, eingestellt und schließlich PLA selektiv entfernt. Dieser Prozess erlaubt die Herstellung strukturierter Palladium-Nanoröhrchen, deren Wände Poren definierter Größe aufweisen (Abb. 2.21b). Da Palladium seinerseits eine hohe Oberflächenenergie besitzt, können weitere Benetzungsschritte erfolgen. Wir stellten beispielsweise Palladium/Polystyrol-Kompositröhrchen mit einer Kern-Schale-Morphologie her (Abb. 2.21a). Weitere Beispiele für funktionalisierte Nanoröhrchen sind Blei-Zirkonium-Titanat-(PZT)-Nanoröhrchen. Wir haben das ferroelektrische Oxide PZT in Nanoröhrchen mittels dieses sakrifiziellen Benetzungs-Verfahrens umgewandelt (Abb. 2.21c). Sie zeigen nach entsprechender Temperung ferroelektrische Hysteresen [75]. Auch bei diesem Verfahren kann die

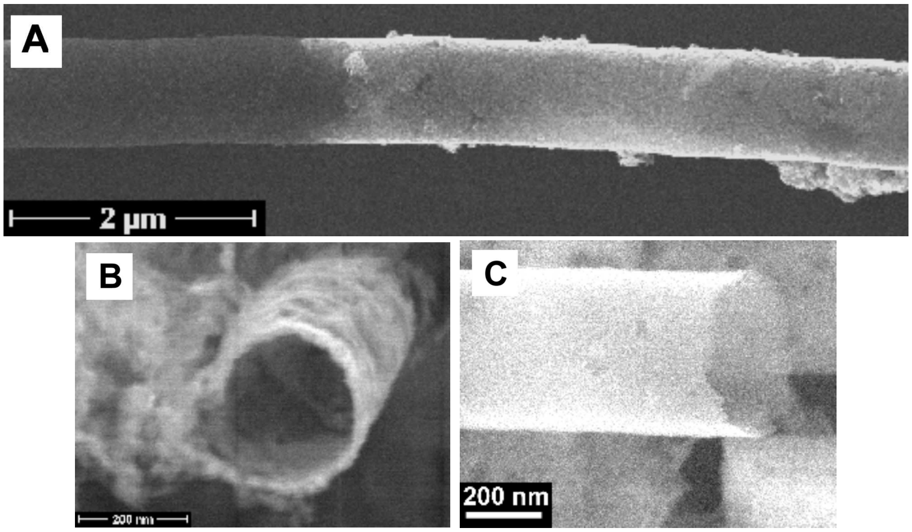

Abbildung 2.21: (a) REM-Aufnahmen von (a) Polystyrol/Palladium-Komposit-Nanoröhrchen. Das Polystyrolröhrchen ist dunkelgrau und teilweise mit einem Netz aus Pd bedeckt (hell); (b) Palladium-Nanoröhrchen;(c) Blei-Zirkonium-Titanat-(PZT)-Nanoröhrchens.

Wandstärke mittels sukzessivem Wiederholens der Benetzung in 20-nm-Schritten vergrößert werden. Dies bietet im Bereich der Photonik längerfristig die Möglichkeit der elektro-optischen Durchstimmbarkeit von Photonischen Kristallen (Kap. 3.1).

2.4.3.3 Funktionalisierung von Porenstrukturen

Neben der Herstellung funktionalisierter Nanoröhrchen als Pulver oder Anordnung parallel ausgerichteter Röhrchen, können auch die porösen Templatstrukturen ihrerseits durch Benetzten der Porenwände mit geeigneten Materialsystemen z. B. hinsichtlich ihrer optischen und magnetischen Eigenschaften funktionalisiert werden.

So ist es uns gelungen photoaddressierbare Polymere wie PMMA-Disperse Red 1 zu infiltrieren, welche einen trimmbaren Brechungsindex besitzen [76]. Außerdem konnten wir Polystyrol gemischt mit HgTe-Quantenpunkten in die Poren der Photonischen Kristalle infiltrieren [77]. Da die Wandstärke der Polymermischung ca. 20 nm ist, sind die einige nm großen Quantenpunkte sehr genau im Photonischen Kristall lokalisiert. Dies ist im Hinblick auf die Untersuchung der Abstrahleigenschaften von Emittern in Photonischen Kristallen, welche über die lokale Zustandsdichte beschrieben wird, sehr wichtig (Kap. 3.1) [78].

3 Anwendungen geordneter poröser Nanostrukturen

3.1 Photonische Kristalle

3.1.1 Einführung

Photonische Kristalle sind Strukturen, in denen der Brechungsindex räumlich periodisch variiert. Diese Variation des Brechungsindexes wird durch die Kombination von mindestens zwei verschiedenen Materialien mit unterschiedlichem Brechungsindex erreicht. Je nachdem, in wievielen Raumrichtungen der Brechungsindex periodisch variiert, werden 1D–, 2D– und 3D–Photonische Kristalle unterschieden. Treffen elektromagnetische Wellen auf den Photonischen Kristall, so werden diese aufgrund der Brechungsindexvariation in der Struktur gestreut. Solange die Wellenlänge der elektromagnetischen Strahlung viel größer ist als die Gitterkonstante des Photonischen Kristalls, verhält sich die Struktur wie ein effektives Medium. Wird die Wellenlänge jedoch vergleichbar mit der Periodizität des Photonischen Kristalls, tritt Bragg-Streuung auf. Ähnlich der Röntgenbeugung, lässt sich Bragg-Streuung als konstruktive Interferenz von Streuwellen deuten, die von parallelen Gitternetzebenen des Photonischen Kristalls ausgesandt werden. Sind die Wellenlängen viel kleiner als die Periodizität der Struktur, lässt sich Lichtausbreitung mittels geometrischer Optik beschreiben.

3.1.1.1 Mathematische Beschreibung von Photonischen Kristallen

Bei der mathematischen Beschreibung von Photonischen Kristallen ist man vor allem an zwei Eigenschaften interessiert, der Dispersionsrelation $\omega(k)$ einer unendlichen periodischen Struktur und den Transmissions/Reflexions-Eigenschaften $I/I_0(\omega)$ einer endlichen periodischen Struktur. Für die meisten experimentell untersuchten Photonischen Kristalle können dabei folgende Annahmen getroffen werden:

- die Dielektrizitätskonstanten der Materialien sind isotrop, d.h. $\varepsilon(\vec{r})$ ist skalar,
- die Dielektrische Funktion $\varepsilon(\vec{r})$ ist frequenzunabhängig,
- $\varepsilon(\vec{r})$ is reell, Absorption kann vernächlässigt werden,
- die magnetische Suszeptibilität $\mu = 1$,
- es existieren keine freien Ladungen ρ und keine Ströme J.

Mit diesen Annahmen vereinfachen sich die Maxwellschen Gleichungen zu

$$\nabla \cdot \vec{D}(\vec{r},t) = \nabla \cdot \varepsilon(\vec{r})\varepsilon_0\vec{E}(\vec{r},t) = 0 \tag{3.1}$$

$$\nabla \cdot \vec{B}(\vec{r},t) = \mu_0 \nabla \cdot \vec{H}(\vec{r},t) = 0 \tag{3.2}$$

$$\nabla \times \vec{E}(\vec{r},t) = -\mu_0 \frac{\partial \vec{H}(\vec{r},t)}{\partial t} \tag{3.3}$$

Methode	Dispersionsrelation $\omega(k)$	Transmission $I(\omega)$	Ref.
Ebene-Wellen	ja	nein	[82]
Sakoda-Ebene-Wellen	nein	ja ($\varepsilon < 2$)	[83, 84]
KKR	ja	ja	[85]
Transfer-Matrix	nein	ja	[86]
FD-TD	ja	ja	[87]

Tabelle 3.1: Methoden zur Berechnung der Dispersionsrelation und der Transmission/Reflexion von Photonischen Kristallen.

$$\nabla \times \vec{H}(\vec{r},t) = \frac{\varepsilon(\vec{r})\varepsilon_0 \partial \vec{E}(\vec{r},t)}{\partial t} \tag{3.4}$$

Dabei bezeichnen $\vec{E}$ das elektrische Feld, $\vec{D}$ die dielektrische Verschiebung, $\vec{H}$ das magnetische Feld und $\vec{B}$ die magnetische Flußdichte. Aus den Rotationsgleichungen (3.3) und (3.4) lassen sich die Wellengleichungen für die Moden des E- und H-Feldes herleiten:

$$\nabla \times \nabla \times \vec{E}(\vec{r},t) = \frac{\varepsilon(\vec{r})}{c^2} \frac{\partial^2 \vec{E}(\vec{r},t)}{\partial t^2} , \tag{3.5}$$

$$\nabla \times \left[\frac{1}{\varepsilon(\vec{r})} \nabla \times \vec{H}(\vec{r},t) \right] = -\frac{1}{c^2} \frac{\partial^2 \vec{H}(\vec{r},t)}{\partial t^2} . \tag{3.6}$$

Es reicht aus eine der beiden Wellengleichungen (3.5) oder (3.6) zu lösen. Die Lösung für das andere Feld kann unter Berücksichtigung der Maxwellschen Gleichungen (3.3) oder (3.4) erhalten werden. Tabelle 3.1 gibt eine Übersicht über die z. Zt. gängigen Methoden zur Lösung der Dispersionsrelation und der Transmission bzw. Reflexion. Es soll hier nicht weiter auf die Details eingegangen werden weshalb auf mehrere Übersichtsartikel verwiesen wird [79, 80, 81].

Um die Dispersionsrelation eines unendlich ausgedehnten Photonischen Kristalls vollständig zu beschreiben, reicht es aus, die Dispersionsrelation $\omega(k)$ der irreduziblen Brillouin-Zone zu berechnen (Bandstruktur). Unsere Bandstrukturrechnungen sind vor allem mit der Ebenen-Wellen-Methode zur Lösung der Dispersionsrelation in enger Zusammenarbeit mit Kurt Busch durchgeführt worden. Die Sakoda-Methode sowie die Transfer-Matrix Methode wurden zur Bestimmung der Transmission verwendet. In Kooperation mit dem M. Agio (Univ. Pavia and Ames Lab) and O. Hess (DLR Stuttgart) wurden auch 2D– und 3D–FD–TD–Simulationen für Defektstrukturen verwendet, sowohl für die Transmission wie auch für die Dispersionsrelation.

Die Lösungen der Maxwellschen Gleichungen nach Gl. (3.5) oder (3.6) sind im Gegensatz zu der Schrödingergleichung oder anderen Wellengleichungen skalierbar. Wird die Gitterkonstante a um den Faktor s vergrößert, so verringern sich die Eigenfrequenzen umgekehrt proportional um den Faktor $1/s$. Die Bandstruktur hängt daher nur von der verwendeten Symmetrie, den Brechungsindizes und der Porosität (r/a-Verhältnis) ab. Daher kann man die Eigenfrequenzen in normalisierten Einheiten von $\omega a/(2\pi c)$ und die Wellenvektoren in Einheiten von $ka/(2\pi)$ darstellen.

3.1.2 2D– contra 3D–Photonische Kristalle

Die physikalischen Auswirkungen der Maxwellschen Gleichungen für einen periodischen Brechungsindex lassen sich im Prinzip an 1D–Photonischen Kristallen zeigen [80, 88]. Im Gegensatz zu 1D–Photonischen Kristallen (Bragg-Stapeln), besitzen 2D– und 3D–Photonische Kristalle einen zuätzlichen Freiheitsgrad: die Symmetrie. 3D–Photonische Kristalle ermöglichen außerdem die vollständige Kontrolle über die Ausbreitung des Lichtes. Dies erlaubt die Manipulation von Licht mit Auswirkungen wie der Unterdrückung der spontanen Emission, der Herstellung von optischen Transistoren und

Kristall-Struktur	Min. n_1/n_2 für dielektrische Stäbe	Min. n_1/n_2 für Luftstäbe	Ref.
Quadratisch	keine Bandlücke	3,51	[90]
Hexagonal	keine Bandlücke	2,66	[90]
Graphit	2,55	$\approx 3{,}2$	[91]

Tabelle 3.2: Literaturübersicht über 2D–Photonische Kristalle und deren minimalen Brechungsindexkontrast n_1/n_2 für eine vollständige 2D Bandlücke.

bei Defekten die Erhöhung der spontanen Emissionsrate (Purcell-Effekt) [89]. Es erlaubt aber auch, 3D–beschränkte Wellenleiter herzustellen, die eine Miniaturisierung von linearen und nichtlinearen optischen Funktionen auf sehr kleinem Raum ermöglichen.

Um die grundlegenden Auswirkungen der Symmetrie auf Photonische Kristalle zu untersuchen sind 2D–Photonische Kristalle ein ideales Modellsystem. Mit ihnen kann man unterschiedliche Gittertypen und die Auswirkung des Brechens einer und beider Translationssymmetrien untersuchen. Allerdings existieren nur wenige "echte" 2D–Photonische Kristalle, da die Struktur für elektromagnetische Wellen in der dritten Dimension unendlich sein muss. Numerische Berechnungen von C. Jamois zeigen, dass "unendlich" für Moden mit normalen Gruppengeschwindigkeiten einem Aspektverhältnis $h/(2r) \geq 20$ entspricht. Dies lässt sich nur mit modernsten Plasmastrukturierungsmethoden erreichen. Elektrochemisch hergestelltes makroporöses Silizium kann Aspektverhältnisse $h/(2r) > 100$ erreichen und ist damit ein ideales Modellsystem zur Untersuchung der Eigenschaften von 2D–Photonischen Kristallen.

Die Auswirkungen der Symmetrie des 2D–Gitters auf den Bereich der Interferenztotalreflexion (photonische Bandlücke) sind in Tab. 3.2 dargestellt. Eine besonders große 2D–Bandlücke wird erreicht, wenn die Brillouin-Zone einem Kreis ähnelt, wie es im hexagonalen System der Fall ist. Derartige Systeme haben wir in den letzten fünf Jahren eingehend untersucht (Kap. 3.1.3) [7].

Für eine vollständige Kontrolle der Ausbreitung des Lichtes ist allerdings eine 3D–Beschränkung nötig. Der Idealfall ist ein 3D–Photonischer Kristall, den man dreidimensional maßschneidern könnte. Dies erfordert den Einsatz von 3D–Lithographie, welche derzeit noch nicht in ausgereifter Form zu Verfügung steht. Daher ist man materialseitig auf solche Strukturen angewiesen, die sich mittels konventioneller Lithographie und Mikrostrukturierungstechniken herstellen lassen. Eine Übersicht über Designs von 3D–Photonischen Kristallen mit einer vollständigen Bandlücke ist in Tab. 3.3 aufgelistet. Allerdings ist bis jetzt noch kein 3D–Photonischer Kristall aus dieser Liste mit einer perfekten Ordnung und einer Ausdehnung von mind. 10 Gitterperioden in alle Richtungen im infraroten Spektralbereich hergestellt worden. Realisierung basieren entweder auf Selbstordnungsphänomenen und leiden unter Gitterfehlern (invertierte Opale) [92] oder sie basieren auf Mikrostrukturierungstechnologien und erlauben nur eine sehr begrenzte Anzahl von Gitterkonstanten (Holzstapel-Strukturen) [93]. Mein Ziel ist es durch die Kombination von Selbstordnung und Lithographie zu ausgedehnten, defektfreien 3D–Photonischen Kristallen zu gelangen (Kap. 3.1.4).

Ein Ausweg aus dem Dilemma, einerseits 3D–Kontrolle über die Lichtausbreitung zu erzielen und andererseits mit der planaren Mikrostrukturierungstechnologie kompatibel zu sein, sind 2,5D–Photonische Kristalle. In diesem Fall ist die Kontrolle der Lichtausbreitung in der Ebene über einen 2D–Photonischen Kristall gegeben. In der dritten Dimension wird das Licht über totale interne Reflexion kontrolliert. Typische Realisierungen sind entweder Membranstrukturen oder vergrabene Schichtstrukturen. Im Ersteren ist das äußere Medium, welches den totalen internen Reflexionswinkel definiert, Luft (n = 1), im anderen Fall ein Dielektrikum mit niedrigerem Brechungsindex wie z.B. Siliziumdioxid (n = 1,4) in dem die wellenführende Siliziumschicht vergraben ist. Wie wir in Kap. 3.1.5 zeigen, kann dieses System eine vollständige 3D–Kontrolle der Ausbreitung des Lichtes ermöglichen, solange wie in wenigstens einer Dimension Translationssymmetrie existiert. Wird die Translationssymmetrie allerdings gebrochen wie bei Wellenleiterknicken oder Punktresonatoren, existieren keine Blochmoden

3D–Bandlücke (Bänder)	Kristall-Struktur	Trivial-Name	$\Delta\omega/\omega$ für Si/Luft[%]	Ref.
2–3	Diamant	Diamant	29	[82]
	Diamant-ähnlich	Yablonovit	19	[94]
	Diamant-ähnlich	**Kielovit**	22	[95]
	Diamant-ähnlich	Holzstapel	20	[96]
	Diamant-ähnlich	2D–Schicht-Diamant	21	[97]
4–5	sc	Spiral-Struktur	17	[98]
	Tetragonal	Square-Spiral-Struktur	24	[99]
	bc-orthorhombisch	2D–Schicht-Tetragon	23	[100]
5–6	**Inv. sc**	**Inv. Scaffold**	7	[101]
8–9	Inv. fcc	Inv. Opal	4,25	[102]
16–17	Inv. hcp	Inv. hexagonaler Opal	2,8	[103]

Tabelle 3.3: Literaturübersicht über 3D–Photonische Kristalle mit theoretisch berechneter Bandlückenbreite $\Delta\omega/\omega$ für einen Brechungsindexkontrast von n_1/n_2 = 3,4. Je niedriger die Moden sind zwischen denen die Bandlücke liegt, desto robuster ist die Bandlücke. Die fettgedruckten Kristalle lassen sich aus Makroporösem Silizium herstellen.

mehr, und die 3D–Kontrolle über das Licht ist nicht mehr möglich. Streuverluste treten auf, die zu einer Abschwächung der übertragenen Lichtleistung führen.

Sind Streuverluste vorhanden, so muss man den 2,5D-Photonischen Kristall neu optimieren. Während Blochmoden in Schichtkristallen einen sehr hohen Brechnungsindexkontrast Δn zwischen wellenleitender Schicht mit n_{core} und äußerer Schicht n_{clad} erfordern (starke Wellenleiterführung), sind die Streuverluste proportional zu $\Delta\varepsilon^2$ [104]. Dies bedeutet, dass ein sehr geringer Brechungsindexkontrast die Verluste minimiert (schwache Wellenleiterführung). Dies ist die Herangehensweise von Gruppen, die mit GaAs– oder InP–Schichtkristallen arbeiten [105, 106]. Allerdings steigt mit kleiner werdendem Brechungsindexkontrast Δn die Ausdehnung der geführten Moden. Im Grenzfall der ebenen Welle, sind wie im 2D–Fall unendlich tiefe Poren notwendig. Dies stellt sehr hohe Ansprüche an die Ätztechnologie, welche im Moment bei der Herstellung von InP-Schichtkristallen mit Δn = 0,17 der limitierende Faktor sind. Makroporöses Silizium ist ein idealer Kandidat für einen solchen Schichtkristall, da man einerseits sehr tiefe Poren erzeugen kann und außerdem porositätmodulierte Schichtkristalle herstellen kann (Kap. 3.1.5.2).

3.1.3 2D–Photonische Kristalle aus selbstgeordneten Porenstrukturen

Die wesentlichen optischen Messungen an 2D–Photonischen Kristallen aus Makroporösem Silizium sind von Albert Birner während seiner Dissertation in Kooperation mit V. Lehmann (Infineon Technologies AG), S.W. Leonard (University of Toronto) und P. Kramper (Universität Konstanz) durchgeführt worden. Die Proben hatten eine Gitterkonstante a = 1,5 μm und damit eine photonische Bandlücke im Bereich von λ = 3–5 μm. Die optischen Messungen an diesen Proben sind in [7] zusammengefasst. Jörg Schilling und Stefan Schweizer gelang es, die Gitterkonstanten weiter zu reduzieren, so dass wir heute in der Lage sind, Photonische Kristalle mit a = 1000, 700 und 500 nm herzustellen, die Bandlücken im nahen infraroten (NIR) Spektralbereich besitzen (Abb. 3.1a). Um die photonische Bandlücken unterhalb der Absorption von Silizium zu erzeugen, ist es uns gelungen Photonische Kristalle aus porösen Aluminiumoxidstrukturen herzustellen, welche für a = 500 nm eine photonische Bandlücke um λ = 1 μm aufweist (Abb. 3.1a). Neben der Gitterkonstante a, hängt die photonische Bandlücke von der Porosität P und damit über Gl. (2.14) von r/a ab (Abb. 3.1b). Ähnlich dem 1D–Fall ist für Strukturen die aus $\frac{\lambda}{n4}$–Schichten bestehen eine besonderes große erste Bandlücke zu erwarten.

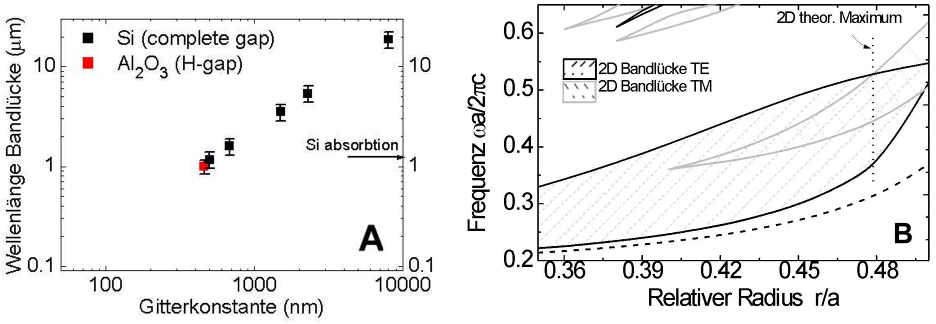

Abbildung 3.1: (a) Photonische Bandlücke als Funktion der Gitterkonstante von realisierten 2D–Photonischen Kristallen aus Makroporösem Silizium und porösem Aluminiumoxid. (b) Numerisch berechnete *gapmap* (Lage der Bandlücke im Frequenzraum für unterschiedliche Porositäten (r/a)) eines 2D–Photonischen Kristall aus Silizium mit hexagonalem Gitter [107]. Die Lichtgerade des 2D–Silizium Photonischen Kristalls für unterschiedliche r/a is gestrichelt eingezeichnet.

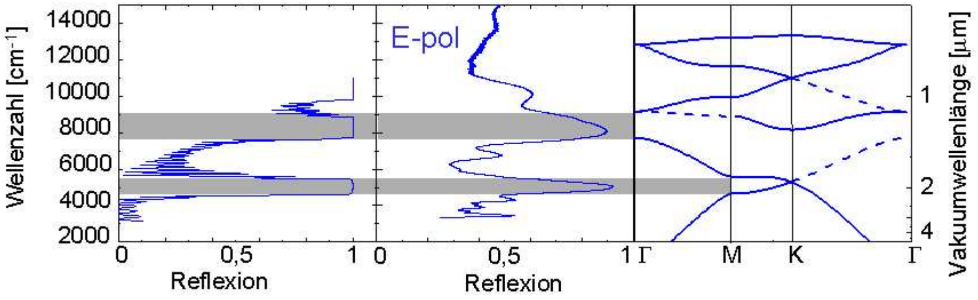

Abbildung 3.2: Reflexionsrechnung (Transfer-Matrix-Methode), Reflexionsmessung und Bandstruktur für einen Photonischen Kristall aus Makroporösem Silizium (a = 500 nm, r/a = 0,425, E-Pol, Γ-M). Die gestrichelten Linien entsprechen nicht ankoppelbaren Bändern, die grauen Bereiche sind Bereiche totaler Reflexion.

Die optischen Messungen an 2D–Photonischen Kristallen aus Makroporösem Silizium und porösem Aluminiumoxid werden im Folgenden kurz zusammengefasst. Messungen an den $a = 1{,}5\ \mu$m-Strukturen wurden überwiegend vor Beginn meiner Habilitation durchgeführt (siehe Literaturverweise).

3.1.3.1 2D–Photonische Kristalle

Die Transmission an 2D–Photonischen Kristallen mit mehr als zehn Gitterperioden a kann man als Volumenmessung ansehen, da die Abschwächung des Lichtes pro Porenreihe ca. 10 dB ist [108]. Albert Birner bestimmte in seiner Dissertation die Lage der Bandlücke im Frequenzraum für unterschiedliche Porositäten (*gapmap*) an a = 1,5 μm-Strukturen [109]. Diese Strukturen haben Ihre erste photonische Bandlücke im Bereich zwischen λ = 3–5 μm. Die Reduzierung der Gitterkonstante und die Bestimmung der optischen Eigenschaften von Photonischen Kristallen mit a = 500 nm, und damit einer Photonischen Bandlücke um λ = 1,3 μm, wurden im Rahmen der Dissertation von Jörg Schilling durchgeführt (Abb. 3.2) [110]. Die Übereinstimmung der 2D–Bandstruktur mit den optischen Messungen ist sehr gut. Eine weitere Reduzierung der Gitterkonstante macht im Falle von Silizium keinen Sinn, da die erste Bandlücke schon nahe an der Absorptionskante von Silizium liegt.

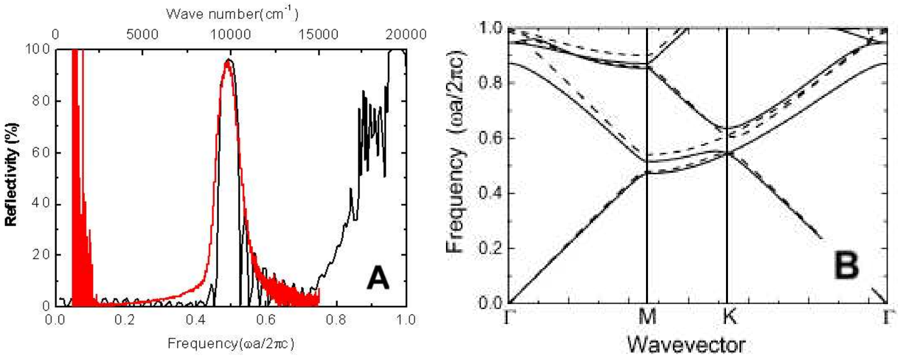

Abbildung 3.3: (a) Reflexionsmessung (rot) und Reflexionsrechnung (schwarz) an einem porösen Aluminiumoxid-Kristall. (b) Entsprechende photonische Bandstruktur des 2D–Kristalls (ε = 1,4, $r/a = 042$, E-Pol.) [114].

In Zusammenarbeit mit der Universität Karlsruhe haben wir die höheren Bandlücken an den Photonischen Kristallen mit a = 1,5 μm optisch untersucht, die spektral im Bereich von $\lambda \sim$ 1–2 μm liegen. Mittels eines phasen- und amplitudenaufgelösten Weisslichtinterferometers konnte gezeigt werden, dass jede Bandlücke durch einen Phasensprung oberhalb und unterhalb der Bandlücke charakterisiert ist [111]. Dies ist eine wesentlich genauere Methode als die konventionelle Bestimmung, bei der eine Abschwächung von 3 dB als Bandkantengrenze definiert ist [112].

Außerdem wurden mittels winkelaufgelösten Reflexionsmessungen die höheren Bragg-Reflexe vermessen. Ein Photonischer Kristall ist nur unterhalb von $\omega a/(2\pi c) < a/b$ ein perfekter Spiegel wobei b die Periodizität entlang der Oberfläche ist. So treten für Messungen in Γ-K-Richtung höhere Reflexe schon für $\omega a/(2\pi c) > 0,577$ auf, wogegen für Messungen in Richtung Γ-M erst für $\omega a/(2\pi c) > 1$ Bragg-Reflexe auftreten. Für Frequenzen oberhalb dieser Frequenz können Moden mit einem Wellenvektor parallel zur Oberfläche angeregt werden und es kommt zu Bragg-Reflexen. Die Winkelabhängigkeit der Bragg-Reflexe für eine Grenzfläche Si/Luft lässt sich sehr gut über die Gittergleichung beschreiben, wobei starke Bragg-Reflexionen auftreten, wenn verschwindende Transmission und ein Gitter-Reflex zusammen treffen [113].

Aluminiumoxid lässt sich als perfekt geordnete 2D–Porenstruktur herstellen (Kap. 2.3.1.3). Seine elektronische Bandlücke ist im ultravioletten Spektralabereich und ist somit geeignet für einen 2D–Photonischen Kristall im sichtbaren und NIR-Spektralbereich. Abbildung 3.3 zeigt eine Reflexionsmessung an einem Photonischen Kristall aus porösem Al_2O_3 (siehe Abb. 2.12) und die entsprechenden Reflexionsrechnungen sowie die 2D–photonischen Bandstruktur [114]. Es ist eine hervorragende Übereinstimmung zwischen Experiment und Theorie erkennbar. Die Reflektion innerhalb der photonischen Bandlücke liegt bei über 90%. Die Abschwächung pro Porenreihe ist in dieser Struktur ungefähr 1,5 dB [115], d.h. es werden mindestens 10 Porenreihen bei einer Reflexionsmessung optisch durchdrungen. Die leichte Verbreiterung der Reflexionsspektren im Vergleich zur Theorie liegt an der Apertur der *cassé-grains*-Optik von total 30^o. Während bei Silizium der Einfluss der *in-plane* wie auch *out-of-plane* Verkippung wegen des effektiven hohen Brechungsindizes kaum eine Rolle spielt, ist bei Aluminiumoxid eine Verbreiterung des Reflexionspeaks zu höheren Frequenzen deutlich zu erkennen [114].

Der Al_2O_3–Photonische Kristall hat aufgrund seines niedrigen Brechungsindizes ($\varepsilon = 1,4 - 1,6$) keine vollständige Bandlücke und nur eine sehr kleine Bandlücke in der H-Polarisation. Dies kann allerdings durch eine Replikation mit einem Halbleiter oder einem Metall kompensiert werden (Kap. 3.2).

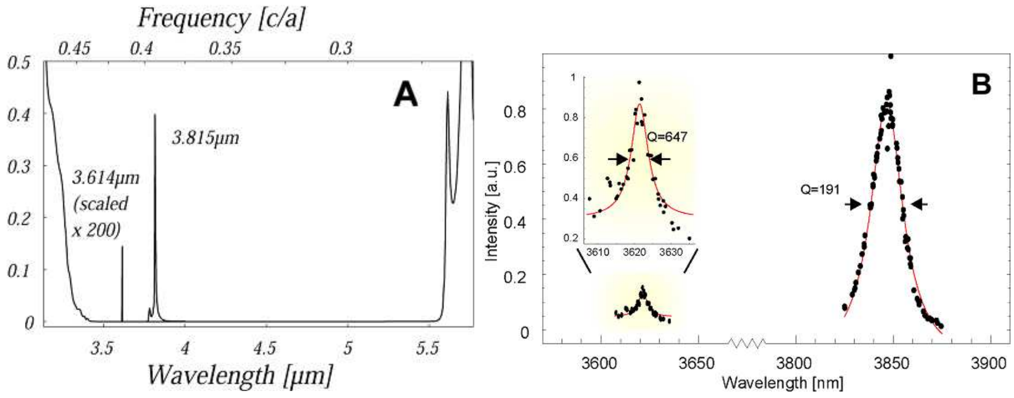

Abbildung 3.4: (a) Theoretisch bestimmte Transmission innerhalb der 2D Photonischen Bandlücke für eine Mikrokavität. (b) Experimentell bestimmte Transmissionen durch eine Mikrokavität, welche sowohl von der spektrale Lage als auch vom Q-Wert sehr gut mit der Theorie übereinstimmen [116].

3.1.3.2 Defekte in 2D–Photonischen Kristallen

Baut man Störstellen in den Photonischen Kristall ein, so können photonische Zustände innerhalb der photonischen Bandlücke entstehen. Abhängig von ihrem Streupotential können in Anlehnung an die Festkörperphysik tiefe oder flache Störstellen erzeugt werden. Der einfachste Fall im 2D–Photonischen Kristall ist das Auslassen eines Loches. Dies erzeugt tiefe Störstellen, die mehrere Moden erlauben (Monopol, Quadropol, Hexapol, etc.). Allerdings können auf Grund der Symmetrie nicht an alle Moden angekoppelt werden. P. Kramper hat eine solche Kavität in seiner Doktorarbeit experimentell eingehend untersucht und zwei Moden, die mit seinem Aufbau angeregt werden können, gemessen [116]. Dabei wurde mittels Rasternahfeldmikroskopie die Feldverteilung im Defekt gemessen und Güten von Q = 190 und 650 bestimmt, welche sowohl energetisch wie auch bezüglich der Güte mit FD-TD-Rechnungen sehr gut übereinstimmen (Abb. 3.4).

Koppelt man Punktdefekte aneinander, so entstehen Defekt-Bänder in der photonischen Bandlücke. Der einfachste Fall ist der eines geraden Wellenleiters, da hier die Translations-Symmetrie in eine Richtung erhalten bleibt. Die Lösungen der Maxwellschen Gleichungen sind Blochmoden und können damit in einer reduzierten Bandstruktur, die der eines 1D—Photonischen Kristalls entspricht, dargestellt werden. Projiziert man die 2D–Bandstruktur in Richtung zum Beispiel eines Wellenleiters in Γ-K-Richtung, ergibt sich die 1D—"projizierte Bandstruktur". Dabei bleiben die vollständigen 2D–Bandlücken erhalten. In ihnen können die Wellenleiterbänder eingezeichnet werden. Obwohl der Wellenleiter mit seiner Breite von a eigentlich nur eine Mode beherbergen sollte, ist er multi-modig. Dies liegt daran, dass ein Photonischer Kristall-Wellenleiter parallel auf zwei unterschiedlichen Wellenführungen basiert: Wellenführung aufgrund von totaler interner Reflexion und Wellenführung aufgrund von Bragg-Reflexion. Beide Moden koexistieren und interferieren bei gleicher Symmetrie, was zu Mini-Stopbändern innerhalb der photonischen Bandlücke führt.

S.W. Leonard hat einen geraden Wellenleiter aus Makroporösem Silizium, welcher durch Auslassen einer Porenreihe in Γ-K-Richtung entsteht, vermessen (W1-Wellenleiter). Die Transmissionsmessungen stimmen hervorragend mit der Theorie überein und die Wellenleitermode hat einen monomodigen Transmissionsbereich für die TE-Polarisaton von $\Delta\omega/\omega \approx 10\%$ [117].

Interessanterweise zeigt die Auskopplung aus dem Wellenleiter einen sehr kleinen Divergenzwinkel von einigen Grad, was bei einem Modendurchmesser im Wellenleiter im Bereich der Wellenlänge eigentlich nicht zu erwarten ist [118]. Dies liegt wahrscheinlich an dem Gittereffekt des Photonischen Kristalls ähnlich den Messungen von Lezec et al. an metallischen Einzelspalten mit periodischen Korrugationen [119]. Numerische Berechnungen von Mario Agio bestätigen diese Annahme (Abb. 3.5)

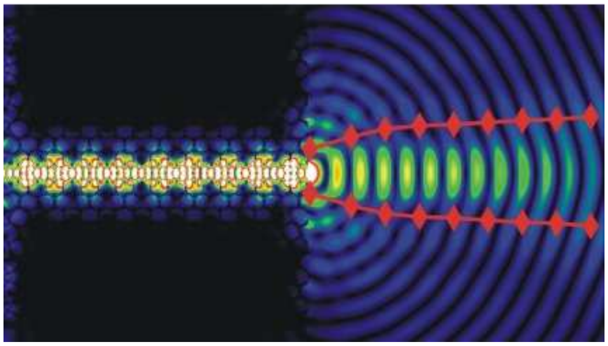

Abbildung 3.5: Fehlfarben-Darstellung der Intensitätsverteilung der propagierenden Moden innerhalb und außerhalb eines W1-Wellenleiter bei einer bestimmten Frequenz. Das ausgekoppelte Licht propagiert mit einer anormal niedrigen Divergenz. Die roten Punkte auf der FD-TD Berechnung zeigen die experimentell gemessenen Breiten des Strahls an verschiedenen Positionen außerhalb des Wellenleiters [118].

Geknickte Wellenleiter und Verzweiger wie z.B. der Y-Strahlteiler können nicht in Form von Bandstrukturen dargestellt werden, da es keine Translationssymmetrie gibt. Beide Strukturen sind von S.W. Leonard [120] und P. Kramper [118] in ihren Dissertationen untersucht worden. Jeder Knick entspricht einem Resonator, so dass drei Phänomene berücksichtigt werden müssen : Rückreflexionen, Modenvermischung und Streuung. Es ist daher schwer 100%ige monomodige Transmission durch einen photonischen Wellenleiterknick zu erreichen. Dieses Problem ist Gegenstand umfangreicher Forschung.

3.1.4 3D–Photonische Kristalle aus selbstgeordneten Porenstrukturen

Durch periodische Modulation des Porendurchmessers von geordneten Makroporen mit der Tiefe (siehe Kap. 2.2.3.2), ergibt sich eine dreidimensionale Strukturierung. Jörg Schilling untersuchte dieses System eingehend in seiner Dissertation [27].

Im Falle einer sinusförmigen Modulation des Porendurchmessers ausgehend von einem 2D–hexagonalen Gitter ergibt sich ein invertierter, einfach hexagonaler 3D–Photonischer Kristall. Allerdings führt die quadratische Form der Poren zu einer Reduzierung dieser Symmetrie. Der Photonische Kristall lässt sich korrekt als invertierter, basiszentrierter orthorhombischer Kristall beschreiben (Abb. 3.6). Die Reduzierung der Symmetrie führt zu einer Aufhebung der Entartung der Bänder entlang der Γ-A Richtung und einer Polarisationsabhängigkeit. Es entsteht Formdoppelbrechung, welche optisch einfach nachweisbar ist. Dieser Kristall kann entsprechend der Wachstumparameter photonische Bandlücken entlang der Poren haben (Γ-A Richtung) sowie auch in der Γ-M-K-Γ-Ebene. Allerdings war es nicht möglich, theoretisch eine Konfiguration zu bestimmen, die eine vollständige 3D–Bandlücke aufweist.

Stephen Leonard konnte vor kurzem zeigen [121], dass ausgehend von einem 2D–quadratischen Gitters eine nicht verschwindende 3D-photonische Bandlücke von $\Delta\omega/\omega = 4\%$ zwischen dem 5. und 6. Band existiert (Abb. 3.7). Es handelt sich bei diesem Kristall um einen invertierten, einfach kubischen 3D–Kristall (Tab. 3.3). Dabei ist zu berücksichtigen, dass die Porenbäuche durch Durchbrüche miteinander verbunden sind, d.h. dass beide Medien Luft und Silizium jeweils kokontinuierlich sind. Dies scheint eine allgemeine notwendige Voraussetzung für vollständige 3D–Bandlücken zu sein [101]. Eine ähnliche Konfiguration im hexagonalen Gitter führt jedoch nicht zu einer vollständigen Bandlücke. Sie ist also keine hinreichende Bedingung.

Die Entwicklung von optischen Messaufbauten zur Untersuchung des 3D–Kristalls sowie die Bestimmung seiner optischen Eigenschaften wurden im Rahmen der Dissertation von Jörg Schilling durchgeführt [27]. Jörg Schilling hat sich in seiner Dissertation ausschließlich mit dem hexagonalen 3D–Kristall beschäftigt, da die theoretischen Grundlagen für den einfach kubischen Kristall mit vollständiger photonischer Bandlücke erst nach der Abgabe seiner Dissertation entstanden sind. Es wurden

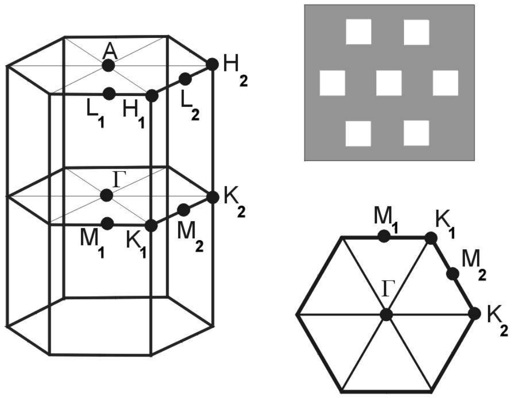

Abbildung 3.6: Hochsymmetriepunkte eines basiszentrierten orthorhombischen Kristalls ausgehend von einem einfach hexagonalen 3D–Kristall.

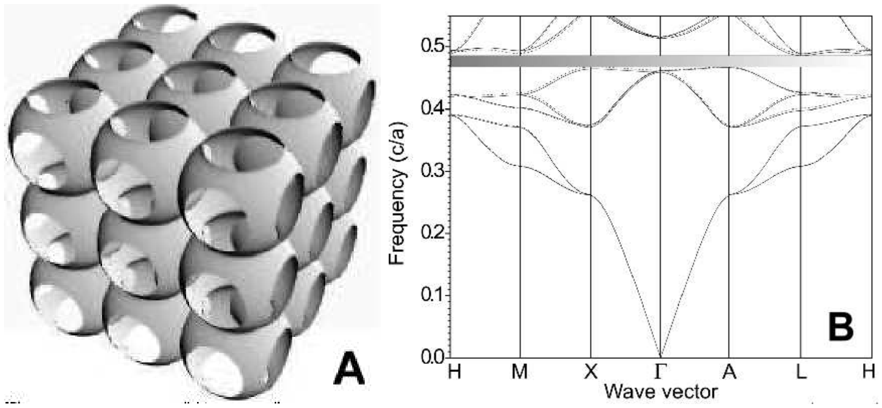

Abbildung 3.7: (a) Schema eines einfach kubischen 3D–Makroporenkristall. (b) Bandstruktur des 3D–Photonischen Kristalls. Es existiert eine Bandlücke von 4% zwsichen dem 5. und 6. Band (nach [121]).

polarisationsabhängige Transmissions- und Reflexionsmessungen entlang Γ-A, Γ-M sowie Γ-K durchgeführt, welche eine sehr gute Übereinstimmung mit der Theorie [122] ergaben. Aufgrund der hohen Güte der Strukturen waren Fabry-Perot Oszillationen im dielektrischen wie auch im Luftband zu erkennen. Daraus konnten experimentell die Gruppengeschwindigkeiten ableitet werden, die hervorragend mit den Steigungen der Dispersionsrelation übereinstimmten [123]. Winkelabhängige Messungen erlaubten die Bestimmung der Dispersionsrelation entlang A-H und A-L. Es konnte gezeigt werden, dass für entsprechende Modulationshübe, der basiszentrierte orthorhombische Photonische Kristall eine polarisationsunabhängige omnidirektionale Totalreflexion aufweist, die sich über eine spektrale Breite von normalisiert $\Delta\omega/\omega \approx 4\%$ erstreckt (Abb. 3.8).

Durch den Einbau einer planaren Defektschicht in den 3D–Kristall konnten quantitative Werte für die Reflexion über die Finesse gewonnen werden. Eine Serie von 3D–Photonischen Kristallen ergab eine Abschwächung von 4 bis 4,5 dB / Modulationsperiode. Dies entspricht bei einem Defekt, der mit sieben Modulation umgeben ist, einer experimentell bestimmten Güte (Q-Faktor) von 140. Bei der Auswertung wurde die Frequenzabhängigkeit des Phasensprungs bei der Interferenztotalreflexion an einem Photonischen Kristall berücksichtigt und eine angepasste Formel für die Finesse und die Güte erarbeitet [27].

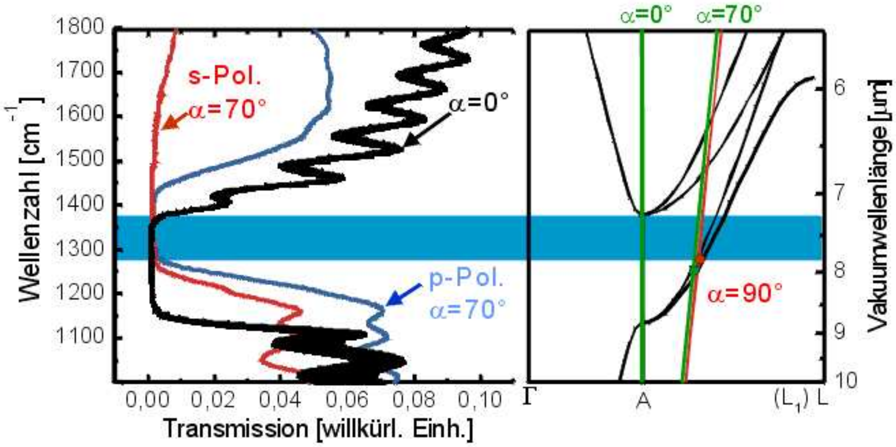

Abbildung 3.8: Transmissionsmessungen für α=0^o und α=70^o und Vergleich mit der Bandstruktur für das Modell kreisrunder Poren. Links: Transmissionsmessungen für Kippungen in Richtung Γ-M. Rechts: Bandstruktur für Γ-A-L, Einfallsgerade für α=0^o und α=70^o in grün, Einfallsgerade für α=90^o in rot [123].

3.1.5 2,5D–Photonische Kristalle

Da 3D–Photonische Kristalle schwer herzustellen sind und 2D–Photonische Kristalle keine Wellenführung in der dritten Dimension erlauben, arbeiten heute viele Gruppen weltweit mit Schichtstrukuren, bei denen in zwei Dimensionen Photonische Kristall-Effekte das Licht führen und in der dritten klassisch über totale interne Reflexion gearbeitet wird, weshalb solche als 2,5D–Photonische Kristalle bezeichnet werden. Um totale interne Reflexion in z-Richtung zu erreichen, gibt es zwei Möglichkeiten: Variation des Brechungsindizes oder Variation des Porendurchmessers. Während in der Literatur ausschließlich über die Variation des Brechungsindizes für Schichtstrukturen berichtet wird, erlaubt das System Makroporöses Silizium auch die Variation des Porendurchmessers mit der Tiefe. Im Folgenden sollen beide Varianten theoretisch diskutiert werden.

3.1.5.1 Index-modulierte Schichtstrukturen

Planare Schichtstrukturen aus Silizium oder III-V Verbindungen wurden in den letzten Jahren ausführlich für aktive und passive photonische Kristallkomponenten untersucht. Eine typische Struktur ist in Abb. 3.9a dargestellt. Sie besteht aus einer inneren Schicht mit einem hohen Brechungsindex n_{core} und äußeren Schichten mit einem niedrigeren Brechungsindex n_{clad}. Im Fall von Membranstrukturen ist n_{clad} = 1, im Fall von vergrabenen Schichtstrukturen ist $n_{\text{core}} > n_{\text{clad}} > 1$. Im Rahmen der Doktorarbeit von Cécile Jamois untersuchten wir theoretisch die Eigenschaften von 2,5D–Photonischen Kristallen, die aus dem Schichtsystem SiO_2/Si/SiO_2 bestehen. Bei dieser Struktur durchdringen die Poren die gesamte Schichtstruktur. Eine mögliche Realisierung dieser Struktur ist auf SOI-Basis mit ICP-Ätzen möglich und Gegenstand aktueller Forschungsbemühungen. Im Folgenden werden kurz die wesentlichen theoretischen Unterschiede eines 2,5D–Photonischen Kristalls im Vergleich zu einem 2D–Photonischen Kristall diskutiert.

Die endliche Dicke der Schichtstruktur in Richtung der Poren (z-Richtung) führt zu zwei wesentlichen Veränderungen in der photonischen Bandstruktur. Zum einen sind die Polarisationen im Vergleich zum 2D–Fall nicht mehr vollständig entkoppelt. Sie können aber noch bei in z-Richtung symmetrischen Strukturen in gerade und ungerade Moden eingeteilt werden. Zum anderen sind nicht mehr alle Moden in der Schichtstruktur geführt. Es ist möglich, dass die Moden in der inneren Schichtstruktur an Moden außerhalb koppeln. Dies führt entweder zu Streuung oder zu geleiteten Moden in der äußeren Schicht. Intuitiv kann das über die totale interne Reflexion der Wellenleiterführung in der Schichtstruk-

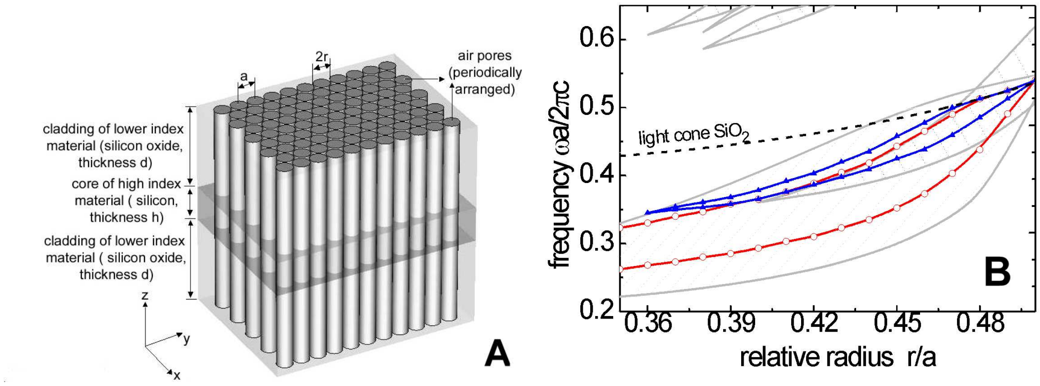

Abbildung 3.9: (a) Schema eines SOI-Schichtkristalls. Die wellenführende Schicht besteht aus einem 2D-Silizium Photonischen Kristall, welcher in einem 2D-Siliziumoxid Photonischen Kristall eingebettet ist. (b) Numerisch berechnete *gapmap* eines SOI-Schichtkristalls mit $h = 0,64a$ [107]. In rot sind die geraden Moden dargestellt, in blau die ungeraden Moden. In grau unterlegt ist die 2D-Silizium *gapmap* (aus Abb. 3.1b). Gestrichelt ist die Lichtgerade für SiO_2 eingezeichnet.

tur verstanden werden. Ist der Winkel, in dem die Mode auf die äußere Schicht trifft, größer als der totale interne Reflexionswinkel, so wird das Licht nicht mehr in der inneren Schicht geführt. Theoretisch lässt sich dies über die Wellenvektor- und Energie-Erhaltung an der Grenzfläche berechnen und über Lichtgeraden in die Bandstruktur einzeichnen. Unterhalb der Lichtgeraden werden die Moden in der inneren Schicht auf jeden Fall geführt, oberhalb der Lichtgeraden ist dies im Allgemeinen nicht der Fall. Für den Fall unserer SOI-Schichtstruktur entspricht die Lichtgerade dem untersten Band des 2D–SiO_2 Photonischen Kristalls, der die lichtführende Siliziumschicht umschließt.

Cécile Jamois optimierte in Ihrer Dissertation den SOI-Schichtkristall, wobei zur Reduzierung des Parameterraumes auf die integrierte Optik zurückgegriffen werden kann [107]. Um eine große Bandlücke unterhalb der Lichtgeraden zu erreichen, ist es naheliegend, dass der Wellenleiter monomodig sein sollte. Es gilt für die Höhe h eines Schichtwellenleiters für monomodigen Wellenleiterführung:

$$h_{\mathrm{mono}} \leq \frac{\lambda_0}{2\sqrt{n_{\mathrm{core}}^2 - n_{\mathrm{clad}}^2}} . \tag{3.7}$$

Nimmt man die 2D–optimierten Porositäten für die äußere und innere Schicht an, kann man n_{core} und n_{clad} als effektive Brechungsindizes bestimmen und damit auch die Schichtdicke h für eine bestimmte Wellenlänge. Es ergibt sich für die Abschätzung aus Gl. (3.7) eine Schichtdicke von h_{mono} = 500 nm für λ_0 = 1,55 μm und für eine 3D–Optimierung des photonischen Schichtkristalls h_{opt} = 470 nm. Dies zeigt, dass Gl. (3.7) eine gute Abschätzung der Schichtdicke erlaubt und den Parameterraum für 3D–Optimierung reduzieren kann.

Für die optimale Schichtdicke wurde eine SOI-*gapmap*, d.h. die Lage der Bandlücke im Frequenzraum für unterschiedliche Porositäten (r/a), erstellt (Abb. 3.9b) [107]. Desweiteren ist der Lichtkegel für SiO_2 eingezeichnet. Der Vergleich zwischen den geraden dielelektrischen Bändern, welche vor allem TE-polarisiert sind, mit dem TE-Bändern eines idealen 2D–Photonischen Kristalls zeigt eine Verschiebung zu höheren Frequenzen. Dies liegt daran, dass ein Teil des Feldes in die äußere SiO_2-Schicht eindringt und somit der effektive Brechungsindex reduziert wird (*Confinement*-Faktor < 100%). Die Verschiebungen der Luftbänder können nicht so einfach erklärt werden, da hier eine stärkere Polarisationsmischung auftritt. Sie sind aber limitiert durch die Lichtgerade für große r/a. Für r/a = 0,46 gibt es eine absolute Bandlücke für beide Polarisationen von $\Delta\omega/\omega$ = 8,5 %. Dies ist ungefähr die Hälfte der spektralen Breite der Bandlücke eines 2D–Photonischen Kristalls aus Silizium und lässt sich durch

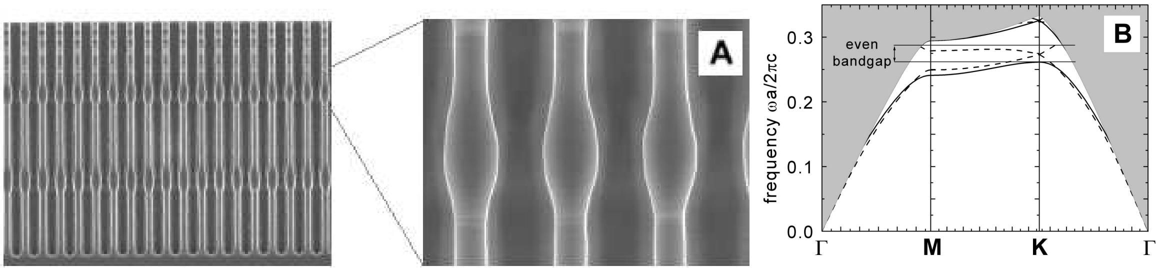

Abbildung 3.10: (a) REM-Seitenansichten eines Porositäts-modulierten Photonischen Kristalls aus Makroporösem Silizium. (b) Bandstruktur des optimierten Designs für die selbe Konfiguration. Gestrichelte Linien sind ungeraden Moden, durchgezogene Linien sind gerade Moden. Eine maximale Bandlücke von 10% für die geraden Moden ist im optimierten Fall möglich [107].

den kleineren *Confinement*-Faktor begründen. Für viele Anwendungen reicht eine Polarisation aus und es ergibt sich für die geraden Moden, welche überwiegend TE-Polarisationscharakter haben, $\Delta\omega/\omega =$ 27 % für dieselben Parameter. Die Breite der Bandlücke für TE-Polarisation (siehe Abb. 3.9) ist über eine großen r/a Bereich (0,35–0,47) größer als 20%.

Um Wellenleiter in diese Schichtkristalle zu integrieren, müssen ähnlich dem 2D–Fall, die projizierte Bandstruktur in Γ–K –Richtung bestimmt und dreidimensional die geführten Moden in einem Wellenleiter berechnet werden. Obwohl für r/a = 0,46 die größte Bandlücke existiert, liegt bei der projizierten Bandstruktur die Bandlücke oberhalb der Lichtgeraden. Es ist daher nicht eindeutig klar, ob geführte Moden in einem Wellenleiter, der innerhalb dieser Bandlücke liegt, existieren. Wird ein kleineres r/a-Verhältnis gewählt, so liegen die Moden energetisch niedriger und sind auch bei der projizierten Bandstruktur unterhalb der projizierten Lichtgeraden. Die Gruppe um Ortwin Hess hat unseren W1-Wellenleiter in dem SOI-Kristall mittels 3D–FD-TD für ein r/a = 0,366 berechnet (Abb. 3.14) [124]. Zum Vergleich wurden in die gleiche Abbildung 2D–Berechnungen der Wellenleitermoden gelegt. Korrigiert man die Modenfrequenz der 2D–Moden, um den niedrigeren *Confinement*-Faktor im 3D–System zu berücksichtigen, so ergeben sich am Rand der 1D-Brillouin-Zone (J-Punkt) energetisch relativ die gleichen Moden mit sehr ähnlichen Feldverteilungen. Diese Ähnlichkeiten der 2D–berechneten Moden mit den 3D–berechneten Moden in der Nähe des J-Punktes erlauben uns in Zukunft schnelle Abschätzungen der Frequenzlage sowie der Gruppengeschwindigkeit [124].

3.1.5.2 Porositäts-modulierte Schichtstrukturen

Die zweite Möglichkeit eines planaren Photonischen Kristalls besteht aus einer Struktur in der der effektive Brechungsindex über die Porosität variiert wird. Dies bedeutet, dass die Poren eine periodische Oszillation Ihres Durchmessers aufweisen. Interessanterweise ist eine solche Struktur mit Makroporösem Silizium realisierbar (Abb. 3.10). Zur Optimierung des Designs versuchten wir ähnlich wie im Falle des index-modulierten Photonischen Kristalls eine maximale Bandlücke unterhalb der Lichtgeraden zu erzielen. Eine erste Abschätzung kann anhand der 2D–Silizium-*gapmap* erfolgen (Abb. 3.1b). Die Lichtgerade ist energetisch sehr niedrig und variiert nur sehr schwach mit dem Porendurchmesser. Um eine maximale Bandlücke zu erzielen, muss der Porendurchmesser in der äußeren Schicht sehr groß und in der inneren wellenführenden Schicht sehr klein sein. Allerdings ist aus Abb. 3.1b ersichtlich, dass keine vollständige Bandlücke existiert. Wir beschränken daher unsere Optimierung auf den Fall gerader Moden. Aus Gl. 3.7 lässt sich für den realistischen Fall von r/a = 0,38 in der inneren Schicht und r/a = 0,48 in der äußeren Schicht eine effektive Dicke der wellenführenden Schicht von $h = 1,2a$ bestimmen. Optimierungen von Cécile Jamois zeigen, dass es eine maximale Bandlücke von nur $\Delta\omega/\omega \approx 10$ % für

Methode	Parameter	Δn_{max}	min. Schaltzeit (s)
Verkippung	Symmetrie	-	10^{-3}
Temperatur	r/a	-	1-100
Mechanisch	r/a, Symmetrie	-	10^{-3}
Infiltration mit PA-Polymeren	$\varepsilon_{\text{Pore}}$	0,1 (irrev.), 0,01 (rev.)	1000
Infiltration mit Ferroelektrika	$\varepsilon_{\text{Pore}}$	10^{-3}	10^{-11}
Infiltration mit Flüssigkristallen	$\varepsilon_{\text{Pore}}$	0,2	10^{-5}
Freie Ladungsträger	ε_{Vol}	0,1	10^{-12}
Nichtlineare Effekte	ε_{Vol}	0,1	10^{-13}

Tabelle 3.4: Möglichkeiten der Durchstimmbarkeit der Interferenztotalreflexion von Photonischen Kristallen.

gerade Moden gibt (Abb. 3.10b) [107, 125]. Aufgrund von Polarisationsmischungen ist es in diesem Fall nicht günstig, das System für den Fall der starken Wellenleiterführung zu optimieren.

Eine Alternative ist die Möglichkeit der schwachen Wellenleiterführung. Aufgrund der einstellbaren Variation des Porendurchmessers und der hohen Aspektverhältnisse können sehr schwache Brechungsindexvariationen mit entsprechenden großen Monomodendurchmessern (Gl. 3.7) hergestellt werden. In diesem Fall arbeitet man weit oberhalb der Lichtgeraden und versucht, Verluste zu minimieren. Mittels Störungstheorie konnten Bensity et al. zeigen, dass die Streuverluste in Schichtwellenleitern mit $\Delta\varepsilon^2$ gehen [104]. FD-TD Rechnungen von Bogaerts et al. bestätigen diese Abschätzungen [126]. Für endliche Strukturen ist diese Möglichkeit also sehr attraktiv, da neben der Reduktion von Verlusten auch der Monomodendurchmesser ohne Probleme auf den Kerndurchmesser einer Glasfaser von ca. 9 μm angepasst werden kann. Dieses Design ist Gegenstand zukünftigen Forschungsbemühungen.

3.1.6 Durchstimmbarkeit

Wir haben uns in den letzten Jahren intensiv mit Möglichkeiten der Durchstimmbarkeit Photonischer Kristalle beschäftigt. Mechanisches Verkippen des Photonischen Kristalls ist wahrscheinlich die einfachste Methode der Verschiebung der Interferenztotalreflexion. Temperaturänderungen sind nur bedingt einsetzbar und verursachen sehr kleine Effekte auf die Bandstruktur. Mechanische Spannungen können sehr effektiv sein, wenn die Symmetrie des Kristalls verändert wird. So wurde gezeigt, dass Scherspannungen von nur wenigen Prozent die komplette 2D–Bandlücke zerstören [127]. Wir haben uns in den letzten Jahren mit Infiltration von Materialien in die Poren beschäftigt (Kap. 2.4.3) sowie der Veränderung des Brechungsindizes der Dielektrika mittels freier Ladungsträger (Tab. 3.4). Auch nichtlineare optische Effekte können instantane Veränderung des Brechungsindex hervorrufen und sind Gegenstand aktueller Forschung.

3.1.6.1 Veränderung der Interferenztotalreflexion durch Verkippung des Photonischen Kristalls

Die wahrscheinlich einfachste Methode der Verschiebung der Interferenztotalreflexion ist die Verkippung des Photonischen Kristalls. In Abb. 3.11 ist die Abhängigkeit der oberen Bandkante eines 3D–Photonischen Kristalls aus Makroporösem Silizium als Funktion der Verkippung untersucht worden. Es ist möglich die Bandkante des Photonischen Kristalls in Γ-A Richtung durch eine Verkippung in A-L (Γ-M) Richtung um ca. 4% zu verschieben. Die Methode der Verkippung ist auch in 2D–Photonischen Kristallen durch eine Drehung von Γ-M in Γ-K möglich.

3.1.6.2 Infiltration von Materialien mit einem veränderlichen Brechungsindex

Die Methode der Polymerinfiltration erlaubt die Funktionalisierung der Luftporen mit Materialien mit variablem Brechungsindex (Kap. 2.4.3). So konnten wir zeigen, dass photoaddressierbare Polyme-

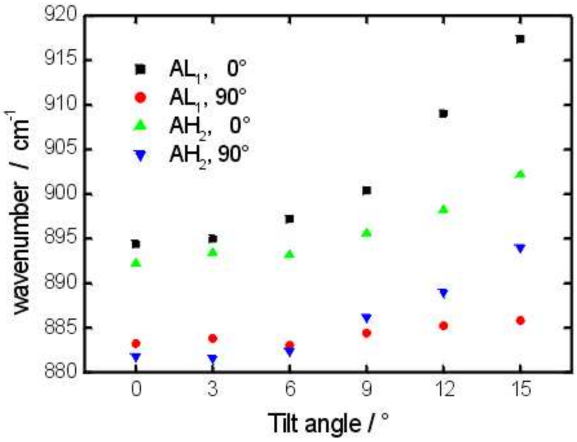

Abbildung 3.11: Veränderung der oberen Bandkante des 3D–photonischen Stoppbandes durch Verkippung. Es sind zwei Verkippungen für jeweils zwei Polarisationen dargestellt (siehe Abb. 3.6).

re (PMMA-DR1) oder Mischungen aus Opferpolymeren und Vorläuferverbindungen ferroelektrischer Oxide die Porenwände benetzen und Röhrchen bilden [75, 76]. Theoretisch sind die zu erwartenden Effekte auf die photonische Bandlücke bei ca. 20-30 nm dicken Wandbeschichtungen gering [128]. Allerdings sind durch konsekutive Beschichtungsschritte dickere Röhrenwände zugänglich.

Da Flüssigkristalle niedrig-viskoser sind, gelang die komplette Befüllung der Poren mit Flüssigkristallen. NMR-Messungen von Flüssigkristallen in den Makroporen zeigen, dass die Ausrichtung der Flüssigkristalle in den Poren die *radial-escape*-Konfiguration hat [129]. Die Flüssigkristall-Direktoren sind an der Porenoberfläche senkrecht zu und im Zentrum parallel zu der Porenachse ausgerichtet. Erste Ergebnisse bezüglich des thermischen Schaltens der photonischen Bandlücke wurden schon in der Dissertation von Albert Birner berichtet [130]. Es konnte eine Verschiebung der photonischen Bandlücke von 70 nm zwischen der isotropen und nematischen Flüssigkristallphase von E5–Flüssigkristallen gemessen werden. Dies sind 50 nm weniger als man bei einer vollständigen Ausrichtung der Direktoren entlang der Porenachse annehmen würde (Abb. 3.12a). Die NMR-Messungen können diese Veränderung gut erklären. Desweiteren haben wir in Zusammenarbeit mit der Universität Paderborn auch das thermische Schalten von Flüssigkristallen in 3D–Photonischen Kristallen aus Makroporösem Silizium durchgeführt (Abb. 3.12b). Der nächste Schritt ist das Schalten mittels einem externen Feld. Hier bieten sich Magnetfelder an, da die Siliziumporenwände leitfähig sind und somit elektrische Felder nicht verwendet werden können. Das Magnetfeld H zum Flüssigkristallschalten in kleinen Poren ist $H \sim 1/r$, so dass im Falle von 1 μm-Poren magnetische Felder von ca. 10 T nötig sind. Wir arbeiten gerade an der Möglichkeit, mittels Beimischung von magnetischen Nanostäben (Kap. 2.4.2.2) die Schaltfelder zu reduzieren, da sich die Flüssigkristalle entlang der Metallstäbchen ausrichten werden.

3.1.6.3 Veränderung der Photonischen Bandstruktur mittels freier Ladungsträger

Durch Bestrahlung einer Bruchkante eines 2D–Photonischen Kristalls mit einem Pump-Laser werden freie Ladungsträger erzeugt. Dadurch kommt es zu einer Verringerung des Brechungsindexes des Silizium selbst. Bei Vernachlässigung der Absorption gilt

$$\varepsilon(\omega) = \varepsilon_{Si} - \frac{\omega_p^2}{\omega^2} \tag{3.8}$$

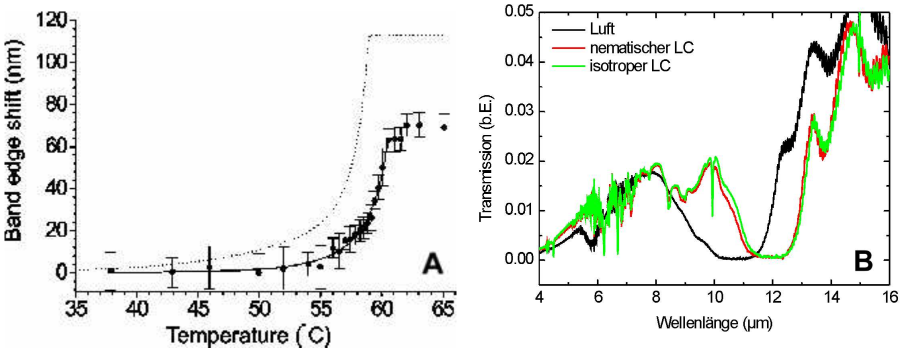

Abbildung 3.12: (a) Veränderung der 2D–photonischen Bandlücke durch thermisches Schalten von Flüssigkristallen in den Poren eines 2D-Photonischen Kristalls. Die Differenz der zu erwartenden (gepunktete Linie) und der gemessenen Verschiebung (Punkte) liegt in der *radial-escape* Ausrichtung der Flüssigkristalle begründet [130]. (b) Thermisches Schalten von Flüssigkristallen in einem 3D–Photonischen Kristall aus Makroporösem Silizium. Transmissionsmessung in Γ-A Richtung ohne Flüssigkristall (schwarz), mit Flüssigkristall in nematischer Phase bei 25^{o}C , mit Flüssigkristall in isotroper Phase bei 65^{o}C (grün) (von G. Mertens, Universität Paderborn).

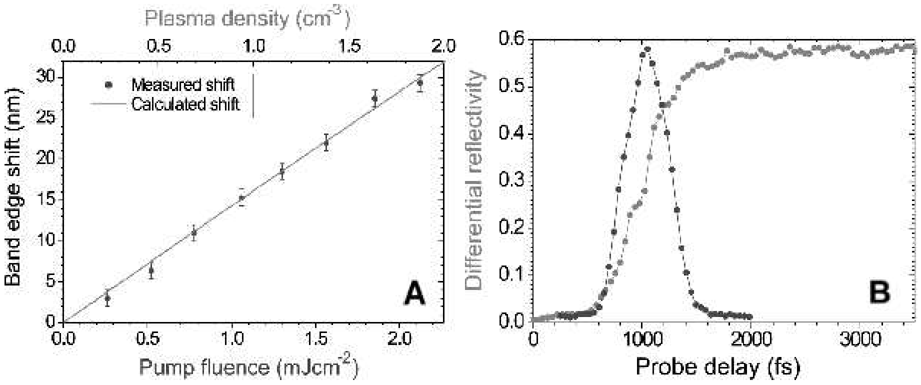

Abbildung 3.13: (a) Verschiebung der Bandkante der optisch gepumpten Oberflächenschicht in Abhängigkeit von der Intensität des Pumplasers. Die experimentellen Werte wurden für eine Reflektivität von R = 0,3 bestimmt. Die experimentell bestimmten Verschiebungen stimmen mit den theoretisch berechneten sehr gut überein (Linie). (b) Zeitlicher Verlauf des Anstiegs der Reflektivität (hellgrau) für λ = 1900 nm nach Eintreffen des Pumplasers mit λ = 800 nm [131].

Dies führt zu einer Verschiebung der Bandlücke zu höheren Frequenzen in der Oberflächenschicht des gepumpten Kristalls gegenüber dem ungepumpten Kristall. Dies konnte durch die Verschiebung des Bereiches der Totalreflexion in den Reflektionsspektren von 2D–Photonischen Kristallen mit a = 500 nm experimentell nachgewiesen werden. Bei einer Energiedichte des Pumplasers von 2,1 mJ/cm^2, welches einer freien Ladungsträgerdichte von $N = 2{\cdot}10^{19}$ cm^{-3} und damit nach $\omega_p^2 = Ne^2/(\varepsilon_0 m^*)$ sowie Gl. (3.8) einer Brechungsindex-Reduzierung um $\Delta n \approx 0{,}06$ entspricht, konnte eine Verschiebung der Bandkante um 29 nm beobachtet werden. Die relative Änderung der Reflexion für Frequenzen in der Umgebung der Bandkante betrug dabei bis zu 250% und hatte damit eine Dynamik von 23 dB, die mit einer typischen Zeitkonstante von 400 fs erreicht werden konnte (Abb. 3.13) [132, 131]. Dies ist die schnellste Verschiebung einer Bandkante die bis dato gemessen wurde und eröffnet neue Möglichkeiten des optischen Schaltens. So könnten die freien Ladungsträger auch über einen n$^+$/n Übergang elektrisch in den photonischen Kristall injiziert werden.

Dieser ultraschnellen Anschaltzeit steht im Falle des Siliziums eine lange Ausschaltzeit von einigen ns gegenüber. Die angeregten Elektronen können aufgrund der indirekten Bandlücke des Silizium nur über Augermechanismen rekombinieren. Jörg Schilling hat durch Abschätzungen zeigen können, dass durch Einbringen von Goldatomen und besonders durch die Erhöhung der Oberflächenrekombination durch beispielsweise Aufbringen von Nickelatomen eine Reduzierung der Lebensdauer der freien Ladungsträger bis in den Pikosekundenbereich möglich ist [27]. Dieser ultraschnelle Schaltmechanismus könnte ein Baustein für das *packet switching* in optischen Netzwerken darstellen [133].

3.1.7 Anwendungen

Das Potential von Photonischen Kristallen liegt in der Möglichkeit, die Dispersionsrelation des Lichtes maßzuschneidern und diese nachträglich durchzustimmen. So zeigen Photonische Kristalle im allgemeinen höhere dispersive Eigenschaften als konventionelle Bauelemente. Anwendungsgebiete liegen u.a. im Bereich des Mobilfunks im GHz-Bereich, der Nachrichtenübertragung im NIR-Bereich als auch der Optolelektronik und der Schmuck- und Farbindustrie mit Anwendungen im sichtbaren Spektralbereich. Wir haben uns in den letzten Jahren auf zwei Anwendungen konzentriert, die auf der langsamen, aber einstellbaren Dispersionsrelation des Lichtes basieren: Zum einen den Bereich der einstellbaren Dispersionkompensation in der Glasfaserübertragung, zum anderen die Herstellung von kompakten Gasabsorptionselementen [134].

3.1.7.1 Durchstimmbare Dispersionskompensation

Im Bereich der Dispersionkompensation wird versucht, die chromatische Dispersion der Glasfaser durch eine negative Dispersion des Photonischen Kristalls zu kompensieren. Da die Veränderungen bzw. die absoluten Werte der Gruppengeschwindigkeiten sehr groß bzw. sehr klein sein können, lassen sich sehr kompakte Dispersionkompensatoren entwickeln. Zum Beispiel zeigt die Grundmode von W1-Wellenleitern in der SOI-Struktur eine sehr flache Dispersion in der Nähe des J-Punktes. Ausserdem ist die Feldverteilung der Mode zu einem großen Teil in den Luftlöcher lokalisiert. Dies ermöglicht durch Infiltration eines Materials mit veränderlichem Brechungsindex ein Trimmen bzw. Durchstimmen. Cécile Jamois hat in Ihrer Doktorarbeit diverse gerade Wellenleiter in SOI-Strukturen mit Gruppengeschwindigkeiten von kleiner 0,02c berechnet (Abb. 3.14). Diese Strukturen werden zur Zeit hergestellt und zukünftig von Infineon Technologies AG im Rahmen eines BMBF Projektes charakterisiert.

3.1.7.2 Gassensorik

In der Literatur wurden überwiegend Anwendungen für die integrierte Optik im Wellenbereich von 1.3 – 1.55 μm beschrieben. Die Maxwellschen Gleichungen sind skalierbar, d.h. die photonischen Bandstrukturen gelten für beliebige Größenskalen. Ein Bereich der bisher stiefmütterlich behandelt wurde, ist der Bereich der Gassensorik im mittelinfraroten Spektralbereich (3-20 μm). Passive photonische Kristall-Bauelemente können in neuartigen miniaturisierten Sensoren Verwendung finden. Wir haben zusammen mit dem Fraunhofer-Institut für Physikalische Messtechnik ein Konzept entwickelt, um die herkömmlichen Gasabsorptionsküvetten um einen Faktor 10-50 zu verkleinern (Abb. 3.15) [134]. Eine einstellbare, langsame Gruppengeschwindigkeiten in Luftbändern des photonischen Kristalls wird dabei mit der Absorptionslinie einer spezifischen Infrarotschwingung eines Analyten in Übereinstimmung gebracht. Es ist zu erwarten, dass die langsameren Gruppengeschwindigkeiten zu einer effektiv erhöhten Wechselwirkungsstrecke nach $L_{\mathrm{eff}} = L \cdot c/v_g$ führen. Da wir Moden mit einer Feldverteilung in den Luftporen des Photonischen Kristalls auswählen, ist eine erhöhte Absorption der IR-Schwingung des Analyten zu erwarten. Besonders vorteilhaft ist die obere Bandkante der ersten photonischen Bandlücke, da hier eine sehr hoher Feldanteil (>80%) in der Luft auftritt [80]. Eine Durchstimmbarkeit ist relativ einfach durch Verkippung eines 2D– oder 3D–Photonischen Kristalls möglich (siehe Kap. 3.1.6.1).

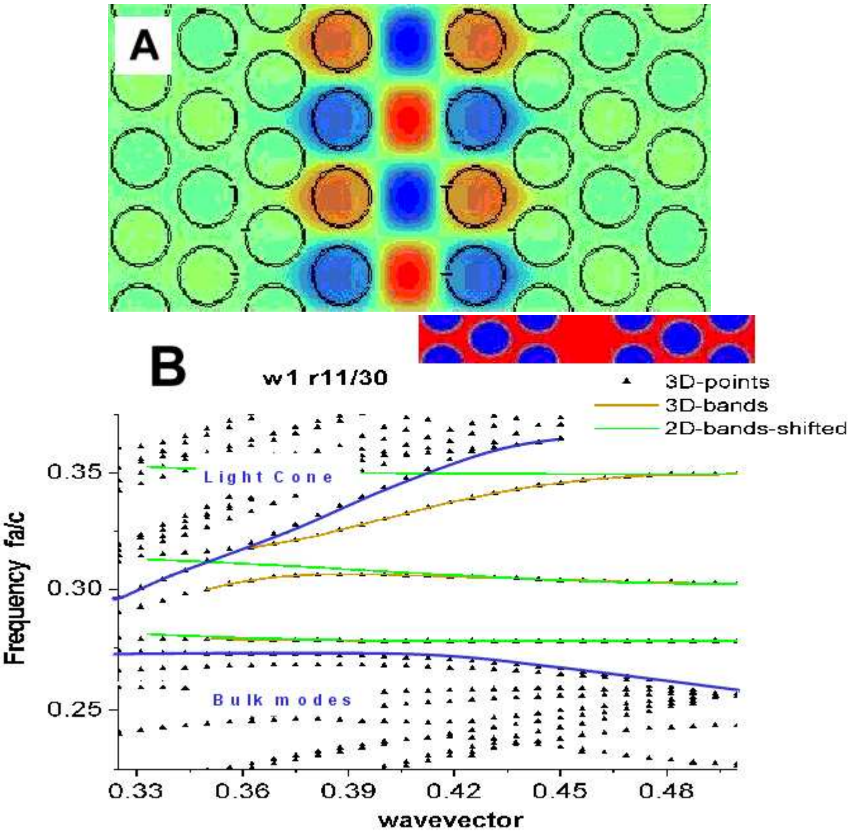

Abbildung 3.14: (a) Berechnete Feldverteilung einer W1-Grundmode (2D). (b) 3D–Bandstruktur eines W1-Wellenleiters im SOI-Schichtkristall (nach C. Hermann, DLR Stuttgart). Vergleichend dazu sind in grün die 2D–Bandstruktur eines W1-Wellenleiters im 2D–Silizium Photonischen Kristall. Die Bänder sind um den effektiven niedrigeren Brechungsindex im SOI-Schichtkristall korrigiert worden.

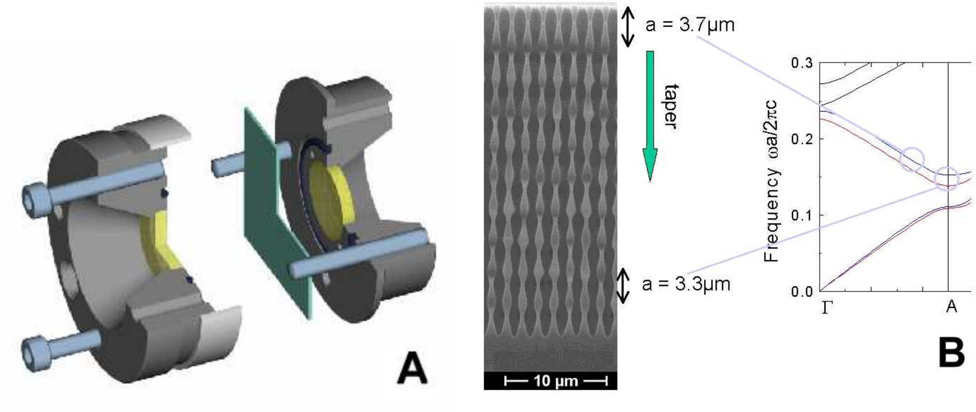

Abbildung 3.15: (a) Schematisches Bild einer Photonischen Kristall-Gasküvette. In grün ist der Photonische Kristall dargestellt. (b) Gechirpter 3D–Photonischer Kristall und korrespondierende Einkopplungen in die 3D–Bandstruktur.

Allerdings ist zu erwarten, dass aufgrund der niedrigen Gruppengeschwindigkeiten die Einkopplung des Lichtes wegen der erhöhten effektiven Reflektivitäten erschwert sein wird. Dies kann z.B. durch einen *gechirpten* Photonischen Kristall, wie er für den 3D–Fall in Abb. 3.15 dargestellt ist, erreicht werden [134].

3.2 Plasmonische Anregungen und Plasmonische Kristalle

3.2.1 Metallo-dielektrische Photonische Kristalle

Ersetzt man in einem Photonischen Kristall eines der beiden Dielektrika durch ein Metall, ergeben sich ganz neue Möglichkeiten. So kann z.B. durch Infiltration von Silber in einen Photonischen Kristall aus Al_2O_3, der im Sichtbaren aufgrund des niedrigen Brechungsindexes keine Bandlücken aufweist (Kap. 3.1.3), eine vollständige Bandlücke erzeugt werden. Außerdem ergeben sich neben den klassischen Blochmoden theoretisch auch Oberflächenplasmonen-Bänder mit sehr langsamen Gruppengeschwindigkeiten. Ein metallo-dielektrischer Kristall ist in Abb. 2.18a dargestellt. Die dazugehörige Bandstruktur, welche von Alexander Moroz berechnet wurde, ist in Abb. 3.16 dargestellt [5].

Der Brechungsindex eines Metalls lässt sich im einfachsten Fall über die Drude-Formel beschreiben

$$\varepsilon(\omega) = \varepsilon_\infty \left\{ 1 - \frac{\omega_p^2}{\omega(\omega + i\gamma)} \right\} , \tag{3.9}$$

wobei ε_∞ die dielektrische Konstante für sehr hohe Frequenzen ist. ω_p ist die Plasmafrequenz, welche von der freien Elektronendichte im Metall und der effektiven Masse abhängt $\left(\omega_p = \frac{Ne^2}{\varepsilon_0 m^*}\right)$. γ ist die Absorption durch das freie Elektronengas. Für den kurzwelligen Grenzfall ($\omega \to \infty$) geht $\varepsilon(\omega) \to \varepsilon_\infty$. Der metallo-dielektrische Kristall ist bei Vernachlässigung der Absorption ein dielektrischer Photonischer Kristall. Ähnlich wie im 2D– dielektrischen Photonischen Kristall entkoppeln E- und H-Polarisation. Allerdings gibt es neben der unterschiedlichen Feldverteilung im Falle der metallo-dielektrischen Photonischen Kristalle im langwelligen Grenzfall ($\omega \to 0$) noch einen viel grundlegenderen Unterschied: Aufgrund der unterschiedlichen Randbedingungen des elektrischen Feldes an der Oberfläche des Metalls (E_x und E_y nicht-stetig aber E_z stetig), gibt es für die E-Polarisation eine Grenzfrequenz ω_{cutoff}, unterhalb derer keine Moden erlaubt sind. Die Moden für H-Polarisation sind kontinuierlich (bis auf eventuelle photonische Bandlücken). Der Photonische Kristall entspricht also in diesem Grenzfall einem klassischem Metallstreifen-Polarisator.

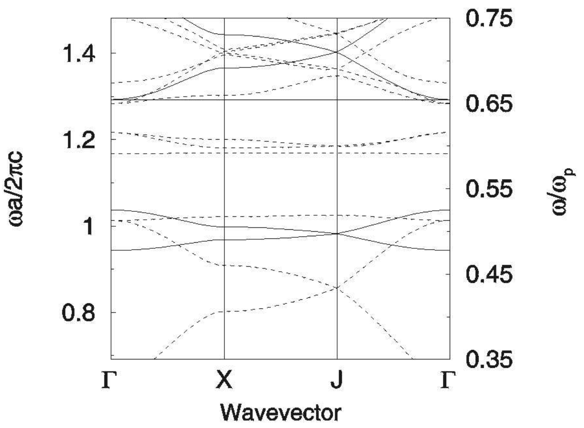

Abbildung 3.16: Bandstruktur für den metallo-dielektrischen Photonischen Kristall ähnlich dem aus Abb. 2.18 nach [5]. Gestrichelt ist die E-Polarisation (TM), durchgezogen ist die H-Polarisation (TE).

Es gibt aber auch für die H-Polarisation ein neues Phänomen: es gibt Eigenmoden, bei der sich die Feldverteilung ausschließlich an der Oberläche des Metalls lokalisiert. Dies sind Oberflächen-Plasmonen-Zustände, die von kleinen Metallpartikeln her bekannt sind und weiter unten diskutiert werden (Kap. 3.2.2). Oberflächenplasmonen sind in erster Näherung Einzelstab-Phänomene. In einem periodischen Gitter kann es allerdings zu Kopplungen der Einzelplasmonen kommen und damit theoretisch zur Ausbildung von Bändern, d.h. Oberlächenplasmonen-Blochmoden. Die optischen Messungen an den metallo-dielektrischen Photonischen Kristallen und deren Interpretation sind Gegenstand der Doktorarbeiten von Jinsub Choi und Yun Luo. Da in unserer spezifischen Struktur aus Abb. 2.18a der minimale Abstand zweier Metallstäbe mehrere zehn Nanometer beträgt, realistisch eher 100 nm, sind die Kopplungskonstanten der Oberflächenplasmonen sehr gering, die Q-Werte sehr hoch und damit die Bänder sehr flach. Außerdem ist es fraglich ob bei so niedrigen Kopplungskonstanten und realistischen Annahmen der Absorption von Silber überhaupt etwas durch diese Moden transmitiert wird. Um Oberflächenplasmonenkopplungen zu messen sind die kleineren Silberstabensembles aus Abb. 2.17 wesentlich geeigneter. Hier beträgt die Gitterkonstante 100 nm und der minimale Abstand lässt sich zwischen 20 und 70 nm einstellen (Kap. 2.4.2.2). Experimentell wurden an Silberpunkten in ähnlichen System Abschwächungen aufgrund von Absorption von Silber von 1 μm^{-1} gemessen [135].

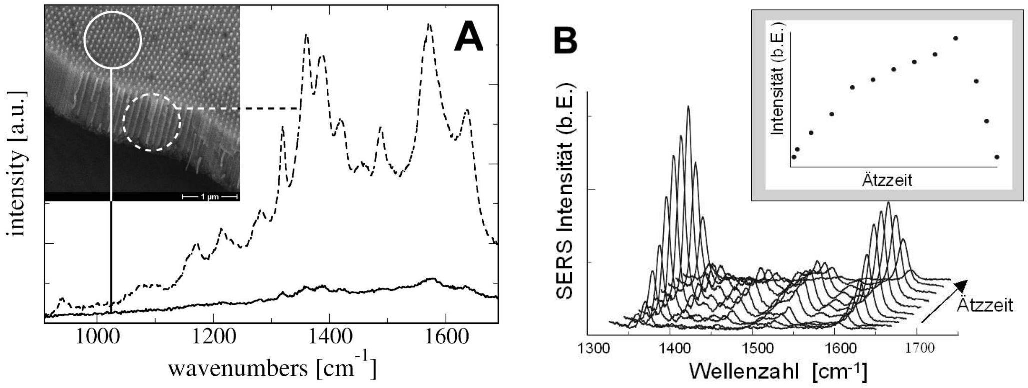

Abbildung 3.17: (a) Oberflächenverstärktes Ramanspektrum von Proflavine, welches zum einen auf Silbernanostäben im Templat gemessen wurde sowie von der Seite auf freiliegenden Silberstäben. Die Anregungswellenlänge ist λ = 514,5 nm; Einsatz: REM-Bild der Probe und Zuordnung zu den Messpunkten. (b) Oberflächenverstärktes Ramanspektrum von Oxazine 170, welches mit λ = 632,8 nm während des Ätzens der Matrix und damit der Freilegung der Silbernanostäbe gemessen wurde. Einsatz: SERS-Intensität als Funktion der freigelegten Silberstabfläche.

3.2.2 Oberflächenplasmonen an metallischen Nanostäben

Unterhalb der Plasmafrequenz eines Metalles, können an der Grenzfläche Metall/Dielektrikum Oberflächenwellen als Lösung der Maxwellschen Gleichungen existieren. Sie haben im langwelligen Grenzfall für eine planare Metalloberfläche und ein Dielektrikum mit ε_b eine lineare Dispersionsrelation $\omega = ck_x/\sqrt{\varepsilon_b}$, welche asymptotisch für höhere k-Werte gegen $\omega = \sqrt{\varepsilon_\infty/(\varepsilon_\infty + \varepsilon_b)}$ geht [79]. Bei Nanostrukturen im Bereich der Wellenlänge hängt die Plasmonenresonanz von der Größe der Strukturen ab. Man kann diese im Rahmen der Mie-Theorie beschreiben [136]. Auch die Dämpfung der Resonanz kann von der Größe der Teilchen abhängen, wenn die Teilchen kleiner als die freie Weglänge der Elektronen sind. Die Messungen an sehr langen Silberstäben sind Transmissionsmessungen in Lösung [136] werden im Rahmen der Dissertation von Guido Sauer und Ulrike Rehn durchgeführt. Die theoretischen Feldverstärkungen σ_{plasmon} an Silbernanostäben bei Vernachlässigung der chemischen Komponenten liegen im Bereich von 10. Dies ist gering im Vergleich zu nicht-regelmäßigen Teilchen [137]. Stäbe erlauben aber aufgrund des Templatverfahrens eine wesentlich höhere Reproduzierbarkeit und sind daher für Anwendungen wie den oberflächenverstärkten Ramaneffekt wesentlich geeigneter. Die Ramanverstärkung geht mit $\sigma^4_{\text{plasmon}}$, ist also für Stäbe im Bereich von $\sigma^4_{\text{plasmon}} \approx 10^4$ unter Vernachlässigung von chemischen Komponenten. Da die Stäbe ein Aspektverhältnis von ca. 20–30 haben, und die Stabdichte im Templat $75 \cdot 10^9$ Stäbe/Zoll^2 ist, sind die absoluten Verstärkungen sehr gut messbar. Im Rahmen der Doktorarbeit von Guido Sauer haben wir den oberflächenverstärkten Ramaneffekt an Silberstäben mit einem Durchmesser von 35 nm gemessen (Abb. 3.17a). Durch Ätzen des Templats und $in-situ$ Ramanmessungen, konnten wir erstmalig auch den linearen Zusammenhang der Ramanverstärkung mit der Länge des Stabes messen (Abb. 3.17b) [138].

3.3 Magnetische Nanostab-Ensembles

Im Rahmen der Dissertation von Kornelius Nielsch haben wir Nickel Nano-Stabensembles mit einem Durchmesser von 30 nm und einem Porenabstand von 100 nm (siehe Kap. 2.4.2.2) magnetisch untersucht [49]. Was bewirkt der 2D–hexagonale Kristall in einem magnetischen System ?

Jeder magnetische Nanostab ist ein Eindomänenteilchen. Er hat also genau zwei Zustände. Höhere Quantenzustände wie in photonischen System gibt es nicht. Nichtsdestoweniger, führt die Kopplung zwischen den Stäben zu Umschalt-Bändern in einem 2D–Kristall, oder magnetisch formuliert, zu einer unendlichen Anzahl an Barkhausensprüngen, die zu einem kontinuierlichen Umschaltverhalten führen (Abb. 3.18a) [139]. Eine andere Eigenschaft sind die kollektiven Anregungen von Spins, sog. Spinwellen. Diese haben höhere Quantenzahlen und könnten prinzipiell zu einer Kopplung wie bei Oberflächenplasmonen führen. Allerdings haben wir bis jetzt nur Einzelstabphänomene experimentell nachweisen können. Im ersten Unterabschnitt werden kurz die magnetischen Eigenschaften des 2D–Nanostabensembles dargestellt und im zweiten Unterabschnitt die experimentellen Messungen an Spinwellenquantisierungen in Nanostäben.

3.3.1 Statische magnetische Eigenschaften

SQUID-Magnetometer Messungen an unseren 2D–Nanostabensembles haben die höchsten jemals gemessen Koerzivitäten von 1200 Oe gezeigt und sie weisen 100 % Remanenz auf (Abb. 3.18b). Obwohl die Nanostäbe bestrebt sind sich antiferromagnetisch auszurichten, ist eine vollständige Magnetisierung des Ensembles möglich. Größere Stabdurchmesser erhöhen die Streufeldwechselwirkung im Ensemble und reduzieren damit magnetische Anisotropie und Koerzivität des Nickelensembles [8, 140, 141, 142].

Im entmagnetisierten Zustand weisen die Nickel-Nanostabensembles eine labyrinth-artige Domänenstruktur auf, wie MFM-Untersuchungen zeigen (Abb. 1.1c). Jeder magnetische Nano-Stabmagnet ist ein Eindomänenteilchen, welches sich in Porenrichtung magnetisieren lässt. Erfolgreich ist es gelun-

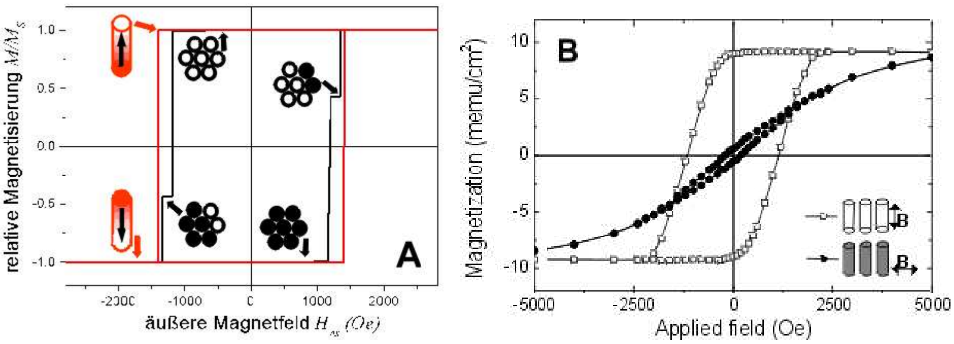

Abbildung 3.18: (a) Hysteresen für einen einzelnen Nickelstab und einer hexagonalen Anordnung von sieben Nickelstäben in einem äußeren Feld $\vec{H}_{ex}$ entlang der Stabachse. Die ersten Barkhausen-Sprünge sind erkennbar [143]. (b) SQUID-Magnetometer Hysterese eines Ni-Nanostabensembles mit a = 110 nm und r = 15 nm. Die Remanenz ist 100% wenn das Magnetfeld entlang der Poren angelegt wird [8].

gen mit einem äußeren Magnetfeld und dem Dipolfeld einer stark magnetischen MFM-Spitze präzise abgegrenzte Probenbereiche nahezu vollständig umzumagnetisieren. Diese Untersuchung zeigt, dass sich im Prinzip ein Nanostab einzeln beschreiben lässt [144]. Die Magnetisierungsmessungen der gesamten Probe mit SQUID und MFM zeigen eine sehr gute Übereinstimmung mit mikromagnetischen Rechnungen von Riccardo Hertel [143] und makroskopischen Isingmodellen. Diese Modellierungen ergeben, dass die Streufeldwechselwirkungen sich über einige zehn Gitterperioden erstrecken [145].

3.3.2 Spinwellen-Quantisierung

Im ferromagnetischen Ordnungszustand sind alle Spins im Grundzustand aufgrund der Austauschwechselwirkung parallel ausgerichtet. Thermische Anregungen oder Anregungen durch Mikrowellenfelder führen zu einer Präzessionsbewegung der Spins. Erfolgen die Präzessionsbewegungen kohärent, so spricht man von Spinwellenanregungen, welche durch einen Wellenvektor k beschrieben werden können. Spinwellen sind das magnetische Pendant zu Gitterschwingungen (Phononen). Es gibt Oberflächenspinwellen und quantisierte Volumen-Spinwellen. Die ersteren sind vor allem durch dipolare Wechselwirkung gekennzeichnet und heißen nach Ihren Entdeckern Damon-Eshbach-Moden. Sie laufen entlang von Oberflächen mit einem Wellenvektor, welcher parallel zu Oberfläche ist. Stehende Volumen-Spinwellen sind vor allem von der Austauschwechselwirkung dominiert und sind nur in hinreichend reduzierten Geometrien sichtbar. Die quantisierten Energieniveaus der Spinwellen haben eine ähnliche Abhängigkeit vom Durchmesser der Dünnschicht wie von der Quantentopfbreite in der Festkörperphysik. Ohne äußeres Magnetfeld gilt für die Frequenzen $\nu \approx \pi^2 D n^2 / r^2$ wobei r der Durchmesser der Schicht ist, n die Quantenzahl, und D die Spinwellensteifigkeitskonstante ist, welches das Analogon zur reziproken effektive Masse ist. Abbildung 3.19a zeigt die experimentell gemessenen Spinwellen an einer Fe-Dünnschicht von Grünberg et al. [146]. Es sind deutlich Oberflächenspinwellen wie auch die ersten vier stehenden Volumen-Spinwellen zu erkennen.

Sind mehrere ferromagnetische Lagen miteinander durch dünne nicht-ferromagnetische Schichten gekoppelt, kommt es zur Wechselwirkung der Einzelmoden und zu einer Ausbildung von Spinwellenbändern. Dabei können zwei Mechanismen zur Kopplung beitragen: magnetische Streufelder (langreichweitig) und Austauschkopplung (kurzreichweitig). Periodische ferromagnetische Strukturen kann man daher magnonische Kristalle nennen [4].

Prof. Kuok (Univ. Singapur) hat mittels Brillouin-Streuung unsere ferromagnetischen 2D–Nanostabensembles charakterisiert [147]. Dabei konnten wir erstmals die ersten drei quantisierten Volumen-Spinwellen-Moden in einem Nanostab messen (Abb. 3.19b) [148]. Arias and Mills haben für ein Ein-

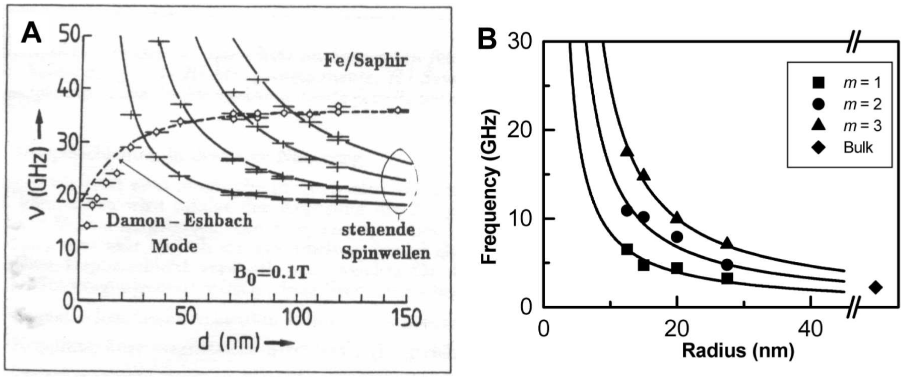

Abbildung 3.19: (a) Experimentell gemessenen Spinwellen in einem dünnen Film (1D—Beschränkung) nach [146]. (b) Experimentell gemessene Spinwellen in einem Nanostab (2D–Beschränkung) [148].

zelstabsystem kürzlich die Spinwellen-Moden berechnet [149]. Es lassen sich wie im Falle von Dünnschichten die Eigenmodenfrequenzen mit $\nu \propto Dn^2/r^2$ nähern, welches eine sehr gute Übereinstimmung mit den Messungen ergibt. Allerdings konnten wir bis jetzt keine direkte dipolare Kopplung der Nanostäbe erkennen. Dieses Phänomen ist Gegenstand aktueller Forschung.

3.4 Schlussfolgerung

Ziel meiner Habilitation war es durch Kombination von Selbstordnung und Lithographie perfekt geordnete 2D– und 3D–Porenstrukturen herzustellen. Dies ist meinem Team und mir sowohl für das Materialsystem Makroporöses Silizium als auch für poröses Aluminiumoxid gelungen. Dabei ist hervorzuheben, dass es uns im Falle des porösen Aluminiumoxides gelungen ist, mittels geeigneter Kombination von Vorstrukturierung und Selbstordnung, perfekt geordnete Strukturen mit einem Abstand kleiner als der der Lithographie zu erzeugen. Mittels neu entwickelter Methoden gelang die Replikation dieser monodispersen, hochgeordneten Porenstrukturen mit Metallen (Ni, Co, Au, Ag, ...) als auch mit Polymeren. Dabei wurde ein Verfahren entwickelt, welches jedes Polymer, das im flüssigen Zustand prozessierbar ist, in Polymernanoröhrchen abformen kann.

Dieses Baukastensystem bestehend aus 2D– und 3D–periodischen Strukturen ermöglicht das Studium der Kopplung und der Interferenzen unterschiedlichster Wechselwirkungen und ist damit Modellsystem für die Physik und die Photonik, *sui generis*.

Während die Theorie viele dieser Wechselwirkungen mit Hilfe periodischer Randbedingungen in Form von Blochmoden lösen kann, gab es vor Beginn meiner Dissertation aufgrund der fehlenden Realisierungen von periodischen 2D- und 3D-Nanostrukturen kaum Möglichkeiten der Überprüfung der Theorien. Die sehr gute Übereinstimmung zwischen Experiment und Theorie im Falle Photonischer wie auch Magnetischer Kristalle bestätigt, dass die verwendeten Materialsysteme ein Modellsystem für das Studium physikalischer Wechselwirkungen sind.

3.5 Danksagung

Ich möchte an dieser Stelle all denen danken, die durch ihre Unterstützung zu dieser Arbeit beigetragen haben.

Prof. Ulrich Gösele danke ich für die joviale Unterstützung meiner Arbeiten am Max-Planck-Institut für Mikrostrukturphysik Halle und der stimulierenden wissenschaftlichen Diskussionen. Ich habe viel von ihm über die deutsche Forschungslandschaft, Forschungsstrategien und Forschungsmanagement gelernt.

Je rémercie chaleuresement Jean-Noel Chazalviel qui a continué à travailler sur le modèle de l'instabilité lineaire depuis ma thèse et de qui j'ai appris l'électrochemie de silicium. Je rémercie aussi fortement Ionel Solomon, qui m'a encadré pendant ma thèse et qui m'a fait apprendre la recherche. Finalement, je suis très indepte à Francois Ozanam avec qui j'aimais travailler ensemble et qui a été toujours un bon copain. A l'ôutre Rhin, bedanke ich mich bei Gottfried Bauer, der mein deutscher Doktorvater ist und mit dem ich während der ganzen Jahre eine freundschaftliche Beziehung hatte. In den letzten Jahren konnte ich ihm die Photonischen Kristalle schmackhaft machen.

Ganz besonderer Dank gilt meinen ersten beiden Doktoranden am Max-Planck-Institut, Dr. rer. nat. Jörg Schilling und Dr. rer. nat. Kornelius Nielsch. Mit Ihnen habe ich mir gemeinsam das Gebiet der Photonischen bzw. Magnetischen Kristalle erarbeitet und auf Ihren Dissertationen basiert ein Großteil meiner Habilitation. Sie haben außerdem die neue Generation an Doktoranden sehr gut experimentell ausgebildet.

Den Doktoranden der zweiten Generation Cécile Jamois und Jinsub Choi bin ich auch zu tiefem Dank verpflichtet (Merci et Ko map sup ni da). Sie haben einen signifikanten Teil zu unserem Verständnis der geordneten Porenstrukturen und der Photonischen Kristalle beigetragen und große Teile Ihrer Arbeiten finden sich in meiner Habilitationsschrift wieder.

Yun Luo und Ulrike Rehn sind die Doktoranden der dritten Generation. Auch Ihnen möchte ich danken und Teile Ihrer Arbeiten sind Bestandteil meiner Habilitationsschrift (Xie Xie und Danke).

Torsten Geppert, Doktorand der vierten Generation, möchte ich für das Korrekturlesen meiner Habilitation danken.

Außerdem möchte ich meinen beiden externen Doktoranden Martin Steinhart (Universität Marburg) und Guido Sauer (Universität Erlangen) für die sehr gute Zusammenarbeit danken, die mich mit Martin Steinhart nun schon seit 15 Jahren verbindet. Teile Ihrer Arbeiten finden sich auch in der Habilitationsschrift wieder.

Zu ganz besonderem Dank bin ich Dr. Frank Müller verpflichtet. Er leitete die Gruppe poröse Materialien/Photonische Kristalle vor mir. Seine breiten wissenschaftlichen Kenntnisse und seine guten Ideen haben viel zum Erfolg der Arbeiten unser Gruppe beigetragen und es hat mir immer große Freude gemacht, mit ihm wissenschaftlich zu diskutieren.

Seit kurzem arbeitet Stefan Schweizer bei uns und auch ihm bin ich zu Dank verpflichtet. Seine Kenntnisse in der Elektrochemie des Siliziums ermöglichten einen sehr schnellen Einstieg in das Porenwachstum.

Auch bin ich Dr. Petra Göring zu großem Dank verpflichtet, da Sie nun fast selbstständig das Aluminiumoxid-Labor leitet und mir somit viel Arbeit abnimmt.

Dr. Reinald Hillebrand und Prof. Wolfram Hergert danke ich für die vielen Rechnungen zu Bandstrukturen und Transmissionen an Photonischen Kristallen, die sehr gute Unterstützung bei der Organisation der Sommerschule über Photonische Kristalle in Wittenberg 2002 und die Unterstützung bei der Lehre.

Stefan Richter möchte ich für die Arbeiten an HgTe-Quantendots danken, die auch Ihren Platz in dieser Arbeit gefunden haben.

Desweiteren möchte ich unseren beiden studentischen Hilfskräften Katrin Schwirn und Sven Matthias danken, die es nicht immer einfach mit uns allen hatten, da Sie am Ende der Hierarchie standen und viele Betreuungs- und Servicetätigkeiten machen mussten, zu denen kein anderer Lust hatte. Vielen, vielen Dank für alles.

Außerdem möchte ich Andreas Herbst meinen Dank aussprechen, der den reibungsfreien Ablauf im Chemielabor ermöglicht und sich um alles das kümmert, was nicht in Veröffentlichungen erwähnt wird.

Riccardo Hertel danke ich für die vielen stimulierenden Diskussionen über Magnetische Kristalle und die vielen Berechnungen, die er durchgeführt hat. Mein Dank gilt dabei selbstverständlich auch der Unterstützung dieser Tätigkeiten durch Prof. Jürgen Kirschner.

Desweiteren danke ich allen anderen Kollegen am Max-Planck-Institut, die zum Gelingen dieser Arbeit beigetragen haben.

Darüberhinaus sind viele Ergebnisse in Kooperation mit anderen Wissenschaftlern entstanden. Ich möchte Dr. Stephen Leonard und Prof. Henry van Driel (Univ. Toronto), Dr. Patrick Kramper und Prof. Vahid Sandoghdar (Univ. Konstanz/ETH Zürich), Dr. Volker Lehmann (Infineon Technologies AG), Dr. M. Chrisophersen, St. Lölkes und Prof. H. Föll (Univ. Kiel), Dr. G. von Freymann und Prof. M. Wegener (Univ. Karlsruhe), Prof. H. Kuok (Univ. Singapur), Dr. S. Fischer and Prof. H. Kronmüller (MPI für Metallforschung), Dr. T. Schweinboeck and Prof. D. Weiss (Univ. Regensburg), Prof. J.H. Wendorff (Univ. Marburg) und Prof. S. Schneider (Univ. Erlangen-Nürnberg), G. Böttger, M. Schmidt und Prof. M. Eich (TU Hamburg-Harburg), Guido Mertens and Prof. Heinz Kitzerow (Univ. Paderborn) Dank sagen.

Besonderer Dank geht an Kurt Busch nach Karlsruhe mit dem ich viel gemeinsam habe und mit dem es mir immer ein Freude macht, wissenschaftlich wie auch organisatorisch zusammen zuarbeiten. Vielen Dank Kurt !

Last but not least, danke ich meiner Familie, vor allem meiner Partnerin Kristin, die mit mir nach dem Diplom und der Dissertation auch noch die Mühen der Habilitation teilte. Dickes Bussi an Janina, Oskar und Georg, die mich immer wieder in das alltägliche Leben zurückgeholt haben.

Literaturverzeichnis

[1] John, S., *Phys. Rev. Lett.* **58** (1987) 2486.

[2] Yablonovitch, E., *Phys. Rev. Lett.* **58** (1987) 2059.

[3] Psarobas, I., N. Stefanou und A. Modinas, *Phys. Rev. B* **62** (2000) 278.

[4] Nikitov, S., P. Tailhades und C. Tsai, *J. Magn. Magn. Mater.* **236** (2001) 320.

[5] van der Lem, H. und A. Moroz, *J. Opt. A: Pore Appl. Opt.* **32** (2000) 395.

[6] Sánchez-Pérez, J., D. Caballero, R. Mártinez-Sala, C. Rubio, J. Sánchez-Dehesa, F. Meseguer, J. Llinares und F. Gálvez, *Phys. Rev. Lett.* **80** (1998) 5325.

[7] Schilling, J., R. Wehrspohn, A. Birner, F. Müller, R. Hillebrand, U. Gösele, S. Leonard, J. Mondia, F. Genereux, H. van Driel, P. Kramper, V. Sandoghdar und K. Busch, *J. Opt. A: Pore Appl. Opt.* **3** (2001) 121, siehe Anhang.

[8] Nielsch, K., R. Wehrspohn, J. Barthel, J. Kirschner, U. Gösele, S. F. Fischer und H. Kronmüller, *Appl. Phys. Lett.* **79** (2001) 1360, siehe Anhang.

[9] Parker, A., R. McPhedran, D. McKenzie, L. Botten und N. Nicorovici, *Nature* **409** (2001) 36.

[10] Lohrengel, M., *Mater. Sci. Eng.* **11** (1993) 243.

[11] Chazalviel, J.-N., R. Wehrspohn und F. Ozanam, *Mat. Sci. Eng. B* **69-70** (2000) 1, siehe Anhang.

[12] Uhlir, A., *Bell Syst. Technol. J.* **35** (1956) 333.

[13] Wehrspohn, R., J.-N. Chazalviel, F. Ozanam und I. Solomon, *Thin Sol. Films* **5** (1997) 297, siehe Anhang.

[14] Ghandi, S., *VLSI Fabrication Principles*, John Wiley and Sons (1983).

[15] Lehmann, V., Luigart und Stengel, *Mat. Sci. Eng. B* **69-70** (2000) 11.

[16] Wehrspohn, R., J.-N. Chazalviel und F. Ozanam, *J. Electrochem. Soc.* **145** (1998) 2958.

[17] Lehmann, V. und S. Rönnebeck, *J. Electrochem. Soc.* **146** (1999) 2968.

[18] Chao, K., S. Kao, C. Yang, M. Hseu und T. Tsai, *Electrochem. Solid-State. Lett.* **3** (2000) 489.

[19] Ponomarev, E. und C. Levy-Clement, *J. Porous Mater.* **7** (2000) 51.

[20] Wehrspohn, R. B., F. Ozanam und J.-N. Chazalviel, *J. Electrochem. Soc.* **146** (1999) 3309, siehe Anhang.

[21] Chazalviel, J.-N., F. Ozanam, N. Gabouze, S. Fellah und R. Wehrspohn, *J. Electrochem. Soc.* , im Druck.

[22] Wehrspohn, R., *Porous amorphous silicon - pore formation and photoluminescent properties*, Dissertation, Ecole Polytechnique, Frankreich und Universität Oldenburg (1997).

[23] Chazalviel, J.-N., R. Wehrspohn, F. Ozanam und I. Solomon, *Mater. Res. Soc. Proc.* **452** (1997) 403.

[24] Vyatkin, A., V. Starkov, V. Tzeitlin, H. Presting, J. Konle und U. König, *J. Electrochem. Soc.* **149** (2002) G70.

[25] Lehmann, V. und H. Föll, *J. Electrochem. Soc.* **137** (1990) 653.

[26] Lehmann, V., *J. Electrochem. Soc.* **140** (1993) 2836.

[27] Schilling, J., *Herstellung und optische Eigenschaften von 2D- und 3D- photonischen Kristallen aus makroporösem Silizium*, Dissertation, Martin-Luther-Universität Halle-Wittenberg (2002).

[28] Lehmann, V., *J. Electrochem. Soc.* **143** (1996) 1313.

[29] Grüning, U., V. Lehmann und C. Engelhardt, *Appl. Phys. Lett.* **66** (1995) 3254.

[30] Grüning, U., V. Lehmann, S. Ottow und K. Busch, *Appl. Phys. Lett.* **68** (1996) 747.

[31] Birner, A., U. Grüning, S. Ottow, A. Schneider, F. Müller, V. Lehmann, H. Föll und U. Gösele, *Phys. Stat. Sol. (a)* **165** (1998) 111.

[32] Zhang, X., *J. Electrochem. Soc.* **138** (1991) 3750.

[33] Christophersen, M., *persönliche Mitteilung* .

[34] Güntherschulze, A. und H. Betz, *Elektrolytkondensatoren*, M. Krayn Verlag, Berlin (1937).

[35] Pollak, C., *Anodised Electrical Condensers und Current Directing Devices*, Britisches Patent Nr. 933 (1898).

[36] Bengough, G. und J. Stuart, *Producing An Oxide Film by The Chromic Acid Process and Dyeing It by Immersion in Dyestuff Solution*, Britisches Patent Nr. 223994 (1923).

[37] Masuda, H. und F. Fukuda, *Science* **268** (1995) 1466.

[38] Li, A., F. Müller und U. Gösele, *Electrochem. Sol. State Lett.* **3** (2000) 131.

[39] Masuda, H., H. Yamada, M. Satoh, H. Asoh, M. Nakao und T. Tamamura, *Appl. Phys. Lett.* **71** (1997) 2770.

[40] Masuda, H., H. Asoh, M. Watanabe, K. N. M. Nakao und T. Tamamura, *Adv. Mater.* **13** (2001) 189.

[41] Jessensky, O., F. Müller und U. Gösele, *Appl. Phys. Lett.* **72** (1998) 1173.

[42] Keller, F., M. Hunter und D. Robinson, *J. Electrochem. Soc.* **100** (1953) 411.

[43] Kape, J., *Trans. Inst. Met. Finish.* **45** (1966) 34.

[44] Parkhutik, V. und V. Shershulsky, *J. Phys. D: Appl. Phys.* **25** (1992) 1258.

[45] Li, F., L. Zhang und R. Metzger, *Chem. Mater.* **10** (1998) 2470.

[46] Despic, A. und V. Parkhutik, Bd. 20 von *Modern Aspects of Electrochemistry*, New York, Plenum Press (1984), 397ff.

[47] Wehrspohn, R., A.-P. Li, K. Nielsch, F. Müller, W. Erfurth und U. Gösele, Bd. PV 2000-4 von *Electrochemical Society Proceedings*, Electrochemical Society (2000), 271ff.

[48] Thamida, S. und H. Chang, *Chaos* **12** (2002) 240.

[49] Nielsch, K., *Hochgeordente ferromagnetische Nanostabensembles - Elektrochemische Herstellung und magnetische Charakterisierung*, Dissertation, Martin-Luther-Universität Halle-Wittenberg, Physik (2002).

[50] Wehrspohn, R., K. Nielsch, A. Birner, J. Schilling, F. Müller, A.-P. Li und U. Gösele, Bd. PV 2000-25 von *Electrochemical Society Proceedings*, Electrochemical Society (2001), 168ff.

[51] Choi, J., G. Sauer, K. Nielsch, R. Wehrspohn und U. Gösele, *Chem. Mater.* , eingereicht.

[52] Thompson, G. und G. Wood, *Nature* **290** (1981) 230.

[53] Nielsch, K., J. Choi, K. Schwirn, R. B. Wehrspohn und U. Gösele, *Nanoletters* **2** (2002) 677, siehe Anhang.

[54] Choi, J., K. Nielsch, M. Reiche, R. B. Wehrspohn und U. Gösele, *J. Vac. Sci. Techn. B* , eingereicht.

[55] Asoh, H., K. Nishio, M. Nakao, T. Tamamura und H. Masuda, *J. Electrom. Soc.* **148** (2001) 152.

[56] Schmuki, P., *J. Sol. State. Electrochem.* **6** (2002) 145.

[57] Lharch, M., J.-N. Chazalviel, F. Ozanam, M. Aggour und R. Wehrspohn, *Phys. Stat. Sol.* , eingereicht (siehe Anhang).

[58] Foss, C., G. Hornyak, J. Stockert und C. Martin, *J. Phys. Chem.* **98** (1994) 2963.

[59] Caboni, V., Italienisches Patent Nr. 339232 (1936).

[60] Sauer, G., G. Brehm, S. Schneider, K. Nielsch, R. Wehrspohn, J. Choi, H. Hofmeister und U. Gösele, *J. Appl. Phys.* **91** (2002) 3243, siehe Anhang.

[61] Zagiel, A., P. Natishan und E. Gileadi, *Eletrochim. Acta* **35** (1990) 1019.

[62] Dobrev, D., J. Vetter, N. Angert, und R. Neumann, *Appl. Phys. A* **69** (1999) 233.

[63] Sun, M., G. Zangari, M. Shamsuzzoha und R. M. Metzger, *Appl. Phys. Lett.* **78** (2001) 2964.

[64] Yin, A. J., J. Li, W. Jian, A. J. Bennett und J. Xu, *Appl. Phys. Lett.* **79** (2001) 1039.

[65] Nielsch, K., F. Müller, A. Li und U. Gösele, *Adv. Mater.* **12** (2000) 582.

[66] Matthias, S., J. Schilling, K. Nielsch, F. Müller, R. Wehrspohn und U. Gösele, *Adv. Mater.* , im Druck.

[67] Fleming, J., S. Lin, I. El-Kady, R. Biswas und K. Ho, *Nature* **417** (2002) 52.

[68] Nicewarner-Peña, S., R. Freeman, B. D. Reiss, L. He, D. Peña, I. Walton, R. Cromer, C. Keating und M. Natan, *Science* **294** (2001) 137.

[69] Martin, C., *Science* **266** (1994) 1961.

[70] de Gennes, P. G., *Rev. Mod. Phys.* **57** (1985) 827.

[71] Kistler, S., *Wettability*, Bd. 49 von *Surfactant Science Series*, Kap. 6, Marcel Dekker, New York (1993).

[72] Ausseré, D., A. M. Picard und L. Léger, *Phys. Rev. Lett.* **57** (1986) 2671.

[73] Steinhart, M., J. Wendorff, A. Greiner, R. Wehrspohn, K. Nielsch, J. Schilling, J. Choi und U. Gösele, *Science* **296** (2002) 1997, siehe Anhang.

[74] Steinhart, M., J. Wendorff, R. Wehrspohn, H. Hofmeister und U. Gösele, *Adv. Mater.* , eingereicht.

[75] Luo, Y., M. Alexe, R. Wehrspohn, U. Gösele, M. Steinhart, J. Wendorff und Ramesh, *Nature Mater.* , eingereicht.

[76] Luo, Y., R. Wehrspohn, U. Gösele, M. Steinhart, J. Wendorff, G. Böttger, M. Schmidt und M. Eich , unveröffentlichte Ergebnisse.

[77] Richter, S., J. Schilling, M. Zacharias, R. Wehrspohn, U. Gösele, M. Steinhart und J. Wendorff, *Adv. Mater* , eingereicht.

[78] Fussel, D. , persönliche Mitteilung.

[79] Sakoda, K., *Optical Properties of Photonic Crystals*, Springer (2001).

[80] Joannopoulos, J., R. Meade und J. Winn, *Photonic crystals: Molding the flow of light*, Princeton University Press (1995).

[81] Busch, K., *C.R. Physique* **3** (2002) 53.

[82] Ho, K., C. Chan und C. Soukoulis, *Phys. Rev. Lett.* **65** (1990) 3152.

[83] Sakoda, K., *Phys. Rev. B* **52** (1995) 8992.

[84] Sakoda, K., *Phys. Rev. B* **52** (1995) 7982.

[85] Stefanou, N., V. Karathanos und A. Modinos, *J. Phys. Condens. Matter* **4** (1992) 7389.

[86] Pendry, J. und A. MacKinnon, *Phys. Rev. Lett.* **69** (1992) 2772.

[87] Taflove, A., *Computational Electrodynamics: The Finite-Difference Time-Domain Method*, Artech House, Boston (1995).

[88] Chigrin, D., A. Lavrinenko, D. A. Yarotsky und S. Gaponenko, *J. Lightwave Techn.* **17** (1999) 2018.

[89] Birner, A., R. Wehrspohn, U. Gösele und K. Busch, *Adv. Mater.* **13** (2001) 377, siehe Anhang.

[90] Meade, R., K. Brommer, A. Rappe und J. Joannopoulos, *Appl. Phys. Lett.* **61** (1992) 495.

[91] Barra, A., D. Cassagne und C. Jouanin, *App. Phys. Lett.* **72** (1998) 627.

[92] Blanco, A., E. Chomski, S. Grabtchak, M. Ibisate, S. John, S. Leonard, C. Lopez, F. Meseguer, H. Miguez, J. Mondia, G. A. Ozin, O. Toader und H. Driel, *Nature* **405** (2000) 437.

[93] Noda, S., K. Tomoda, N. Yamamoto und A. Chutinan, *Science* **289** (2000) 604.

[94] Yablonovitch, E., T. Gmitter und K. Leung, *Phys. Rev. Lett.* **67** (1991) 2295.

[95] Christophersen, M., J. Carstensen, A. Feuerhake und H. Föll, *Mat. Sci. Eng.* **B 69-70** (2000) 194.

[96] Ho, K., C. Chan, C. Soukoulis, R. Biswas und M. Sigalas, *Sol. State Commun.* **89** (1994) 413.

[97] Johnson, S. und J. Joannopoulos, *App. Phys. Lett.* **77** (2000) 3490.

[98] Chutinan, A. und S. Noda, *Phys. Rev. B* **57** (1998) R2006.

[99] Toader, O. und S. John, *Science* **292** (2001) 1133.

[100] Fan, S., P. Villeneuve, R. Meade und J. Joannopoulos, *Appl. Phys. Lett.* **65** (1994) 1466.

[101] Sözüer, H. und J. Haus, *J. Opt. Soc. Am. B* **10** (1993) 296.

[102] Sözüer, H., J. Haus und R. Inguva, *Phys. Rev. B* **45** (1992) 13962.

[103] Busch, K. und S. John, *Phys. Rev. E* **58** (1998) 3896.

[104] Benisty, H., C. Weisbuch, D. Labilloy, M. Rattier, C. Smith, T. Krauss, R. Delerue, R. Houdre, U. Oesterle, C. Jouanin und D. Cassagne, *J. Lightwave Techn.* **17** (1999) 2063.

[105] Ferrini, R., D. Leuenberger, M.Mulot, M. Qui, J. Moosburger, M. Kamp, A. Forchel, S. Anand und R.Houdré, *IEEE J. Quantum Electron.* **38** (2002) 786.

[106] Bensity, H., S. Olivier, C. Weisbuch, M. Agio, M. Kafesaki, C. Soukoulis, M. Qui, U. Oesterle, A. Karlson, B. Jaskorzynska, A. Talneau, J. Moosburger, M. Kamp, A. Forchel, R. Ferrini, R. Houdré und U. Oesterle, *IEEE J. Quantum Electron.* **38** (2002) 805.

[107] Jamois, C., R. Wehrspohn, J. Schilling, F. Müller, R. Hillebrand und W. Hergert, *IEEE J. Quantum Electron.* **38** (2002) 805, siehe Anhang.

[108] Leonard, S., H. van Driel, K. Busch, S. John, A. Birner, A.-P. Li, F. Müller, U. Gösele und V. Lehmann, *Appl. Phys. Lett.* **75** (1999) 3063.

[109] Birner, A., A. Li, F. Müller, U. Gösele, P. Kramper, V. Sandoghdar, J. Mlynek, K. Busch und V. Lehmann, *Mater. Sci. Semincon. Proces.* **3** (2000) 487.

[110] Schilling, J., A. Birner, F. Mueller, R. B. Wehrspohn, R. Hillebrand, U. Goesele, K. Busch, S. John, S. W. Leonard und H. M. van Driel, *Opt. Mater.* **17** (2001) 7.

[111] von Freymann, G., M. Wegener, J. Schilling, R. Wehrspohn und K. Busch , unveröffentlichte Ergebnisse.

[112] Birner, A., *Optische Wellenleiter und Mikroresonatoren in 2D-Photonischen Kristallen aus Makroporösem Silizium*, Dissertation, Martin-Luther-Universität Halle-Wittenberg (2000).

[113] von Freymann, G., M. Wegener, J. Schilling, R. Wehrspohn und K. Busch , unveröffentlichte Ergebnisse.

[114] Choi, J., J. Schilling, K. Nielsch, R. Hillebrand, M. Reiche, R. Wehrspohn und U. Gösele, *Mater. Res. Soc. Proc.* **722** (2002) L5.2, siehe Anhang.

[115] Liguda, C., G. Böttger, A. Kuligk, R. Blum, M. Eich, H. Roth, J. Kunert, W. Morgenroth, H. Elsner und H. Meyer, *App. Phys. Lett.* **78** (2001) 2434.

[116] Kramper, P., A. Birner, M. Agio, C. M. Soukoulis, F. Müller, U. Gösele, J. Mlynek und V. Sandoghdar, *Phys. Rev. B* **64** (2001) 233102.

[117] Leonard, S. W., H. van Driel, A. Birner, U. Gösele, und P. Villeneuve, *Opt. Lett.* **25** (2000) 1550.

[118] Kramper, P., *Optische Eigenschaften von 2D-Photonischen Kristallen*, Dissertation, Universität Konstanz (2002).

[119] Lezec, H., A. Digeron, E. Deveaux, R. Linke, L. M. Moreno, F. Garcia-Vidal und T. Ebbesen, *Science* **297** (2002) 820.

[120] Leonard, S., *Optical properties of 2D photonic crystals from macroporous silicon*, Dissertation, University of Toronto, Dept. of Physics (2001).

[121] Leonard, S. W., *Appl. Phys. Lett.* , eingereicht.

[122] Schilling, J., F. Müller, S. Matthias, R. Wehrspohn, U. Gösele und K. Busch, *Appl. Phys. Lett.* **78** (2001) 1180, siehe Anhang.

[123] Schilling, J., F. Müller, R. Wehrspohn und U. Gösele, *Mater. Res. Soc. Proc.* **722** (2002) L6.8, siehe Anhang.

[124] Hermann, C., O. Hess, C. Jamois und R. Wehrspohn , unveröffentlichte Ergebnisse.

[125] Hillebrand, R., C. Jamois, R. Wehrspohn, U.Gösele und W. Hergert, *Phys. Stat. Sol.* , eingereicht.

[126] Bogaerts, W., P. Bienstman, D. Taillart, R. Baets und D. de Zutter, *Opt. Quantum Electron.* **34** (2002) 195.

[127] Kim, S. und V. Gopalan, *Appl. Phys. Lett.* **78** (2001) 3015.

[128] Choi, D. und S. Kang, *Bull. Korean Chem. Soc.* **20** (1999) 1186.

[129] Mertens, G., *persönliche Mitteilung* .

[130] Leonard, S. W., J. Mondia, H. van Driel, O. Toader, S. John, K. Busch, A. Birner, U. Gösele und V. Lehmann, *Phys. Rev. B* **61** (2000) R2389.

[131] Leonard, S., H. van Driel, J. Schilling und R. Wehrspohn, *Phys. Rev. B* **66** (2002) 1211xx, , siehe Anhang.

[132] van Driel, H., S. Leonard, J. Schilling und R. Wehrspohn, *Mater. Res. Soc. Proc.* **722** (2002) L3.1.

[133] Leonard, S. W., H. M. van Driel, J. Schilling und R. Wehrspohn, *Ultrafast all-optical band-edge switching in photonic crystals*, Patentanmeldung.

[134] Feist, A., A. Lambrecht, J. Schilling, F. Müller und R. Wehrspohn, *Vorrichtung und Verfahren zur qualitativen und quantitativen Bestimmung von Gasen und Flüssigkeiten mit PBG-Struktur*, Patentanmeldung.

[135] Quiten, M., A. Leitner, J. Krenn und F. Aussenegg, *Opt. Lett.* **23** (1998) 1331.

[136] Kreibig, U. und M. Vollmer, *Optical Properties of Metal Clusters*, Springer, Berlin (1995).

[137] Kottmann, J. und O. Martin, *Opt. Expr.* **8** (2001) 655.

[138] Sauer, G., G. Brehm, S. Schneider, K. Nielsch, R. Wehrspohn, J. Choi, P. Miclea und U. Gösele, *J. Appl. Phys.* , in Vorbereitung.

[139] Bertotti, G., *Hysteresis in Magnetism*, Chestnut Hill, MA, Academic Press.

[140] Nielsch, K., F. Müller, G. Liu, R. Wehrspohn, U. Gösele, S. Fischer und H. Kronmüller, Bd. PV-2000-8 von *Electrochemical Society Proceedings*, Electrochemical Society (2002).

[141] Nielsch, K., R. Wehrspohn, S. Fischer, H. Kronmüller, J. Barthel, J. Kirschner und U. Gösele, *Mater. Res. Soc. Proc.* **636** (2001) D1.9.1.

[142] Nielsch, K., R. Wehrspohn, S. Fischer, H. Kronmüller, J. Barthel, J. Kirschner, T. Schweinboeck, D. Weiss und U. Gösele, *Mater. Res. Soc. Proc.* **705** (2002) Y9.3.1.

[143] Hertel, R., *J. Appl. Phys.* **90** (2001) 5572.

[144] Nielsch, K., R. Wehrspohn, J. Barthel, J. Kirschner, S. Fischer, H. Kronmüller, T. Schweinböck, D. Weiss und U. Gösele, *J. Magn. Magn. Mater.* **249** (2002) 234.

[145] Nielsch, K., R. Hertel, R. B. Wehrspohn, J. Barthel, J. Kirschner, U. Gösele, S. F. Fischer und H. Kronmüller, *IEEE Trans. Magn.* **38**, im Druck.

[146] Grünberg, P., C. M. an W. Vach und M. Grimsditch, *J. Magn. Magn. Mater.* **28** (1982) 319.

[147] Wang, Z.-K., M.-H. Kuok, S.-C. Ng, H. Fan, D. J. Lockwood, K. Nielsch und R. B. Wehrspohn, *Mater. Phys. Mechan.* **4** (2001) 22.

[148] Wang, Z.-K., M.-H. Kuok, S.-C. Ng, D. J. Lockwood, M. G. Cottam, K. Nielsch, R. B. Wehrspohn und U. Gösele, *Phys. Rev. Lett.* **89** (2002) 027201, siehe Anhang.

[149] Arias, R. und D. Mills, *Phys. Rev. B* **63** (2001) 134439.

A Ausgewählte Veröffentlichungen

A.1 Materialien

1. R.B. Wehrspohn, J.-N. Chazalviel, F. Ozanam, und I. Solomon, 'Electrochemistry and photoluminescence of porous amorphous silicon', *Thin Sol. Films* **297** (1997) 5.
2. R. B. Wehrspohn, F. Ozanam, und J.-N. Chazalviel, 'Macro- and Nano-pore formation in p-type silicon', *J. Electrochem. Soc.* **146** (1999) 3309.
3. J.-N. Chazalviel, R.B. Wehrspohn, und F. Ozanam, 'Electrochemical preparation of porous semiconductors: from phenomenology to understanding', *Mat. Sci. Eng. B* **69-70** (2000) 1.
4. K. Nielsch, J. Choi, K. Schwirn , R. B. Wehrspohn, und U. Gösele, 'Self-ordering regimes of porous alumina: the 10%porosity-rule', *Nano Lett.* **2** (2002) 677.
5. M. Lharch, J.-N. Chazalviel, F. Ozanam, M. Aggouir, und R.B. Wehrspohn, 'In situ Investigation of Porous Anodic Films of Silica', *Phys. Stat. Sol.* (2002), Druck.
6. G. Sauer, G. Brehm, S. Schneider, K. Nielsch, R.B. Wehrspohn, J. Choi, H. Hofmeister, und U. Gösele, 'Highly-ordered monocrystalline silver nanowire arrays', *J. Appl. Phys.* **91** (2002) 3243.
7. M. Steinhart, J.H. Wendorff, A. Greiner, R.B. Wehrspohn, K. Nielsch, J. Schilling, J. Choi, und U. Gösele, 'Polymer nanotubes via wetting of ordered templates', *Science* **296** (2002) 1997.

A.2 Anwendungen

1. A. Birner, R.B. Wehrspohn, U. Gösele, und K. Busch, 'Silicon-based photonic crystals', *Adv. Mater.* **13** (2001) 377.
2. R.B. Wehrspohn und J. Schilling, 'Electrochemically-prepared 2D photonic crystals', *Mater. Res. Soc. Bull.* **8** (2001)623.
3. J. Schilling, R.B. Wehrspohn, A. Birner, F. Müller, R. Hillebrand, U. Gösele, S.W. Leonard, J.P. Mondia, F. Genereux, H.M. van Driel, P. Kramper, V. Sandoghdar, aund K. Busch, 'A model system for 2D and 3D photonic crystals: Macroporous silicon', *J. Opt. A: Pure Appl. Opt.* **3** (2001) 121.
4. C. Jamois, R.B. Wehrspohn, J. Schilling, F. Müller, R. Hillebrand, und W. Hergert, 'Silicon-Based Photonic Crystal Slabs: Two Concepts', *IEEE J. Quant. Electron.* **38** (2002) 805 .
5. S.W. Leonard, H. van Driel, J. Schilling, und R.B. Wehrspohn, 'Ultrafast band edge tuning of a twodimensional silicon photonic crystal via free-carrier injection', *Phys. Rev. B* **66** (2002) 1211xx.
6. J. Choi, J. Schilling, K. Nielsch, R.B. Wehrspohn, M. Reiche, und U. Gösele, 'Porous alumina photonic crystals obtained via imprint method', *MRS Symp. Proc.* **722** (2002) L5.2 edited by R.B. Wehrspohn et al..
7. J. Schilling, S. Matthias, F. Müller, R.B. Wehrspohn, und K. Busch, 'Three-dimensional photonic crystals based on macroporous silicon with modulated pore diameter', *Appl. Phys. Lett.* **78** (2001) 1180.
8. J. Schilling, F, Müller, R.B. Wehrspohn, und U. Gösele, 'Dispersion relation of 3D hexagonal photonic crystals', *MRS Symp. Proc.* **722** (2002) L6.8 edited by R.B. Wehrspohn et al..

9. K. Nielsch, R.B. Wehrspohn, J. Barthel, J. Kirschner, U. Gösele, S. F. Fischer, und H. Kronmüller, 'Perpendicular storage medium based on 100nm period Ni Nanowire arrays', *Appl. Phys. Lett.* **79** (2001) 1360.
10. Z.-K. Wang, M.-H. Kuok, S.-C. Ng, D. J. Lockwood, M. G. Cottam, K Nielsch, R. B. Wehrspohn, und U. Gösele, 'Spin wave quantization in ferromagnetic nanowire arrays', *Phys. Rev. Lett.* **89** (2002) 027201.

ELSEVIER

Thin Solid Films 297 (1997) 5–8

thin solid films

Electrochemistry and photoluminescence of porous amorphous silicon

R.B. Wehrspohn *, J.-N. Chazalviel, F. Ozanam, I. Solomon

Laboratoire de Physique de la Matière Condensée, CNRS–École Polytechnique, 91128 Palaiseau Cedex, France

Abstract

A systematic study of the electrochemistry of hydrogenated amorphous silicon (a-Si:H) is presented in order to explain pore formation in this material. The similarity of the cyclovoltammograms of amorphous and crystalline silicon demonstrates that the basic electrochemical reactions are similar in both materials. A striking difference between the electrochemistry of these two materials is the existence of an instability which limits the maximum thickness of the porous amorphous material that can be obtained. We explain this instability by the large value of the resistivity of amorphous silicon in comparison with that of the electrolyte, and model this phenomenon by a linear stability analysis. We detected the same phenomenon during anodization of highly resistive p-type crystalline silicon. The photoluminescence intensity of porous a-Si:H is quite comparable with that of crystalline silicon of the same thickness. © 1997 Elsevier Science S.A.

Keywords: Luminescence; Silicon

1. Introduction

Highly luminescent porous silicon obtained by anodization of single-crystal wafers in a hydrofluoric acid electrolyte has been the object of extended studies in recent years [1]. Porous silicon prepared from heavily doped amorphous silicon films has been found to be highly photoluminescent [2].

The electrochemistry of the preparation of porous silicon has been studied extensively for crystalline silicon (c-Si), but very little work has been carried out for amorphous silicon. In this work, we perform a systematic study of the electrochemistry and pore formation in hydrogenated amorphous silicon. We show that the thickness of the porous layer in a-Si:H is highly limited by an instability specific to this material. A maximal thickness of only 0.5 μm can be reached under standard conditions [3]. We attribute the instability to the high resistivity of the material compared with that of the electrolyte. An elementary linear stability analysis is in good agreement with experimental results. The model was extended to highly resistive crystalline p-type silicon where we observed the same instability.

2. Experimental details

Device-grade, hydrogenated amorphous silicon produced in a 13.56 MHz, capacitively coupled PECVD reactor at a substrate temperature of 250 °C, was deposited onto a stainless steel substrate. The geometry of the reactor and the deposition conditions are published elsewhere [4]. The doping level varies between 0.05% and 1.5% diborane in the gas phase, the thickness of the layers is about 2 μm. The resistivities of our samples vary between 10^6 and 10^4 Ω cm for 0.05% B and 1.5% B respectively.

The cyclovoltammetric analysis was carried out in a polytrifluorochloroethylene cell with N_2 circulation under potentiostatic conditions. The electrolyte consisted of 0.1 M HF and 0.9 M NH_4Cl (pH 2). The geometry of the cell is described elsewhere [3]. The ohmic drop in the amorphous silicon layer was compensated electronically during the measurement. The porous a-Si:H was formed in a three-electrode cell, consisting of a platinum counter-electrode and an Ag/AgCl reference electrode coupled to the electrolyte by a KCl bridge. Anodization was performed in a galvanostatic arrangement. The percentage of hydrofluoric acid in the electrolyte was varied between 5% and 50%.

Photoluminescence (PL) measurements were carried out at room temperature in air. Excitation was provided by the 476 nm or the 351 nm line of a Kr^+ laser. The luminescence signal was then filtered and dispersed by a 27.5 cm focal length monochromator and detected by a cryostatically cooled, computer-driven CCD from EG&G. The spectral sensitivity of the system was calibrated by a tungsten lamp at 3300 K. The power density of the 476 nm line was about 10 mW cm^{-2}.

---

* Corresponding author. Tel: +33 1 69 33 46 66; fax: +33 1 69 33 30 04; e-mail: rw@pmcsun1.polytechnique.fr

0040-6090/97/$17.00 © 1997 Published by Elsevier Science S.A.
PII S0040-6090(96)09362-5

3. Results and discussion

3.1. Electrochemistry

Cyclic voltammetry of crystalline silicon has been studied in detail [5]. The conditions of preparation of porous silicon are found to depend mostly on the HF concentration and current density. Electropolishing occurs at high current densities and low HF concentrations. Pore formation occurs at low current densities and high HF concentrations. Fig. 1 shows a typical cyclovoltammetric curve. The first peak determines the different regimes. The cyclovoltammetric curve for amorphous silicon shows the same global behavior but the first current peak is not visible, only a slight change in the slopes could be detected and interpreted as a rudimentary peak. Investigations of Chazalviel et al. [5] have shown that for crystalline silicon the peak and adjacent valley exhibit a dependence on crystal orientation. The disappearance of the valley is clearly due to the complete loss of crystal structure for a-Si:H.

An electrolyte containing 25% HF (HF:H_2O:ethanol in a ratio 5:9:6) and a current density of 10 mA cm^{-2} produces a reasonably thick porous layer for all doping levels. Thus we take these conditions as a standard. Fig. 2 shows the potential plotted against the anodization time during electrochemical etching of an amorphous layer. For standard crystalline silicon (resistivity of about 1 Ω cm) the potential remains small and nearly constant during anodization (about 0.5 V). The high value of the potential for porous a-Si:H is clearly associated with the ohmic drop inside the a-Si:H layer. Fig. 2 shows three different regimes during pore formation in a-Si:H. The first regime (region A) is attributed to the formation of a nanoporous layer. The decrease in potential is proportional to the thickness of the porous layer multiplied by the resistivity of the bulk material considering that the electrolyte in the pores has a high conductivity. Therefore, the slope is finite in contrast with the case of crystalline silicon which is about 4–6 orders of magnitude more conductive. The etching rate is about 85 Å s^{-1} in this case, which can be interpreted as a porosity of about 75% considering Faraday's law and assuming that two electrons are needed for the dissolution of one silicon atom as in c-Si. The second regime (region B) is a new regime, not observed in crystalline p-type silicon. This fast voltage drop is due to the formation of large channels which quickly grow toward the stainless steel substrate. We have confirmed this picture by atomic force microscopy plan view and scanning electron microscopy (SEM) lateral view investigations (Fig. 3). In the third regime (region C), finally, the highly doped contact layer between a-Si:H and the stainless steel is dissolved, resulting in peeling off of the whole deposit. Fig. 4 shows schematically what happens during anodization of amorphous silicon.

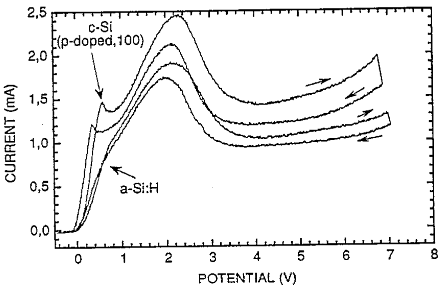

Fig. 1. Cyclovoltammetry of porous c-Si and a-Si:H. The current density is plotted against the applied potential under potentiostatic conditions. The current peak between 0 and 1 V determines the transition between pore formation and electropolishing.

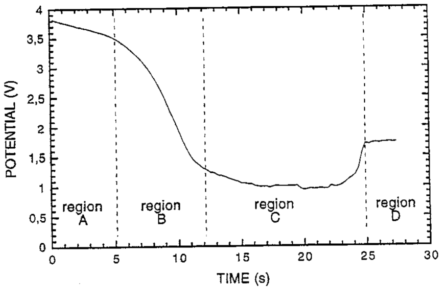

Fig. 2. Variation of the electrode potential ($E_{electrode} - E_{reference}$) as a function of the etching time for a current density of 10 mA cm^{-2}. Region A corresponds to the formation of porous silicon. Region B corresponds to the formation of channels and region C to the dissolution of the interface. In region D, the layer peels off and the anodization potential of the stainless steel substrate is reached.

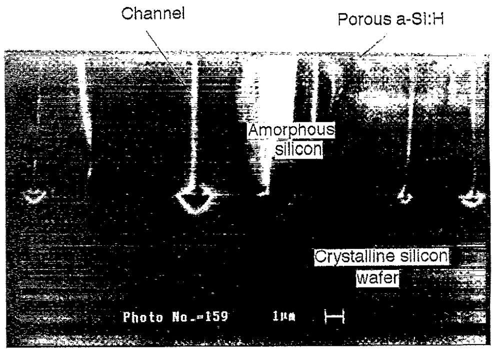

Fig. 3. SEM lateral view of an anodized a-Si:H layer. The first hundreds of nanometers show the porous a-Si:H layer, then large channels, due to the instability, extend to the interface a-Si:H–c-Si. The amorphous layer was deposited onto a c-Si wafer. Here, slight etching of the wafer at the bottom of the pipes has already occurred.

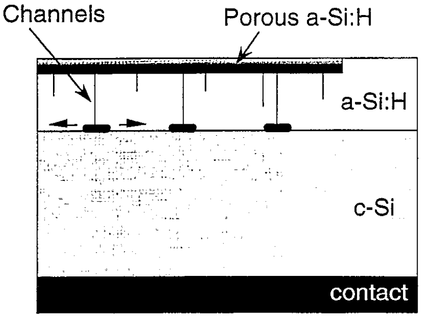

Fig. 4. Schematic picture of the processes occurring during the anodization of a-Si:H. Referring to Fig. 2, region A corresponds to the porous a-Si:H layer, region B to the pipes and region C to the dissolution of the interface.

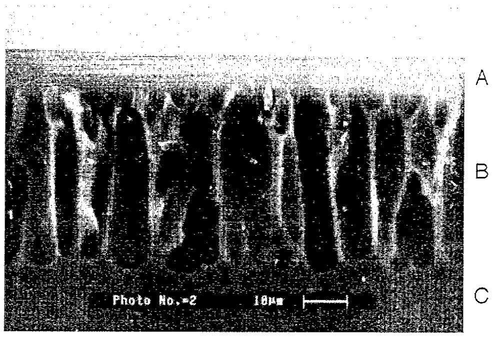

Fig. 5. SEM lateral view of porous silicon from highly resistive p-doped c-Si. 'A' corresponds to the nanoporous layer, 'B' to the large channels resulting from the instability, 'C' is the c-Si wafer.

3.2. Discussion

The resistivity of our a-Si samples is about 4–6 orders of magnitude higher than the resistivity of the electrolyte. The resistivity of the electrolyte, obtained by impedance measurements, varies between 2 and 30 Ω cm for mixtures containing variable concentrations of HF in 30% ethanol. In a linear stability analysis, we show that the instability can be explained by simple electrostatic considerations: the resistivity of amorphous silicon is higher than that of the electrolyte, therefore every perturbation on the electrolyte–silicon interface is enhanced by accumulated field lines. If the local current density reaches the electropolishing regime, large channels are created. In the case of crystalline silicon, the electrolyte has a higher resistivity than bulk c-Si, small perturbations are damped and the interface stays stable.

Analytically, we have solved the Laplace equation for a growing sinusoidal electrolyte–silicon interface:

$$\Delta \Phi(x,y)=0 \text{ and } \left.\frac{\mathrm{d}y}{\mathrm{d}t}\right|_{\text{interface}}=kJ$$

The ratio of bulk material resistivity to the resistivity of the electrolyte is the crucial parameter, determining the amplitude of the fluctuation and therefore the maximal thickness that can be obtained. According to the calculation the amplitude δy of the sinewave profile is found to evolve as

$$\delta y \propto \exp(\alpha t)$$

with

$$\alpha \propto \left(1-\frac{\rho_{\text{electrolyte}}}{\rho_{\text{bulk}}}\right)$$

More details about this calculation are described elsewhere [3]. Taking these considerations into account, we have been able to increase the thickness of our porous layers by more than a factor of two by increasing the resistivity of the electrolyte. The same instability occurs in the anodization of highly resistive crystalline p-type silicon (100 and 1000 Ω cm) which confirms the model (Fig. 5). In summary, we conclude that the nano-scale pore formation in amorphous silicon is based on a similar mechanism as for c-Si, except that the thickness of the porous layer is severely limited by an instability occurring during anodization.

3.3. Photoluminescence

Hydrogenated amorphous silicon has almost no detectable photoluminescence at room temperature. After electrochemical treatment, the amorphous layer exhibits room temperature photoluminescence with a peak energy of 1.5 eV (Fig. 6). A more detailed description is published elsewhere [3]. The absolute photoluminescence intensity of porous a-Si:H, in practice, is not very strong, which makes it hardly visible with the naked eye. This is not due to a low quantum efficiency, but to the small thickness of the samples that can be obtained by anodization of amorphous silicon films. The luminescence observed under an optical microscope of about 1 μm resolution is homogeneous, contrary to what has been observed by Bustarret et al. [2] for heavily doped silicon.

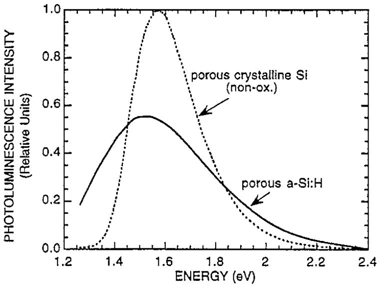

Fig. 6. Photoluminescence spectra of porous silicon obtained from a-Si:H compared with that of non-oxidized crystalline porous Si of the same thickness, obtained with the same electrochemical preparation (excitation 476 nm, 10 mW cm^{-2}).

4. Conclusion

We have studied the electrochemical conditions of the preparation of porous silicon from hydrogenated amorphous silicon. Pore formation in crystalline and amorphous silicon is based on similar electrochemical mechanisms. A striking difference between these two materials is that the maximum thickness of the porous amorphous layer is severely limited by an instability occurring during pore formation. We have explained this instability by the large value of the ratio of the resistivity of the amorphous material to that of the electrolyte. We have confirmed this model by the observation of the same instability in highly resistive p-type crystalline silicon. Because of the limited amount of porous silicon, the total luminescence is weak in comparison with that of porous crystalline silicon. However, normalized photoluminescence intensities (photoluminescence of samples of the same thickness) are quite comparable.

Acknowledgements

The authors are grateful to Jean-Luc Beaunier for the SEM pictures.

References

[1] L.T. Canham, *Appl. Phys. Lett., 57* (1990) 1046.
[2] E. Bustarret, M. Ligeon and M. Rosenbauer, *Phys. Status Solidi B, 190* (1995) 111.
[3] R.B. Wehrspohn, J.-N. Chazalviel, F. Ozanam and I. Solomon (1996) unpublished results.
[4] R.B. Wehrspohn, J.-N. Chazalviel, F. Ozanam and I. Solomon, *Phys. Rev. Lett., 77* (1996) 1885.
[5] J.-N. Chazalviel, M. Etman and F. Ozanam, *J. Electroanal. Chem., 297* (1991) 533.

Journal of The Electrochemical Society, **146** (9) 3309-3314 (1999)
S0013-4651(99)01-085-X CCC: $7.00 © The Electrochemical Society, Inc.

Nano- and Macropore Formation in p-Type Silicon

R. B. Wehrspohn,[a] F. Ozanam,[b] and J.-N. Chazalviel[b],*

[a]*Philips Research Laboratories, Redhill, Surrey RH1 5HA, United Kingdom*
[b]*Laboratoire de Physique de la Matière Condensée, CNRS-École Polytechnique, 91128 Palaiseau Cedex, France*

We present an analytical model describing the instability of the interface during anodization of p-type resistive silicon in HF electrolyte, leading to porous silicon formation. Our analytical approximations are applicable to p-type amorphous and crystalline silicon with resistivities in the range from about 0.1 to 10,000 Ω cm. For all kinds of p-type silicon, nanopore formation is predicted to occur first, as it is governed by properties of the silicon/electrolyte barrier. Then, pores of increasing diameter are expected to grow, up to sizes of the order of a characteristic cutoff length. Structures above that size occur only when the resistivity of silicon is larger than that of the electrolyte.

Manuscript received January 25, 1999.

Porous silicon is formed by anodization of p-type silicon in hydrofluoric acid and has been studied theoretically by several groups.[1-8] A current-state-of-the-art summary is given by Allongue.[9] Three different pore formation regimes have been observed experimentally as a function of the dopant concentration. For degenerately doped p-type silicon, a special type of macropores has been observed experimentally and attributed to tunneling of holes through the space-charge region.[8] For moderately doped p-type silicon, nanopore formation is observed with structures in the range of 2-100 nm. For highly resistive crystalline and amorphous p-type silicon, macropore formation (0.4 to 10 μm diam) is observed below a thin layer of nanopores.[3] Previously, macropore formation in low-doped Si had been reported in anhydrous electrolyte only.[10,11] In a recent article, we have explained the occurrence of a macropore regime in aqueous electrolytes when the resistivity of the electrolyte exceeds that of silicon.[5] This model was based on a linear stability analysis of the interface, in which the role of the interface was oversimplified and assimilated to that of an interfacial resistance.

The initial stage of nanopore formation in p-type silicon has been recently modeled by Valance[1] using a linear stability analysis. However, the results are only numerical and no analytical approximation is given. Moreover, the calculated diameter of the nanopores is in apparent contradiction with the experimental data. One reason for this unphysical pore-radius value lies in the assumption for the stabilizing mechanism prevailing at short scale, which is assumed to originate from surface tension. This *ansatz* is frequently used, for example, for modeling dendrite growth during crystallization in a temperature gradient.[12] However, as discussed below, there is no evidence that the equilibrium thermodynamics of the surface plays a role at all during pore formation, which appears essentially governed by kinetic factors.

On the other hand, in addition to our own reports, macropore formation at low-doped p-Si in aqueous-containing electrolytes has recently been reported by two other groups.[13-15] These authors propose that the key element which accounts for this formation arises from inhomogeneities in the dissolution kinetics,[13,14] or from local enhancement of the hole transport to the interface at the pore tips.[15]

Therefore, in any case (nano- or macropore formation), taking into account the interface appears mandatory, either for accounting for nanopore formation, or for telling between the various proposals accounting for macropore formation. In the present article, we extend our previous analytical model, in order to incorporate a more detailed description of the interface suited to the case of nanopore formation. We first briefly recall our initial model (the "two-region" model), then introduce our extended model (the "unified" model), and finally discuss the results and the model limitations in connection with the literature.

Model A: the Two-Region Model

Our recent model for macropore formation in highly resistive crystalline p-type silicon and amorphous silicon[5] is based on a linear stability analysis. It applies in the simplest case where the potential drop during anodization occurs mainly in the electrolyte and in the silicon bulk. The space-charge and interface region are approximated by an interfacial specific resistance, which is reasonable considering that the major part of the potential drop occurs in the silicon bulk and not at the interface.[16]

The onset of macropore formation can be simulated by a linear stability analysis à la Mullins and Sekerka.[17] Assuming that the planar silicon/electrolyte interface undergoes a small deformation $\delta\Delta$, it reads

$$y(x, t) = \Delta(t) + \delta\Delta(x, t) \quad [1]$$

where (x, y) represents a point of the interface and Δ is the position of the unperturbed planar growth front at time t. The computation can be performed for a sine wave perturbation only, since a linear superposition of all Fourier modes q in reciprocal space reconstructs any small surface perturbation in real space. Hence we take

$$\delta\Delta(x, t) = \delta_0 \cos(qx) \exp[\beta(q)t] \quad [2]$$

where q is the wavenumber of the perturbation and $\beta(q)$ the amplification rate of the growth front deformation. A positive β means amplification or instability of the growth front whereas a negative β means attenuation or stable interface. The exact calculation is published elsewhere,[4,18] here only the important results are summarized. It consists in solving Laplace equation ($\Delta\phi = 0$) and computing the current density J for the silicon/electrolyte system, with a potential drop $R_i J$ across the interface, assuming that the growth of the porous layer is ruled by Faraday's law ($\partial y/\partial t \propto J$). The solution is

$$\alpha(q) = \frac{\rho_s - \rho_{porous}}{\rho_s + R_i q + \rho_{porous}} q \quad [3]$$

where α is the normalized amplification coefficient $\alpha = \beta/(d\Delta/dt)$, ρ_{porous} is defined as ρ_e/P with ρ_e the electrolyte resistivity, ρ_s the silicon resistivity, and P is the porosity. The current density is of minor importance and only affects the porosity (increasing the current density results in a higher porosity). This dependence has a slight effect on the magnitude of the instability but does not affect its onset significantly. This calculation has been remade in more detail by explicitly taking into account the resistance of the back contact and a current-dependent porosity. However, the overall behavior does not change and remains correctly described by Eq. 3.[18]

Model B: the Unified Model

According to Beale *et al.*[7] and in agreement with flatband-potential measurements,[19-21] a depletion layer is present at the interface under typical dissolution conditions. This suggests that the electrochemical reaction rate is limited by the flow of holes overcoming the barrier to react at the interface. In the previous model, the space-charge region (SCR) has been approximated by an interfacial specific resistance R_i, a reasonable assumption, since the fluctuation wavelength of the

---

* Electrochemical Society Active Member.

S0013-4651(99)01-085-X CCC: $7.00 © The Electrochemical Society, Inc.

macropores was much larger than the thickness of the space-charge region. This approximation allows for restricting the potential computation to two regions, only silicon bulk and electrolyte. In order to understand the nanopore and macropore formation during dissolution, the stability analysis must be carried out by computing the potential drop in three regions, including the space-charge region (Fig. 1). For amorphous silicon, the density of states N at the Fermi level is approximately constant. In the absence of perturbation, solving Poisson equation in the space-charge region results in an exponential band bending profile, which we use for the following calculation. The changes in the calculations and in the results when taking a parabolic band bending profile like in crystalline silicon are further discussed below.

Typically, the potential profile $\Phi(y)$ during anodization exhibits distinct variations in the electrolyte, the porous silicon, and the bulk silicon electrode (Fig. 2). Since the electrolyte in the pores of the porous material has a higher conductivity than the porous silicon skeleton, we set $\rho_{\text{porous}} \approx \rho_e$, and choose the origin at the back side of the porous layer. In the absence of interface perturbation, the potential drop in the electrolyte and the porous layer takes the form

$$\Phi_e \approx \rho_e J y \qquad [4a]$$

where the resistivity of the electrolyte can be determined by high-frequency impedance measurements. In silicon, two contributions are superimposed. The first one arises from the space charge and, assuming a constant density of states N in the gap, has the following form

$$\Phi_{\text{SCR}}(y) = \Phi_{\text{sc}}[\exp(-y/\lambda) - 1] \qquad [4b]$$

where λ is the space-charge region width $\lambda = \sqrt{\epsilon\epsilon_0 (Ne^2)^{-1}}$ and $e\Phi_{\text{SC}}$ is the band bending. The second one arises from the silicon bulk and is given by

$$\Phi_s = \rho_s J y \qquad [4c]$$

At sufficiently low doping densities, the potential drop across the Helmholtz layer can be neglected, since it is much smaller than the potential drop across the SCR. However, when the doping level is increased and even in the absence of surface states, this small potential drop $\epsilon\epsilon_0 E_S / C_H$ is no longer negligible and takes part of the applied potential[22] (with E_S the surface electric field, and C_H the Helmholtz capacitance). Therefore, Φ_{SC} in Eq. 4b has to be corrected for this potential drop

$$\Phi_{\text{SC}} = \Phi^0_{\text{SC}} - \epsilon\epsilon_0 E_S / C_H \qquad [4d]$$

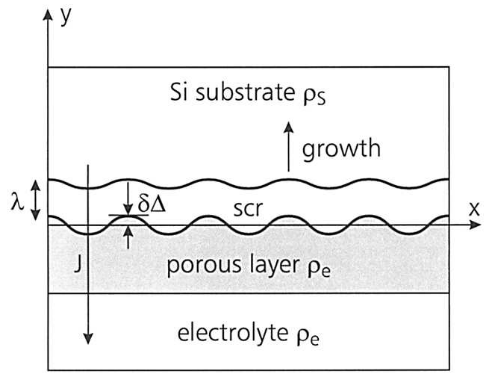

Figure 1. Scheme of model B. For the sake of simplicity, the electrolyte and the porous layer are assumed to have the same resistivity ρ_e and are treated as one layer with semi-infinite thickness. The space-charge region (SCR) has a width λ and the silicon substrate is treated as semi-infinite with a resistivity ρ_s. The sinusoidal SCR/electrolyte interface perturbation has a wavelength $2\pi/q$ and an amplitude $\delta\Delta$.

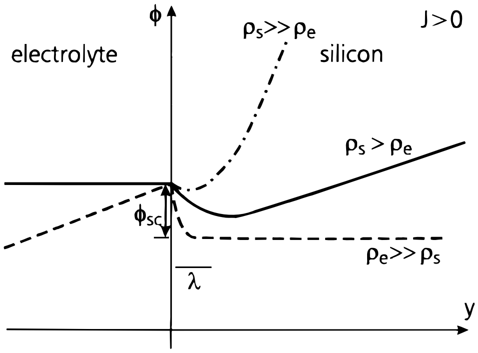

Figure 2. Potential distribution in an electrolyte/silicon junction under applied bias. For low-resistive silicon with $\rho_e > \rho_s$, the potential drop occurs mainly in the electrolyte and at the interface (solid line). For resistive silicon with $\rho_s > \rho_e$, the potential drop is mainly in the silicon bulk and at the interface. For highly resistive silicon, the current is limited by the silicon bulk (dotted line). In this case, which is close to lightly doped amorphous silicon, the Schottky barrier approximation fails.

Here Φ^0_{SC} is the total potential drop at the interface and writes $\Phi^0_{\text{SC}} = V_{\text{FB}} - V$, where V_{FB} is the flatband potential and V the applied potential.

The current density may be determined by considering the transport mechanism across the interface and the space-charge region. Two limitations can occur: hole transport across the SCR and charge transfer across the interface. In the following, we adopt a treatment inspired by Crowell and Sze for Schottky junctions[23] and assume that the two limitations are in series. However, in the case of a Schottky junction, charge transfer across the interface is limited by thermionic emission. In the present case it is rather limited by the reaction kinetics at the interface. The hole current flow J reads

$$J_y = -eN_A \frac{\exp[e\epsilon\epsilon_0 E_S/(kTC_H)]}{\dfrac{1}{v_R} + \dfrac{1}{v_D}} \exp(-e\Phi^0_{\text{SC}}/kT) \qquad [5]$$

where N_A is the acceptor concentration, v_D an effective velocity due to drift and diffusion across the SCR, and v_R a characteristic reaction velocity. A good approximation for v_D is given by

$$v_D \approx \mu E_S \qquad [6]$$

with μ the hole mobility and E_S the surface electric field, which can be estimated by

$$E_S \approx \frac{\Phi_{\text{SC}}}{\lambda} - \rho_s J \qquad [7]$$

where the second term is negligible for $\rho_s < 10^4\ \Omega$ cm at practical current densities.

We now perform a linear stability analysis similar to that carried out in model A. The advancing speed of the porous-silicon/bulk-silicon interface $d\Delta/dt$ is proportional to the current density J_y according to Faraday's law

$$\frac{d\Delta}{dt} = -KJ_y = KJ \qquad [8]$$

with J the measured hole current density ($J > 0$) and K a positive constant. Any small perturbation of the current density results in a perturbation of the growth rate

$$\frac{d\delta\Delta}{dt} = -K\delta J_y \qquad [9]$$

S0013-4651(99)01-085-X CCC: $7.00 © The Electrochemical Society, Inc.

or, considering a constant porous silicon growth velocity

$$\frac{d\delta\Delta}{dt} = -\frac{\delta J_y}{J} = \alpha\delta\Delta \qquad [10]$$

Then, the instability parameter α gets

$$\alpha = -\frac{\delta J_y}{J\delta\Delta} \qquad [11]$$

The term $\delta J_y/J$ can be obtained by taking the derivative of Eq. 5 and by identifying $\delta v_D/v_D$ with $\delta E_S/E_S$, which yields

$$-\frac{\delta J_y}{J} = -\frac{e\delta\Phi^0_{SC}}{kT} + S\frac{\delta E_S}{E_S} \qquad [12]$$

where

$$S = \frac{e\epsilon\epsilon_0 E_S}{kTC_H} + \frac{v_R}{v_R + v_D}$$

The variation of the total potential drop at the interface $\delta\Phi^0_{SC}$ is calculated by matching the various first-order changes associated with Eq. 4a-4c when a small perturbation is introduced according to Eq. 1. Whereas the introduction of a small perturbation in Eq. 4a and 4c is rather straightforward, the implementation for Eq. 4b is more complex. Solving Poisson equation in the presence of the perturbation yields a solution of the type

$$\Phi_{SCR}(x, y) = \Phi_{SC}[\exp(-y/\lambda) - 1] + A\cos(qx)\exp(-y/\lambda') \qquad [13]$$

with $(\lambda')^{-2} = \lambda^{-2} + q^2$. The boundary conditions are vanishing of the $\cos(qx)$ terms at infinite y and potential continuity at the silicon/electrolyte interface, which sets the constant A. Differentiation of the final expression of the potential and evaluation of the result at the interface yields $\delta\Phi^0_{SC}$ and δE_S. The exact calculation steps are published elsewhere.[18] After some mathematical reformulating, the solution for α reads

$$\alpha = \frac{(\rho_s - \rho_e)JC_1 + \left(\frac{1}{\lambda'} - \frac{1}{\lambda}\right)S}{1 + \frac{\rho_e J}{q}C_1} \qquad [14]$$

with

$$C_1 = \frac{e}{kT} - \frac{S}{\lambda' E_S}$$

As discussed below, in the usual cases one has $S < 1$ and, since $\lambda E_S > kT/e$, C_1 usually reduces to $e/(kT)$. In this case, the origin of the various terms in Eq. 14 can be traced back. In the presence of an interface fluctuation, the first term in the numerator comes from the change of current path length in the liquid and solid phases, thus a change in the interface potential due to the distinct resistivities in the electrolyte and in the solid. It may be viewed as a "pure" electrostatic effect. The second term in the numerator of Eq. 14 comes from the change of the interface electric field associated with the interface fluctuation. It describes the effect of interface fluctuations on hole transport across the SCR and the interface. Finally, the second term in the denominator arises from the change in barrier potential that comes in addition to the mere electrostatic effect.

The parameter S stems from the dependence of the electrochemical current density on surface electric field. It involves two contributions.

The first one, $e\epsilon\epsilon_0 E_S/(kTC_H)$, is due to a barrier lowering effect arising from the drop in the Helmholtz region.[22] It is of the order of $[e\Phi_{SC}/(kT)]\,(C_{SC}/C_H)$, where C_{SC} is the SCR capacitance. For a typical band bending of 100 meV and $C_H = 10\ \mu F/cm^2$, $e\epsilon\epsilon_0 E_S/(kTC_H)$ reaches about 0.1 for $\rho_s = 1\ \Omega$ cm and scales as $N_A^{1/2}$. The image-potential picture suggested by Beale *et al.*[7] has not been considered (the optical dielectric constant of the electrolyte is smaller than that of the semiconductor, hence the image potential has a sign opposite of that for a metal/semiconductor junction).

The second term, $v_R/(v_R + v_D)$, depends upon the serial limitations of transport across the SCR and reaction at the interface. Practical values for v_D range between 10^5 and 10^7 cm/s and are proportional to $N_A^{1/2}$. In principle, the reaction velocity v_R may be deduced from simultaneous measurements of the current density J and the flatband potential V_{FB}: the current density is known to follow a Schottky law of the type $J = J_0\exp(eV/kT)$, hence (as can be deduced from Eq. 5 in the limit $v_R << v_D$), $v_R \approx (J_0/N_A e)\exp(eV_{FB}/kT)$. From the measurements of Ronga *et al.* ($J = 10$ mA/cm^2 at V = 0.1 V, with $V_{FB} = 0.2$ V, for $N_A = 1.5 \times 10^{15}$ cm^{-3}),[22] this gives $v_R \sim 10^3$ cm/s (verifying the condition $v_R << v_D$).

However, this derivation rests on the assumption that the flatband potential is a fixed quantity, that does not depend on electrode potential. As a matter of fact, if surface states are present, a positive shift of the flatband potential may occur when the potential is varied from negative values (where capacitance measurements are usually performed in order to determine V_{FB}) to positive values (where current is measured). This effect may lead to an underestimate of v_R. In a recent paper,[24] Kang and Jorné have even suggested that the band bending may not change at all in the region of porous-silicon formation, and that the $J \propto \exp(eV/kT)$ behavior may just result from a variation of the Helmholtz potential (*i.e.*, the hole concentration at the surface would be potential independent, but v_R would vary with potential). While we regard this viewpoint as extreme and hard to reconcile with the moderate values of the surface capacitance[20] (markedly smaller than the Helmholtz capacitance), the existence of surface-state charging in the relevant potential range is ascertained by the capacitance measurements of Memming and Schwandt.[20] The corresponding shift of V_{FB}, given by the Helmholtz capacitance times the integrated surface charge, may be of the order of 100 mV, which might rise the value of v_R to the order of 10^5 cm/s, still much smaller than v_D. Although this is only a rough order of magnitude, we have used this value as a constant in the following.

Therefore, for the typical values mentioned above, S is always smaller than 1 when ρ_s varies from 0.1 to 10,000 Ω cm, and it goes through a minimum slightly lower than 0.1 for $\rho_s \sim 10\ \Omega$ cm (see Fig. 3). The barrier-lowering term is dominant for higher doping levels, whereas the reaction-velocity term is dominant for higher resistivities. The latter situation will also apply to a-Si:H.

Discussion

Macro- and nanopore formation.—For typical values of the parameters, when q varies, Eq. 14 predicts that four regimes should be observed depending upon the magnitude of $1/q$ as compared to three characteristic lengths (see Fig. 4). These lengths are λ, $\xi = kT/(e\rho_e J)$ and $(\lambda\xi S)^{1/2}$. ξ may be viewed as a crossover length for the transport

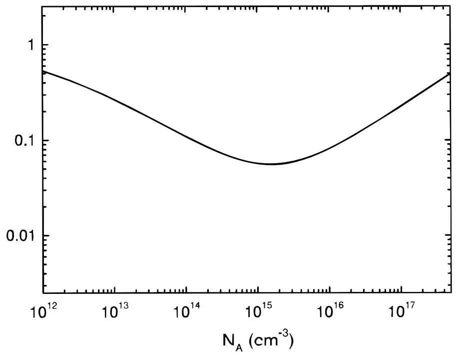

Figure 3. Variation of the S parameter as a function of Si acceptor concentration N_A. S describes the influence of surface electric field on electrochemical current density (Eq. 12). It plays a key role on the magnitude of the short-scale instability (Eq. 14-16).

S0013-4651(99)01-085-X CCC: $7.00 © The Electrochemical Society, Inc.

from the electrolyte across the interface[25]: for a surface element of typical size smaller than ξ, the interfacial resistance $kT/(eJ)$ comes into play and limits the transfer across the interface; on the contrary, for a surface element of typical size larger than ξ, the interfacial resistance becomes negligible and only transport in the electrolyte will limit the transfer. ξ directly derives from the Schottky law and is not affected by the details of the transport mechanism across the SCR. For typical values $J = 10$ mA cm^{-2} and $\rho_e = 10\ \Omega$ cm, ξ is of the order of 3 mm whereas typical values for λ range from 0.015 to 5 μm when ρ_s varies from 0.1 to 10,000 Ω cm.

Regime I.—When $q >> 1/\lambda$, the instability parameter α gets

$$\alpha \approx Sq \qquad [15]$$

In this regime, the instability parameter is always positive and independent of the bulk resistivities. It only depends on the properties of the interface, *i.e.*, the ratio of the reaction velocity of silicon dissolution to the diffusion velocity of holes across the SCR, and/or that of the SCR capacitance to the Helmholtz capacitance. This is the region of nanopore formation. Hence, the unified model explains why nanoporous silicon is identically obtained for a-Si:H and crystalline silicon in a large range of resistivities from about 0.1 to about 10,000 Ω cm.[3-5,18] The above results put forward the key role of the transport limitation due to the interface in nanopore formation.

Regime II.—When $(\lambda\xi S)^{-1/2} << q << 1/\lambda$, α can be approximated by

$$\alpha \approx \frac{S}{2}\lambda q^2 \qquad [16]$$

Here again, the instability parameter is positive and independent of the bulk resistivities, but it depends upon the screening length in silicon. Regimes I and II are special features of the unified model and are not described in the two-region model.

Regime III.—When $1/\xi << q << (\lambda\xi S)^{-1/2}$, α can be approximated by

$$\alpha \approx J(\rho_s - \rho_e)\frac{e}{kT} \qquad [17]$$

In this regime, the instability is independent of the perturbation wavelength and depends only on ξ and the ratio of the resistivities. If one identifies the quantity $kT/(eJ)$ with the interfacial resistance R_i, the result of the unified model is similar to that obtained in the two-region approximation, provided that $R_i q$ is larger than ρ_e (which is equivalent to the condition $q > 1/\xi$) and ρ_s [which requires $q > (\rho_s/\rho_e)/\xi$]. The instability threshold predicted in the two-region model and in the unified model is in line with the observation of macropore formation for highly resistive c-Si and amorphous silicon.

Regime IV.—When $q << 1/\xi$, Eq. 14 reduces to

$$\alpha \approx q\frac{\rho_s - \rho_e}{\rho_e} \qquad [18]$$

In this regime the instability appears as soon as ρ_s exceeds ρ_e; it depends only on q and on the ratio of the resistivities ρ_s/ρ_e. In this approximation, Eq. 18 yields results similar to those obtained in the two-region approximation (Eq. 3), provided that ρ_e is larger than ρ_s and $R_i q$ in Eq. 3, which means only in a case where the interface is stable. In the opposite case, the stability parameter predicted by the unified model is larger than that predicted by the two-region model (model A). This discrepancy is discussed below.

Physical interpretation.—The first three regimes stem from the geometry of the SCR at a rippled interface. In regime I, the back side of the SCR does not “follow” the surface ripple and stays flat, leading to a strong enhancement of the current at the hollow sites. In regime II, the back side of the SCR follows the perturbation only partly: it exhibits an attenuated ripple with significant narrowing of the SCR at the hollow sites. This effect leads to an instability of the growth front somewhat attenuated as compared to regime I. Finally, in regime III, the SCR follows the perturbation in such a way that its local narrowing becomes unimportant for influencing the transport across the interface. The stability of the growth front then becomes determined by the resistivities ρ_e and ρ_s. The transition between regimes III and IV is also described by model A. It corresponds to the crossover from the limitation of the current density by the interface (regime III), to the limitation by transport in bulk phases (regime IV).

The nanopore formation regime (regimes I and II) can be described in a more intuitive picture similar to the two-region model as follows: the space-charge region (SCR) can be regarded as a zone of thickness λ and high effective resistivity “ρ_{SCR}”, several orders of magnitude higher than the resistivity of the electrolyte. Then a phenomenon similar to the case of the two-region model is observed (Eq. 3): the potential drops mainly in the SCR and not in the electrolyte. Hence, for every surface perturbation at a scale shorter than λ ($q >> 1/\lambda$), the SCR just acts as a very high resistivity substrate. In this case, the interface is always unstable, independently of the resistivity of bulk silicon (c-Si or a-Si:H), as in regime I of the unified model. The smallest-size structures grow first, then larger and larger structures develop, up to sizes of the order of λ. As a qualitative argument, and although this amounts to extending a result derived in the linear regime to nonlinear conditions of application, one can say that, at a given layer thickness Δ, the typical size of the largest structures is of the order of $2\pi/q$, where q is such that $\alpha(q) = 1/\Delta$.

For a large-scale perturbation (regimes III and IV), the SCR can be approximated as a fixed interfacial resistance R_i and the perturbation is sensitive to the resistivity of the neutral substrate: (*i*) if $\rho_S > \rho_e$, the interface is unstable at any q, resulting in macropore formation; (*ii*) if $\rho_S < \rho_e$, the interface becomes stable at small q, hence only nanostructures (up to a size actually larger than λ, as discussed below) can be formed: the growth front remains flat at large scale, as is usually observed in porous silicon formation on moderately resistive p-Si substrates.

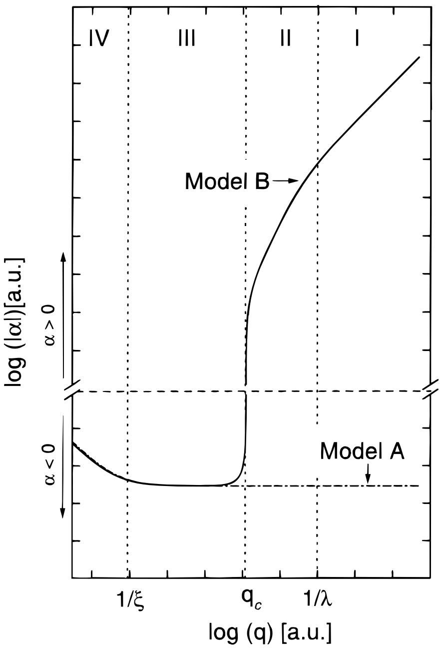

Figure 4. Typical variation of the instability parameter α as a function of the perturbation wavenumber q, for the case $\rho_s < \rho_e$. The curve labeled model A has been drawn according to Eq. 3, and that labeled model B according to Eq. 14. Notice the four regimes described in the text.

For $\rho_S < \rho_e$, the transition between macrostability and nanoinstability (Fig. 4) actually corresponds to a critical perturbation wavelength $2\pi/q_c$, where

$$q_c \approx \sqrt{\frac{2}{\lambda \xi S}} \qquad [19]$$

Notice that q_c is actually smaller than $1/\lambda$. It corresponds to the crossover between regimes II and III. The value $q = 1/\lambda$ (I-II crossover) corresponds to the scale where the instabilizing effect of the SCR starts to diminish, but only at larger scales ($\sim 2\pi/q_c$) does the stabilizing effect of the bulk resistivities become dominant.

A numerical calculation of α as a function of q has been performed from Eq. 3 and 14, with the values $\rho_s = 0.1$ to $1000\ \Omega$ cm. The results are shown in Fig. 5. For $1\ \Omega$ cm silicon ($\lambda \approx 0.05\ \mu$m, $S \approx 0.1$), $\rho_e = 10\ \Omega$ cm, a current density J of 10 mA cm^{-2}, and a layer of thickness $\Delta > \lambda/S$, the wave vector corresponding to the largest structures is given from Eq. 16, by $q \sim (\lambda S \Delta/2)^{-1/2}$, *i.e.*, the characteristic size of the largest structures is $\sim$300 nm for $\Delta = 1\ \mu$m, in fair agreement with literature values,[8] and it increases proportionally to $\Delta^{1/2}$. Under the same conditions, we get $q_c \approx 4000$ cm^{-1}. Thus, the corresponding wavelength $2\pi/q_c$ is about 15 μm, which is compatible with the largest scale of the roughness at the porous-silicon/substrate interface.[26] These figures remain unchanged as long as the barrier-lowering term dominates S. However, when the reaction-velocity term dominates, $q_c \propto N_A^{1/2}$. On the other hand, q_c always scales as $J^{-1/2}$.

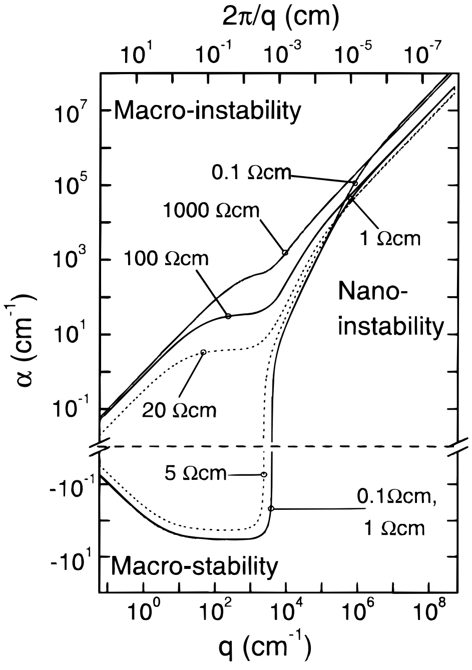

Figure 5. Instability parameter α as a function of the perturbation wavenumber q. The electrolyte resistivity ρ_e has been fixed to 10 Ω cm, the current density $J = 10$ mA/cm^2, $\Phi_{SC} = 100$ mV, and $v_R = 10^5$ cm/s. The space-charge region width λ is (0.015, 0.047, 0.11, 0.21, 0.47, and 1.5 μm) and v_D is ($3.2 \cdot 10^7$, 10^7, $4.5 \cdot 10^6$, $2.3 \cdot 10^6$, 10^6, $3.2 \cdot 10^5$ cm/s) for ρ_s (0.1, 1, 5, 20, 100, and 1000 Ω cm), respectively. A negative $\alpha(q)$ means stability for perturbation wavelength $2\pi/q$ whereas a positive α means instability, *i.e.*, pore formation on the scale $2\pi/q$. Curves have been derived from model B (regimes I-III) and model A (small q regime). The two calculations smoothly match in the plateau region.

Model limitations.—A first questionable assumption of our unified model regards the band shape in the SCR. We have assumed an exponential profile for the bandedges, as obtained for a semiconductor with a constant density of states in the bandgap. This choice appears reasonable for a-Si:H, but not for c-Si in which the band bending is parabolic. The above model cannot be exactly transposed to such a case, but analytical expressions can be obtained through separate solving of Poisson equation in the regions of large and small band bending. It turns out that the final approximate expression for the instability parameter is closely similar to Eq. 14, and that the limiting cases corresponding to regimes I-IV are still described according to Eq. 15-18. Therefore, we conclude that our fully analytic model correctly describes the instability in c-Si.

Another question is about the modeling of the electrochemical kinetics at the interface. Considering that the current is proportional to a reaction velocity (*i.e.*, $J = ev_R p_S$, where p_S is hole concentration at the surface) could certainly be an oversimplification. However, this approximation appears reasonable in the regime of porous silicon formation, since the reaction is known to be limited by the transfer of a first hole at the interface. Furthermore, we have derived Eq. 15-18 in the limit where the variation of applied potential is taken by the SCR and the Helmholtz potential does not vary (except for the small drop $\epsilon\epsilon_0 E_S/C_H$), and we have assumed $v_D > v_R$, *i.e.*, hole transport across the interface and the SCR is controlled by the electrochemical kinetics. On the basis of experimental results,[21] this limit seems to be a reasonable approximation. We regard the variation of the Helmholtz potential induced by surface states as a small contribution, unlike the assumption of Kang and Jorné.[24] However, it should certainly be taken into account for a true quantitative description.

When the silicon resistivity is varied, our model does not hold in various limits: (*i*) for low-resistivity silicon ($\rho_s < 0.01\ \Omega$ cm), tunneling through the space-charge region occurs. In this case Eq. 5 is no longer valid and has to be replaced by an expression for the tunneling current. (*ii*) When silicon resistivity exceeds electrolyte resistivity, some differences appear between model A and model B in regime IV, as mentioned above. Specifically, the instability parameter α predicted by the unified model is higher than that obtained from the two-region model. This increased sensitivity to the high resistivity of the silicon substrate actually proceeds from oversimplifications made in the expression of the potential in bulk Si, *i.e.*, one type of solution of Poisson equation has been retained only. For those reasons, we regard model B as incorrect in regime IV and the curves from model A have been drawn instead in Fig. 5. (*iii*) For very resistive silicon ($\rho_s > 10{,}000\ \Omega$ cm), the current gets strongly limited by the silicon bulk resistivity, and the Schottky-diode approximation starts to fail (see Fig. 1).[16] Taking into account the general solution leads to complex algebra. In order to obtain solvable analytic expressions, some drastic assumptions have to be made (*e.g.*, special band bending shape or constant Fermi level in the SCR), which are not generally justified.[27] A more elaborate treatment for moderately doped a-Si:H would then be necessary. Notice, however, that in this limit one may reasonably infer that v_D is dramatically reduced and that the instability parameter will stay close to $\alpha = q$ through the whole q range.

Comparison with other work.—In the calculation of Valance,[1] an $\alpha(q)$ shape similar to our regime I has been obtained. However, regimes III-IV are not observed since Valance does not take into account the potential drop in the electrolyte and the silicon bulk. In order to determine the most probable perturbation wavelength (*i.e.*, the dominant pore diameter), he assumes a cutoff mechanism for large q, namely, surface tension. He finds as most probable a perturbation wavelength 100 to 1000 nm for doping levels of 10^{15} to 10^{16} cm^{-3}. However, on the basis of X-ray measurements, Binder *et al.*[28] determined that the typical sizes of luminescent nanostructures are on the order of 1 to 5 nm for materials of this doping level. Thus, this attempt does not appear to give results in agreement with experiments, and it appears questionable. First, as Valance himself remarks, the cutoff frequency strongly depends on the value of surface tension, which has not been investigated extensively.[29] Also, it

S0013-4651(99)01-085-X CCC: $7.00 © The Electrochemical Society, Inc.

is not clear why an equilibrium concept such as surface tension should play a role at all in such a deep off-equilibrium situation. A more realistic cutoff would occur from assuming that v_R depends upon surface curvature κ as $v_R^0(1 + a\kappa)$, where a is some characteristic interatomic length. Such an assumption could model an increased chemical reactivity of silicon protrusions. It would lead to a modified high q regime of the type $\alpha = qS - q^2 a v_D/(v_R + v_D)$, hence a cutoff at $q \sim S/a$ leading to small-scale stability, in typical agreement with experiment if $S \sim 0.1$ to 1. Furthermore, there are several other cutoff mechanisms which are equally probable: the mechanical fragility of the structure, the chemical (not electrochemical) etching of the structures, etc. Therefore, for the sake of clarity and consistency, we have not included any cutoff mechanism in our model.

As mentioned above, Ponomarev and Lévy-Clément (PLC)[13,14] have reported on macropore formation for p-Si in fluoride-containing, mixed aqueous-organic electrolytes. Although they find that macropore formation is affected by the resistivity of the silicon substrate, their observations do not appear to quantitatively match the simple criterion $\rho_s > \rho_e$. They suggest that the discrepancy with us might be due to the fact that our treatment does not take into account the diffusion contribution to the electronic currents. Since holes are majority carriers in p-type Si, diffusion currents are expected to be sizeable in the space-charge region only, a contribution clearly taken into account in the second model described in the present work. Recent results from Lehmann and Rönnebeck (LR) also confirm macropore formation at low-doped Si in aqueous fluoride electrolytes, and the authors put forward the key role of diffusion across the SCR in the macropore formation process.[15] Especially, the field enhancements at the pore tips and the associated narrowing of the SCR at these locations are assumed to be responsible for the pore-tip dissolution and for the pore-wall passivation.

We think that the present calculation essentially agrees with these qualitative suggestions by providing a semiquantitative framework: when anodization starts, pore growth is sustained by an actual field enhancement at the pore tips, as explained by LR. As anodization proceeds, structures of increasing sizes are formed [maximum size $\sim S\Delta$, up to characteristic size λ (regime I), then the size of the largest structures increases more slowly, as $(\lambda S\Delta)^{1/2}$, regime II]. For low-doped silicon, such structures may reach micron size. They can certainly be termed macropores, and are clearly compatible with the observations of PLC and LR, including for the $N_A^{-1/2}$ scaling. However, for characteristic sizes larger than $(\lambda\xi S)^{1/2}$, our model predicts that charge-carrier collection at the pore tips becomes governed by drift in bulk silicon, rather than by diffusion in the SCR, hence the stability of the pore front is determined by ρ_e/ρ_s. The large-size regime (regime III) occurs for $\Delta \sim kT/[eJ|\rho_s - \rho_e|]$, which is clearly attained during anodization of amorphous silicon (very large ρ_s), but barely reached for crystalline silicon, even of high resistivity (for 1000 Ω cm p-Si and $\Delta = 50$ μm, the roughness of the macropore front can be ascribed to the onset of regime III, see Fig. 2 of Ref. 5). At larger Δ, this effect will be further perturbed by ionic-diffusion limitations in the electrolyte, not taken into account in the present work. The exact values provided by our calculation might be questioned since, as mentioned above, we are applying a linear-stability argument to a nonlinear regime. However, since nanoporous silicon exhibits a resistivity similar to that of the electrolyte, the same stability argument applies to the growth front of the nanoporous layer (notice that the "macropores" as reported by PLC and LR are actually filled with nanoporous silicon, hence they can indeed be regarded as a roughened growth front of the nanoporous layer). Thus, we think that the existence of the various regimes and the predicted orders of magnitudes of the largest structures at a given time may be reasonably relied upon, as can be checked by comparison with published data.[5]

Interestingly, when the Si substrate is sufficiently resistive for neglecting the potential drop in the Helmholtz region, we think that our approach points to the significant role of electrochemical kinetics, here described by the v_R parameter, in the pore-formation mechanism. Especially, some peculiarities of PLCs results as compared to LRs might be sought in terms of changes in v_R. It is to be noted that PLCs typical working conditions are closer to the electropolishing regime than those of "standard" porous-silicon formation (more dilute fluoride electrolyte, limited solubility of the fluosilicate species in the organic media). In the framework of our above treatment, this would certainly tend to decrease v_R (and even give rise to important nonlinear effects, out of the scope of our treatment). Also, it has been observed that a smoother interface of the porous layer with its substrate is achieved by anodizing silicon at lower temperature.[30] Besides the mass-transport limitations invoked by the authors (and not considered here), these observations might be rationalized in terms of variations of v_R as well as variations of ρ_e and ρ_s.

Conclusions

We have modeled porous silicon formation during anodization of p-type silicon by a linear stability analysis. Our analytical approximations are applicable to p-type amorphous and crystalline silicon with resistivities in the range of about 0.1 to 10,000 Ω cm. In agreement with our previous conclusions, the actual long-range stability of the growth front requires $\rho_e > \rho_s$. However, in practical conditions, this asymptotic behavior is seldom reached, and structures of increasing size are predicted to occur as a function of anodization time for all kinds of p-type silicon. Nanopore formation occurs first, and is only governed by properties of the transport across the SCR and the silicon/electrolyte interface. For resistive silicon, this small-scale regime progressively extends up to the micrometer range, leading to formation of structures that can be termed macropores. Finally, these results provide an overall satisfactory picture of the depth inhomogeneity of porous silicon layers, especially when grown on resistive substrates.

Acknowledgment

The authors are grateful to Dr. V. Lehmann for sending them a preprint of Ref. 15 before publication.

Philips Research Laboratories assisted in meeting the publication costs of this article.

References

1. A. Valance, *Phys. Rev. B*, **55**, 9706 (1997).
2. Y. Kang and J. Jorné, *J. Electrochem. Soc.*, **144**, 3104 (1997).
3. R. B. Wehrspohn, J.-N. Chazalviel, F. Ozanam, and I. Solomon, *Phys. Rev. Lett.*, **77**, 1885 (1996); R. B. Wehrspohn, J.-N. Chazalviel, F. Ozanam, and I. Solomon, *Thin Solid Films,* **297**, 5 (1997).
4. J.-N. Chazalviel, R. B. Wehrspohn, F. Ozanam, and I. Solomon, *MRS Symp. Proc.*, **452**, 403 (1997).
5. R. B. Wehrspohn, J.-N. Chazalviel, and F. Ozanam, *J. Electrochem. Soc.*, **145**, 2958 (1998).
6. V. P. Parkhutik, in *Proceedings of International Symposium of Advanced Luminescent Materials*, D. J. Lockwood, P. M. Fauchet, N. Koshida, and S. R. J. Brueck, Editors, PV 95-25, p. 105, The Electrochemical Society Proceedings Series, Penning, NJ (1996).
7. M. I. J. Beale, N. G. Chew, M. J. Uren, A. G. Cullis, and J. D. Benjamin, *Appl. Phys. Lett.*, **46**, 86 (1985).
8. R. L. Smith and S. D. Collins, *J. Appl. Phys.*, **71**, R1 (1992) and references therein.
9. P. Allongue, in *INSPEC Data series*, L. Canham, Editor, IEE (1997).
10. E. K. Propst and P. A. Kohl, *J. Electrochem. Soc.*, **141**, 1006 (1994).
11. M. M Rieger and P. A. Kohl, *J. Electrochem. Soc.*, **142**, 1490 (1995).
12. M. E. Glicksmann and S. P. March, in *Handbook of Crystal Growth*, T. J. Hurle, Editor, p. 1075, North-Holland, Amsterdam (1993).
13. E. A. Ponomarev and C. Lévy-Clément, *Electrochem. Solid-State Lett.*, **1**, 42 (1998).
14. E. A. Ponomarev and C. Lévy-Clément, *J. Porous Mater.*, To be published.
15. V. Lehmann and S. Rönnebeck, *J. Electrochem. Soc.*, **146**, 2968 (1999).
16. H. Henisch, *Semiconductor Contacts*, p. 136, Clarendon Press, Oxford (1989).
17. W. W. Mullins and R. F. Sekerka, *J. Appl. Phys.*, **35**, 444 (1964).
18. R. B. Wehrspohn, Ph.D. Thesis, Ecole Polytechnique, France (1997).
19. R. Memming and G. Schwandt, *Surf. Sci.*, **4**, 109 (1966).
20. R. Memming and G. Schwandt, *Surf. Sci.*, **5**, 97 (1966).
21. F. Gaspard, A Bsiesy, M. Ligeon, F. Muller, and R. Hérino, *J. Electrochem. Soc.*, **136**, 3043 (1989).
22. I. Ronga, A. Bsiesy, F. Gaspard, R. Hérino, M. Ligeon, F. Muller, and A. Halimaoui, *J. Electrochem. Soc.*, **138**, 1403 (1991).
23. C. R. Crowell and S. M. Sze, *Solid-State Electron.*, **9**, 1035 (1966).
24. Y. Kang and J. Jorné, *J. Electrochem. Soc.*, **144**, 3104 (1997).
25. B. Sapoval, *Phys. Rev. Lett.*, **73**, 3314 (1994).
26. G. Lérondel, R. Romestain, and S. Barret, *J. Appl. Phys.*, **81**, 6171 (1997).
27. H. Henisch, Private communication, 1996.
28. M. Binder, T. Edelmann, T. H. Metzger, G. Mauckner, G. Goerigk, and J. Peisl, *Thin Solid Films*, **276**, 65 (1996).
29. A. Valance, *Phys. Rev. B*, **52**, 8323 (1995).
30. S. Setzu, G. Lérondel, and R. Romestain, *J. Appl. Phys*, **84**, 3129 (1998).

ELSEVIER

Materials Science and Engineering B69–70 (2000) 1–10

MATERIALS SCIENCE & ENGINEERING B

www.elsevier.com/locate/mseb

Electrochemical preparation of porous semiconductors: from phenomenology to understanding

J.-N. Chazalviel [a,*], R.B. Wehrspohn [b], F. Ozanam [a]

[a] *Laboratoire de Physique de la Matière Condensée, École Polytechnique, 91128 Palaiseau, France*
[b] *Philips Research Laboratories, Cross Oak Lane, Redhill, Surrey RH1 5HA, UK*

Abstract

Many semiconductors, besides silicon, can be made porous by anodisation. Theories for pore formation in an electrode must explain how current flow is favoured at the bottom of the pores. Existing theories for porous silicon include 'chemical' theories generally based on some kind of autocatalytic mechanism, 'physical' theories focussing on hole access to the surface, and numerical simulations often based on random-walk approaches. The fact that many semiconductors can be made porous suggests that the mechanisms leading to porous silicon formation have to do more with the semiconducting character of the electrode, than with specific features of silicon electrochemistry, which tends to favour the 'physical' theories. However, the problem of the initial stages of pore growth may be addressed through a linear stability analysis of the interface, a framework which can incorporate physical as well as chemical aspects. Application to the growth of porous silicon from p-Si allows one to understand the observed change in the distribution of structure sizes as the layer thickens, and the dependence of these sizes on the resistivity of the starting material. This approach seems promising for reaching a more general understanding of the mechanism of pore formation in other semiconductors. © 2000 Elsevier Science S.A. All rights reserved.

Keywords: Porous semiconductors; Porous silicon; Formation mechanisms; Anodisation

1. Introduction

Porous silicon has recently aroused considerable interest, especially in view of its photoluminescence properties [1–3]. Its preparation, generally based on electrochemical dissolution (anodisation) in aqueous HF electrolyte, is now controlled up to a remarkable level of reproducibility, allowing for the manufacturing of complex tailored structures [4,5]. However, the fabrication parameters are only known on an empirical basis, and the very mechanism of porous silicon formation, after almost 50 years of conflicting theories, remains as yet poorly understood [1–3,6].

The variety of possible experimental conditions [substrate type (n, n^+, p, p^+), anodisation in the dark or under illumination, ...] and the different morphologies that may be obtained (from microporous to macroporous, with sometimes texturations related to crystallographic directions), have been a formidable challenge for the understanding of the formation mechanisms. Existing theories can be divided into those focussing on the electrochemical aspects of the dissolution, and those where the dominant role is played by the semiconducting character of silicon. According to the first category of authors, the fact that silicon is readily made porous has to be sought in terms of the specific features of silicon electrochemistry. The second category of authors has rather emphasised the role of the space charge in inducing various interface instabilities. Both kinds of theories are able to make the qualitative prediction of pore formation, but up to now none has been worked out into a really quantitative form, that would correctly yield numerical figures such as, for example, porosity and characteristic structure sizes.

During many years, the fact that silicon seemed to be about the only semiconductor that could be made porous (and especially microporous) by anodisation has been standing as an argument in favour of the first kind of theories: as a matter of fact, the electrochemistry of silicon is rich in many peculiarities, and if the semiconducting character of the electrode were playing the dominant role, why can't other semiconductors be

---

[*] Corresponding author. Tel.: +33-1-6933-4663; fax: +33-1-6933-3004.

E-mail address: jnc@pmc.fr (J.-N. Chazalviel)

0921-5107/00/$ - see front matter © 2000 Elsevier Science S.A. All rights reserved.
PII: S0921-5107(99)00285-8

made porous? Also, some metals, such as aluminium or stainless steel, are known to be prone to pit formation, though they are not semiconductors. However, the morphologies of porous silicon and these pitted metals were quite distinct, the typical pit size in metals falling generally in the micrometer range [7]. Meanwhile, other semiconductors have been made porous (and many times microporous), with morphologies often related to those of porous silicon: SiC [3,8–10], Ge [3,11], Ge/Si alloys [3,12], various III–V [13–18] as well as II–VI [19] semiconductor compounds. Also, the morphology of porous silicon may not be too different from that of many 'photoelectrochemically etched' II–VI semiconductors, which had been studied in some detail in the early eighties [20–22] and surprisingly disregarded by the porous silicon community. Finally, silicon has been made porous in non-aqueous media where its electrochemistry is significantly different from that in aqueous media [23,24]. This accumulation of facts suggests that the specific character of silicon among other semiconductors may be due to a focusing of researchers on its case, rather than to the specific features of its electrochemistry, which leads one to consider the second kind of theories with more attention.

In the following, we will first give an overview of the various semiconductors made porous and the proposed theories (if any). The models proposed for the case of porous silicon, which represent most of the existing theoretical literature, will be reviewed in some more detail. In a third part, we will specialise to the theories devoted to the onset of pore formation. We will present our recent model and data, based on a linear-stability analysis of the electrochemical interface, for the case of p-Si, and finally discuss the implications for the case of other semiconductors and electrolytes.

2. So many different porous semiconductors

Putting aside the case of porous silicon, II–VI semiconductors are probably the ones for which the origin of pore formation was questioned first. CdSe [20], CdTe [21], ZnSe [22] have long been found to undergo extreme surface roughening under anodic polarisation. Polarisation was applied under illumination for n-type ('photoelectrochemical etching') or in the dark for p-type, with rather similar results. The small size of the structures observed under SEM (down to 100 nm and possibly smaller) was standing in contrast to the rather flat surfaces obtained, e.g. by chemical etching in bromine/methanol mixtures. Although these experiments were mainly devoted to improving the photoelectrochemical characteristics of semiconducting electrodes, and these etches have not been described in terms of the formation of a porous layer (especially, the depth of the pores is not known), the striking similarity with the pictures obtained for porous silicon suggests a relationship between the two processes. As a matter of fact, a recent study has demonstrated the possibility of making porous p-$Cd_{0.95}Zn_{0.05}Te$ by anodisation in the dark [19], a result most probably related to these ancient studies. It has been suggested that the inhomogeneous etching in these systems arises from the inhomogeneity of the initial surface, through the preferential etching of surface defects and of locations in the vicinity of dopants [22]. The characteristic size of the observed structures, and its decrease with increasing sample doping, were given as arguments in favour of this model.

The elaboration of porous III–V semiconductors by anodisation has also been reported (see extensive reference list in [14]). GaAs [13,14], GaP [14,15], InP [14,16,17] and GaN [18] have all been made porous. However, variations in the conditions of formation of the porous layer and in the obtained morphologies are observed. Microporous GaAs was formed by anodisation of n-type material in HCl in the dark. Formation of the porous layer was initiated by pit formation, a process attributed to breakdown of the deep-depletion layer. In the same way, for n-GaP in the dark, porous layer formation is initiated by formation of etch pits, then the porous layer grows radially from the pits, underneath a thin layer of preserved bulk material. Typical structure size is 100 nm. It has been suggested that the initial pits develop at defects (dislocations) and radial pore growth occurs through enhancement of the electric field at the space-charge-layer boundary [15]. n-type InP has been made porous by photoelectrochemical dissolution. Here the structures (from ~50 nm to several μm) are strongly affected by the crystallography, which has pointed anisotropy of surface reactivity as an important ingredient for porous-layer formation [16,17]. Finally, n-GaN has recently been made porous by photoelectrochemical dissolution in $H_2SO_4 + 10\%$ ethanol, with structures in the 10–100 nm range [18].

Various column-IV semiconductors have been made microporous using recipes inspired from those used for porous silicon (see extensive reference list in [3]). p-type Ge [3,11] and Si_xGe_{1-x} ($x = 0.8$–0.95)[3,12] have been made microporous by anodisation in ethanolic HF. n-type and p-type SiC have been made porous by anodisation in ethanolic HF, either in the dark or under UV illumination [3,8–10]. Depending upon the experimental conditions (n- or p-type, dark or illumination), the reported structure sizes range from 20 nm to 1 μm, with 'fragments of size considerably lower than average' [10]. Konstantinov et al. suggest that size of the obtained 'fibres' is determined by a self-regulation mechanism, due to increase of fibre resistance when its diameter becomes so small that the fibre is depleted from its carriers [9]. Finally, p-type hydrogenated amorphous silicon [25] and $Si_{1-x}C_x$ alloys [26] have been made porous by dark anodisation in ethanolic HF. The structures are similar to those obtained in p-Si, but the thickness of the microporous layer is limited by the formation of macropores, an instability of the growth front attributed to the high resistivity of the starting material [25].

3. So many different theories

Among the theories worked out for explaining the formation of porous silicon, there is obvious agreement that pore growth results from the fact that the bottom of the pores is a favoured path for the electrochemical current. [Notice that pore initiation may involve an effect (e.g. proximity of the dopants [27]) that may not be relevant for pore growth]. The key point is to identify the mechanism through which such a favoured path arises. One may search the origin of this mechanism in the electrochemistry or in the semiconductor physics, since both aspects are present at the interface. For the 'chemical' theories, enhanced current at the bottom of the pores is due to some kind of 'autocatalytic' effect: the current flow becomes easier and easier as current is flowing, due to a change of the local conditions: more 'active' ('depassivated') surface, catalytic effect of a reaction product or a reaction intermediate, … For the 'physical' theories, enhanced current at the pore bottoms results from easier access of the semiconductor holes to these locations. A key ingredient is often the semiconductor space charge, which becomes thinner around the pore bottoms, as can be found by solving three-dimensional Poisson's equation around a semi-spherical pore bottom. There are, however, several ways through which space-charge thinning may affect the electrochemical current. Finally, many models have been based on random-walk simulations. These models often yield morphologies (in 2-D) highly suggestive of the observed ones (in 3-D), but it is not always clear what is the physical mechanism simulated by the random walk (a random walk may represent any Laplacian process, for example diffusion, but just as well migration in an electric field).

3.1. The 'chemical' models

Unagami [28] proposed that current flow at the pore bottoms in p-Si is favoured because the pore walls are blocked by a layer of silicic acid. More recently, Parkhutik et al. [29,30] have suggested that the bottom of the pores is coated with a passive oxide layer which is electrochemically dissolved (the so-called virtual passive layer). These ideas are in line with accepted formation mechanisms of pits in metals [7]. However, in-situ infrared spectroscopy during porous-silicon formation on p-Si has shown that no detectable amount of oxide is present at the surface of silicon, which appears essentially hydrogenated, and only in dilute fluoride electrolytes has the presence of a submonolayer oxide been detected [31,32]. These experimental results stand as an indication against such models. From an analysis of the photocurrent frequency response of n-Si photoanodes in fluoride electrolytes, Kooij and Vanmaekelbergh [33] postulated the existence of a mobile Si(I) surface intermediate that would act as a catalyst for the dissolution reaction, and they suggested that pores on n-Si could be initiated by such intermediates. Soares et al. [34] proposed that a similar role could be played by SiF surface species. These are examples of autocatalytic mechanisms, which are certainly able to lead to pore formation, but such intermediates have as yet not been identified.

Chemical effects inside the semiconductor may also be considered. Corbett et al. [35] have proposed that silicon dissolution can lead to the formation of vacancies in the near-surface region. The regions with a higher concentration of vacancies would dissolve more readily. Allongue et al. [36] have shown that anodisation is accompanied by incorporation of hydrogen into the silicon lattice, and have suggested that these interstitial hydrogen sites could act as pore initiators. These mechanisms can also be termed autocatalytic, the 'catalytic' species being the vacancies or the interstitial hydrogen sites near the silicon surface. These effects are qualitatively plausible, at least for pore initiation. The weakness of the theories is the difficulty to turn them into quantitative predictions, and to assess the reality of the invoked effects experimentally.

3.2. The 'physical' models

The electrochemical dissolution of silicon involves the transfer of several charges (between 2 and 4), but it is generally agreed that, in the regime of porous silicon formation, the reaction rate is determined by the first step, associated with the first hole supplied to the surface [37]. This provides a reasonable basis for the theories that have sought the origin of porous silicon formation in the mechanism of hole access to the surface. It seems intuitively clear that hole capture by a 'forest' of pores will be favoured at the pore bottoms. However, due to the different configuration of the band bending, the cases of n- and p-Si have to be considered separately.

There is now reasonable agreement on the formation of macroporous silicon from n-Si [27,38–42]. When anodisation is performed in the dark, pore growth results from reverse breakdown of the depletion layer which is thinner near pore bottoms, a process whose initiation is made easier by surface defects [43]. When anodisation is performed under illumination from the backside, holes move to the interface by diffusion, until they are captured by the depletion layer which accelerates them toward the pore bottoms. The current density at the pore bottoms is limited by the onset of electropolishing. The spacing between the pores is fixed by the space-charge-layer thickness. Its average size then decreases with increasing doping. The pore diameter and the porosity are determined by the ratio of the applied current density to the electropolishing current density. This understanding of the formation mechanism has allowed good control of the geometrical parameters of macropore arrays. Especially, when long, uniform-diameter macropores are made, depletion of fluoride species when the porous layer thickens leads to a change in the electropolishing current density, which can be corrected for.

The mechanism of microporous silicon formation from p-Si (or n-Si under front illumination) is much more controversial. For p-Si, hole transfer to the interface is thought to take place through a thin depletion layer [44]. Thinning of the depletion layer in the vicinity of the pore bottoms may affect the transfer rate in various ways.

A historical proposal by Beale et al. [45] was that there is an image-potential barrier lowering, which is more pronounced as the barrier is thinner (hence, the transfer rate is increased at the pore bottoms). However, an image-potential barrier lowering can hardly be present at a semiconductor/electrolyte interface, since the optical dielectric constant of the electrolyte is much lower than that of the semiconductor (hence, a mobile charge in the semiconductor generates an image charge of the same sign, and is *repelled* rather than *attracted* by this image charge). Nevertheless, the idea of a barrier lowering may remain relevant: for example, if part of the applied potential appears in the Helmholtz layer [46], the barrier will be decreased by the corresponding amount. If the Helmholtz potential drop is proportional to the surface electric field, the barrier lowering will be inversely proportional to the space-charge-layer thickness.

Alternately, if hole transfer through the space-charge layer is ruled by the same mechanism as in Schottky diodes (thermionic-diffusion mechanism [47]), even without any barrier lowering, the rate depends on the average space-charge electric field, hence it must increase as the space-charge layer becomes thinner.

Finally, the role of quantum effects has been emphasised by Lehmann and Gösele and other authors [48,49]. Due to quantum confinement, the energy of valence-band states is lowered in the walls between the nanopores, hence these regions are not accessible to thermal holes, which can then be transferred to the interface only at the pore bottoms. The variations in the tunneling probability through silicon nanocrystallites have further been reported to account for the size-distribution of silicon nanocrystallites in porous silicon obtained from p^+ substrate [50].

3.3. The simulation approaches

The development of random-walk simulations for solving Laplacian problems has stimulated studies for modelisation of porous silicon formation. When an aggregate is growing by the condensation of particles whose motion is ruled by a Laplacian field (concentration in a diffusion problem, electrostatic potential for the case of electric-field migration), the growth of the aggregate can be simulated on a computer by sending particles from a large distance, allowing them to move at random, until they touch the aggregate and then freeze. Such simulations are usually performed in two dimensions. Solution to the elementary problem yields a ‘diffusion-limited aggregate’ (DLA) of fractal dimension 1.66. Various changes in the rules and different boundary conditions may be incorporated, in order to simulate specific physical phenomena. Such approaches can readily be transposed to the case of porous silicon formation if the surface of the aggregate is termed interface, and a particle touching the interface results in removal of an elementary silicon building block.

Smith et al. showed that the DLA structure obtained by a standard random-walk process can be turned into a rather uniform structure, much more similar to the morphology of porous-silicon from p-Si, if the random-walking particles are launched from a point located at a *finite* distance from the aggregate (‘finite diffusion length’) [51,52]. For the case of n-Si, Erlebacher et al. [53] introduced a characteristic length l representing the drift-diffusion length in the space-charge layer, a model elaborated further by John and Singh [54,55]. The random walkers diffuse from infinity until they reach a point at a distance l from the aggregate, they are then incorporated at the nearest site on the aggregate. Aleksandrov and Novikov used a similar algorithm, where the role of l is played by the average inter-impurity distance [56]. They further extend their simulation to three dimensions, and investigate the changes in morphology and porosity as the parameters are varied. Other simulations include resistor-network modelling [57] and random Monte-Carlo dissolution [58]. These simulations are attractive, in that they lead to precise predictions, including for the case of a thick grown porous layer, and often produce pictures in striking similarity to the experimental SEM data. However, the physical basis of the chosen recipes is sometimes unclear. For example, simulating hole diffusion in the neutral region by a random walk is certainly correct for the case of n-Si (not for p-Si), but jump to the nearest aggregate site may be an oversimplified model for transport through the space charge and electrochemical reaction. These methods can become very powerful, when the physics and the chemistry are sufficiently well understood to be fully incorporated into their mathematical framework.

3.4. Initial stages of pore growth: linear stability analysis

Another class of methods, which can potentially lead to quantitative predictions, is that of linear stability analysis. These methods have been developing since the pioneering work of Mullins and Sekerka, on the stability of a growing front [59]. Let us consider a moving interface where some transformation takes place (here silicon surface under dissolution conditions, but also surface of a solid growing from the melt, or boundary between any two phases under off-equilibrium conditions). Let us assume that the interface is initially flat, and let us introduce a small perturbation of its shape. The interface will be stable if solving the equations of the system leads to damping of the small perturbation at later times. Otherwise, the interface will be unstable. In practice, it is convenient to consider *small sinewave perturbations* of the front, say:

$$yx, t = 0 = \Delta t = 0 + \delta\Delta \cos qx, \qquad (1)$$

where x is coordinate along the interface (here in 2-D, which does not affect the validity of the approach), y interface position at location x and time t, Δ unperturbed interface position, $\delta\Delta$ amplitude of the sinewave perturbation and $2\pi/q$ perturbation period. The equations of the problem can be linearized in $\delta\Delta$, which generally leads to considerable simplifications as compared to the case of an interface of arbitrary shape. One obtains an evolution law of the type

$$\partial\delta\Delta\partial t = \beta q\delta\Delta \qquad (2)$$

Stability of the interface for such a perturbation is ruled by the sign of the quantity $\beta(q)$, which is determined by the equations of the system. Knowledge of the $\beta(q)$ function allows one to predict the evolution of a *small* perturbation of arbitrary shape, by virtue of Fourier transform and linear superposition of the *small* perturbations. In practice, there is generally a limited range of q for which the interface is unstable. The value of q for which β is maximum gives the characteristic scale $2\pi/q$ of the perturbations that will first appear when starting from a flat interface (Fig. 1).

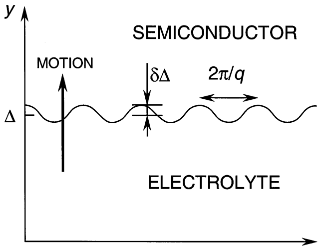

Fig. 1. Scheme of the interface in a linear stability analysis. Here for anodic dissolution of a semiconductor.

This approach has been applied to a study of porous-silicon formation on n-Si, by Kang and Jorné [60] and by Valance [61]. It correctly predicts the order of magnitude of the characteristic pore size. More recently, Valance has tried to extend it to the case of p-Si, but the predictions hardly match the observed nanostructure size and their dependence on doping [62]. We have reconsidered this calculation, with the further concern of extending it to the case of highly resistive semiconductors, such as amorphous silicon [63]. In the following, we will first present the advantages of a linear-stability approach, then present an extension of our calculation, and finally discuss its limitations and the changes which should be introduced for analysing the case of other semiconductors.

3.5. Interest of the linear-stability approach

Besides the ease of leading to quantitative predictions, linear stability analysis is convenient in that it allows one to incorporate many different factors, for example physical and chemical features, without any significant difficulty. The initial step will generally consist in solving the steady-state one-dimensional problem of a flat interface with constant uniform current density J, in the framework of the desired model. This will lead to profiles of the electrostatic potential $\phi(y)$, the hole concentration $p(y)$, and the other relevant concentrations [fluoride, intermediate (catalytic) species, …]. In a second step, the small sinewave perturbation $\delta\Delta$ of the interface will be taken into account and the same problem will be addressed with this modified boundary condition, keeping only the terms up to first order in $\delta\Delta$. For each function of y involved [potential $\Phi(y)$, hole concentration $p(y)$, …] an associated first-order correction will appear [respectively $\delta\Phi(y)$, $\delta p(y)$, …]. Matching these functions at the actual boundary $\Delta + \delta\Delta\cos(qx)$ will finally allow to relate them to $\delta\Delta$ and determine the associated variation in current density δJ.

We have introduced the quantity β, which characterises the increasing rate of $\delta\Delta$ [$\delta\Delta$ is proportional to $\exp(\beta t)$]. Rather than with β $(= \delta\Delta^{-1}\,\mathrm{d}\delta\Delta/\mathrm{d}t)$, the instability is more conveniently described by the exponent $\alpha = \beta/(\mathrm{d}\Delta/\mathrm{d}t) = (\delta\Delta^{-1}\,\mathrm{d}\delta\Delta/\mathrm{d}t)/(\mathrm{d}\Delta/\mathrm{d}t)$, which characterises the increase of $\delta\Delta$ with increasing *thickness* of the growing layer (and has dimensions of inverse *length*). α will typically have the form of a rational fraction. Positive terms in the numerator of α will arise from the *destabilising* effects, i.e. those leading to increased current flow near the concave parts of the Si surface:

- preferential hole diffusion (for n-Si)
- shortening of hole path through the space charge (for n-Si)

- Schottky-barrier lowering due to increased potential drop in the Helmholtz layer (for p-Si)
- increase in diffusion velocity (Crowell-Sze [47]) due to space-charge-layer thinning (for p-Si)
- increase in wavefunction amplitude at the interface (for p-Si: this is the linear-stability version of the quantum effects as originally invoked by Lehmann and Gösele [48])
- reduced diffusion of intermediate catalytic species from the interface to the electrolyte

Negative terms in the numerator will arise from *stabilising* effects, i.e. those leading to reduced current flow near the concave parts of the Si surface:

- 'surface tension' leading to an increase of the equilibrium redox potential as compared to a flat interface (as discussed below, the relevance of this effect to porous silicon formation is questionable)
- decreased reaction *kinetics* due to steric problems
- reduced diffusion of fluoride species from the electrolyte to the interface
- reduced diffusion of inhibiting species from the interface to the electrolyte (e.g. sparingly soluble reaction product, a classical mechanism for electropolishing)

Finally, positive terms in the denominator may arise from '*moderating*' effects which tend to uniformise the interface, but are unable to change the sign of α:

- diffusion of holes or reactants parallel to the interface
- presence of surface states, which may hinder most of the destabilising effects listed above for p-Si

The following example will show how these general ideas may be turned into a practical application. The calculations will be only sketched, as more details can be found in [63].

3.6. A linear stability analysis for porous-silicon formation from p-Si

We consider the case of p-Si (doping N_A). We assume that there are no surface states, that the electrolyte composition is uniform, and that the electrochemical transfer is limited by reaction of the first hole at the interface. Transfer of the hole to the vicinity of the interface is determined by the band bending $e\Phi_{SC}$ and a characteristic 'diffusion velocity' $v_D = \mu E_S$, where μ is hole mobility and E_S surface electric field [64]. The surface reaction rate is characterised by a velocity v_R (for a semiconductor/metal interface, this is just the thermal velocity of electrons v_{th}, corresponding to thermionic emission theory. At a semiconductor/electrolyte interface, v_R will generally be much smaller than v_{th}). Since these two limitations are in series, Crowell and Sze's theory [47,64] can be applied, with v_{th} replaced by v_R. Hence, the $J(V)$ characteristics of the planar interface is given by:

$$J = eN_A \frac{\exp(-e\Phi_{SC}kT)}{\frac{1}{v_D}+\frac{1}{v_R}} = eN_A \frac{\exp[e\varepsilon\varepsilon_0 E_S(kTC_H)]}{\frac{1}{v_D}+\frac{1}{v_R}} \exp(-e\Phi_{SC}^0 kT), \tag{3}$$

where C_H is the Helmholtz capacitance and $e\Phi_{SC}^0 = e(V_{fb} - V)$ is the band bending uncorrected for the Helmholtz potential drop (V_{fb} stands for flatband potential). For ease of calculation, we assume an exponential band-bending profile

$$\Phi y = \Phi_{SC}[\exp(-y\lambda) - 1], \tag{4}$$

where we have taken the interface at $y = 0$ and the semiconductor at $y > 0$. The exponential approximation is perfectly justified for an amorphous semiconductor with constant trap density of states N in the gap $[\lambda = (\varepsilon\varepsilon_0/Ne^2)^{1/2}]$. We have verified that it is a reasonable approximation for a usual semiconductor [63]. If the resistivity of the semiconductor is not negligible, we must add a contribution ρJy to the potential profile, where ρ is resistivity of the medium (ρ_e for the electrolyte at $y < 0$, and ρ_s for the semiconductor at $y > 0$).

When the small sinewave perturbation $\delta\Delta\cos(qx)$ is applied to the interface, the variation of the current density can be written by differentiation of Eq. (3):

$$\frac{\delta J}{J} = -\frac{e\delta\Phi_{SC}^0}{kT} + S\frac{\delta E_S}{E_S} + \frac{v_D}{v_R + v_D}\frac{\delta v_R}{v_R}, \tag{5}$$

where $S = [e\varepsilon\varepsilon_0 E_S/(kTC_H)] + v_R/(v_R + v_D)$. The first-order correction to the potential profile is of the form:

$$\delta\Phi = \cos(qx)[A\ \exp(-y/\lambda') + B\ \exp(-qy)\ (y > 0), \tag{6a}$$

$$\delta\Phi = C\cos(qx)\exp(qy) \quad (y < 0) \tag{6b}$$

where $\lambda' = (\lambda^{-2} + q^2)^{-1/2}$. Matching the potential at the interface allows one to determine the constants and to deduce the expressions of $\delta\Phi_{SC}^0$ and δE_S as a function of $\delta\Delta$, whence the first two terms in Eq. (5) [63,65] (this treatment is done in the approximation that $q\lambda$ is not too small). The last term in Eq. (5) depends on how v_R is affected by the perturbation. Here we consider that the classical hypothesis of a 'surface tension' term is not appropriate for such a far-from-equilibrium problem, and just assume that v_R is decreased on the concave parts of the silicon surface (steric hindrance or lower concentration of 'active' dihydride and trihydride sites). This is only a simple approximation, which neglects the role of crystallographic effects (though such effects are often observed [24,38,66]). It can be written as $v_R = v_R^0(1 + a\kappa)$, where κ is surface curvature and a some characteristic interatomic length. Using $\delta J/J = \lambda'^{-1}\alpha\delta\Delta$, the resulting approximate value for α is then

$$\alpha \approx \frac{(\rho_s - \rho_e)JC_1 + (\lambda^{-1} - \lambda^{-1})S}{1 + \rho_e JC_1/q} - q^2 a \frac{v_D}{v_D + v_R}, \tag{7}$$

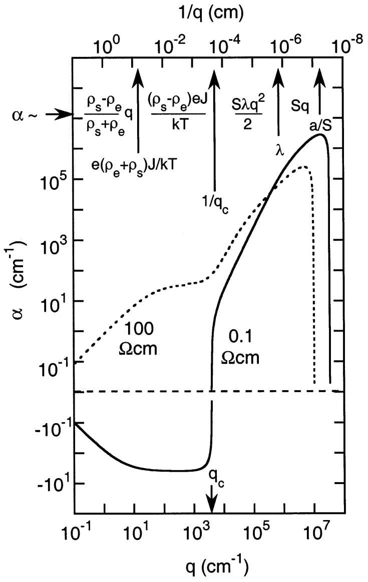

Fig. 2. Typical $\alpha(q)$ curves in the model presented here, for two values of p-Si resistivity, and reasonable values of the other parameters ($J = 10$ mA cm^{-2}, $\rho_e = 10$ Ω cm, $\Phi^0_{SC} = 100$ mV, $v_R = 10^5$ cm s^{-1}, $a = 1$ Å). The various regimes and the typical coordinates of the crossover points are indicated in the top.

where $C_1 = e/kT - S/\lambda' E_S$. At low q values, the approximations used in deriving this expression break down, and the correct expression reduces to

$$\alpha \approx \frac{(\rho_s - \rho_e)q}{\rho_s + \rho_e + kTq/eJ} \ . \tag{8}$$

The two expressions smoothly match in the region $(\rho_e + \rho_s)eJ/kT < q < [2|\rho_s - \rho_e|eJ/(\lambda SkT)]^{1/2}$.

4. Discussion

A typical $\alpha(q)$ curve is shown in Fig. 2. The regimes corresponding to dominance of the various terms in Eqs. (7) and (8) can be identified. These variations can be taken as a qualitative indication on the morphology as a function of porous layer thickness. The maximum value of α occurs for $q \sim S/a$ (for $v_R < v_D$, as is plausibly the case), and $\alpha_{max} \sim S^2/a$. This means that the porous layer will start forming after dissolution of a silicon thickness on the order of a few (a/S^2), and the characteristic pore size of this material will be $\sim a/S$. Since S is on the order of 0.1–1, structures of a few nanometer size are correctly predicted. From a naive examination of the $\alpha(q)$ curve, one may expect that, as the layer is growing to a thickness Δ, instabilities at values of q such that $\alpha(q) \sim 1/\Delta$ start developing. This would predict the development of structures of increasingly large sizes (maximum characteristic size $\sim S\Delta$). Beyond a characteristic size λ, the maximum size should increase more slowly, as $\sim (\lambda S\Delta)^{1/2}$. Finally, the development of large scale instabilities would be expected to occur only if the resistivity of silicon is larger than that of the electrolyte (an effect observed for amorphous silicon [25]). Otherwise, a maximum structure size $1/q_c \sim [\lambda SkT/(2(\rho_e - \rho_s)eJ)]^{1/2}$ would be expected.

As a test experiment, we have anodised a 100 Ω cm p-Si sample at 20 mA cm^{-2} for 50 min in a HF:H_2O:ethanol (35:35:30) mixture. The ~80 μm porous layer was then impregnated with wax and polished at a 1/8 radian bevel angle. Fig. 3 shows a SEM picture of the bevel. Whilst the first few micrometers of the porous layer appear homogeneous at the SEM resolution, micron-size structures develop in depth. These structures consist of large 'channels' made of porous silicon, separated by thinner walls apparently made of bulk silicon. The characteristic size of these structures has been digitally analyzed line by line. Fig. 4 shows the average size of the porous parts and the bulk parts along such a section, as a function of depth in the layer.

As expected from the theory, the characteristic structure sizes increase about linearly with depth, up to a characteristic size on the order of λ for the walls, and significantly larger than λ for the porous channels (for this sample, $\lambda \sim 0.5$ μm). However, in contrast to the above naive expectation, these sizes reach an asymptotic value and do not seem to increase significantly beyond a few λ. This observation is consistent with those by Lehmann and Rönnebeck [67]. The mismatch with the prediction is probably due to the unjustified use of the linear theory far beyond the linear regime. Dealing with a porous material as a superposition of small sinewave perturbations is very crude indeed. However, we will now examine whether the theory can still be useful in such conditions.

When the material becomes microporous, the linear approximation can still be used to study the perturbations of the porous front, i.e. on a scale much larger than the characteristic pore size. Since the nanowalls are under depletion, the resistivity of the porous layer is essentially that of the electrolyte, and the very same theory can still apply. However, when the structure becomes composed of porous channels separated by bulk walls, connectivity of the electrolyte is lost, and the porous layer can no more be considered as a homogeneous medium with a resistivity ρ_e. Examination of the current-path geometry indicates that an effective resistivity $\rho_e^* = \rho_e\Delta/l$, where l is characteristic pore diameter, would be more appropriate. Using such an ansatz, the pore front is found to stabilize even for

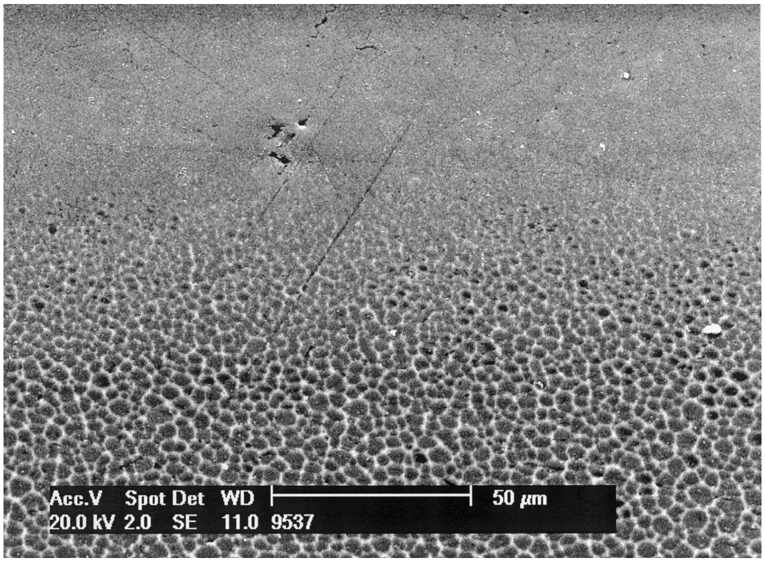

Fig. 3. SEM picture of the first 10 μm of a porous layer (p-Si 100 Ω cm, 20 mA cm^{-2}, HF:H_2O:ethanol 35:35:30) bevelled at 1/8 radian angle. Notice the uniformity of the first few μm, and the patterns of increasing size appearing at larger depths. Darker means higher porosity.

silicon substrates somewhat more resistive than the electrolyte. The maximum structure size is then set by $eJ\rho_c^*/kT \approx \lambda S q^2$, that is (using $\Delta \approx 1/\alpha$ and $l \approx 1/q$), $\alpha \approx (eJ\rho_c/kT)(q/\alpha) \approx \lambda S q^2$, hence a characteristic size $1/q_c^* \approx [(kT/eJ\rho_c)\lambda^2 S^2]^{1/3}$. This would explain that the maximum structure size reaches a plateau, at a value somewhat larger than the space-charge thickness. However, here we are clearly touching the limits of use of linear stability analysis.

The overall good agreement of the predictions with observations is rewarding. In spite of its limitations to the initial growth stages, linear stability analysis is certainly a good way of setting the problem. The difficulty for previous attempts to account for microporous Si formation from p-Si [62] probably arises from the improper choice of destabilising and stabilising effects. Especially, it is important that the destabilising parameter S be not too small (initial characteristic pore size is $\sim a/S$). Here, depending upon the doping, S is governed by the barrier-lowering effect (higher dopings) or the diffusion-velocity term (lower doping). Tunneling should obviously be considered for p$^+$ substrates. Also, it would certainly be desirable to take other (possibly important) effects into account: plausible role of quantum effects among the destabilising terms, changes introduced by the presence of interface states, depletion of fluoride species in the electrolyte when the layer becomes thicker than a few tens of μm, etc… A more critical question now is whether we can intuitively understand the difference between p-Si and n-Si: why does the instability occur in the nanometer range for p-Si and only in the micron range for n-Si? The linear stability analyses in the literature do yield the correct scale for n-Si [60,61] but the underlying physics is not very explicit. It can be inferred that the essential difference, in the case of n-Si, is the possibility for the holes to diffuse laterally during their migration in the space charge and before they are transferred at the interface.

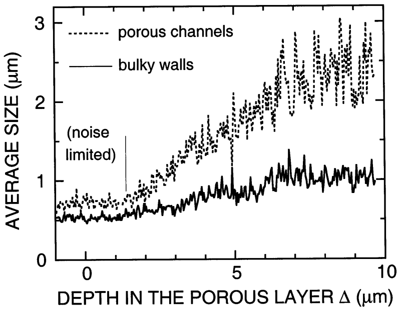

Fig. 4. Line by line digital analysis of the data in Fig. 3: average size of the porous-silicon (dark) and bulk-silicon (bright) regions along a horizontal line, as a function of depth. Notice the increase of these characteristic sizes as a function of depth.

This is a clear-cut difference with the case of p-Si. It must result in a decrease of the destabilising term ($\propto q$), which can then overcome the stabilising term ($\propto q^2$) only at lower q.

We can now consider the case of other semiconductors. This is rather an open field as compared to the case of silicon. A long standing question has been why, in contrast to silicon, most of them cannot be made microporous. We have seen that this fact has been largely challenged recently. However, it is clear that lower chemical reactivities (represented in our example by the single parameter v_R) or the presence of a large density of surface states (unusually small for the case of Si in HF electrolyte) will adversely affect the destabilising terms, hence making the stabilising term ($\propto q^2$) dominate at large q. A similar argument may explain why silicon has been made only macro-porous in non-aqueous electrolytes [23,24]. Further work on each specific case is clearly needed.

5. Conclusion

The numerous efforts to understand the origin of porous silicon formation are now leading to some understanding. It seems more and more clear that the phenomenon of pore formation is general for all semiconductors, and that physical effects, generally associated with the space charge, play a major role in the formation mechanism. Chemical factors should however not be overlooked. The linear stability analysis methods provide a convenient tool for discussing the initial stages of pore growth, especially as they are able to incorporate the chemical as well as the physical aspects of the problem. Predictive capability on the morphology of thick porous layers is more difficult to reach. The methods based on random-walk simulations are certainly most promising for these aspects, provided the physics and chemistry underlying the simulations are properly identified. This may leave us with the hope that a good understanding of electrochemical formation of porous semiconductors is presently on the way.

Acknowledgements

The authors are grateful to D. Hathaway for the SEM picture and to B.H. Erné for useful discussions and communicating results before publication.

References

[1] R.L. Smith, S.D. Collins, J. Appl. Phys. 71 (1992) R1.
[2] G.C. John, V.A. Singh, Phys. Rep. 263 (1995) 93.
[3] A.G. Cullis, L.T. Canham, P.D.J. Calcott, J. Appl. Phys. 82 (1997) 909.
[4] S. Ottow, V. Lehmann, H. Föll, J. Electrochem. Soc. 143 (1996) 385.
[5] M. Thönissen, M. Krüger, G. Lerondel and R. Romestain, In: L. Canham (Ed.), Properties of Porous Silicon, EMIS Datareviews Series No. 18, IEE, Exeter, 1997, pp. 349–355.
[6] P. Allongue, In: L. Canham (Ed.), Properties of Porous Silicon, EMIS Datareviews Series No. 18, IEE, Exeter, 1997, pp. 3–11.
[7] G.S. Frankel, ECS Conf. Proc. 97-7 (1997) 1.
[8] J.S. Shor, I. Grimberg, B.Z. Weiss, A.D. Kurtz, Appl. Phys. Lett. 62 (1993) 2836.
[9] A.O. Konstantinov, C.I. Harris, E. Janzen, Appl. Phys. Lett. 65 (1994) 2699.
[10] O. Jessensky, F. Müller, U. Gösele, Thin Solid Films 297 (1997) 224.
[11] S. Miyazawa, K. Sakamoto, K. Shiba, M. Hirose, Thin Solid Films 255 (1995) 99.
[12] M. Schoisswohl, J.L. Cantin, M. Chamarro, H.J. von Bardeleben, T. Morgenstern, E. Bugiel, W. Kissinger, R.C. Andreu, Phys. Rev. B 52 (1995) 11898.
[13] P. Schmuki, J. Fraser, C.M. Vitus, M.J. Graham, H.S. Isaacs, J. Electrochem. Soc. 143 (1996) 3316.
[14] D.J. Lockwood, P. Schmuki, H.J. Labbé, J.W. Fraser, Physica E 4 (1999) 102.
[15] B.H. Erné, D. Vanmaekelbergh, J.J. Kelly, Adv. Mater. 7 (1995) 739.
[16] P.A. Kohl, C. Wolowodiuk, F.W. Ostermayer Jr, J. Electrochem. Soc. 130 (1983) 2288.
[17] T. Takizawa, S. Arai, M. Nakahara, Jpn. J. Appl. Phys. 33 (Part 2) (1994) L643.
[18] J. van de Lagemaat, Thesis, Utrecht, 1998.
[19] B.H. Erné, private communication (1999).
[20] R. Tenne, G. Hodes, Appl. Phys. Lett. 37 (1980) 428.
[21] N. Müller, R. Tenne, Appl. Phys. Lett. 39 (1981) 283.
[22] R. Tenne, H. Flaisher, R. Triboulet, Phys. Rev. B 29 (1984) 5799.
[23] M.M. Rieger, P.A. Kohl, J. Electrochem. Soc. 142 (1995) 1490.
[24] E.A. Ponomarev, C. Lévy-Clément, J. Porous Mater. 7 (2000) 51.
[25] J.-N. Chazalviel, R.B. Wehrspohn, F. Ozanam, I. Solomon, MRS Symp. Proc. 452 (1997) 403.
[26] F. Ozanam, R.B. Wehrspohn, J.-N. Chazalviel, I. Solomon, Phys. Stat. Sol. (a) 165 (1998) 15.
[27] V.M. Dubin, Surf. Sci. 274 (1992) 82.
[28] T. Unagami, J. Electrochem. Soc. 127 (1980) 476.
[29] V.P. Parkhutik, L.K. Glinenko, V.A. Labunov, Surf. Technol. 20 (1983) 265.
[30] Y.E. Makushok, V.P. Parkhutik, J.M. Martínez-Duart, J.M. Albella, J. Phys. D: Appl. Phys. 27 (1994) 661.
[31] A. Venkateswara Rao, F. Ozanam, J.-N. Chazalviel, J. Electrochem. Soc. 138 (1991) 153.
[32] A. Belaïdi, M. Safi, F. Ozanam, J.-N. Chazalviel, O. Gorochov, J. Electrochem. Soc. 146 (2000) 2659.
[33] S. Kooij, D. Vanmaekelbergh, J. Electrochem. Soc. 144 (1997) 1296.
[34] D.M. Soares, M.C. dos Santos, O. Teschke, Chem. Phys. Lett. 242 (1995) 202.
[35] J.W. Corbett, D.I. Shereshevskii, I.V. Verner, Phys. Stat. Sol. (a) 147 (1995) 81.
[36] P. Allongue, C. Henry de Villeneuve, L. Pinsard, M.C. Bernard, Appl. Phys. Lett. 67 (1995) 941.
[37] R. Memming, G. Schwandt, Surf. Sci. 4 (1966) 109.
[38] V. Lehmann, H. Föll, J. Electrochem. Soc. 137 (1990) 653.
[39] X.G. Zhang, J. Electrochem. Soc. 138 (1991) 3750.
[40] P.C. Searson, J.M. Macaulay, F.M. Ross, J. Appl. Phys. 72 (1992) 253.

[41] M.J.J. Theunissen, J. Electrochem. Soc. 119 (1973) 351.
[42] V. Lehmann, A. Luigart, V. Corbel, ECS Proc. 97-7 (1997) 132.
[43] P. Schmuki, L.E. Erickson, D.J. Lockwood, Phys. Rev. Lett. 80 (1998) 4060.
[44] F. Gaspard, A. Bsiesy, M. Ligeon, F. Muller, R. Hérino, J. Electrochem. Soc. 136 (1989) 3043.
[45] M.I.J. Beale, N.G. Chew, M.J. Uren, A.G. Cullis, J.D. Benjamin, Appl. Phys. Lett. 46 (1985) 86.
[46] I. Ronga, A. Bsiesy, F. Gaspard, R. Hérino, M. Ligeon, F. Muller, A. Halimaoui, J. Electrochem. Soc. 138 (1991) 1403.
[47] C.R. Crowell, S.M. Sze, Solid State Electron. 9 (1966) 1035.
[48] V. Lehmann, U. Gösele, Appl. Phys. Lett. 58 (1991) 856.
[49] L. Jia, S.L. Zhang, S.P. Wong, I.H. Wilson, S.K. Hark, Z.F. Liu, S.M. Cai, Appl. Phys. Lett. 69 (1996) 3399.
[50] S. Frohnhoff, M. Marso, M.G. Berger, M. Thönissen, H. Lüth, H. Münder, J. Electrochem. Soc. 142 (1995) 615.
[51] R.L. Smith, S.F. Chuang, S.D. Collins, J. Electron. Mater. 17 (1988) 533.
[52] R.M. Vadjikar, A.K. Nath, J. Mater. Sci. 30 (1995) 5466.
[53] J. Erlebacher, K. Sieradzki, P.C. Searson, J. Appl. Phys. 76 (1994) 182.
[54] G.C. John, V.A. Singh, Phys. Rev. B 52 (1995) 11125.
[55] G.C. John, V.A. Singh, Phys. Rev. 56 (1997) 4638.
[56] L.N. Aleksandrov, P.L. Novikov, JETP Lett. 65 (1997) 714.
[57] H. Yan, X. Hu, J. Appl. Phys. 73 (1993) 4324.
[58] Y.M. Weng, J.Y. Qiu, Y.H. Zhou, X.F. Zong, J. Vac. Sci. Technol. B 14 (1996) 2505.
[59] W.W. Mullins, R.F. Sekerka, J. Appl. Phys. 35 (1964) 444.
[60] Y. Kang, J. Jorné, J. Electrochem. Soc. 140 (1993) 2258.
[61] A. Valance, Phys. Rev. B 52 (1995) 8323.
[62] A. Valance, Phys. Rev. B 55 (1997) 9706.
[63] R.B. Wehrspohn, F. Ozanam, J.-N. Chazalviel, J. Electrochem. Soc. 146 (1999) 3309.
[64] E.H. Rhoderick, Metal-Semiconductor Contacts, Clarendon, Oxford, 1978, p. 82.
[65] R.B. Wehrspohn, Thesis, Oldenburg and Palaiseau, 1997.
[66] S. Rönnebeck, J. Carstensen, S. Ottow, H. Föll, Electrochem. Sol. State Lett. 2 (1999) 126.
[67] V. Lehmann, S. Rönnebeck, J. Electrochem. Soc. 146 (1999) 2968.

VOLUME 2, NUMBER 7, JULY 2002

NANO
LETTERS

Self-ordering Regimes of Porous Alumina: The 10% Porosity Rule

Kornelius Nielsch, Jinsub Choi, Kathrin Schwirn, Ralf B. Wehrspohn,* and Ulrich Gösele

Max-Planck-Institute of Microstructure Physics, Weinberg 2, 06120 Halle, Germany

Received February 28, 2002; Revised Manuscript Received April 29, 2002

ABSTRACT

Transmission electron microscopy analysis of self-ordered porous alumina obtained by electrochemical anodization shows that self-ordering requires a porosity of 10%, independent of the specific anodization conditions. This corresponds to a volume expansion of alumina to aluminum of about 1.2. We propose that self-ordering of porous alumina with any interpore distance is possible if the applied potential, which mainly determines the interpore distance, and the pH value of the electrolyte, which mainly defines the pore radius, match the 10% porosity rule.

The formation of disordered porous alumina by the anodization of aluminum has been widely studied to protect and decorate the surface of aluminum and to make inorganic membranes.[1] Since Masuda et al. reported the two-step anodization process to obtain self-ordered alumina structures in 1995,[2] new areas of applications have emerged in the fields of magnetic storage,[3] solar cells,[4] carbon nanotubes,[5] catalysts,[6] and metal nanowires.[7–8] This increasing attraction of porous alumina as template is mainly due to its relatively easy and low-cost processing. To date, it is possible to fabricate well-defined self-ordered porous alumina with 50, 60, 100, 420, and 500 nm interpore distance.[9] Alumina templates with interpore distances between 100 and 420 nm might be achieved via prepatterning methods such as imprint lithography or e-beam lithography.[10,11] However, lithographic methods are very cost and time intensive and are not necessary for a variety of template applications. Therefore, it would be extremely beneficial to obtain a general rule to obtain self-ordered pores with any lattice constant.

The arrangement and shape of alumina pores are determined by the applied voltage, temperature, and type and concentration of the electrolyte. For instance, if special self-ordering conditions are used to anodize the aluminum, hexagonally arranged arrays with circular pores can be obtained (Table 1). Here, we define self-ordered to be when more than the nearest neighbor is arranged hexagonally as determined by the radial distribution function.[9]

Experimental details of the fabrication of highly ordered alumina pore arrays have been reported elsewhere.[9,12,13] After anodization, the total amount of Al ions was estimated by measuring the aluminum concentrations in the electrolyte Al^{3+}_{aq} with atomic absorption spectroscopy. By relating this value to the total amount of oxidized aluminum atoms that are calculated from the charge flow during the anodization ($Al_{tot} = 1/3 \int I\,dt$), we estimated the amount of alumina $W_{Alox}/W_{Al} = (1 - Al^{3+}_{aq}/Al_{tot})$ with W_{Al} the weight of aluminum,

---

* Corresponding author. Tel: (+49) 345 5582726. Fax: (+49) 345 5511223. E-mail: wehrspoh@mpi-halle.de

10.1021/nl025537k CCC: $22.00

Table 1: Results of Structural Property of Self-ordered Porous Alumina Analyzed from TEM Images in Figure 1[a]

electrolyte	interpore distance D_{int}	inner wall thickness D_{inner}	pore diameter D_p (= $2r$)	porosity P	pK_s
H_2SO_4 25 V, 0.3 M	66.3 nm	7.2 nm	24 nm	12%	0.1
$(COOH)_2$ 40 V, 0.3 M	105 nm	9.1 nm	31 nm	8%	1.125
H_3PO_4 195 V, 0.1 M	501 nm	54 nm	158.4 nm	9%	2.1

[a] Note that the porosity of alumina is always about 10%.

W_{Alox} the weight of alumina. The volume expansion ξ is determined by

$$\xi = \frac{V_{\mathrm{Alox}}}{V_{\mathrm{Al}}} = \frac{W_{\mathrm{Alox}}}{W_{\mathrm{Al}}} \times \frac{\rho_{\mathrm{Al}}}{F_w \times \rho_{\mathrm{Alox}}} \tag{1}$$

where ρ_{Al} is the density of aluminum (2.7 g/cm^3), ρ_{Alox} the density of porous alumina (3.2 g/cm^3, measured value), and F_w the weight fraction of aluminum ions in alumina (F_w = 0.53). The density of porous alumina was estimated by the floating method using thallous formate−malonate/H_2O mixtures.

We have analyzed in detail the cell structure of the self-ordered porous alumina by transmission electron microscopy (TEM). Figure 1 (a−c) shows TEM images of porous alumina with well-arranged arrays anodized in H_2SO_4, $(COOH)_2$, and H_3PO_4, respectively. At first glance, neglecting the scale, all three TEM pictures look similar. Indeed, analysis of the pictures yields a constant ratio of the radius of the pores r to the interpore spacing D_{int} (Table 1). Moreover, the walls between pores consist of a dark inner layer, far from the pore, and relatively bright outer layer. Numerical analysis of Figure 1 shows that the ratios are for all self-ordered regimes constant of about $D_{\mathrm{inner}}/D_{\mathrm{outer}} = 0.2 \pm 0.02$ (Table 1).

It has been reported by Thompson et al.[14] that the outer layer is anion-contaminated, whereas the inner layer consists of a dense pure alumina. This explains the different contrast in TEM. Interestingly, Thompson et al. found that the ratio of the inner to outer layer strongly depends on the acid. For example, $D_{\mathrm{inner}}/D_{\mathrm{outer}} = 0.05$ for H_2SO_4, 0.1 for $(COOH)_2$, and 0.5 for H_3PO_4.[15] However, they had concentrated their work on disordered pore regimes. In the case of a well-defined self-ordered porous alumina, we observe always the same r/D_{int} as well as the same $D_{\mathrm{inner}}/D_{\mathrm{outer}}$. The porosity of a hexagonal structure is given by

$$P = \frac{2\pi}{\sqrt{3}}\left(\frac{r}{D_{\mathrm{int}}}\right)^2 \tag{2}$$

Since r/D_{int} is constant for self-ordered porous alumina, the optimum porosity is around 10% (Table 1). Note that the slightly larger pore diameter of the H_2SO_4 sample is due to chemical attack of the pore walls. Note that in the disordered growth regime, the porosity can be significantly larger or even smaller than 10%.[16] For example, using 160 V instead of 195 V in 0.1 M H_3PO_4, the porosity is about 40%.

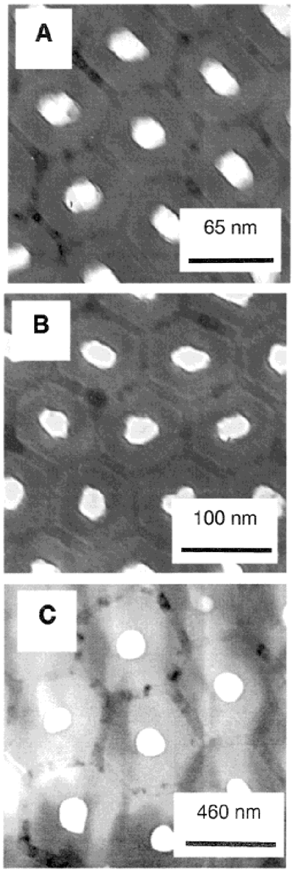

Figure 1. Transmission electron micrographs of self-ordered porous alumina fabricated at (a) 25 V in 1.7 wt % H_2SO_4, (b) 40 V in 2.7 wt % $(COOH)_2$, and (c) 195 V in 1 wt % H_3PO_4.

It is well known for alumina that the interpore distance, D_{int}, is linearly proportional to the applied cell potential U with a proportionality constant k of approximately $k \approx$ 2.5 nm/V

$$D_{\mathrm{int}} = kU \tag{3}$$

where under optimum conditions $D_{\rm int} \approx 2D_{\rm B}$, where $D_{\rm B}$ is the thickness of the barrier. This condition guarantees that no new pores nucleate between existing pores. This is similar to macroporous *p*-type silicon where the wall thickness is twice the depletion width.[17] Therefore, the interpore distance and barrier-oxide thickness are determined solely by the applied potential. On the other hand, it is reported that the pore diameter, *2r*, is affected strongly by dissolution velocity of alumina that is determined by the pH value in the solution.[18] The lower the pH, the lower the potential threshold for field-enhanced dissolution at the pore tip. Depending on the potential, the shape and the diameter of the pore are defined similar to mesopores in silicon.[19] The smallest pores can be obtained in the lowest pH value, i.e., in the strongest acid. For example, for a pH of 1.09 in H_2SO_4, the diameter *2r* is 24 nm (Table 1). From our experimental observations of the 10% porosity rule, eq 3 can be written for self-ordered pore growth as

$$U = \sqrt{\frac{2\pi}{\sqrt{3}P}}\,\frac{r}{k} \tag{4}$$

where, under optimum self-ordering conditions, $P = 10\%$. From eq 4, the required potential, U, to obtain self-ordered alumina growths for a given pore radius, i.e., pH value, can be calculated. As a matter of fact, H_2SO_4, $(COOH)_2$, and H_3PO_4 have different pH values. Therefore, we obtain different self-ordering regimes for different potentials (eq 4). Moreover, changing the concentration would also lead to a change of the pH value. Indeed, increasing the concentration by a factor of 10, leads to a 20% decrease in the optimum interpore distance. For example, increasing from 1 to 10 wt % H_2SO_4 leads to a reduction of the lattice constant from 65 to 50 nm.[9,10] A similar relationship is also observed for H_3PO_4.[13]

Beyond the local matching of the 10% porosity rule for a one-unit cell as analyzed by TEM, also global matching must occur. Indeed, numerical image treatment of the sample surface has shown that for the ordered pore regimes (Table 1) the areal pore nucleation density corresponds to the optimum pore nucleation density n given by $n = 2k^{-2}U^{-2}/\sqrt{3}$.

The observation of the 10% porosity rule strongly supports our previously proposed mechanical stress model.[12,13] It was proposed that in addition to the short-range order determined by eq 3, a force promoting medium range order must exist. In contrast to macroporous silicon, porous alumina consists of two different materials: an aluminum substrate and a porous alumina layer. When aluminum is anodized to alumina, there is a significant volume expansion ξ, which leads to mechanical stress in the thin alumina layer. For nonporous layers, the stress is maximal ($\xi_{\rm max} \sim 2$) and it will decrease with porosity. As shown by Jessensky et al., if $\xi < 1.2$, i.e., the initial porosity is large, the force promoting ordering is too small and the pore array remains disordered. If $\xi \approx 1.2$, there is a small force promoting ordered pore growth. If $1.3 < \xi < \xi_{\rm max}$, the size of the domains will decrease and finally disappear. We have shown that $P = 10\%$ will lead to optimally ordered pore growth. We measured the ratio $W_{\rm Alox}/W_{\rm Al}$ by analyzing the amount of Al^{3+} ions in the solution after anodization by atomic absorption spectroscopy. In the case of self-ordered alumina, 23% Al^{3+} ions are detected in the solution, taking into account that each aluminum atom needed three charges to dissolve. Thus, the self-ordered alumina maintains 77% of Al^{3+} ions, which corresponds to a volume expansion by a factor of 1.23 (eq 1). This is in good agreement with the values of Jessenky et al. obtained from gravimetric measurements.[12] Also, it is in line with results obtained by Li et al. who performed thickness measurements assuming 10% porosity of porous alumina.[13]

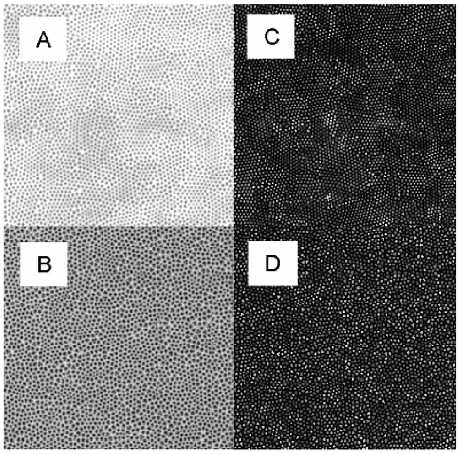

Figure 2. Scanning electron micrographs from phosphoric acid samples anodized for 24 h (A) and 48 h (B) in 1 wt % H_3PO_4 at 195 V, resulting in 500 nm interpore distance. C and D: Numerical image treatment of A and B, respectively, showing the domain size in false colors.

From these findings, it can be expected that after long anodization times in the ordered regime the 10% porosity rule cannot be maintained, when the conditions at the pore bottom will change due to diffusion limitations. Figure 2 shows two SEM images of porous alumina obtained by anodization in H_3PO_4 after 24 h (a) and 48 h (b). Numerical image treatment (Figure 2c,d) of these pictures shows that the size of the ordered domains (false colors) decreases with anodization time. Analysis of a series of porous alumina structures shows that the domain size does not linearly increase with time but has a maximum (Figure 3). The reason the domain size decreased after a critical time can be explained as an aberration from the 10% porosity rule due to a change of the pH value at the pore tip. In addition, we observed that the shape of pores after long anodization is not any more a circle as it is observed in the ordering regimes but a triangle or a polygon. Current transients show that the current increases again after a critical time, implying the change of conditions at the tip (Figure 3). These results suggest that there is an optimum anodization time to obtain the largest domain size. This goes beyond the results of Li

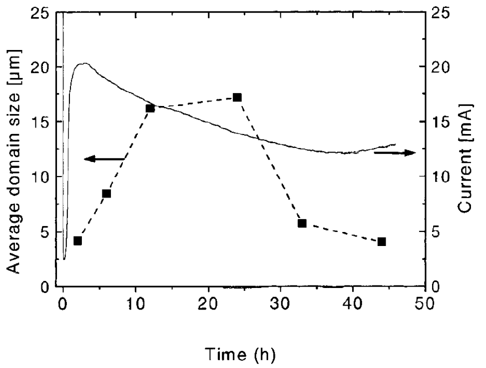

Figure 3. (left axis) Average domain size as a function of the anodization time during anodization in 1 wt % H_3PO_4 at 195V. The domain size is obtained by numerical picture treatment. First the domain size increases due to self-ordering, but after a critical time shown by the dashed line the domain size decreases again. (right axis) Current transient during of the same sample, showing first a current decrease typical for self-ordering, and then after a critical time the current increases.

et al. who reported that the average domain area is a linear function of anodization time.[20]

In summary, have presented a TEM analysis of self-ordered porous alumina obtained by electrochemical anodization. We find that self-ordering of porous alumina requires a porosity of 10%, independent of the specific anodization conditions. This corresponds to a volume expansion of alumina to aluminum of about 1.2. Therefore, to obtain self-ordered porous alumina for a given interpore distance, the applied potential, which mainly determines the interpore distance, and the pH value of the electrolyte, which mainly defines the pore radius, should match to fulfill the 10% porosity rule. Based on the 10% porosity rule, we were able to explain the deviations of ordered growth after long time anodization in terms of a change of the pH value at the pore tip.

Acknowledgment. The authors thank W. Erfurth, U. Doss, and S. Hopfe for technical support and F. Müller for stimulating discussion and numerical support.

References

(1) Furneaux, R. C.; Rigby, W. R.; Davidson, A. P. *Nature* **1989**, *337*, 147.
(2) Masuda, H.; Fukuda, K. *Science* **1995**, *268*, 1466.
(3) Nielsch, K.; Wehrspohn, R. B., Barthel, J.; Kirschner, J.; Gösele, U.; Fischer, S. F.; Kronmüller, H. *Appl. Phys. Lett.* **2001**, *79*, 1360.
(4) Karmhag, R.; Tesfamichael, T.; Wackelgard, E.; Niklasson, G. A.; Nygren, M. *Solar Energy* **2000**, *68*, 329.
(5) Che, G.; Lakshmi, B. B.; Fisher, E. R.; Martin, C. R. *Nature* **1998**, *393*, 346.
(6) Che, G.; Lakshmi, B. B.; Martin, C. R.; Fisher, E. R.; Ruoff, R. S. *Chem. Mater.* **1998**, *10*, 260.
(7) Zhang, Z. B.; Gekhtman, D.; Dresselhaus, M. S.; Ying, J. Y. *Chem. Mater.* **1999**, *11*, 1659.
(8) Sauer, G.; Brehm, G.; Schneider, S.; Nielsch, K.; Wehrspohn, R. B.; Choi, J.; Hofmeister, H.; Gösele, U. *J. Appl. Phys.* **2002**, *91*, 3243.
(9) Wehrspohn, R. B.; Li, A. P.; Nielsch, K.; Müller, F.; Erfurth, W.; Gösele, U. In *Oxide Films*, Hebert, K. R.; Lillard, R. S.; MacDougall, B. R., Eds.; Electrochemical Society: Pennington, 2000; PV-2000-4, 271.
(10) Masuda, H.; Yamada, H.; Satoh, M.; Asoh, H.; Nakao, M.; Tamamura, T. *Appl. Phys. Lett* **1997**, *71*, 2770.
(11) Li, A.-P.; Müller, F.; Gösele, U. *Electrochem. Sol.-State Lett.* **2000**, *3*, 131.
(12) Jessensky, O.; Müller, F.; Gösele, U. *Appl. Phys. Lett.* **1998**, *72*, 1173.
(13) Li, A.-P.; Müller, F.; Birner, A.; Nielsch, K.; Gösele, U. *J. Appl. Phys.* **1998**, *84*, 6023.
(14) Thompson, G. E.; Wood, G. C. Anodic Films on Aluminum, In *Treatise on Materials Science and Technology*; Scully, J. C., Ed.; Academic Press: New York, 1983; Vol. 23, Chapter 5, p 205.
(15) Thompson, G. E.; Wood, G. C. *Nature* **1981**, *290*, 230.
(16) Ono, S.; Masuko, N *Corrosion Science* **1992**, *33*, 503.
(17) Chazalviel, J.-N.; Wehrspohn, R. B.; Ozanam, F. *Mater. Sci. Eng. B* **2000**, *69*-*70*, 1.
(18) Parkhutik, V. P.; Shershulsky, V. I. *J. Phys. D: Appl. Phys.* **1992**, *25*, 1258.
(19) Lehmann, V.; Stengl, R.; Luigart, A. *Mater. Sci. Eng. B.* **2000**, *69*-*70*, 11.
(20) Li, F.; Zhang, L.; Metzger, R. M. *Chem. Mater.* **1998**, *10*, 2470.

NL025537K

BREVIA

CHEMISTRY

Polymer Nanotubes by Wetting of Ordered Porous Templates

M. Steinhart,[1,2] J. H. Wendorff,[1] A. Greiner,[1] R. B. Wehrspohn,[2]* K. Nielsch,[2] J. Schilling,[2] J. Choi,[2] U. Gösele[2]

We have developed a simple technique for the fabrication of polymer nanotubes with a monodisperse size distribution and uniform orientation. When either a polymer melt or solution is placed on a substrate with high surface energy, it will spread to form a thin film, known as a precursor film, similar to the behavior of low molar mass liquids (*1*, *2*).

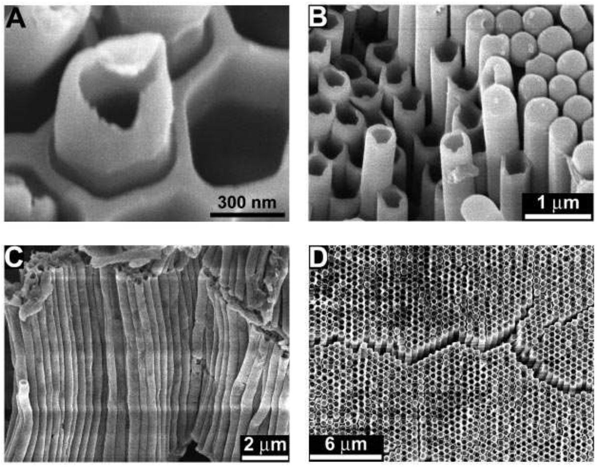

Fig. 1. Scanning electron micrographs of nanotubes obtained by melt-wetting. (**A**) Damaged tip of a PS nanotube ($M_n \sim$ 850,000 g/mol) protruding from a porous alumina membrane. The substrate, on which the pore array was located, has been removed to uncover the tube tips. (**B**) Ordered array of tubes from the same PS sample after complete removal of the template. (**C**) Array of aligned PTFE tubes. (**D**) PMMA tubes with long-range hexagonal order obtained by wetting of a macroporous silicon pore array after complete removal of the template.

Similar wetting phenomena occur if porous templates are brought into contact with polymer solutions or melts: A thin surface film will cover the pore walls in the initial stages of wetting. This is because the cohesive driving forces for complete filling are much weaker than the adhesive forces. Wall wetting and complete filling of the pores thus take place on different time scales. The latter is prevented by thermal quenching in the case of melts or by solvent evaporation in the case of solutions, thus preserving a nanotube structure. If the template is of monodisperse size distribution, aligned or ordered, so are the nanotubes, and ordered polymer nanotube arrays can be obtained if the template is removed. Any melt-processible polymer, such as polytetrafluoroethylene (PTFE), blends, or multicomponent solutions can be formed into nanotubes with a wall thickness of a few tens of nanometers. Owing to its versatility, this approach should be a promising route toward functionalized polymer nanotubes.

We used ordered porous alumina and oxidized macroporous silicon templates with narrow pore size distribution (*3*). Extended regular pore arrays were prepared by lithography. The pores are well-defined, straight, with a smooth inner surface and with diameters D_p between 300 and 900 nm. To process melts, we placed the polymer on a pore array at a temperature well above its glass transition temperature, in the case of amorphous polymers, or its melting point, in the case of partially crystalline polymers. The liquid polymer forms a thin wetting film covering the entire pore surface on a time scale ranging from a few minutes to half an hour. Polymer solutions were dropped on the templates at ambient conditions (fig. S1A) (*4*). The resulting nanotubes obtained from either method had wall thicknesses between 20 and 50 nm and lengths of up to 100 µm. Oligomers as well as polymers with molecular masses M_n up to several hundreds of thousands of grams per mol were processed. Figure 1 depicts nanotubes formed from several polymers by melt-wetting. The tip of a polystyrene (PS) nanotube ($M_n \sim$ 850,000 g/mol) formed in an alumina template was uncovered by etching the alumina substrate with aqueous potassium hydroxide (Fig. 1A) (*4*). Figure 1B shows the same sample after the complete removal of the template. Figure 1C depicts an array of aligned PTFE nanotubes obtained by wetting an alumina template and Fig. 1D a highly ordered array of polymethyl methacrylate (PMMA; $M_n \sim$ 80,000 g/mol) nanotubes prepared by wetting a macroporous silicon template. After selectively dissolving the template, the remaining nanotube array still exhibits its hexagonal long-range order.

The wetting technique can be easily extended to prepare functionalized nanotubes, for example, palladium/polymer composite nanotubes. We first wetted the porous templates with a solution containing poly-L-lactide (PLLA) and palladium(II)acetate under ambient conditions. After evaporation of the solvent dichloromethane, a PLLA/palladium(II)acetate film covered the pore walls. The template was subsequently annealed in vacuum at temperatures of up to 300°C to degrade PLLA (*5*) and to reduce Pd. In a second wetting step, molten PS was added, so that Pd/PS composite tubes were formed (fig. S1B). Energy-dispersive x-ray microanalysis verified the presence of Pd (fig. S1C), and selected area electron diffraction of single composite tubes revealed that it was metallic with a typical crystallite size of 2 to 3 nm (fig. S1D). As demonstrated by this example, template-wetting should have an outstanding potential in providing customized nanotubes for a broad range of applications in nanoscience.

References and Notes

1. P. G. de Gennes, *Rev. Mod. Phys.* **57**, 827 (1985).
2. S. F. Kistler, in *Wettability*, *Surfactant Science Series*, vol. 49, J. C. Berg, Ed. (Dekker, New York, 1993), chap. 6.
3. R. B. Wehrspohn, J. Schilling, *MRS Bull.* **8**, 623 (2001).
4. Materials and methods are available as supporting material on *Science* Online.
5. M. Bognitzki *et al.*, *Adv. Mater.* **12**, 637 (2000).
6. Support from the Deutsche Forschungsgemeinschaft (WE 2637/1-1 and WE 496/19-1) and transmission electron microscopy investigations by C. Dietzsch are gratefully acknowledged.

Supporting Online Material

www.sciencemag.org/cgi/content/full/296/5575/1997/DC1
Materials and Methods
Fig. S1

---

[1]Institute of Physical Chemistry and Center of Materials Science, Philipps-University, Hans-Meerwein-Strasse, D-35032 Marburg, Germany. [2]Max-Planck-Institute of Microstructure Physics, Weinberg 2, D-06120 Halle, Germany.

*To whom the correspondence should be addressed. E-mail: wehrspoh@mpi-halle.de

JOURNAL OF APPLIED PHYSICS VOLUME 91, NUMBER 5 1 MARCH 2002

Highly ordered monocrystalline silver nanowire arrays

G. Sauer, G. Brehm, and S. Schneider
Institute of Physical and Theoretical Chemistry, University Erlangen-Nuremberg, Egerlandstrasse 3, D-91058 Erlangen, Germany

K. Nielsch, R. B. Wehrspohn,[a] J. Choi, H. Hofmeister, and U. Gösele
Max-Planck-Institute of Microstructure Physics, Weinberg 2, D-06120 Halle, Germany

(Received 18 September 2001; accepted for publication 15 November 2001)

Highly ordered silver nanowire arrays have been obtained by pulsed electrodeposition in self-ordered porous alumina templates. Homogeneous filling of all the pores of the alumina template is achieved. The interwire distance is about 110 nm corresponding to a density of silver nanowires of 61×10^9 in.$^{-2}$ and the diameter can be varied between 30 and 70 nm. The silver wires are monocrystalline with some twin lamella defects and grow perpendicular to the $\langle110\rangle$ direction. The previously encountered difficulty to obtain 100% filling of the alumina pores is discussed in the framework of electrostatic instabilities taking into account the different potential contributions during electrodeposition. To obtain homogeneously filled pore membranes, a highly conductive metal containing electrolyte, a homogeneous aluminum oxide barrier layer, and pulsed electrodeposition are a prerequisite.
[DOI: 10.1063/1.1435830]

I. INTRODUCTION

We report on the preparation of ordered silver nanowire arrays obtained by pulsed electrodeposition in porous alumina. Nearly 100% filling of the nanometer sized pores with silver has been obtained. The difficulty of achieving a homogeneous filling is based on instabilities occurring during growth of the highly conducting silver nanowires. In other publications concerning filling of nanopores with silver the problem of the homogeneity of the filling is not addressed and it can be deduced from the data that only a very low filling fraction has been achieved.[1–3] Furthermore, so far most people dealing with the filling of porous materials used disordered alumina, track-etched polycarbonate-membranes, or other disordered pore arrays as templates,[4–6] which even in case of homogeneous pore filling would yield disordered wire arrays with a large dispersion in the pore diameter. Possible applications for such ordered wire arrangement include photonic crystals[7] and surface enhanced Raman spectroscopy (SERS).[8] Other applications might be based on the sharp size distribution of the wire dimensions replicating the high order of the template. After dissolving the alumina matrix, these wires can be either used as conducting nanowires in nanodevices or as templates for hollow cylinders similar to hollow spheres.[9] This article is organized as follows. We first report on the porous alumina template preparation. Then we will present the filling procedure and characterize the silver nanowire arrays. Finally we discuss the instabilities occurring during silver nanowire growth in the framework of a linear stability analysis.

II. TEMPLATE PREPARATION

Hexagonally ordered porous alumina templates have been prepared via a two-step anodization process, which is reported in detail elsewhere.[10–12] Briefly, a first long-duration oxidation of high purity aluminum and subsequent complete dissolution of the formed porous alumina leads to patterned aluminum substrates. The surface keeps the regular hexagonal texture, formed during the first oxidation process by self-assembly, which acts as a mask for the second anodization (Fig. 1). After the second oxidation, an ordered nanopore array is obtained. The diameter and depth of the pores as well as the distance between them and the degree of ordering depends critically on the anodization parameters. Typical parameters used in this work are 0.3 M oxalic acid, $U_{\mathrm{ox}}=40$ V, and $T=2\,^\circ\mathrm{C}$. To obtain homogeneous electrodeposition into the pores in the final step it is highly necessary to previously reduce the alumina barrier thickness at the pore bottom. The thinning is achieved by chemical etching and/or by current limited anodization steps.[13] First, isotropic chemical pore widening reduces the barrier thickness and increases the pore diameter. Then, the sample is oxidized several times for 10–15 min using constant current conditions, reducing the current after each step by a factor of 2. The anodization potential decreases slowly with decreasing barrier thickness. The thinning is stopped when the anodization potential reaches a value of 6 to 7 V, which is equivalent to a barrier layer thickness of about 10 nm. Further thinning might cause the oxide structure to peel off of the aluminum substrate during the deposition. Applying current limited anodization steps not only results in a thinning of the barrier oxide, but also in a modification of the pore structure. The originally straight pores branch out at the formation front because the pore density is inversely proportional to the square of the anodizing potential (Fig. 1).[14,15] The splitting up of the pores

---

[a] Author to whom correspondence should be addressed; electronic mail: wehrspoh@mpi-halle.de

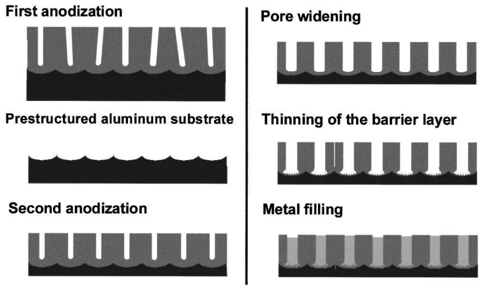

FIG. 1. Schematic diagram describing the fabrication of a highly ordered porous alumina matrix and the preparative steps necessary for the subsequent filling of the structure. The Al substrate is prestructured by a long-time anodizing until the pores arrange in a hexagonal lattice. Then the aluminum oxide is selectively removed. Starting from a prestructured Al substrate, a highly ordered alumina pore structure is obtained in a second anodization step. Afterwards, the barrier layer is thinned and the pores are widened by isotropic chemical etching. For further thinning of the barrier layer two current-limited anodization steps are used and dendrite pore formation occurred at the barrier layer. Then, the pores are filled by pulsed electrodeposition with silver.

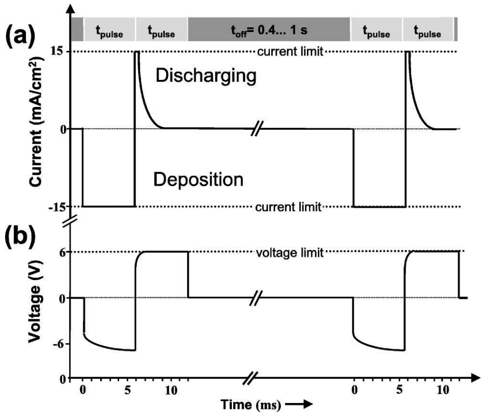

FIG. 2. Current and potential transients during electrodeposition. First a current-limited negative pulse t_{pulse} is applied to deposit Ag. Then a positive pulse is applied to discharge the capacitance of the alumina barrier layer. The cycle is repeated after t_{off} in order to avoid depletion of metal ions near the deposition interface.

into the barrier layer leads to the formation of several nucleation sites in each pore at the beginning of the electrodeposition. Since the potential drop at the deposition interface depends critically on the barrier thickness, it has to be highly uniform. This is achieved by our thinning process described above.

III. ELECTRODEPOSITION

The pores are filled with silver under constant current conditions adopting the concept of pulsed electrodeposition. To achieve homogeneous filling of the pores, the choice of a suitable electrolyte is crucial. In order to avoid corrosive attack of the alumina template, the *p*H of the electrolyte has to be adjusted between 4 and 8.[16] Therefore it is hardly possible to work with cyanide containing silver baths, which generally require a higher *p*H. To supply the deposition interface sufficiently fast with metal ions the concentration of electroactive silver species has to be as high as possible, otherwise hydrogen evolution can become dominant. Furthermore, pulsed electrodeposition through an insulating barrier layer requires high negative polarization (U_{pulse} as high as -8 V). Consequently, the electrolyte must not contain other electroactive species like, e.g., nitrate ions, which also might react in side reactions under these conditions. Finally, stability analysis shows (see below) that the conductivity in the electrolyte has to be quite high to obtain uniform deposition into the pores. Based on these considerations the choice of a suitable electrolyte is not trivial. As the presence of nitrate ions and other electroactive species is excluded silver sulfate (8.5 g/l) was chosen as the silver ion source. Diammoniumhydrogencitrate (200 g/l) was added to ensure a high conductivity and to adjust the *p*H value to around 4.5. Furthermore, diammoniumhydrogencitrate has the function of a repairing agent as it favors the formation of stable alumina during the positive polarization in the pulse sequence (see below). Finally, the electrolyte contained potassiumthiocyanate (105 g/l), which was necessary to dissolve precipitated silver salt through complexation. The pulsed electrodeposition consists of modulated pulses in the millisecond range (Fig. 2). During each pulse of negative current ($t_{\text{pulse}} = 6$ ms, $I_{\text{pulse}} = 15$ mA/cm^2), silver is deposited at the pore bottom. A relatively high current density is applied in order to increase the number of nucleation sites in each pore.[12] After the deposition pulse, another pulse with positive polarization ($t_{\text{pulse}} = 6$ ms, $U_{\text{pulse}} = 6$ V) was applied to discharge the capacitance of the barrier layer and to interrupt the electric field at the deposition interface immediately. The positive pulse also repairs discontinuities in the barrier oxide, an important mechanism especially at the beginning of the electrodeposition. The current for this second pulse is also limited to $I_{\max} = 15$ mA/cm^2. To avoid depletion of the silver ions at the deposition interface, the ion concentration has to recover before the next double pulse is applied. Introducing a delay time t_{off} of typically 0.4–1 s is sufficient to ensure the restoration of a high silver concentration at the pore bottom before the subsequent deposition pulse appears. This improves the homogeneity of the deposition and prevents excessive hydrogen evolution. During the electrodeposition, the potential required to ensure the desired current density is measured for each pulse. Hence the electrodeposition can easily be followed via a potential versus pulse number plot (Fig. 3). Generally, the plot can be divided into three regions. At the beginning of the filling process the electrons have to tunnel through the barrier oxide before they react with the silver ions and nucleation takes place at numerous sites in each pore. The surface available for electrodeposition is quite large. Further electrodeposition leads to a filling of the branched structure and thus the electrochemically active surface area decreases, accompanied by an increase in the deposition potential (first region). When the deposited silver

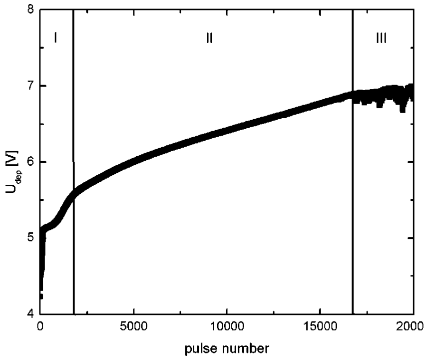

FIG. 3. Voltage-pulse-number curve during the filling process of porous alumina with Ag. In regime I the dendride-like nucleation pores are filled with Ag. The potential increases due to a reduction of the deposition area. In regime II the silver wires grow and the potential increases slightly. In regime III the silver wires reach the top of the alumina template and the noise and slight potential drop are due to the uncontrolled increase in deposition area.

reaches the beginning of the straight part of the pores the increase in the deposition potential slows down distinctly, but still proceeds (second region). The decreasing silver concentration in the pore channel can be made responsible for a gentle increase in the deposition potential in this region, but it cannot explain the significant rise of more than one volt. The filling of the pores continues until the deposition potential drops or exhibits some noise (third region), which is due to an increase of the electroactive surface arising from silver deposition on top of the porous alumina matrix. Although the significant increase in the deposition potential, especially in the second region, is not completely understood yet, the potential versus pulse number plot at least allows one to follow and control the filling process. Additionally the charge can be calculated from the measured data and thus allows one to estimate the degree of pore filling and to control the wire length.

IV. CHARACTERIZATION

The filled alumina templates were examined by scanning electron microscopy (SEM) to determine the degree of pore filling and the extension of the silver nanowires. By etching the filled porous structure from the top, nanowires ending somewhat below the membrane surface became observable for scanning electron microscopy (SEM) examination. Etching of the samples was performed by Ar sputtering with an ion mill (Gatan Duo Mill 600) and led to a funnel-shaped excavation in the surface. The depth of the hole was correlated with the etching time. Figure 4 shows two top view micrographs and one side view micrograph of a highly ordered alumina pore structure filled with silver. The pore diameter is approximately 35 nm and the interpore distance is 110 nm. The thickness of the porous layer is approximately 2 μm. Figure 4(a) was taken before etching the sample. In some pores, the silver nanowires reached the pore opening and excessive electrodeposition yielded three-dimensional growth of silver particles on top of the matrix structure (bright spots). In most of the remaining (not completely filled) pores, the top of the nanowires can be seen (different gray levels indicate different levels of residual pore depth). Figure 4(b) shows the same sample after etching the initially 2 μm thick porous structure by about 200 nm. As can be seen clearly, almost every pore is filled with silver to this level indicating fluctuations in the height of the filling of less than 10%. The same information can be obtained from Fig. 4(c). Simple cutting of an (unthinned) substrate with wire cutting pliers leads to a fracture of the rigid alumina layer. Most of the pores are filled with silver wires (bright sticks) to at least 90% in height. The lack of wires in some of the pores as well as the presence of twisted and ruptured wires can easily be explained by the mechanical stress evolving during the process of the cleavage of the alumina membrane.

Crystallinity and surface configuration of the silver wires were further analyzed by high-resolution transmission electron microscopy (HRTEM). After dissolving the alumina matrix such wires have been placed on electron microscopy copper grids covered by a thin carbon film. Although arranged randomly on the carbon film, the silver wires tend to

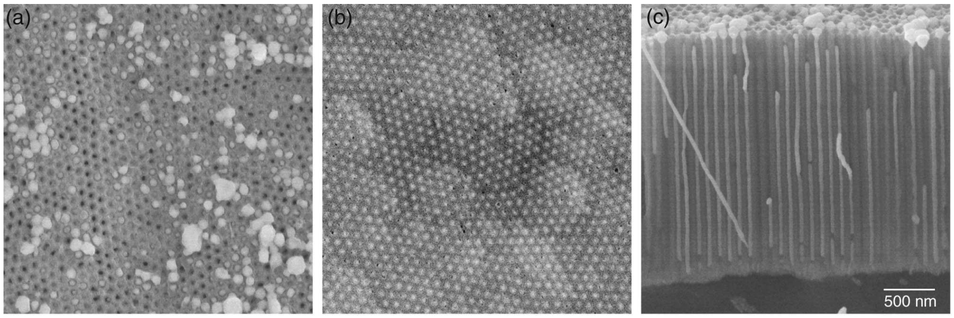

FIG. 4. SEM micrographs of a silver-filled alumina membrane. (a) Top view of an unthinned sample, (b) top view of the same sample approximately 200 nm underneath the initial surface, and (c) side view of a fracture.

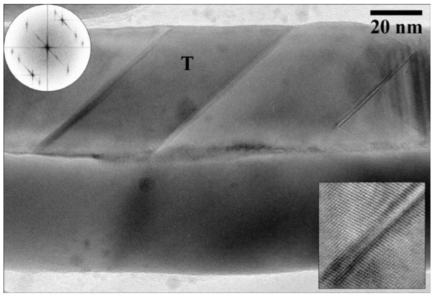

FIG. 5. HRTEM image of a segment of two adjacent silver nanowires. The upper one exhibits three planar defects shown in more detail in the box below. The diffractogram (circular inset) reflects the lattice relation between the twin lamella "T" and wire matrix.

align parallel in groups because of capillary forces acting during evaporation of the solvent. Figure 5 shows a HRTEM image of a segment of two adjacent wires touching each other along a nearly horizontal line. From selected area electron diffraction these silver wires are found to be single crystalline. Nevertheless, they contain a certain extent of lattice defects such as twin boundaries and stacking faults. While the wire in the lower part of Fig. 5 does not exhibit lattice defects in the frame of this image, the upper wire has three planar defects that may be recognized as narrow bands of stronger contrast running obliquely across the wire. Their structures are shown in more detail in the boxes beneath. From the course of the lattice plane fringes seen here, and reflected also by the diffractogram (Fourier transform) of the image given in the circular inset, the $\langle 110\rangle$ zone axis of the silver lattice is deduced to be perpendicular to the wire axis. The wires have generally a face-centered-cubic (fcc) lattice, which was also confirmed by x-ray diffraction analysis. They do not show indications of neither oxide coverage nor incorporation.

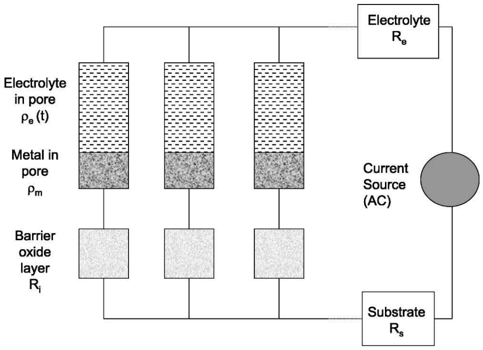

FIG. 6. Schematic diagram of the electric circuit during pulsed electrodeposition.

TABLE I. Resistivities (at 38 °C) of some metals and electrolytes used in this work and similar work in literature.

Material	Resistivity in Ω cm
nickel (bulk)	6.3×10^{-6}
silver (bulk)	1.4×10^{-6}
nickel Watts-bath electrolyte	14
Metzger Co bath	77
Xu Ni bath	500
silver containing electrolyte (this work)	5.2

V. DISCUSSION

As mentioned in the Introduction, most studies have not discussed the achieved degree of filling of the pores with either silver[1–3] or other metals like Au,[17] Co,[18–21] Fe,[22] or Ni.[23] In the present work we demonstrated that under very specific conditions of pulsed electrodeposition, one can obtain a nearly 100% homogeneous filling of pore arrays also with silver. In a former publication we have shown that it is indeed possible to fill homogeneous nickel and cobalt into porous alumina.[13]

Now we are presenting a model to explain the physical reasons underlying this process. The key ingredients of our model are a thin homogeneous barrier layer, pulsed electrodeposition, and a highly conducting electrolyte. Figure 6 shows a schematic diagram of the equivalent electrical circuit applicable during pulsed electrodeposition. Starting from the current source, there is a resistance in the aluminum substrate (R_s), then all the pores are in parallel consisting of a thin interfacial oxide layer (R_i), the deposited metal (ρ_m), and the electrolyte (ρ_e). Finally, there is a common resistance of the electrolyte in the electrochemical cell (R_e). For a stability analysis, we can neglect the potential drop in the aluminum substrate and the electrolyte since they are simple series resistances and do not contribute significantly to the instability. The first instability arises from the fact that the alumina barrier layer at the pore bottom is not uniform. If it would be uniform, then it would represent an overall series resistance like R_e or R_s. However, due to the electrochemical process, there are always fluctuations in the barrier layer thickness. Therefore as already pointed out by Zagiel *et al.*,[24] the barrier layer thickness and therefore the overall potential drop iR_i should be as small as possible compared to the potential drop across ρ_e and ρ_m. This is the reason for thinning the alumina barrier layer to typically 10 nm. However, this still results in a significant contribution to the potential drop of ~6 V in the barrier layer compared to a few tenths mV for the electrolyte solution (Table I). Therefore and because of the rectifying nature of the barrier layer, we have applied a self-limiting current process by using pulsed electrodeposition. During the 6 ms negative pulses, all of the metal ions in the pore are deposited due to the high current. Thus once all the ions have been deposited in one specific pore, the current flow is reduced and other pores with a slightly thicker barrier layer take over the current. A uniform filling of the pore bottom is achieved and the impact of fluctuations of R_i is reduced due to a time dependent electrolyte resistivity ρ_e(t). During the positive pulse, the capacitance of the barrier layer is discharged. Moreover, as pointed out by Dobrev *et al.*,[25] the use of positive pulses leads to monocrystalline nanowires. They speculate that during the positive pulse, a certain amount of current will lead to the preferential dissolution of the defect rich metal deposit of the previous negative pulse, thus promoting monocrystalline growth.

Another electrostatic instability arises during the growth of the silver wires. Since the Ag nanowires are always more conductive than the electrolyte, small fluctuations in the length of the wire will be enhanced and will lead to nonuniform growth. Similar to the case of pore growth in highly resistive *p*-type silicon, this effect can be described by a linear stability model. Following Wehrspohn *et al.*,[26,27] we can define a instability coefficient α

$$\alpha = \frac{\rho_e - \rho_m}{\rho_e + qR_i + \rho_m} q, \qquad (1)$$

where q is the fluctuation wavenumber (in cm^{-1}). If α is negative, the metal wire front grows uniformly, i.e., the filling is homogeneous. If α is positive, the metal wire front will in general be unstable and an inhomogeneous filling will occur. The inverse $1/\alpha$ represents the typical length for which one silver wire will start to grow faster in one pore than in the others. To obtain a homogeneous filling because of negative α, the resistivity of the electrolyte must be lower than that of the metal wire. Such a condition is unrealistic for any metal since the conductivity of pure metals ($\sim\mu\Omega\,\mathrm{cm}$) is a few orders of magnitude higher than that of concentrated electrolytes ($\sim 10\ \Omega\,\mathrm{cm}$). The only possibility to fill a thin layer of porous alumina rather homogeneously is therefore to increase $1/\alpha$ so that it is larger than the membrane thickness. This means the onset of the instability will not occur below this critical thickness and a homogeneous filling is possible. Since $\rho_m \ll \rho_e$, the critical thickness $1/\alpha$ simplifies to $1/\alpha = 1/q + R_i/\rho_e$. For $q \approx 10^5\ \mathrm{cm}^{-1}$, $R_i \approx 36\ \Omega\,\mathrm{cm}^2$ for a current density $I = 15\ \mathrm{mA/cm}^2$ and a porosity of 9%, $\rho_e \approx 10\ \Omega\,\mathrm{cm}$, $1/\alpha$ is limited by the term R_i/ρ_e, i.e., interface or barrier-layer limited. Thus the barrier layer thickness is proportional to the critical thickness $1/\alpha$ and the conductivity of the electrolyte is inversely proportional to $1/\alpha$. This underlines the importance of using highly conductive electrolytes like Watts-bath-type electrolytes in the case of Ni and Co nanowires. Indeed, the Xu group[28] and the Metzger group[29] both obtain very good Ni filling degrees in alumina pore arrays applying these rules. Xu uses barrier layer thinning, pulsed electrodeposition, and high temperature deposition to increase the mobility of the ions in the organic electrolyte.[28] Metzger uses pulsed electrodeposition, barrier layer thinning, and also highly conducting electrolytes. However, in both studies, the resistivities are much higher than for the Watts-bath type electrolyte used in our work.[13] Therefore instabilities have to be compensated in these groups by decreased pulse duration. However, a drawback of the latter strategy is that a thicker barrier layer has to be used to reduce the discharge time of the barrier layer capacitance. The thicker barrier layer leads to significantly higher overpotentials during deposition and to a worse crystallinity of the nanowires.[29]

VI. CONCLUSIONS

A highly efficient method of depositing silver into the nanochannels of ordered porous alumina is presented. Nearly 100% of the pores were filled with silver and only small fluctuations in the growth rate in different pores were observed. The silver nanowires are monocrystalline with some twin-lamella defects. The growth direction is perpendicular to the $\langle 110 \rangle$ direction. The wire diameter can be varied from 30 to 70 nm depending on how the alumina template is prepared. Based on a linear stability analysis, we have modeled the electrochemical filling behavior. To obtain homogeneously filled pore membranes, a homogeneous aluminum oxide barrier layer, pulsed electrodeposition, and a highly conductive electrolyte are a prerequisite.

ACKNOWLEDGMENTS

The authors thank S. Hopfe for the SEM sample preparations and Dr. H.-N. Lee for the x-ray measurements.

[1] Q. Zhang, Y. Li, D. Xu, and Z. Gu, J. Mater. Sci. Lett. **20**, 925 (2001).

[2] I. Mikuslkas *et al.*, Opt. Mater. **17**, 343 (2001).

[3] F. Müller, A. D. Müller, M. Kröll, and G. Schmid, Appl. Surf. Sci. **171**, 125 (2001).

[4] X. Jiang *et al.*, J. Mater. Chem. **11**, 1775 (2001).

[5] V. M. Cepak and C. R. Martin, J. Phys. Chem. B **102**, 9985 (1998).

[6] N. F. Jana *et al.*, Chem. Commun. (Cambridge) **7**, 617 (2001).

[7] H. van der Lem and A. Moroz, J. Opt. **2**, 395 (2000).

[8] G. Sauer (unpublished).

[9] F. Caruso, R. A. Caruso, and H. Möhwald, Chem. Mater. **11**, 3309 (1999).

[10] H. Masuda and K. Fukuda, Science **268**, 1466 (1995).

[11] H. Masuda, K. Yada, and A. Osaka, Jpn. J. Appl. Phys., Part 2 **37**, L1340 (1998).

[12] O. Jessensky, F. Müller, and U. Gösele, Appl. Phys. Lett. **72**, 1173 (1998).

[13] K. Nielsch, F. Müller, A.-P. Li, and U. Gösele, Adv. Mater. **12**, 582 (2000).

[14] F. Keller, M. S. Hunter, and D. L. Robinson, J. Electrochem. Soc. **100**, 411 (1953).

[15] A.-P. Li, F. Müller, A. Birner, K. Nielsch, and U. Gösele, J. Appl. Phys. **84**, 6023 (1998).

[16] P. P. Mardilovich, A. N. Govyadinov, N. I. Mazurenko, and R. Paterson, J. Membr. Sci. **98**, 143 (1995).

[17] X. Y. Zhang *et al.*, J. Mater. Chem. **11**, 1732 (2001).

[18] H. Zeng, M. Zheng, R. Skomski, D. J. Sellmyer, Y. Liu, L. Menon, and S. Bandyopadhyay, J. Appl. Phys. **87**, 4718 (2000).

[19] A. Kazadi Mukenga Bantu *et al.*, J. Appl. Phys. **89**, 3393 (2001).

[20] T. Thurn-Albrecht, J. Schotter, G. A. Kästle, N. Emley, T. Shibauchi, L. Krusin-Elbaum, K. Guarini, C. T. Black, M. T. Tuominen, and T. P. Russell, Science **290**, 2126 (2000).

[21] H. Q. Cao, Z. Xu, H. Sang, D. Sheng, and C. Y. Tie, Adv. Mater. **13**, 121 (2001).

[22] Y. Peng, H.-L. Zhang, S.-L. Pan, and H.-L. Li, J. Appl. Phys. **87**, 7405 (2000).

[23] P. M. Paulus, F. Luis, M. Kröll, G. Schmid, and L. J. de Jongh, J. Magn. Magn. Mater. **224**, 180 (2001).

[24] A. Zagiel, P. Natishan, and E. Gileadi, Electrochim. Acta **35**, 1019 (1990).

[25] D. Dobrev, J. Vetter, N. Angert, and R. Neumann, Appl. Phys. A: Mater. Sci. Process. **69**, 233 (1999).

[26] R. B. Wehrspohn, J.-N. Chazalviel, and F. Ozanam, J. Electrochem. Soc. **145**, 2958 (1998).

[27] R. B. Wehrspohn, F. Ozanam, and J.-N. Chazalviel, J. Electrochem. Soc. **146**, 3309 (1999).

[28] A. J. Yin, J. Li, W. Jian, A. J. Bennett, and J. M. Xu, Appl. Phys. Lett. **79**, 1039 (2001).

[29] M. Sun, G. Zangari, M. Shamsuzzoha, and R. M. Metzger, Appl. Phys. Lett. **78**, 2964 (2001).

ADVANCED MATERIALS

Silicon-Based Photonic Crystals**

By *Albert Birner*, *Ralf B. Wehrspohn*,
Ulrich M. Gösele,* and *Kurt Busch*

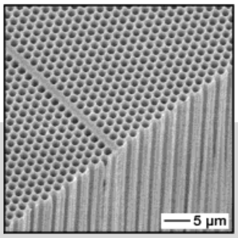

Photonic crystals can be thought of as optical analogues of semiconductors. Here recent advances in photonic crystals based on silicon are reviewed. After summarizing the theory of photonic bandgap materials, the preparation and linear optical properties of 1D, 2D, and 3D silicon-based photonic crystals are discussed. Laterally structured porous silicon with a defect line is shown in the Figure.

1. Introduction

In semiconductors electrons propagate in a periodic potential, which originates from the atomic lattice. This modifies the dispersion relation of free electrons and a band structure with a bandgap occurs in the case of semiconductors. The incorporation of electrically active defects allows the manipulation of the electronic properties, which gave birth to a large variety of electronic devices. There are distinct electrical and electro-optical properties of the different semiconductor materials, the dominant and most studied semiconductor being silicon.

For more than ten years, the optical analogues to electronic semiconductors, the so-called photonic crystals, have been the subject of intense international research efforts. Photonic crystals are materials with a periodically varying index of refraction. This allows the control of the propagation of electromagnetic waves, similar to electrons in a semiconductor crystal. By analogy with semiconductors, the periodicity of the underlying lattice structure is of the same order of magnitude as the wavelength of the electromagnetic radiation.

Despite the far-reaching analogies between electronic waves in semiconductors and electromagnetic waves in photonic crystals, there are pronounced differences between the two as is noticeable from the corresponding equations of motion. Electrons are described by a scalar wavefield. In contrast, the electromagnetic field is vectorial by nature. Furthermore, the time-independent Schrödinger equation allows solutions with negative energy eigenvalues, whereas the corresponding wave equation in electrodynamics contains only the square of the eigenfrequencies, hence negative eigenvalues are excluded from the outset. It may be inferred from the few photonic crystals that appear in nature, in contrast to ubiquitous semiconductor materials, that these differences have a disadvantageous effect on the likelihood of the formation of photonic bandgaps. From the multitude of the optical phenomena only, for example, the colorful speckles of opals, some crystallites on the wings of butterflies and the spine of the seamouse[1] can be attributed to photonic crystal effects. Due to the extreme requirements of miniaturization, substantial progress in nanotechnology has recently allowed the artificial manufacturing of photonic crystals for optical frequencies to be considered in a controlled way. Therefore, photonic crystals may play a key role in the realization of novel integrated optical devices. Besides important technological aspects, photonic crystals provide entirely new avenues of basic research through their potential in controlling the propagation of electromagnetic waves, in particular in the field of nonlinear and quantum optics.[2]

There are many types of dielectric materials for photonic crystals under current investigation: group II–VI, III–V, and IV semiconductors as well as oxides, polymers, and metallodielectric structures. In this review, we will focus on recent advances in silicon-based photonic crystals, which is the dominant material in semiconductor industry. In Section 2, we will briefly review the theoretical basis of photonic bandgap materials. Then we will discuss preparational aspects of 1D, 2D, and 3D photonic crystals made out of silicon and present

---

[*] Prof. U. M. Gösele, Dr. A. Birner,[+] Dr. R. B. Wehrspohn
Max-Planck-Institut für Mikrostrukturphysik
Weinberg 2, D-06120 Halle (Germany)
E-mail: goesele@mpi-halle.de

Dr. K. Busch
Institut für Theorie der Kondensierten Materie, Universität Karlsruhe
PO Box 6980, D-76128 Karlsruhe (Germany)

[+] Current address: Infineon Technologies, Memory Products, D-01099 Dresden, Germany.

[**] The authors are indebted to Drs. Volker Lehmann, Stefan Ottow, and Ulrike Grüning (Siemens Corp.) and Prof. Helmut Föll and co-workers (University of Kiel) for their essential help in the technological realization of the macroporous structures and to Prof. Wolfram Hergert (Martin-Luther University, Halle), Dr. Reinald Hillebrand, Dr. Frank Müller, Jörg Schilling, and Sven Matthias for collaboration and discussions in the area of photonic crystals. We gratefully acknowledge fruitful cooperation with the Universities of Toronto and Constance (Germany) and the MIT as well as financial support from the Deutsche Forschungsgemeinschaft under grant Bu 1107/2-1.

0935-9648/01/0603-0377 $ 17.50+.50/0

some linear optical properties of the photonic crystals. Finally, we give an outlook on dispersion-relation engineering and its impact on nonlinear and quantum optical properties of these photonic crystals.

2. Theory

The simplest way to calculate photonic band structures is to apply the methods of electronic band structure calculations.

Albert Birner received his diploma in physics at the University of Regensburg in 1996 and his Ph.D. in physics from the Martin-Luther-University of Halle-Wittenberg, Germany. Dr. Birner has been an employee of Infineon Technologies AG in Dresden since October 1999. His R&D work is related to integration of innovative processes and process modules for future DRAM generations. His primary interests are in the fields of porous silicon, photonic crystals, photonics, and optics.

Ralf B. Wehrspohn received his diploma in physics at the University of Oldenburg in 1995. He then carried out a Ph.D. at the Ecole Polytechnique in France on thin film technology and electrochemistry. In 1998 he joined the Philips Research Laboratories in Redhill, UK, to work on thin film transistors for active-matrix liquid crystal displays (AMLCDs). Since the end of 1999 he has been responsible for the activities on photonic crystals and self-ordered porous materials at the Max Planck Institute of Microstructure Physics in Halle.

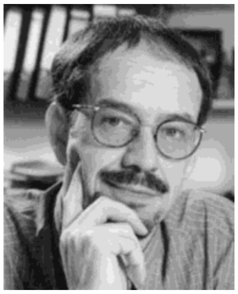

Ulrich M. Gösele has been a director at the Max Planck Institute of Microstructure Physics, Halle, Germany, since 1993. For many years he was a J.B. Duke Professor of Materials Science at Duke University in North Carolina. Prior to that he worked at the Siemens Research Laboratories in Munich. He has had visiting appointments at IBM's Watson Research Center, the NTT LSI Laboratories in Atsugi, Japan, and the Atomic Energy Board in South Africa. His research interests include defects and diffusion process in semiconductors, quantum effects in porous silicon, self-organized structure formation, semiconductor wafer bonding, and photonic crystals.

Kurt Busch is head of a junior research group (Emmy-Noether program of the Deutsche Forschungsgemeinschaft) at the Institute for Theory of Condensed Matter at the University of Karlsruhe (Germany). His research interests lie in light propagation in strongly scattering media and photonic crystals. His undergraduate and postgraduate training was at the University of Karlsruhe (Germany) and partly at the Iowa State University (Ames, USA). His professional experience has included working at Iowa State University (Ames, USA) and at the University of Toronto (Canada).

0935-9648/01/0603-0378 $ 17.50+.50/0

However, various adjustments are necessary to take into account the specific differences between photonic and conventional crystals. First, the electromagnetic field is inherently vectorial by nature, implying that scalar approximations are insufficient. Second, the "scattering potentials" of the dielectric atoms are known beforehand and do not have to be determined self-consistently.

In the following, it is outlined how the widely used plane wave method (PWM)[3] can be applied to the problem of photonic band structure computation. We consider the wave equation for a magnetic field H with harmonic time dependence for a 3D periodic array of scatterers. If the materials differ only in the dielectric but not in the magnetic permeability, we obtain the following wave equation by combining Maxwell's equations.

$$\nabla \times \left(\overleftrightarrow{\epsilon}^{-1}(\vec{r})\nabla \times \vec{H}(\vec{r})\right) - \frac{\omega^2}{c^2}\vec{H}(\vec{r}) = 0 \tag{1}$$

where ω are the eigenfrequencies and c the speed of light. The information about the structure of the photonic crystal is fully contained in the dielectric tensor $\overleftrightarrow{\epsilon}(\vec{r}) = \overleftrightarrow{\epsilon}(\vec{r} + \vec{R})$, which is periodic with respect to the set $\mathcal{R} = \{n_1\vec{a}_1 + n_2\vec{a}_2 + n_3\vec{a}_3; (n_1,n_2,n_3)\}$ of lattice vectors $\vec{R}$, which are generated by the primitive translations $\vec{a}_i$, $i = 1, 2, 3$. We discuss from the outset the general case of an anisotropic tensor. The special case of an isotropic medium can be obtained by replacing the dielectric tensor by a scalar times the unit tensor.

The photonic dispersion relation can be obtained straightforwardly by considering the wave equation (Eq. 1) in reciprocal space, i.e., the dual description of the crystal lattice. To this end, the periodic inverse dielectric tensor is expanded in a Fourier series on $\mathcal{G}$ the reciprocal (dual) lattice corresponding to $\mathcal{R}$:

$$\overleftrightarrow{\epsilon}^{-1}(\vec{r}) = \sum_{\vec{G}\in\mathcal{G}} \overleftrightarrow{\epsilon}^{-1}_{\vec{G}}\, e^{i\vec{G}\vec{r}} \tag{2}$$

where the Fourier coefficients $\overleftrightarrow{\epsilon}^{-1}_{\vec{G}} = (1/V)\int_V d^3r\overleftrightarrow{\epsilon}^{-1}(\vec{r})e^{-i\vec{G}\vec{r}}$ are obtained through an integration over the Wigner–Seitz cell (WSC) whose volume we have designated by V. Using the Bloch–Flouquet theorem, the magnetic field may be expanded into the eigenfrequencies $h^{\lambda}_{\vec{G}}$ as

$$\vec{H}(\vec{r}) \equiv \vec{H}_{\vec{k}}(\vec{r}) = \sum_{\vec{G}\in\mathcal{G}} \sum_{\lambda=1}^{2} h^{\lambda}_{\vec{G}}\, \hat{e}^{\lambda}_{\vec{G}}\, e^{i(\vec{k}+\vec{G})\vec{r}} \tag{3}$$

Here, we utilized the fact that $\nabla\cdot\vec{H}(\vec{r}) = 0$, so that λ labels the two transverse polarizations for any plane wave such that the polarization unity vectors $\hat{e}^{\lambda=1,2}_{\vec{G}}$, $(\vec{k} + \vec{G})/|\vec{k} + \vec{G}|$ form an orthogonal triad. Due to the discrete translational symmetry of the lattice, the wave vector $\vec{k}$ labeling the solution may be restricted to lie in the first Brillouin zone (BZ). As a consequence, the dispersion relation in the infinitely extended momentum space is folded back onto the first BZ, introducing a discrete band index n. However, care must be exercised in identifying the irreducible part of the Brillouin zone (IBZ). The dielectric tensor in Equation 1 may have fewer rotational symmetries than the underlying lattice and consequently the IBZ for a photonic crystal containing anisotropic materials may be considerably larger than the IBZ for the corresponding isotropic crystal. Rather than dealing with an IBZ that changes from problem to problem, one can choose to work with the standard IBZ for the isotropic material and solve Equation 1 for all inequivalent transformations of the given dielectric tensor with respect to the rotational symmetries of the underlying lattice.[4]

Inserting Equations 2 and 3 into Equation 1 results in an infinite matrix eigenvalue problem

$$\sum_{\vec{G}'\in\mathcal{G}} \sum_{\lambda'=1}^{2} M^{\lambda\lambda'}_{\vec{G}\vec{G}'}\, h^{\lambda'}_{\vec{G}'} = \frac{\omega^2}{c^2}\, h^{\lambda}_{\vec{G}} \tag{4}$$

where the matrix elements $M^{\lambda\lambda'}_{\vec{G}\vec{G}'}$ are given by

$$M^{\lambda\lambda'}_{\vec{G}\vec{G}'} = |\vec{k} + \vec{G}|(\hat{e}^{\lambda}_{\vec{G}} \times \overleftrightarrow{\epsilon}^{-1}_{\vec{G}-\vec{G}'} \times \hat{e}^{\lambda'}_{\vec{G}'})|\vec{k} + \vec{G}'| \tag{5}$$

In order to obtain the photonic band and mode structure, Equation 4 has to be solved for both eigenvalues and eigenvectors which for a given wave vector $\vec{k}$ are labeled by the band index n. Then, the electric field corresponding to a given eigenfrequency $\omega_n(\vec{k})$, can be computed from Maxwell's equation

$$\vec{E}_{n\vec{k}}(\vec{r}) = -i\frac{c}{\omega_n(\vec{k})}\, \overleftrightarrow{\epsilon}^{-1}(\vec{r})\, \nabla \times \vec{H}_{n\vec{k}}(\vec{r}) \tag{6}$$

The photonic dispersion relation gives rise to a photonic density of states (DOS), which plays a fundamental role in the understanding of the properties of a photonic crystal. The photonic DOS $N(\omega)$ is defined by "counting" all allowed states of the photonic crystal with a given frequency ω, i.e., by the sum of all bands and the integral over the first BZ of a Dirac-δ function

$$N(\omega) = \sum_{\mathrm{n}} \int_{BZ} d^3k\, \delta(\omega - \omega_n(\mathrm{k})) \tag{7}$$

Figure 1 displays the band structure and densities of states of a hexagonal 2D photonic crystal, which have been computed via the methods outlined above. In 2D photonic crystals the two polarizations of the electromagnetic field decouple if we restrict ourselves to the propagation perpendicular to the axes of the air cylinders. We can thus consider the polarizations of the electric field parallel (E-polarization) and perpendicular (H-polarization) to the cylinder axis separately.[5] Figure 1b shows the corresponding 2D DOS. By analogy with electronic band structure calculations, flat bands in the band structure lead to large values of the DOS.

Transmission calculations through finite slabs of photonic crystalline material are usually based on finite difference time domain (FD-TD) methods[6] and the related transfer matrix method.[7] While these methods can handle disordered structures as well as ordered photonic crystals they also require considerable computational resources. For the special case of cylindrical[8] and spherical[9] geometries an efficient and accurate method based on multiple scattering has recently been developed, which enables the computation of transmission

0935-9648/01/0603-0379 $ 17.50+.50/0

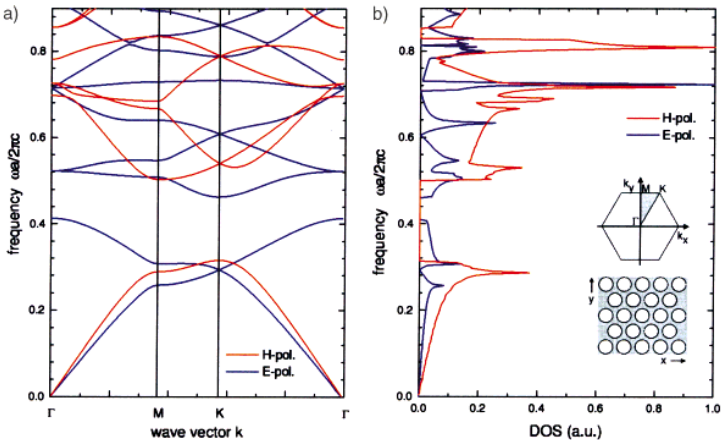

Fig. 1. Photonic band structure of a 2D silicon photonic crystal with a hexagonal arrangement of cylindrical air holes (a) and the corresponding frequency-dependent DOS (b). The inset schematically shows a hexagonal lattice and the corresponding reciprocal lattice. The irreducible part of the first BZ and the high-symmetry points Γ, M, and K are indicated.

through ordered and disordered slabs of cylinders and also allows a direct determination of the band structure of the infinite periodic system.

3. 1D Photonic Crystals

Dielectric mirrors (Bragg reflector) and interference filters were actually the first (1D) photonic crystals. However, they usually are not referred to as crystals because the name crystal is normally reserved for 2D or 3D structures. Typically, these 1D photonic crystals are prepared by layer-by-layer deposition of alternating materials. For example, a layered stack of TiO_2/SiO_2 deposited by sputtering techniques can be used as an optical coating for windows. For these 1D structures today's coating technology allows thin film stacks to be prepared on substrates larger than 3.2 m × 6 m. A stop gap in a desired spectral range can then be achieved by appropriately adjusting the dielectric contrast and the thickness ratios of the alternating layers. The classical layer-by-layer deposition has, however, the disadvantage that only discrete values of the dielectric constant are possible, in the simplest case two values. In Rugate filters[10] the discrete layer structure is replaced by a continuous modulation of the refractive index with depth. This has the beneficial effect that there are fewer sidelobes in the spectra and that one has a greater freedom for filter preparation. Rugate filters are more difficult to prepare with classical plasma-deposition systems since a smooth change from one stoichiometry to the other is technologically difficult to achieve. It has been shown that microporous silicon is a suitable candidate for the fabrication of Rugate filters as shown by Berger et al.[11] Due to the dependence of the porosity of the porous film (i.e., effective refractive index) on the anodization current, the dielectric contrast can be adjusted between 1.5 and 3. However, since the porous layers are still on the substrate and free-standing microporous layers are very fragile, this type of Rugate filter can only be used in reflection mode, i.e., as a Bragg reflector.

There are two problems with simple dielectric filters or mirrors for use in micro-optoelectronics. First, for an angle of incidence greater than a critical angle, light whose frequency lies in the bandgap of the 1D crystal can penetrate through the film (except for omnidirectional reflectors, which consist of very high index material[12]). Second, there is no guidance of the light, which lies energetically outside the photonic bandgap or within a defect band. Recently, an interesting approach has been pursued by the group of Kimerling[13] to create 1D integrated structures. A waveguide with a diameter of about 0.5 µm was structured on a silicon-on-insulator (SOI) substrate using X-ray lithography to provide a periodic arrangement of holes (Fig. 2). They omitted one pore in the center, which acts optically as a resonator having a drastically increased electromagnetic field at the defect site. At the reso-

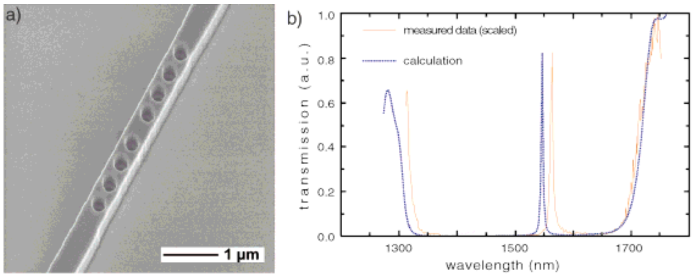

Fig. 2. SEM image of a 1D waveguiding structure made of silicon (a). By incorporating holes at periodic distances one yields a resonator-like functioning of the waveguide, as was demonstrated by transmission calculations (b) [13].

nance frequency, the transmitted intensity was measured to be about 80 % relative to the transmitted intensity outside the photonic bandgap (PBG). The volume of the resonant mode, being proportional to $(\lambda/2n)^3$, was estimated to be $V = 0.055\ \mu m^3$. For the resonance at central wavelength λ_c and half-width $\Delta\lambda$, the value of the measured quality factor of the resonance $Q = \lambda_c/\Delta\lambda$ was about 265, slightly lower than the theoretical value of 280 obtained by numerical simulations. In a classical resonator, this quality factor Q describes the number of periods that a resonant wave packet spends within a cavity. Notice that this simple interpretation does not fully apply to the present situation, since here the average cavity length of $\lambda_c/2$ allows only the existence of a single (longitudinal) resonator mode.

4. 2D Photonic Crystals

If one retains periodicity in the *xy*-plane and lets the *z*-direction be homogeneous, one can describe the propagation within the *xy*-plane in terms of a band structure, which under suitable circumstances exhibits bandgaps in two dimensions (Fig. 1). We term such a structure a 2D photonic crystal. As discussed in Section 2, characteristic of such a 2D photonic crystal is the decoupling of the electromagnetic vector field into two scalar fields, one for each polarization. Since the two polarizations exhibit different behavior each 2D photonic crystal may be utilized to achieve polarization-dependent effects. 2D photonic crystals are much easier to fabricate than 3D structures, since well-known methods for the fabrication of columnar structures[14] may be easily modified for this purpose.

Initially, 2D photonic crystals were constructed either from macroscopic arrangements of sticks or from bundles of glass fibers, and subsequently studied in the microwave or infrared regime. A breakthrough has been achieved by Lehmann's group at Siemens Corp.[15] using their self-developed process of electrochemically growing ordered macropores in silicon. The structures obtained with this method for the first time showed a complete 2D bandgap in the near-infrared (near-IR) at a wavelength of about 4.9 μm. A complete 2D bandgap in this context means a direction- and polarization-independent bandgap for propagation that is confined to the plane of periodicity.[15] In the following we discuss exemplarily the optical properties of 2D photonic crystals based on macroporous silicon.

4.1. Preparation of Macroporous Silicon

A detailed description of the pore formation in macroporous silicon can be found elsewhere.[16–18] Here, we just give a short summary. First, an n-type silicon wafer with ⟨100⟩ orientation is prepatterned by photolithography. Subsequent alkaline etching produces inverted pyramids acting as pore seeds. Under anodic bias and backside illumination the wafer is then etched in hydrofluoric acid. The electronic holes generated by the illumination near the back surface diffuse through the whole wafer and promote the dissolution of silicon mainly at the pore tips. As a result, pores grow straight along the ⟨100⟩ direction with a very high aspect ratio. The spatial arrangement of these pores is controlled through the lithographic mask, whereas their diameter is controlled by the illumination intensity. With suitably adjusted parameters, variations of pore diameters both between neighboring pores and with depth may be minimized to negligible values.

For optical investigations or applications of such structures the porous silicon has to be processed further. The 2D photonic crystal has translational symmetry perpendicular to the pore axes. Therefore, analyzing the band structure requires the photons also to travel perpendicular to the pore axis. Investigations of the properties of defects demand access to the end of, e.g., a waveguide and require parts of the porous silicon to be removed with a precision of about one lattice constant, i.e., a precision of about 1 μm. To meet these specifications, a special microstructuring technique has been developed.[19] First, the pore walls are passivated by a thermal oxide and a chemical vapor deposited (CVD) nitride. Afterwards, an aluminum layer is sputtered onto the porous silicon and structured by conventional photolithography. Although the feature sizes of this second mask are in the 10 μm range, the precision of the structures and the alignment relative to the defects is better than 1 μm. In the opened window of the aluminum mask the passivating oxide and nitride are removed by chemical etching. In a subsequent isotropic plasma etching process the porous silicon in the areas without passivation is etched away, leading to the desired bar structure. The quality of this process is demonstrated in Figure 3, where a bar of porous silicon is shown that consists of about 22 pore layers. The transition from air to the 100 μm deep pores occurs within only one pore layer. By combining the above techniques, we obtain free-standing bars of porous silicon on a silicon sub-

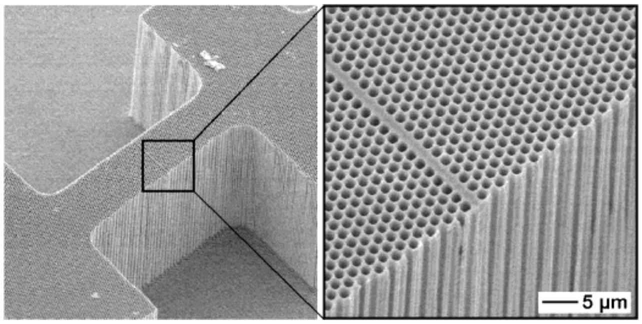

Fig. 3. Laterally structured porous silicon sample with a defect line. The H-like structure facilitates the positioning of a fiber for the coupling in and out of light. The pore separation is 1.5 μm and the height of the porous silicon is 100 μm.

strate that are 100 µm high, 2–200 µm wide, and several millimeters long. In addition, the bars may be aligned with the designed defect structures in the porous silicon.

4.2. Bulk Photonic Crystals

The processed macroporous Si samples described above are extremely well suited to investigating the optical properties of light traveling perpendicular to the pores. We have performed transmission measurements on such bars for different pore diameters, polarizations, and directions. In Figure 4 spectra of defect-free samples with two different pore diameters each consisting of 22 pore layers are shown for the Γ–M direction, H-polarization, and a lattice constant *a* of 1.5 µm. Depending on the pore diameter, the center of the stop-band shifts from 1650 cm^{-1} (6 µm wavelength) for a pore diameter of 1.06 µm up to 2800 cm^{-1} (3.6 µm wavelength) for 1.36 µm. Repeating this measurement for the other directions and for E-polarization, we find a complete gap centered at 3.2 µm for 1.36 µm pore diameter and no overlap of the different stop bands for the 1.06 µm sample. This is in good agreement with theoretical predictions for such structures.

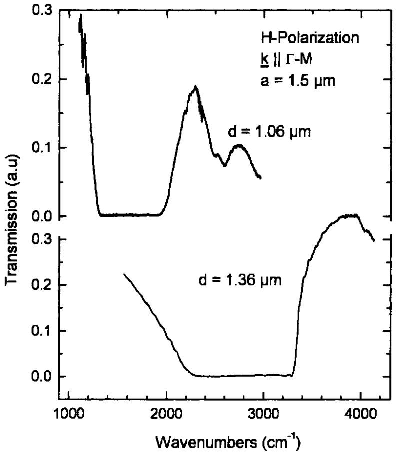

Fig. 4. Transmission spectra of two samples of 2D photonic crystals with different pore diameter *d* along the Γ–M direction, i.e., along the pore rows. The lattice constant *a* is 1.5 µm, the width of the porous silicon bar is 33 µm. The measurement is for H-polarized light, i.e., transverse electric (TE) polarization where the magnetic field is parallel to the pore axes.

In Figure 5 we present a map for the bandgaps resulting from such measurements for a whole set of samples with varying pore diameters (symbols) for *a* = 1.5 µm. For comparison, the theoretical predictions from a plane wave expansion method (see Sec. 2) are shown as solid lines. For the lower filling factors the agreement between theory and experiment is excellent. For very high porosities slight deviations occur, due to the difficulty in preparing and handling these very fragile samples. Therefore, the observed discrepancies are the result of small differences between the real dimensions of the samples and the values used in the calculations.[20]

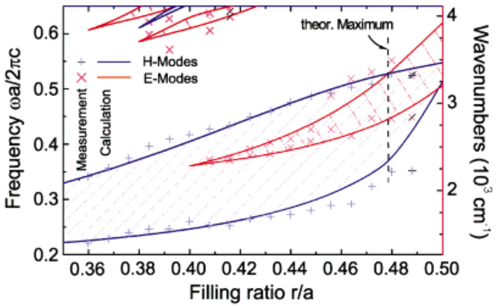

Fig. 5. Dependence of the observed bandgaps on polarization and filling factor (gap map) for a lattice constant *a* of 1.5 µm. Theoretical (solid lines) and experimental (symbols) values show very good agreement [20].

To obtain bandgaps in the opto-electronically interesting region of around 1.3 to 1.55 µm downscaling of the above-described triangular pore lattice is necessary. Recently, we have shown for the first time that it is possible to fabricate pores with a pitch of *a* = 0.5 µm (Fig. 6).[21] The pores fabricated had a radius *r* = 0.18 µm, resulting in an *r*/*a* ratio of 0.43 and a pore depth of 100 µm. To investigate the 2D bandgaps in the near-IR, we have performed reflection measurements similar to those of Rowson et al.[22] The resulting sample spectra are shown in Figure 6. Band structure calculations were performed using 967 plane waves. The shaded spectral ranges represent the theoretically expected regions of high reflectivity. They largely coincide with the bandgaps along the Γ–M direction. Figure 6 reveals good agreement between the theoretically predicted ranges of total reflection and the experimentally determined high reflectivity regions. From the calculated band structure a complete bandgap for E- and H-polarization is expected for the spectral range from 1.22 µm to 1.3 µm, thus incorporating the wavelengths of the second telecommunication window.

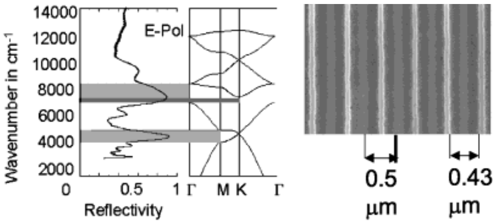

Fig. 6. Left: Measured reflectivity for the Γ–M direction and comparison with band structure calculations for E-polarization. The light-gray shaded regions correspond to regions of high reflectivity. The dark-gray shaded region corresponds to the complete 2D photonic bandgap at around 8000 cm^{-1} (1.25 µm). Right: Cross-sectional SEM image of a structure with a lattice constant of 500 nm and *r*/*a* of 0.43 [21].

0935-9648/01/0603-0382 $ 17.50+.50/0

4.3. Finite Photonic Crystals

For practical purposes finite photonic crystals are important. For a thin slab of a photonic crystal the light will no longer be totally reflected but a certain amount is transmitted. A band structure for such a thin crystal cannot be determined because of the lack of long-range periodicity. However the bandgap of the bulk crystal has to build up with growing number of crystal rows. Besides interesting physical properties, photonic crystals possess a considerable potential for opto-electronic applications. The incorporation of linearly extended defects leads to localized photonic states in the bandgap. Light can be guided through these waveguides, allowing high integration densities for opto-electronic components. However, coupling phenomena have to be understood for the defect design to adjust the minimum distance between two waveguides.

Transmission measurement were performed on 1–4 crystals rows of macroporous silicon using a tunable pulsed laser set-up.[23] For comparison, calculations of the transmittance using the Sakoda approach were performed and a very good agreement with the experimental results was observed. Upon plotting the transmittance on a logarithmic scale against the penetrated crystal thickness a linear relationship is observed.[24] This reveals exponential decay of the transmission with increasing crystal thickness as expected from the case of bulk photonic crystal. From the slope a decay constant of about 10 dB per pore row can be derived for wavelengths deep within the gap. In summary, the bandgap of the bulk crystal is already perceptible for one crystal row. This can be ascribed to the strong refractive index contrast between the air pores and the silicon pore walls as well as to the high perfection of the investigated structures. For integrated defect structures, a minimum distance of about four crystal rows should be considered to avoid crosstalk between neighboring waveguides.

4.4. Defects in Photonic Crystals

If some etch pits are omitted by using a suitable mask for the photolithography, the electronic holes that are generated at the back side through illumination are consumed by the neighboring pores without influencing their position. The result of this procedure is a rather perfect structure with some missing pores at predefined positions, as shown in Figure 7 for a single missing pore. These missing pores disturb the translational symmetry of the periodic lattice and under appropriate conditions lead to localized states (microcavities) in the forbidden spectral region.

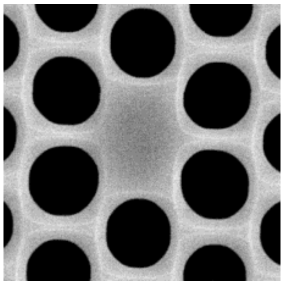

Fig. 7. SEM top view of the region around a missing etch pit after electrochemical pore growth and subsequent pore widening by oxidation/etching steps. The distance between the pores is 1.5 μm, the pore diameters are 1.15 μm [42].

Chaining together such defects in, say, a line creates defect modes with transmission bands inside the photonic bandgap. As propagation is forbidden in the surrounding medium, according to theory waveguides with very sharp bends become possible.[6] In the past, we have analyzed different defect structures: linear[24] and bent waveguide, Y-branch, and microresonator[20] (Fig. 8). Here, we will discuss the impact of the linear defect on the optical properties of the structure in more detail.[24]

FD-TD calculations predict the occurrence of additional states throughout the entire range of the bandgap that are localized at the defect line. As we are experimentally coupling in from a plane wave, we may, however, only excite the states with even symmetry. The theoretical transmission spectrum for a straight waveguide is depicted in the upper part of Figure 9. For lower frequencies, single-mode transmission is expected. In addition, the waveguiding modes are partially reflected at the in- and the out-coupling facets and, therefore, lead to Fabry–Perot resonances. At higher frequencies a small gap is predicted where no states of even symmetry are available. Above the gap, states become available again, but they are so numerous that the resonances can no longer be resolved. The measured spectrum, which is shown in the lower part of Figure 9, shows remarkably good agreement with these predictions: While for low frequencies, single-mode resonances are observed, there is a well-pronounced stop band

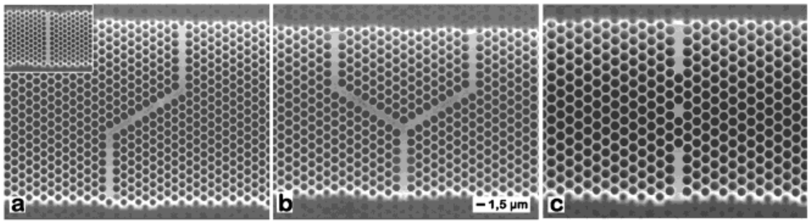

Fig. 8. Different defect structures realized in macroporous silicon with 1.5 μm interpore distance [42].

0935-9648/01/0603-0383 $ 17.50+.50/0

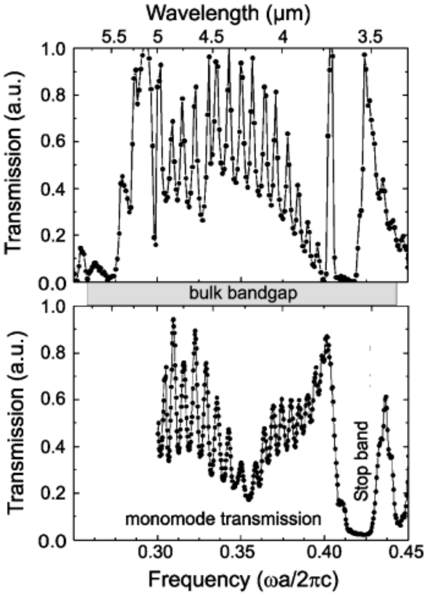

Fig. 9. Experimental transmission spectrum (bottom) of a linear waveguide structure compared to theoretical predictions (top). The bulk bandgap for H-polarization is marked by a gray bar [24].

and a broad transmission band at higher frequencies. Again, the small discrepancies between theory and experiment in the values of the finesse and stop band frequency can be explained by the strong influence of small deviations from the real dimensions to the values used in the calculation.

The observed high finesse results from the low coupling efficiency between the strongly localized waveguide modes and the external plane waves. In a realistic device the waveguide facets could be avoided by connecting other optical elements directly. These linear defects then act as almost ideal waveguides where the light is very well confined to within a few pore rows.

5. 3D Photonic Crystals

Band structure computations showed that for a face-centered cubic (fcc) lattice with a simple basis high dielectric inclusions in a low dielectric matrix do not yield a complete 3D bandgap, not even for an arbitrarily large dielectric contrast. The breakthrough came from the theoretical group at Iowa State University.[3] They discovered a complete photonic bandgap for an arrangement of photonic atoms in a diamond structure, an fcc structure with a two-atom basis, which lifts the polarization degeneracy of the one-atom fcc structure. A corresponding structure, which was manufactured by the group of Yablonovitch[25] and which is now known as "Yablonovite", was the first-fabricated photonic crystal that possessed a complete bandgap, albeit for microwave frequencies. The biggest disadvantage of a "Yablonovite" was that it could not be miniaturized easily. For instance, to obtain a complete photonic bandgap in the optical frequency range it would be necessary to accurately drill long channels less than 1 µm in diameter into a dielectric in a three-dimensionally ordered fashion.

One possibility has been proposed by Föll and co-workers.[26] They have observed that, in principle, macropores can also be used to realize 3D photonic crystal structures. In contrast to the macropores on (100) n-type substrates, which grow perpendicular to the substrate surface, pores on (111) substrates grow in the $\langle 113 \rangle$ crystalline direction. Since pores grow equally well in all three equivalent $\langle 113 \rangle$ directions a structure similar to the Yablonovite may be realized. A slight difference is that in these structures the pores are tilted about 29.5° off the vertical axis whereas in the Yablonovite they have an angle of about 35°. However, calculations from Klose and Dichtel[27] suggest that these structures should exhibit a complete 3D bandgap for an appropriate pore diameter. Föll and co-workers are currently trying to realize these structures by adjusting prepatterning techniques similar to those of the 2D macropore arrays. A disordered pore array, which does not exhibit a bandgap, can be seen in Figure 10.

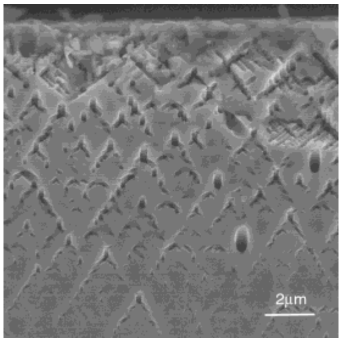

Fig. 10. Disordered 3D macroporous silicon photonic crystal obtained on (111) n-type Si ("Kielovite").

Another possibility for creating a 3D photonic crystal arises form the fact that, according to the established growth model of Lehmann[17,28] for pore formation, the current density at the pore tips is always equal to the critical current density j_{ps}. Therefore, the porosity p is determined by the ratio of the total current density to the critical current density. For a regular arrangements of cells with area A_{cell}, where all pores have the same area A_{pore}, the porosity is thus $p = A_{\mathrm{pore}}/A_{\mathrm{cell}} = j/j_{\mathrm{ps}}$. The total current is controlled by the illumination intensity.

The scanning electron microscopy (SEM) cross-section image in Figure 11 demonstrates the quality of this etching process. The resulting samples have the expected strong asymmetrically varying pore shapes as defined by the current profile.

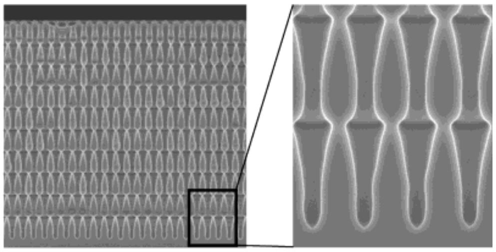

Fig. 11. SEM cross section of a sample etched with 10 periods of modulated light. The lattice constant l_{xy} in the xy-plane is 4.2 µm, in the z-direction l_z = 7.2 µm [29].

In the lateral direction, the sample is homogeneously etched over the whole exposed area without notable defects. With increasing pore depth the HF concentration at the pore tips and therefore also the critical current density j_{ps} as well as the etching speed v are reduced. If the sawtooth-like current density is applied on a linear time scale this leads to a strong variation of about 30 % in the length of a period from top to bottom for a 100 µm deep porous film. Using the reduction of growth speed from the homogeneous model of Lehmann[17] improves this effect dramatically. Up to 25 periods could be etched without notable deviation of the linear fit, leading to a total thickness of over 200 µm.[29] The transmission spectrum in the growth direction of the pores for a sample with a period of l_z = 7.2 µm is shown in Figure 12. Two strong stop bands can be observed near 320 cm^{-1} and 610 cm^{-1}. As the lateral period is significantly smaller than the period in the growth direction, the optical behavior can, to a first approximation, be obtained by using an effective medium model. From the pore diameter, as measured from the SEM cross-section images, we determined the depth dependence of the porosity and then the effective refractive index using the Bruggeman formalism.[30] The calculated transmission spectrum for a multilayer model[31] using ten slabs for each period and eight periods in total is shown as a dotted line in Figure 12. The positions of the stop bands are well reproduced by this simple approximation. The Fabry–Perot-type interference pattern from the reflections at the front and back surfaces, which are very strong in the calculated spectrum, were not resolved in the experiment. The high transmission values around 550 cm^{-1} and below 180 cm^{-1} are artifacts due to the low background intensity of the spectrometer.

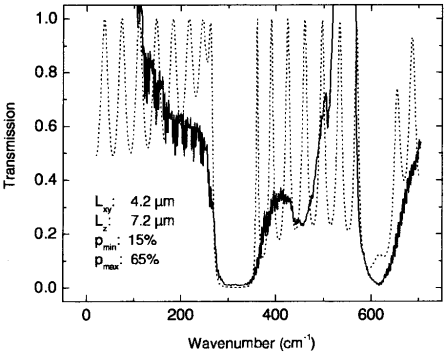

Fig. 12. Transmission spectrum for light travelling parallel to the pore axes (solid line) of the structure depicted in Figure 11 together with the calculated spectrum from a 1D Bruggeman approximation (dotted line). The lattice constant l_{xy} in the xy-plane is 4.2 µm, in the z-direction l_z = 7.2 µm. The porosity varies from p_{min} = 0.15 to p_{max} = 0.65 [29].

These samples demonstrate the ability to generate real 3D photonic crystals by modulating the backside illumination. Although the structures produced so far[32] do not exhibit a complete photonic bandgap, they have strongly nonlinear dispersion relations in all directions, behavior that will be very useful in nonlinear optical experiments. For instance, phase matching may easily be achieved in these structures, which for applications such as mixing experiments of beams with different wavelength may prove useful. In particular, the freedom to design the third, i.e., the z-direction, independently from the periodicity in the xy-plane will provide a very high flexibility.

Based on their initial studies of the diamond-like structures, the Iowa State group discovered another structure that is easier to miniaturize as the "Yablonovite", the so-called "Lincoln-log" structure.[33] This structure resembles a stack of wooden logs in parallel orientation to each other in each layer. Within each layer, SiO_2 was first deposited, patterned, and etched, such that two successive layers are oriented perpendicular to each other. The resulting trenches are then filled by poly-Si layers and finally the SiO_2 is removed completely. The second-nearest layers are displaced with respect to each other by half the bar distance within the layers. While the first of these crystals had a bandgap at a frequency of about 13 GHz (corresponding to a wavelength of about 2.3 cm), the recently fabricated crystals at Sandia National Laboratories[33] exhibit a bandgap at a wavelength of about 1.5 µm. However, the vertical extensions that have been achieved until now are rather small and the effort to produce large-scale 3D crystals will be substantial. The above-mentioned silicon Lincoln-log crystal,[33] for instance, consists of only five layers, i.e., 1.25 unit cells in the vertical direction. Instead of depositing each layer, Noda et al.[34] have applied wafer-bonding technology on III–V semiconductor substrates. This techniques allows multiplicative stacking, i.e., the preparation of a log structure similar to the one at Sandia National Laboratories, bonding two of these single-layer structures together, removing the substrate of the upper one, bonding two of those double-layer structures together, and so on (Fig. 13). Using this technique, a stack of eight layers has been achieved, corresponding to two units cells in the vertical direction.

Several research groups are pursuing a different approach to fabricating 3D photonic crystals: Under appropriate conditions, colloids self-organize into periodic structures that can extend over several hundred unit cells.[35] Due to their cubic symmetry, these crystals cannot possess a complete photonic bandgap, not even for the highest possible ratios of the indices

0935-9648/01/0603-0385 $ 17.50+.50/0

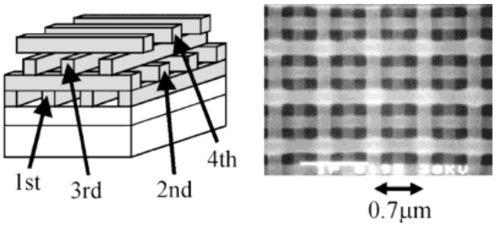

Fig. 13. Left: schematic drawing of one unit cell of the woodpile-structure 3D photonic crystal. Right: Top view SEM image of 3D photonic crystal prepared via the Noda approach. The lattice constant *a* is 0.7 µm, resulting in a bandgap around 1.3 µm [34].

of refraction $\eta = n_2/n_1$ of the constituent materials. However, the inverse structure, the so-called inverse opal, does have a complete bandgap in the higher bands.[5] A simplified recipe for the fabrication of inverse opals is as follows: Firstly, an artificial opal is fabricated, i.e., a close-packed fcc lattice of, for example, monodispersed SiO_2 spheres (diameter ranging from 100 to 1000 nm). The spheres are then sintered, making them shrink slightly and causing neighboring spheres to become firmly connected by a tube-like connection of SiO_2. Next, a high-index material is deposited into the void regions between the spheres. In a final step, in order to increase the dielectric contrast, the 3D network of SiO_2 spheres is removed by selective etching. This process may be called 3D templating. Very recently, the group at the University of Toronto reported the first successful fabrication of silicon-based inverse opals with a complete 5 % photonic bandgap relative to its center frequency for center frequencies at the telecommunication window around 1.5 µm.[36] Here, the voids of the artificial opal were almost completely filled with silicon by CVD. Figure 14 shows an SEM image of such a photonic crystal with a lattice constant of about 0.5 µm.

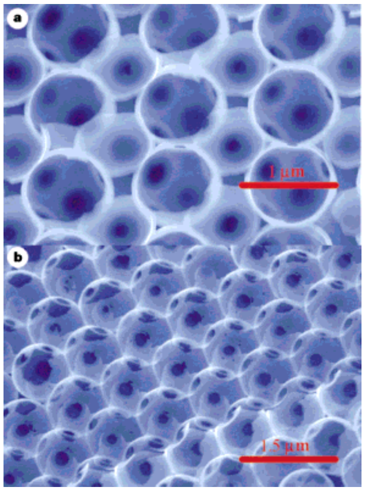

Fig. 14. SEM images of spatially periodic structures that have been obtained by infiltrating an artificial opal with silicon and subsequent removal of the opal. The lattice constant is 500 nm [36].

Using PWM (Sec. 1) it has recently been demonstrated theoretically[5] that it is possible to double the size of the inverse opal PBG by fine tuning the material's synthesis by, for example, careful sintering and control of the infiltration process. The resulting inverse opal structures (see Fig. 14) then consist of a high dielectric backbone with a filling ratio of about 25 %, leaving a large empty volume for infiltration by a low refractive index liquid crystal with strong optical anisotropy. This large volume of birefringent material makes the resulting system highly susceptible to electro-optic tuning effects. In particular, a change in the orientation of the nematic director field with respect to the inverse opal backbone by an external electric field can completely open or close the full, 3D PBG,[4] thus providing novel electro-optical ways to realize tunability of spontaneous emission, wave-guiding effects, and light localization. Recently, we have shown in collaboration with the University of Toronto for the first time as a proof of principle the feasibility of such an optical switch by introducing a liquid crystal into the pores of a 2D macroporous silicon photonic crystal and switching it thermally.[37]

6. Beyond Maxwell

Controlling the light propagation by photonic crystals opens entirely new avenues to applications outside the realm of classical electrodynamics, in particular in the fields of nonlinear optics as well as quantum optics. In order to fit within the scope of this overview article, we will discuss one example from each field.

Solitary waves are well known in various fields of physics: Solitary waves are solutions of nonlinear wave equations and can, for instance, be observed as step-shaped waves running down slightly inclined streets during heavy rain. A defining characteristic of solitary waves is that they do not change their shape during propagation—they are free of dispersion. In a nonlinear dielectric, i.e., a dielectric with an intensity-dependent index of refraction, it is possible that the dispersion- induced decay of a wave packet during propagation may be compensated by self-focussing effects. In this case, a solitary wave forms. The time stability of this type of wave makes it particularly promising as an information carrier, since using solitary waves one can send signals with extremely high pulse rates over long distances without fearing scrambling of successive pulses.

For some time now a slightly different kind of solitary wave, the so-called gap soliton, has been studied in 1D photonic crystals. Here, one starts with a pulse the central frequency of which lies within the bandgap of a photonic crystal. Due to an intensity-dependent index of refraction of at least one of the components of the crystal, an energetic pulse can distort the local band structure to such an extent that it causes the central frequency of the pulse to lie outside the bandgap. While it propagates, a sufficiently energetic pulse forms its own channel of transmission. In contrast to that, however, the investiga-

0935-9648/01/0603-0386 $ 17.50+.50/0

tion of gap solitons in 2D or 3D photonic crystals is still in its infancy, yet promises to yield a wealth of interesting phenomena. Compared to 1D structures, the photonic band structure of higher dimensional crystals offers qualitatively new properties. For instance, the bandgap along one high-symmetry direction may be slightly shifted and the corresponding modes of the photonic crystals may have different symmetries. This leads to quite a number of solitary wave types with various threshold intensities as well as propagation speeds.[38] Consequently, one might use one solitary wave as a switch for another one or gate one solitary wave with the other one. In this respect, one could consider the first solitary wave some sort of "ice-breaker" for the second one. By modifying the intensity in the dielectric, the first solitary wave creates a channel through the "ice" of the photonic bandgap, which the second solitary wave could not enter before. The direction of the channel is then determined by the first solitary wave. Since the ice-channel in this Gedanken experiment freezes on the timescale of picoseconds, one is dealing here with an ultrafast phenomenon.

Quantum optics is another field in which photonic crystals offer qualitatively new possibilities: In a nutshell, the tailoring of the photonic density of states by means of photonic crystals allows far-reaching control of the emission characteristics of corresponding color centers. In illustration of this we discuss the qualitative behavior of an idealized two-level atom in a photonic crystal. If the transition frequency is well within a complete photonic bandgap, the atom cannot decay to its ground state via a one-photon process. A bound photon–atom state is formed instead. Furthermore, calculating the atomic relaxation via an allowed two-photon process for atomic resonance frequencies within a complete photonic bandgap[39] yields lifetimes of several days. Due to the idealization typical of quantum-optical calculations, this lifetime for real systems is certainly too long. However, it can be assumed that the lifetimes of excited atoms or molecules in suitable photonic crystals exceed the corresponding ones in vacuum by several orders of magnitude. This possibility of controlling the spontaneous emission via the tailored density of states alone would be of paramount importance to the achievement of novel quantum-optical effects.

Particularly interesting phenomena occur for frequencies near the edge of a photonic bandgap. In this frequency range, the dispersion relation decreases remarkably (see Fig. 1a), which leads to a very low group velocity, causing the photon–atom interaction to increase. For simplicity, the discussion is restricted to an atom with an excited and a ground state, $|c\rangle$ and $|g\rangle$, respectively, as well as to two corresponding states of the electromagnetic field mode with no and one photon, $|0\rangle$ and $|1\rangle$, respectively. By analogy with the formation of a "binding" as well as an "antibinding" state for the ammonium molecule, due to the strong interaction between the atom and the field the "bare" atomic eigenstates form combined atom–field eigenstates, which in quantum optics are referred to as "dressed states". In order to understand the dynamical behavior of an initially excited atom one has to imagine a decomposition of this initial state into linear combinations of the states that form the Rabi-duplett, which themselves, due to the splitting of their energy levels, evolve differently with time. As the photon remains in an ideal cavity, i.e., in our case the photonic bandgap, the wavefunction of the photon–atom system will oscillate between the states of the Rabi-duplett. If the "bare" atomic transition frequency is in close proximity to a photonic band edge, but still just within the photonic bandgap, the Rabi splitting may become so large that one component of the Rabi-duplett will be pushed outside the photonic bandgap into the photonic conduction band. In contrast to its partner, this state thus acquires a finite lifetime by being coupled with the photonic conduction band. As the initially excited atom may decay "partially", so-called fractional localization occurs.[39,40] Figure 15 shows the relaxation behavior of an excited two-level atom as a function of the position of the bare transition frequency relative to the photonic band edge. A detailed explanation is given in the literature.[40]

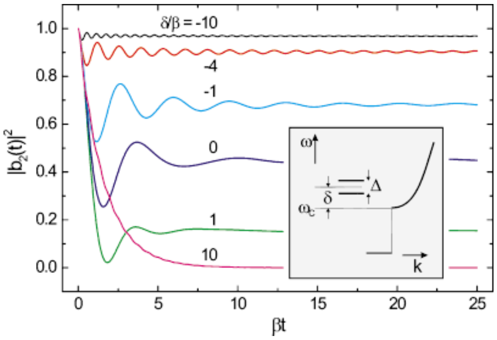

Fig. 15. Temporal evolution of the occupation $|b_2(t)|^2$ of the upper level of an initially excited two-level atom for various values of its transition frequency $\omega_{21} = \omega_c + \delta$ relative to the band edge at ω_c. The photonic conduction band lies at frequencies $\omega > \omega_c$. Characteristic are the damped Rabi oscillations and the finite oscillator amplitude for long times, which correspond to the "partial" decay of the excited level. The fractional localization drops from nearly 1 (far below the band edge in the bandgap) to 0 (in the band).

One may imagine the above situation in terms of an excited atom which emits a photon that, due to the strong Bragg scattering at frequencies near the band edge, finds its way back to the atom where it is reabsorbed. This photon feedback effect makes the atom develop a memory of its previous state. Such and similar memory effects are not limited to band edges but occur wherever the photon density of states changes abruptly.

If only one single excited atom exhibits such a peculiar behavior in a photonic crystal, one is tempted to speculate about the behavior of multi-level atoms, of atoms resonantly driven by laser fields and, finally, about the collective behavior of several atoms embedded in a photonic crystal. Currently, aspects such as the so-called band edge laser are the subject of intense research efforts and discussing them here would certainly go beyond the scope of this review article.[41]

7. Conclusions and Outlook

There exists a strong analogy between electrons in semiconductor crystals and photons ("light particles") in photonic crystals: Multiple scattering at periodically positioned "dielectric atoms" leads to the formation of an optical band structure. Under certain circumstances optical bandgaps form, which fundamentally alter light propagation as well as emission processes of active atoms in these artificial structures. This rather new knowledge gained about one decade ago has triggered intensive research efforts that initially focused on fundamental research on how to "make light stand still". Novel integrated photonic devices have been proposed that, through their miniaturization and high efficiency, could open the door to entirely new classes of all-optical devices. Recent progress in nanofabrication makes it possible that photonic bandgap devices will be realized in the near future, potentially signaling the start of a photonic revolution comparable to the semiconductor revolution, which began half a century ago.

We have reviewed recent progress on 2D photonic crystals based on macroporous silicon in particular. Transmission measurements on bulk and finite macroporous silicon photonic crystals show good agreement with theoretical predictions for a wide range of pore diameters. The lattice constants can be varied in the range from 8000 down to 500 nm, resulting in complete bandgaps in a wavelength range between 20 and 1.3 μm. Passive devices such as waveguides and microresonators have been fabricated and optically characterized, showing good agreement between theoretical calculations and measured transmission spectra. Also first active devices based on liquid-crystal infiltrated macropores have been produced. Periodicity in the third direction can be achieved either by modulating the macropore diameter or by the "Kielovite" technique. The precision of the achieved samples and the presented optical data prove the suitability of electrochemically etched macroporous silicon as a candidate for new optical devices based on photonic crystals in the near and mid infrared spectral range.

Received: August 21, 2000

---

[1] A. R. Parker, R. C. McPhedran, D. R. McKenzie, L. C. Botten, N. A. P. Nicorovici, *Nature* **2001**, *409*, 36.

[2] *Photonic Bandgap Materials* (Ed: C. M. Soukoulis), Kluwer, Dordrecht, The Netherlands **1996**. *Photonic Crystals* (Eds: J. D. Joannopoulos, R. D. Meade, J. N. Winn), Princeton Academic Press, Princeton, NJ **1995**.

[3] K.-M. Ho, C. T. Chan, C. M. Soukoulis, *Phys. Rev. Lett.* **1990**, *65*, 3152.

[4] K. Busch, S. John, *Phys. Rev. Lett.* **1999**, *83*, 967.

[5] K. Busch, S. John, *Phys. Rev. E* **1998**, *58*, 3896.

[6] A. Mekis, J. C. Chen, I. Kurland, S. Fan, P. R. Villeneuve, J. D. Joannopoulos, *Phys. Rev. Lett.* **1996**, *77*, 3787.

[7] M. Sigalas, C. M. Soukoulis, E. N. Economou, C. T. Chan, K. M. Ho, *Phys. Rev. B* **1993**, *48*, 14 121.

[8] R. C. McPhedran, L. C. Botten, A. A. Asatryan, N. A. Nicorovici, P. A. Robinson, C. M. de Sterke, *Phys. Rev. E* **1999**, *60*, 7614.

[9] V. Yannopaps, N. Stefanou, A. Modinos, *J. Phys.: Condens. Matter* **1997**, *9*, 10 261.

[10] B. G. Bovard, *Appl. Opt.* **1993**, *32*, 5427.

[11] M. G. Berger, R. Arens-Fischer, M. Thoenissen, M. Krueger, S. Billat, H. Lueth, S. Hilbrich, W. Theiss, P. Grosse, *Thin Solid Films* **1997**, *297*, 237.

[12] D. N. Chigrin, A. V. Lavrinenko, D. A. Yarotsky, S. Gaponenko, *Appl. Phys.* **1999**, *68*, 25.

[13] J. S. Foresi, P. R. Villeneuve, J. Ferrera, E. R. Thoen, G. Steinmeyer, S. Fan, J. D. Joannopoulos, L. C. Kimerling, H. I. Smith, E. P. Ippen, *Nature* **1997**, *390*, 143.

[14] V. Lehmann, *J. Electrochem. Soc.* **1993**, *140*, 2836. A. P. Li, F. Müller, A. Birner, K. Nielsch, U. Gösele, *J. Appl. Phys.* **1998**, *84*, 6023.

[15] U. Grüning, V. Lehmann, S. Ottow, K. Busch, *Appl. Phys. Lett.* **1996**, *68*, 747. U. Grüning, V. Lehmann, U. Eberl, *Phys. Bl.* **1996**, *52*, 661.

[16] V. Lehmann, H. Föll, *J. Electrochem. Soc.* **1990**, *137*, 653.

[17] V. Lehmann, *J. Electrochem. Soc.* **1993**, *140*, 2836.

[18] A. Birner, U. Grüning, S. Ottow, A. Schneider, F. Müller, V. Lehmann, H. Föll, U. Gösele, *Phys. Status Solidi A* **1998**, *165*, 111.

[19] S. Ottow, V. Lehmann, H. Föll, *J. Electrochem. Soc.* **1996**, *143*, 385.

[20] A. Birner, A.-P. Li, F. Müller, U. Gösele, P. Kramper, V. Sandoghdar, J. Mlynek, K. Busch, V. Lehmann, *Mater. Sci. Semicond. Proc.* **2000**, *3*, 487.

[21] J. Schilling, A. Birner, F. Müller, R. B. Wehrspohn, R. Hillebrand, U. Gösele, K. Busch, S. John, S. W. Leonard, H. M. van Driel, *Opt. Mater.*, in press.

[22] S. Rowson, A. Chenokov, C. Cuisin, J.-M. Lourtioz, *IEEE Proc.—Optoelectron.* **1998**, *145*, 403.

[23] S. W. Leonard, H. M. van Driel, K. Busch, S. John, A. Birner, A.-P. Li, F. Müller, U. Gösele, V. Lehmann, *Appl. Phys. Lett.* **1999**, *75*, 3063.

[24] S. W. Leonard, H. M. van Driel, A. Birner, U. Gösele, P. R. Villeneuve, *Opt. Lett.* **2000**, *25*, 1550.

[25] E. Yablonovitch, T. J. Gmitter, K. M. Leung, *Phys. Rev. Lett.* **1991**, *67*, 2295.

[26] M. Christophersen, J. Carstensen, A. Feuerhake, H. Föll, *Mater. Sci. Eng. B* **2000**, *69*, 194.

[27] R. Klose, K. Dichtel, unpublished results.

[28] V. Lehmann, U. Grüning, *Thin Solid Films* **1997**, *297*, 13.

[29] F. Müller, A. Birner, J. Schilling, U. Gösele, C. Kettner, P. Hänggi, *Phys. Status Solidi A* **2000**, *182*, 585.

[30] D. A. G. Bruggeman, *Ann. Phys. (Leipzig)* **1935**, *24*, 636.

[31] F. Abelès, *Ann. Phys. (Paris)* **1950**, *5*, 596.

[32] J. Schilling, F. Müller, S. Matthias, R. B. Wehrspohn, U. Gösele, K. Busch, *Appl. Phys. Lett.* **2001**, *78*, 1180.

[33] S. Y. Lin, J. G. Fleming, D. L. Hetherington, B. K. Smith, R. Biswas, K. M. Ho, M. M. Sigalas, W. Zubrzycki, S. R. Kurtz, J. Bur, *Nature* **1998**, *394*, 251.

[34] S. Noda, N. Yamamot, M. Imada, H. Kobayashi, M. Okano, *J. Lightwave Technol.* **1999**, *17*, 1948.

[35] W. L. Vos, R. Sprik, A. van Blaaderen, A. Imhof, A. Laghendijk, G. H. Weydam, *Phys. Rev. B* **1996**, *53*, 16 231.

[36] A. Blanco, E. Chomski, S. Grabtchak, M. Ibisate, S. John, S. W. Leonard, C. Lopez. F. Meseguer, H. Miguez, J. P. Mondia, G. A. Ozin, O. Toader, H. M. van Driel, *Nature* **2000**, *405*, 437.

[37] S. W. Leonard, J. P. Mondia, H. M. van Driel, O. Toader, S. John, K. Busch, A. Birner, U. Gösele, V. Lehmann, *Phys. Rev. B* **2000**, *61*, R2389.

[38] N. Aközbek, S. John, *Phys. Rev. E* **1998**, *57*, 2287.

[39] S. John, J. Wang, *Phys. Rev. Lett.* **1990**, *64*, 2418. *Phys. Rev. B* **1991**, *43*, 12 722.

[40] S. John, T. Quang, *Phys. Rev. A* **1994**, *50*, 1764.

[41] S. John, T. Quang, *Phys. Rev. Lett.* **1996**, *76*, 2484. *Phys. Rev. Lett.* **1997**, *78*, 1888. T. Quang, M. Woldeyohannes, S. John, G. S. Agarval, *Phys. Rev. Lett.* **1997**, *79*, 5238. N. Vats, S.John, *Phys. Rev A* **1998**, *58*, 4168. M. Woldeyohannes, S. John, *Phys. Rev. A* **1999**, *66*, 5046.

[42] F. Müller, A. Birner, U. Gösele, V. Lehmann, S. Ottow, H. Föll, *J. Porous Mater.* **2000**, *7*, 201.

www.mrs.org/publications/bulletin

Electrochemically Prepared Pore Arrays for Photonic-Crystal Applications

R.B. Wehrspohn and J. Schilling

Introduction

In the last few years, photonic crystals have gained considerable interest due to their ability to "mold the flow of light."[1] Photonic crystals are physically based on Bragg reflections of electromagnetic waves. In simple terms, a one-dimensional (1D) photonic crystal is a periodic stack of thin dielectric films with two different refractive indices, n_1 and n_2. The two important geometrical parameters determining the wavelength of the photonic bandgap are the lattice constant, $a = d_1(n_1) + d_2(n_2)$, and the ratio of d_1 to a (where d_1 is the thickness of the layer with refractive index n_1, and d_2 is the thickness of layer n_2). For a simple quarter-wavelength stack, the center wavelength λ of the 1D photonic crystal would be simply $\lambda = 2n_1d_1 + 2n_2d_2$. In the case of 2D photonic crystals, the concept is extended to either airholes in a dielectric medium or dielectric rods in air. Therefore, ordered porous dielectric materials like porous silicon or porous alumina are *intrinsically* 2D photonic crystals.

Electrochemically grown pores in metals and semiconductors[2,3] have been studied for about 50 years. However, only in the last 10 years have intense research efforts enabled the preparation of *ordered* arrays of pores with pore diameters in the range of a few nanometers to some tens of micrometers. The most studied materials are porous alumina and macroporous silicon.

Porous alumina has been known for more than a century, but only in 1995 was it first observed that ordered arrays of porous alumina could be achieved.[4] This ordering was initially by self-organization, and the ordered domains were in the micrometer range. However, electron-beam lithography[5] and a related new technique, nanoindentation,[6] allowed the preparation of monodomain porous alumina structures with sizes in the micrometer range.

Macroporous silicon was pioneered in the early 1990s by Lehmann and Föll.[7] Very regular pore arrays in the micrometer range have been obtained by photolithographic prepatterning. These pores were called macropores (in contrast to microporous silicon, which is a sponge-like nanostructured material with photoluminescent properties that was also intensively studied in the early 1990s).[8]

Moreover, recently a few other semiconductors like InP, GaAs, and GaP have been shown to exhibit micrometer-sized pores.[9,10] Whereas standard nanostructuring techniques are limited to small pore aspect ratios ($h/d < 40$), and resolutions are limited by lithographic tools, electrochemically prepared pores exhibit high aspect ratios of 100–10,000 and inherent short-range order. In the following, two materials will be discussed in detail: macroporous silicon and porous alumina. Due to the regular pore arrangements, these materials are extremely well suited as photonic crystals.

Macroporous Silicon

Porous silicon formed by the anodization of *p*-type silicon in hydrofluoric acid has been studied by numerous groups. A current state-of-the-art summary is given by Allongue.[11] Three different pore-formation regimes have been observed experimentally as a function of the dopant concentration. For degenerately doped *p*-type silicon, a special type of mesopore observed experimentally has been attributed to tunneling of holes through the space-charge region.[12] For moderately doped *p*-type silicon, nanopore formation is observed with pores in the range of 2–100 nm. For highly resistive crystalline and amorphous *p*-type silicon, macropore formation (0.4–10 μm in diameter) is observed below a thin layer of nanopores.[13,14] Previously, macropore formation in low-doped Si had been reported in anhydrous electrolyte.[15,16] The wall thickness is about two times the space-charge region, whereas the interpore distance is governed by the properties of the silicon–electrolyte interface, the resistivities of the silicon wafer, and the properties of the electrolyte.[17,18] A detailed description of macroporous silicon formation in *n*-type Si can be found in References 7 and 19. Since in *n*-type silicon holes are minority carriers, the holes have to be generated by back-side illumination. Then they diffuse to the etch front through the wafer. This technique puts high demands on the minority carrier diffusion length, so normally float-zone (FZ) wafers are used. Since in this technique the holes move by diffusion and not by drift as in the *p*-type case, the strong boundary condition is relaxed and thicker walls can be obtained—up to 10 times the space-charge region width.[20] To obtain ordered arrangements of pores, an *n*-type silicon wafer with ⟨100⟩ orientation is first prepatterned by standard photolithography. Subsequent alkaline etching produces inverted pyramids acting as initial pores. Under anodic bias and back-side illumination, the wafer is then etched in hydrofluoric acid. The electronic holes generated by the illumination near the back surface diffuse through the whole wafer and promote the dissolution of silicon mainly at the pore tips. As a result, pores grow straight along the [100] direction with very high aspect ratios. The arrangement of these pores can be controlled by the lithographic mask, and the pore diameter can be controlled by the illumination intensity. By controlling these parameters, variations of the pore diameter with depth can be made negligible. Figure 1 shows a scanning electron microscope (SEM) image of a porous Si sample, which was etched on 0.5 Ω cm *n*-type FZ silicon substrates having a photolithographically defined hexagonal pore arrangement. The pores have a center-to-center distance of 1.5 μm and a depth of 100 μm. The pore diameter after electrochemical etching is 0.9 μm. By subsequent oxidation/etching steps, the pore diameter is increased to up to 1.36 μm. The beveled edge in Figure 1 shows the very good depth homogeneity of the pore diameter.

Porous Alumina

Aluminum is electrochemically oxidized to alumina (Al_2O_3) under positive polari-

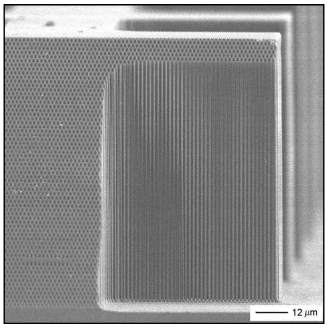

Figure 1. Scanning electron microscope (SEM) image of a perpendicular cut (right side) and beveled cut (left side) in a triangular macroporous silicon array obtained by plasma etching and subsequent polishing. Lattice constant is 1.5 μm. The pore diameter is constant throughout the entire 100-μm pore length.

zation. For certain electrolytes, which weakly dissolve the alumina, the growth of disordered pore arrangements has been observed and studied for a century now. A unique relationship between anodization voltage *U* and interpore distance *a* was found: $a = d + 2\alpha U$, where *d* is the diameter of the pores and $\alpha \sim 1.2$ V/nm.[3,21] In 1995, Masuda and Fukuda[4] first discovered that after long anodization times, self-ordered porous alumina films arranged in a hexagonal pattern can be obtained at the growth front. They have obtained ordered pore arrays with lattice constants of 60 nm,[22] 100 nm,[4] and 500 nm,[6] depending on the anodization conditions. The size of the pore domains increases with time and can reach micrometer size.[23] Domains touching each other have typically different orientations.[24] Mechanical stress between neighboring pores due to the volume expansion of alumina with respect to the aluminum substrate has been proposed as a mechanism for the self-ordering. For example, it is observed that the volume expansion for optimal pore growth is in the range of 1.2–1.4, that is, there is an incorporation yield of 60–70% aluminum in the alumina film.[5]

To obtain monodomain pore arrays, three strategies are possible. First, if one starts with a single-crystal seed, that is, a single pore, one would expect the other pores to arrange themselves hexagonally around it due to repulsive forces. The second strategy is based on the observation of Li et al.[23] As the anodization time increases, one should end up with a single domain since this state represents the total energy minimum of the system. Note that this assumes a monocrystalline aluminum substrate. However, both approaches seem to be quite impractical. Therefore, a third strategy is used. Knowing the optimum potential *U* for a certain interpore distance *a*, the aluminum substrate can be lithographically prepatterned. Since the feature sizes are in the range of 50 nm, electron-beam lithography prepatterning is applied.[5] Figure 2 shows a SEM image of a hexagonally ordered pore array in alumina prepared from an electron-beam lithography prepatterned substrate. The pattern has 200-nm interpore spacing, and the anodic voltage was adjusted to 85 V, based on the relationship between the interpore distance *a* and the potential *U*. The inset in Figure 2 shows the Fourier transform of the image. Very recently, Masuda et al. have shown that in addition to the hexagonal lattice, the square and honeycomb lattices can also be obtained by appropriate prepatterning, resulting in square or triangular pore shapes.[25]

Application to Photonic Crystals

In the following, we will briefly discuss the optical properties of macroporous silicon and porous alumina photonic crystals.

Macroporous Silicon

The processed macroporous Si samples shown in Figure 1 are very well suited to investigate the optical properties of light traveling perpendicular to the pores.[26] Transmission measurements on such bars for samples with a fixed lattice constant $a = 1.5$ μm but varying pore diameters were made for different polarizations and directions. From these data, the bandgap edges were determined as a function of r/a (radius/lattice constant) for a range of wavelengths; they are indicated in Figure 3. For comparison, the theoretical predictions obtained by solving Maxwell's equations by a plane-wave expansion method are shown as solid lines.[27] There is very good agreement between theory and experiment. The 2D silicon photonic crystal exhibits a complete photonic bandgap for both polarizations, transverse magnetic (TM) and transverse electric (TE), and all in-plane directions. A maximum gap-width to midgap frequency ratio of 17% is obtained for r/a of 0.48. To obtain bandgaps in the optoelectronically interesting region around 1.3–1.55 μm, it is necessary to scale down the previously described triangular pore lattice. Recently, we have shown for the first time that it is possible to fabricate pores with a pitch of $a = 0.5$ μm.[28] The pores fabricated had a radius $r = 0.215$ μm, resulting in an r/a ratio of 0.43 and a pore depth of 100 μm.

Figure 4 shows a summary of data obtained by various authors on the bandgap-center wavelength for porous silicon and porous alumina, as a function of lattice constant *a*. For macroporous silicon, the obtained interpore spacings range from 500 nm to 8 μm,[29–32] leading to photonic bandgaps in the region from 1 μm to 20 μm. The electronic bandgap of silicon is at 1.1 μm, so for bandgaps below this wavelength, absorption occurs.

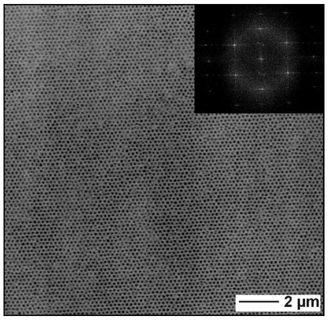

Figure 2. SEM top view of monocrystalline pore arrays in ordered porous alumina prepared with prepattern-guided anodization. The prepattern with a pitch (lattice constant) of 200 nm was induced by using electron-beam lithography. The inset shows the Fourier transform of the image.[5]

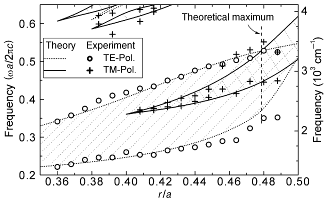

Figure 3. Bandgap edges in porous Si photonic crystals determined from transmission measurements as a function of radius/lattice constant (r/a) *for a range of wavelengths. Data are shown for transverse magnetic (TM, +) and transverse electric (TE, ○) polarizations. The lattice constant was* a = *1.5 μm. Calculated values for TM (solid lines) show very good agreement with the experimental data.[27]*

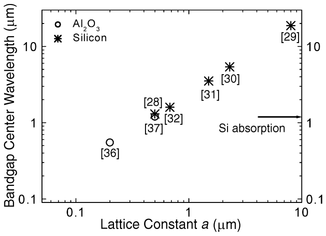

Figure 4. Summary of experimentally measured bandgap-center wavelengths for porous alumina (TE gap) and porous silicon (complete gap) as a function of the lattice constant. (From References 28–32, 36, and 37.)

Defects can be made in the regular porous Si structure by designing the proper lithographic mask. In this way, specific etch pits in the regular pattern are removed. Electronic holes generated at the back side by illumination are consumed by the neighboring pores without great influence on the position of these neighboring pores. The result is a relatively perfect structure with missing pores at predefined positions. These missing pores disturb the translational symmetry and lead to localized states in the forbidden spectral region. Arranging such defects in a line creates defect modes with transmission bands inside the forbidden gap. As propagation is forbidden in the surrounding medium, waveguides with very sharp bends should be possible, according to theory.[33] In the past, different defect structures have been analyzed: linear[34] and bent waveguide, Y-branch, and microresonator.[27] A 2D Mach-Zehnder interferometer with a 500-nm interpore spacing is shown in Figure 5. This device is designed to filter wavelengths based on the interference of two beams. In addition, by modulating the pore diameter, either embedded waveguides or 3D photonic crystals with a hexagonal symmetry can be obtained.[35]

Porous Alumina

The feasibility of using monodomain porous alumina as a 2D photonic-bandgap material has been predicted theoretically. Calculations show that perfectly hexagonal ordered porous alumina exhibits only a photonic bandgap for TE polarized light due to the low refractive index ($n \approx 1.7$). Figure 6 shows the calculated gap frequency range (hatched area) as a function of r/a. A maximum gap-width midgap frequency ratio of 11% is found for $r/a = 0.385$. For porous alumina, the interpore spacing that can be obtained is between 60 nm and 500 nm, leading to theoretical photonic bandgaps centered at wavelengths between 200 nm and 1300 nm, depending on the spacing. Note that the bandgap of alumina (corundum) is around 10 eV, while porous alumina has a lower bandgap due to its amorphous nature. Experimentally, however, absorption for wavelengths above 400 nm is negligible over the size of a photonic crystal. Masuda's group has recently shown transmission measurements through porous alumina photonic crystals with 200-nm and 500-nm interpore distances exhibiting photonic bandgaps around 600 nm[36] and 1300 nm[37] (see data points in Figure 4). Fabrication of more complicated integrated-optics structures seems to be difficult because lithographically defined defects (missing pores) cannot be protected during etching, as is the case for silicon.[38]

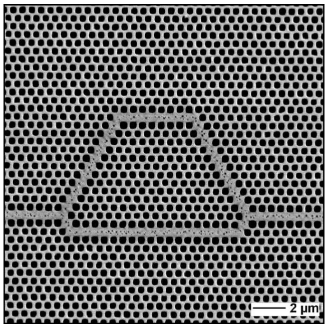

Figure 5. Top-view SEM image of a macroporous silicon photonic crystal with a lattice constant of 500 nm and an integrated two-dimensional Mach-Zehnder interferometer structure. The surface of the waveguide exhibits a small surface roughness.

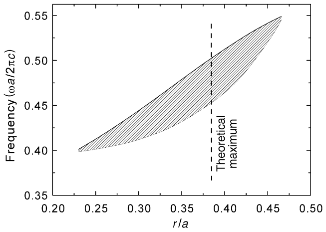

Figure 6. Bandgap map of porous alumina photonic crystals. The maximum gap for TE polarization is at r/a = *0.385 (11% gap midgap ratio). There is no gap for TM polarization in the triangular lattice. (Plane-wave expansion with 271 plane waves,* $\varepsilon = 2.92$.)

Summary

In the last 10 years, ordered pore arrays with high aspect ratios have been studied extensively. Ordered porous dielectric materials are *intrinsically* 2D photonic crystals. Although there are a large variety of materials exhibiting pores, to date only silicon and alumina exhibit the extremely high pore quality required in photonic-crystal applications. Over the last five years, the potential of macroporous silicon as an infrared photonic crystal has been described in numerous publications. Porous alumina is a favorable candidate for photonic crystals operating in the visible range.

Acknowledgments

The authors are indebted to Dr. F. Müller, Dr. A. Birner, Dr. A.P. Li, K. Nielsch, S. Matthias, Dr. K. Busch (Universität Karlsruhe) and Prof. W. Hergert (Martin-Luther-Universität, Halle) for collaboration and discussions in the area of photonic crystals. Concerning the experimental realization and characterization of the samples, the authors are grateful to Infineon Technologies and the Universities of Kiel, Konstanz, and Toronto. Special thanks go to Dr. R. Hillebrand for fruitful discussions and calculation of the bandgap map for porous alumina (Figure 6) and Prof. U. Gösele for substantially supporting the photonic-crystal activity.

References

1. For a comprehensive introduction, see J.D. Joannopoulos, R.D. Meade, and J.N. Winn, *Photonic Crystals* (Princeton University Press, New Jersey, 1995).
2. A. Uhlir, *Bell Sys. Tech. J.* **35** (1956) p. 333.
3. F. Keller, M.S. Hunter, and D.L. Robinson, *J. Electrochem. Soc.* **100** (1953) p. 411.
4. H. Masuda and K. Fukuda, *Science* **268** (1995) p. 1466.
5. A.-P. Li, F. Müller, and U. Gösele, *Electrochem. Solid-State Lett.* **3** (2000) p. 131.
6. H. Masuda, K. Yada, and A. Osaka, *Jpn. J. Appl. Phys., Part 2: Lett.* **37** (1998) p. L1340.
7. V. Lehmann and H. Föll, *J. Electrochem. Soc.* **137** (1990) p. 653.
8. V. Lehmann and U. Gösele, *Appl. Phys. Lett.* **58** (1991) p. 856.
9. J.-N. Chazalviel, R.B. Wehrspohn, and F. Ozanam, *Mater. Sci. Eng., B* **69–70** (2000) p. 1.
10. S. Langa, I.M. Tiginyanu, J. Carstensen, M. Christophersen, and H. Föll, *Electrochem. Solid-State Lett.* **3** (2000) p. 514.
11. P. Allongue, in *INSPEC Data Series,* edited by L. Canham (Institution of Electrical Engineers, London, 1997) p. 3.
12. R.L. Smith and S.D. Collins, *J. Appl. Phys.* **71** (1992) p. R1 and references therein.

13. R.B. Wehrspohn, J.-N. Chazalviel, F. Ozanam, and I. Solomon, *Phys. Rev. Lett.* **77** (1996) p. 1885.
14. R.B. Wehrspohn, J.-N. Chazalviel, F. Ozanam, and I. Solomon, *Thin Solid Films* **297** (1997) p. 5.
15. E.K. Propst and P.A. Kohl, *J. Electrochem. Soc.* **141** (1994) p. 1006.
16. M.M. Rieger and P.A. Kohl, *J. Electrochem. Soc.* **142** (1995) p. 1490.
17. R.B. Wehrspohn, J.-N. Chazalviel, and F. Ozanam, *J. Electrochem. Soc.* **145** (1998) p. 2958.
18. R.B. Wehrspohn, J.-N. Chazalviel, and F. Ozanam, *J. Electrochem. Soc.* **146** (1999) p. 3309.
19. V. Lehmann, *J. Electrochem. Soc.* **140** (1993) p. 2836.
20. V. Lehmann, *J. Electrochem. Soc.* **146** (1999) p. 2968.
21. V.P. Parkhutik and V.I. Shershulsky, *J. Phys. D: Appl. Phys.* **25** (1992) p. 1258.
22. H. Masuda, F. Hasegwa, and S. Ono, *J. Electrochem. Soc.* **144** (1997) p. L127.
23. F. Li, L. Zhang, and R.M. Metzger, *Chem. Mater.* **10** (1998) p. 2470.
24. A.P. Li, F. Müller, A. Birner, K. Nielsch, and U. Gösele, *J. Vac. Sci. Technol., A* **17** (1999) p. 1428.
25. H. Masuda, H. Asoh, M. Watanabe, K. Nishio, M. Nakao, and T. Tamamura, *Adv. Mater.* **13** (2001) p. 189.
26. A. Birner, R.B. Wehrspohn, U. Gösele, and K. Busch, *Adv. Mater.* **13** (2001) p. 377 and references therein.
27. A. Birner, A.-P. Li, F. Müller, U. Gösele, P. Kramper, V. Sandoghdar, J. Mlynek, K. Busch, and V. Lehmann, *Mater. Sci. Semicond. Proc.* **3** (2000) p. 487.
28. J. Schilling, A. Birner, F. Müller, R.B. Wehrspohn, R. Hillebrand, U. Gösele, K. Busch, S. John, S.W. Leonard, and H.M. van Driel, *Opt. Mater.* **17** (2001) p. 7.
29. U. Grüning, V. Lehmann, and C.M. Engelhardt, *Appl. Phys. Lett.* **66** (1995) p. 3254.
30. U. Grüning, V. Lehmann, S. Ottow, and K. Busch, *Appl. Phys. Lett.* **68** (1996) p. 747.
31. A. Birner, U. Grüning, S. Ottow, A. Schneider, F. Müller, V. Lehmann, H. Föll, and U. Gösele, *Phys. Status Solidi A* **165** (1998) p. 111.
32. S. Rowson, A. Chelnokov, C. Cuisin, and J.-M. Lourtioz, in *Proc. IEEE-Optoelectron*, Vol. 145 (Institute of Electrical and Electronics Engineers, Piscataway, NJ, 1998) p. 403.
33. S.-Y. Lin, E. Chow, V. Hietala, P.R. Villeneuve, and J.D. Joannopoulos, *Science* **282** (1998) p. 274.
34. S.W. Leonard, H.M. van Driel, A. Birner, U. Gösele, and P.R. Villeneuve, *Opt. Lett.* **25** (2000) p.1550.
35. J. Schilling, F. Müller, S. Matthias, R.B. Wehrspohn, and U. Gösele, *Appl. Phys. Lett.* **78** (2001) p. 1180.
36. H. Masuda, M. Ohya, H. Asoh, M. Nakao, M. Nohtomi, and T. Tamamura, *Jpn. J. Appl. Phys., Part 2: Lett.* **38** (1999) p. L1405.
37. H. Masuda, M. Ohya, K. Nishio, H. Asoh, M. Nakao, M. Nohtomi, A. Yokoo, and T. Tamamura, *Jpn. J. Appl. Phys., Part 2: Lett.* **39** (2000) p. L1039.
38. H. Masuda, M. Yotsuya, M. Asana, K. Nishio, M. Nakao, A. Yokoo, and T. Tamamura, *Appl. Phys. Lett.* **78** (2001) p. 826. □

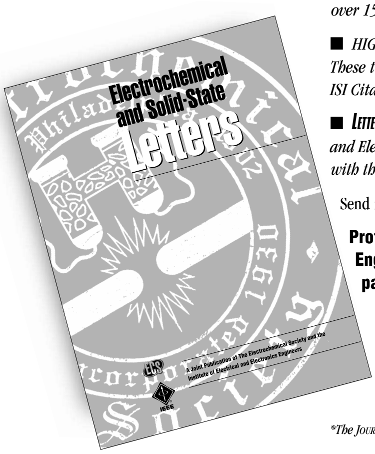

JOSA

Institute of Physics Publishing Journal of Optics A: Pure and Applied Optics
J. Opt. A: Pure Appl. Opt. **3** (2001) S121–S132 PII: S1464-4258(01)26774-9

A model system for two-dimensional and three-dimensional photonic crystals: macroporous silicon

J Schilling[1], R B Wehrspohn[1], A Birner[1,2], F Müller[1], R Hillebrand[1], U Gösele[1], S W Leonard[3], J P Mondia[3], F Genereux[3], H M van Driel[3], P Kramper[4], V Sandoghdar[4] and K Busch[5]

[1] Max Planck Institut für Mikrostrukturphysik, Weinberg 2, D-06120 Halle, Germany
[2] Infineon Technologies, Memory Products, D-01099 Dresden, Germany
[3] Department of Physics, University of Toronto, 60 St George Street, Toronto, Ontario, Canada M5S 1A7
[4] Universität Konstanz, Fachbereich Physik, Fach M696, D-78457 Konstanz, Germany
[5] Institut für Theorie der Kondensierten Materie, Universität Karlsruhe, D-76128 Karlsruhe, Germany

Received 11 July 2001
Published 26 October 2001
Online at stacks.iop.org/JOptA/3/S121

Abstract
A review of the optical properties of two-dimensional and three-dimensional photonic crystals based on macroporous silicon is given. As macroporous silicon provides structures with aspect ratios exceeding 100, it can be considered to be an ideal two-dimensional photonic crystal. Most of the features of the photonic dispersion relation have been experimentally determined and were compared to theoretical calculations. This includes transmission and reflection of finite and bulk photonic crystals and their variation with the pore radius to determine the gap map. All measurements have been carried out for both polarizations separately since they decouple in two-dimensional photonic crystals. Moreover, by inhibiting the growth of selected pores, point and line defects were realized and the corresponding high-Q microcavity resonances as well as waveguiding properties were studied via transmission. The tunability of the bandgap was demonstrated by changing the refractive index inside the pores caused by an infiltrated liquid crystal undergoing a temperature-induced phase transition. Finally different realizations of three-dimensional photonic crystals using macroporous silicon are discussed. In all cases an excellent agreement between experimental results and theory is observed.

Keywords: Photonic crystal, two-dimensional, three-dimensional, macropores, macroporous silicon, birefringence, defects, tunability

From the beginning of research on photonic crystals, a major area of investigation concerned two-dimensional photonic crystals [1]. This was mainly caused by experimental reasons as the fabrication of three-dimensional photonic crystals appeared to be more difficult and cumbersome than that of two-dimensional photonic crystals. Additionally the calculation of bandstructures for two-dimensional photonic crystals is less time consuming and a lot of interesting phenomena (e.g. light localization; at least in a plane) can already be studied in two-dimensional photonic crystals.

However, an ideal two-dimensional photonic crystal consists of a periodic array of infinitely long pores or rods so that the fabrication of a structure which approximates this theoretical model has to exhibit very high aspect ratios (ratio between pore/rod length to pore/rod diameter). Using conventional dry etching techniques only structures with aspect

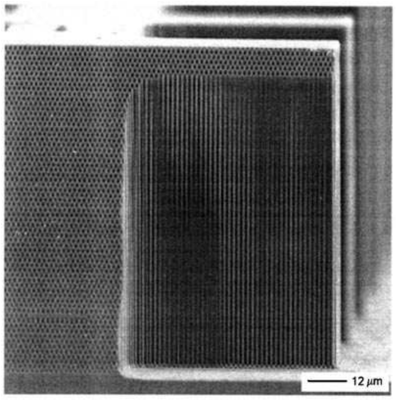

Figure 1. SEM image of a two-dimensional triangular lattice of macropores in silicon with a lattice constant of 1.5 μm. As the pore depth amounts to 100 μm the aspect ratio is $\sim$100. The bevelled etch in front reveals the high uniformity of the structure from the top down to the pore tips.

ratios up to 10–20 are possible. To avoid scattering of light out of the plane of periodicity and to reduce the corresponding loss the so-called slab structures were developed and thoroughly investigated [2, 3]. In such low-aspect structures, one relies on guiding of light in the third dimension and, consequently, deals with a full three-dimensional problem. On the other hand Lehmann and Grüning [4, 5] as well as Lau and Parker [6] proposed macroporous silicon as a model system for two-dimensional photonic crystals. This system consists of a periodic array of air pores in silicon. The pores are etched in hydrofluoric acid applying a photo-electrochemical dissolution process [7, 8]. Using lithographic prestructuring the nucleation spots of the pores can be defined at the surface of the n-type silicon wafer. This also allows the pore pattern and its lattice constant to be controlled over the range from 8 μm down to 0.5 μm. During the etching process the back of the wafer must be illuminated to create electronic holes in the silicon which are consumed during the etching process. Due to electrochemical passivation of the pore walls very high aspect ratios of 100–500 are obtained. As the fundamental bandgap appears in general for wavelengths which are approximately twice the lattice constant, the pores are 50–250 times longer than the wavelengths of the corresponding two-dimensional fundamental bandgap. Therefore, macroporous silicon represents an excellent system to study ideal two-dimensional photonic crystal properties.

In figure 1(*a*) a structure with a triangular two-dimensional pore lattice with a lattice constant of 1.5 μm is shown. The pore depth is 100 μm and the bevelled edge reveals the high uniformity of the pores down to the pore tips.

In the next paragraphs optical experiments performed with such structures are presented and compared with calculations assuming a two-dimensional array of infinitely long macropores. The lattice type, lattice constant and the pore depth of the investigated structures have the same values as the sample shown in figure 1 while the diameter of the pores varies in order to meet the experimental requirements.

1. Two-dimensional photonic crystals based on macroporous silicon

The dispersion relation for light propagation inside a photonic crystal is calculated using the plane-wave method. Due to the two-dimensional periodicity and the uniformity along the third dimension the light propagating in a two-dimensional photonic crystal splits into E-polarized (E-field parallel to the pore axis) and H-polarized (H-field parallel to the pore-axis) waves. The bandstructures for these polarizations differ from each other and so do the bandgaps in width and spectral position. This originates in the different field distributions: typically, the electric field of the H-polarized waves is located in the veins of the structures whereas the electric field of the E-polarized waves concentrates in the connection points of the veins. Figure 2(*a*) shows an example of a bandstructure for our system calculated for wavevectors in the first Brillouin zone along the path Γ-M-K-Γ. The assumed porosity or air filling factor is $p = 0.73$ which corresponds to $r/a = 0.45$ ($r =$ pore radius, $a =$ lattice constant) and the refractive index of silicon in the infrared (IR) is 3.4. For a triangular array of pores, a refractive-index contrast exceeding 2.7 [9] and suitable r/a ratios the bandgaps for E- and H-polarization overlap and a complete two-dimensional photonic bandgap exists. As the refractive-index contrast for air pores in silicon amounts to $\varepsilon_{\mathrm{Si}}/\varepsilon_{\mathrm{Air}} = 3.4$ in the IR, these requirements are fulfilled in our system. The bandstructure shown in figure 2 thus exhibits such a complete bandgap indicated by a grey bar.

In addition to the bandstructure, the density of photonic states (DOS) is computed as well and presented in figure 2(*b*). In the spectral region of the complete photonic bandgap the DOS is zero, such that propagation of light in the plane of periodicity with these frequencies is completely forbidden in the photonic crystal.

To verify these theoretical calculations, transmission measurements through bars of the macroporous silicon photonic crystals along Γ-M and Γ-K directions were carried out. For this purpose bars containing 13 pore rows were cut out using a second lithographic step. The measurements were performed using a Fourier transform infrared spectrometer (FTIR) in the spectral range between 700 and 7000 cm^{-1} (14.3 and 1.43 μm). Figure 3 shows the measured spectra for both directions and both polarizations. They are compared to transmission calculations using the method developed by Sakoda [10]. The spectral positions of regions with vanishing transmission correspond well to the calculated spectrum. For the measurements along the Γ-M direction they can be attributed to the bandgaps already discussed in figure 2 for H-polarized and E-polarized light. However, the vanishing transmission in the range of 2200–3500 cm^{-1} for propagation along the Γ-K direction of E-polarized light cannot entirely be explained through a stopband. A comparison with the bandstructure of figure 2 predicts a photonic band which covers part of this spectral region. However, as was pointed out earlier [11, 12] bands in which the experimentally incident plane wave cannot couple also lead to zero transmission. These bands correspond to Bloch modes whose field distributions are antisymmetric with respect to the plane spanned by the pore axis and the direction of incidence. Consequently, although modes do exist in the photonic crystal they need not to be

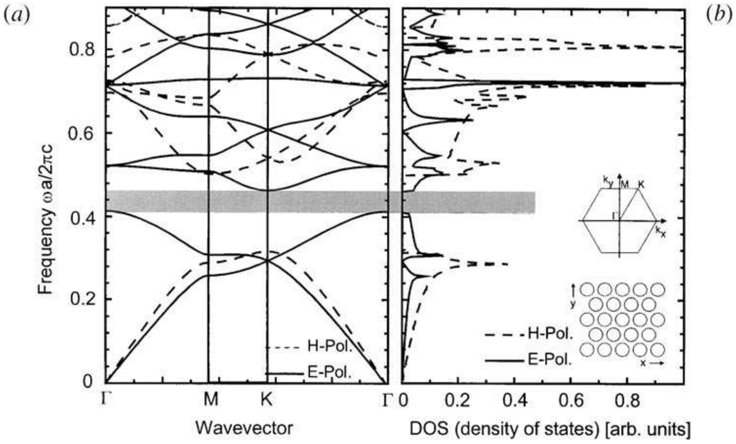

Figure 2. (*a*) Two-dimensional bandstructure of a triangular macroporous silicon photonic crystal ($r/a = 0.45$). (*b*) DOS, inset: two-dimensional hexagonal Brillouin zone and appropriate oriented triangular pore lattice in real space. The grey bar indicates the two-dimensional complete bandgap. In this spectral range neither H- nor E-polarized photonic states exist (DOS = 0).

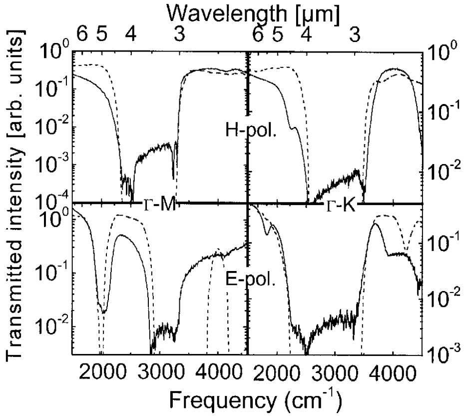

Figure 3. Transmission measurements (solid curve) and calculation (dashed curve) for penetration of a two-dimensional macroporous silicon photonic crystal bar containing 13 pore rows. Transmission for both polarizations (H- and E-polarization) along both high-symmetry directions, Γ-M and Γ-K, are shown.

visible in transmission. Therefore, care has to be taken when directly comparing reflection or transmission measurements with bandstructures: although a bandgap leads always to total reflection/zero transmission, a spectral region exhibiting total reflection/zero transmission does not necessarily coincide with a bandgap. A direct comparison of experiment and theory is therefore rather based on reflection/transmission calculations than on bandstructure calculations alone. In addition to the applied Sakoda method, mainly transfer-matrix and finite difference time domain (FDTD) methods can be used for the calculation of reflection and transmission.

The complete bandgap derived from the bandstructure calculations comprises the interval between 2900 and 3300 cm^{-1} (3.44 and 3.03 μm). It clearly overlaps with all spectral regions with vanishing transmission.

The optimum bandgap cannot be understood by Bragg scattering only. For scatterers whose spatial dimensions are comparable to the wavelength, additional scattering resonances (known as Mie resonances for spherical particles) appear. They depend on the size and shape of the scatterers. Consequently, apart from symmetry, lattice constant and refractive index, the radius of the pores (r/a-ratio) has an influence on the existence, position and the width of the photonic bandgaps. A graphic representation of the relationship between gap frequencies and filling ratio is known as a gap map, which for our structure, has been calculated before [1]. To verify this gap map experimentally, transmission measurements for 17 different samples spanning a wide range of r/a-ratios were carried out. The bandedges were determined from these measurements and are compared with the theoretical predictions in figure 4. The overall correspondence is very good. For lower r/a-ratios only a bandgap for the H-polarization exists. A complete bandgap only appears for $r/a > 0.4$ as then an E-bandgap appears which overlaps with the H-bandgap. With increasing r/a-ratios the E-bandgap widens while the H-bandgap shrinks for very high filling ratios. A maximum complete bandgap of $\Delta\omega/\omega = 16\%$ for $r/a = 0.48$ can be deduced. This relatively large complete bandgap is a consequence of the strong refractive-index contrast between the silicon (pore walls) and air (inside the pores) as well as the synergetic interplay of Mie resonance and Bragg scattering resonance.

Strictly speaking, the bandstructure calculations can only be performed assuming an infinitely extended photonic crystal. Therefore also the bandgap (zero DOS) causing perfect total reflection only appears for infinite bulk photonic crystals. For a very thin slab of the photonic crystal the incident

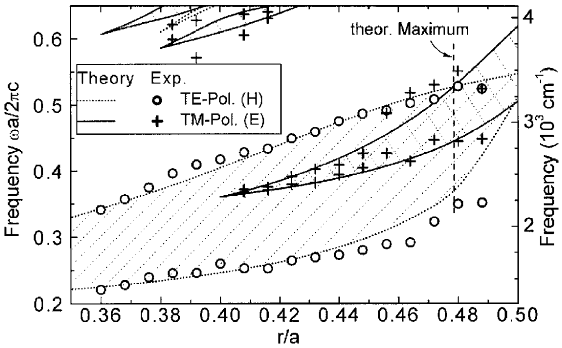

Figure 4. Position of the bandgaps for H-polarized light (dotted curve) and E-polarized light (solid curve) for a two-dimensional triangular macroporous silicon photonic crystal depending on the r/a-ratio (gap map). A complete bandgap appears as an overlap of the gaps for both polarizations and attains its maximum size with a r/a-ratio of 0.48.

light of a frequency within the bulk bandgap is no longer *totally* reflected. A certain amount can penetrate the thin photonic crystal. To investigate this effect four samples containing one, two, three and four crystal rows with a r/a-ratio of 0.453 were fabricated (figure 5(*a*)). Transmission measurements for H-polarized light of different wavelengths along Γ-K were performed (see figure 2) [13]. A tunable laser set-up was used which covered the spectral range between $3 < \lambda < 5$ μm corresponding to the range of the H-bandgap ($3.1 < \lambda < 5.5$ μm) of the corresponding bulk photonic crystal. The experimental results were compared with transmission calculations applying the already mentioned Sakoda method with 4000 plane waves and revealed a very good agreement (figure 5(*b*)). Plotting the transmittance versus the penetrated crystal thickness (figure 5(*c*)) an exponential decay is observed. This corresponds to the expectation that for frequencies within the bandgap the light penetrating into the bulk photonic crystal is exponentially damped. The slope of the line in the logarithmic plot corresponds to a decay constant of 10 dB per crystal row for light with a wavelength near the centre of the bandgap. Even for a bar containing only one pore row the bandgap is already perceptible. This originates in the strong scattering of the single pores due to the large refractive-index contrast between air pores and silicon walls.

In the initial investigations into photonic crystals mostly photonic bandgap properties were studied. However, over the last few years attention has also been drawn to other spectral regions of the dispersion relation that exhibit remarkable properties.

For instance, we recently investigated the birefringence of a two-dimensional macroporous silicon photonic crystal in the spectral region below the first bandgap. From theoretical investigations [14, 15] it was expected that a triangular two-dimensional photonic crystal shows uniaxial properties for $\omega \to 0$. The optical axis coincides in this case with the pore/rod axis. For light propagating in this direction the effective refractive index is independent of the polarization direction (birefringence = 0). However for light propagating in the plane of periodicity the two-dimensional bandstructure reveals different slopes of the E- and H-polarized bands due to different mode distributions in the silicon matrix. This corresponds to different effective refractive indices for these two different polarizations and leads to birefringent behaviour of light propagation perpendicular to the pore axis. We investigated this effect experimentally in transmission using an FTIR spectrometer. The sample consisted of a macroporous silicon crystal with a lattice constant $a = 1.5$ μm and r/a-ratio of 0.429. The transmission along the Γ-M direction through a bar of 235 μm width containing 181 pore rows was measured [16]. In front of the sample a polarizer was placed and aligned with an angle of 45° relative to the pore axis. This defined a certain polarization state of the light incident on the photonic crystal and assured that the radiation consisted of H- and E-polarized components of comparable strengths. After penetration through the sample the beam passes through a second polarizer which is aligned parallel or perpendicular to the first polarizer, respectively. The measured transmission for parallel and crossed polarizers is shown in figure 6. A periodic variation of the transmitted intensity is observed for both polarizer set-ups. The maxima of the parallel polarizer orientation corresponds to the minima of the crossed orientation. This can be explained considering the phase difference which builds up between E- and H-polarized light after penetration through the photonic crystal. This phase difference is given by $\Delta\phi = 2\pi \Delta n_{\mathrm{eff}} df/c$ (Δn_{eff} difference of effective refractive indices, d thickness of penetrated photonic crystal, f light frequency). For parallel orientations of the polarizers a maximum occurs for $\Delta\phi = 2m\pi$ while a minimum appears for $\Delta\phi = (2m+1)\pi$. For the crossed polarizers the opposite is true. The light frequency and the order of the maxima and minima are determined from the transmission curve and with this the birefringence Δn_{eff} can be calculated. It is frequency dependent (figure 7). However, over the entire investigated spectral range its value exceeds 0.3 and attains its maximum at the upper limit of the investigated range (at the lower bandedge of the first E-gap). The largest birefringence measured amounts to 0.366 at a frequency $f = 0.209c/a$. With this it is by a factor of 43 larger than the birefringence of quartz.

The uniaxial behaviour of the triangular two-dimensional photonic crystal in the limit $\omega \to 0$ corresponds to the well

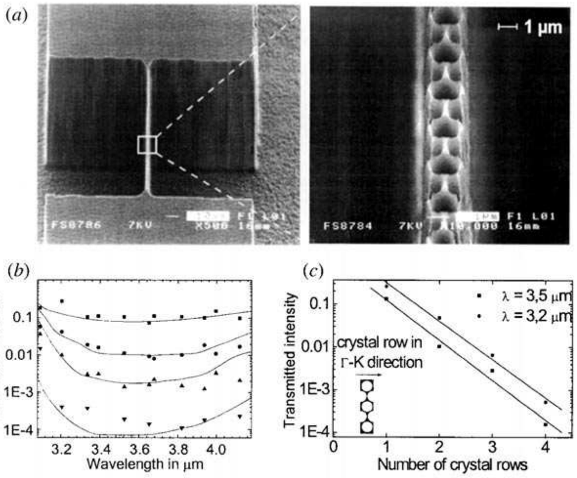

Figure 5. (*a*) SEM image of the macroporous silicon bars with varying thickness. The inset shows an enlarged view of the centre square. (*b*) Measured and calculated transmission for wavelengths within the H-bandgap. Solid curves, calculations for transmission through one, two, three and four crystal rows. Points: measurements for 0.89 ± 0.04 (■), 1.8 ± 0.1 (●), 2.9 ± 0.1 (▲) and 4.2 ± 0.2 (▼) crystal rows. (*c*) Measured transmission as a function of slab thickness for two wavelengths within the bandgap.

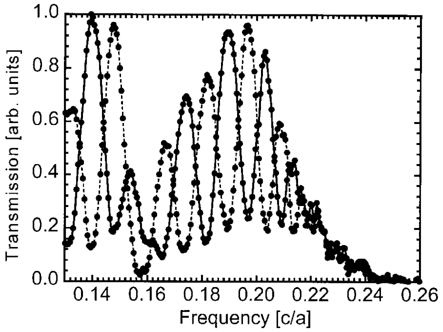

Figure 6. Effect of birefringence: measured transmission in the spectral range below the first bandgap (long wavelength regime). Spectra were recorded for parallel (solid curves) and crossed (dashed curves) orientations of the two polarizers which were placed in front and behind the sample, respectively. The periodic maxima and minima in the transmission spectrum appear due to the phase difference between E- and H-polarized waves accumulating during penetration of the sample.

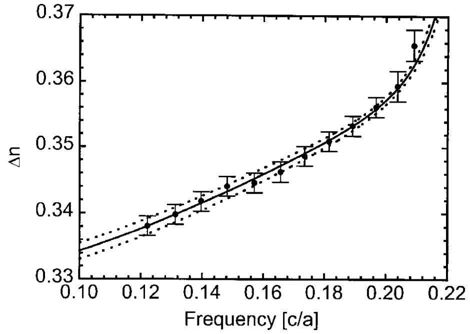

Figure 7. Spectral dependence of birefringence (Δn). Measurements (data points) and calculations (curves). The dashed curves represent the calculated dependence for the upper and lower bounds of the measured value of r/a (0.429 ± 0.002). The largest measured birefringence ($\Delta n = 0.365$) appears near the upper limit of the investigated spectral range close to the bandedge for E-polarization.

known uniaxial birefringence of hexagonal atomic crystals in the visible region. In atomic crystals the scatterers (atoms) have distances in the region of Å and therefore Bragg diffraction occurs for wavelengths in the x-ray region. For these classic atomic crystals the visible region of the spectrum corresponds to the long wavelength limit $\omega \to 0$. In our case, where the lattice constant is of the order of 1 μm, Bragg diffraction occurs in the near and mid IR (causing the bandgaps) while the limit $\omega \to 0$ comprises the long wavelength regions of the mid and far IR.

In the described experiment only the birefringence along one propagation direction in the plane of periodicity was investigated. For the case of a uniaxial crystal this is sufficient, as the birefringence is constant for all propagation directions perpendicular to the optical axis. However, for increasing light frequencies which approach the first bandgap this is no longer true. In this case the value of the birefringence depends on the direction of propagation in the Γ-M-K plane and the optical properties of the crystal can no longer be described by the terms 'uniaxial' or 'biaxial' used in classic crystal optics [17].

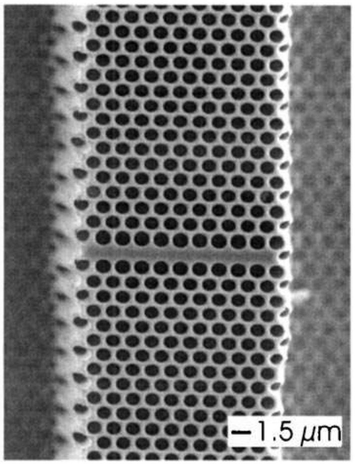

Figure 8. SEM image of a two-dimensional macroporous silicon bar containing a line defect introduced by skipping a line of pore nucleation spots defined by lithography.

2. Defects in two-dimensional macroporous silicon photonic crystals

Since the beginning of the study of photonic crystals special attention was paid to intentional incorporated defects in these crystals. Point or line defects can be introduced into macroporous two-dimensional silicon photonic crystals by omitting the growth of a single pore or a line of pores. This can be achieved by designing a suitable mask for the lithography (the pattern defining process). To demonstrate waveguiding through a linear defect we incorporated a 27 μm line defect along the Γ-K direction into a triangular two-dimensional photonic crystal with a r/a ratio of 0.43 (r = 0.64 μm) [18]. However, due to the photo-electrochemical fabrication process the diameter of the pores in the adjacent rows to the waveguide is increased. Figure 8 shows a picture of a similar structure. The transmission through the line defect was measured with a pulsed laser source having a bandwidth of 200 nm and tunable over the whole width of the H-stopband in the Γ-K direction ($3.1 < \lambda < 5.5$ μm). The measured spectrum (figure 9) exhibits pronounced Fabry–Perot resonances over a large spectral range which are caused by multiple reflections at the waveguide facets. Comparing the spectrum with a FDTD-transmission calculation reveals very good agreement and the comparable finesse of the measured and calculated resonances indicate small losses in the sample. A bandstructure calculation for H-polarization along Γ-K including waveguide modes is depicted in figure 10. The grey-shaded regions represent all possible modes inside the perfect crystal areas adjacent to the line defect. Defect modes bound to the line defect, therefore, occur only in the range $0.27 < f < 0.46$. They split into even and odd modes with respect to the mirror plane which is spanned by the waveguide direction and the direction of the pore axis. As the incoming wave can be approximated by a plane wave, the incident radiation can only couple to the even modes of the waveguide. The odd modes do not contribute to the transmission through the waveguide and, therefore, in this experiment transmission is solely connected with the even modes. The small stopband between the even modes around a frequency of 0.45 is reproduced as a region of vanishing transmission in figure 9 due to anticrossing of the waveguide modes [19]. Furthermore, from the bandstructure it can be concluded that for $0.37 < f < 0.41$ c/a only a single even mode exists. Its bandwidth amounts to 10%.

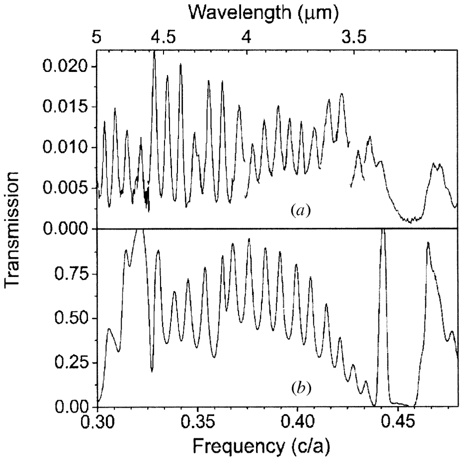

Figure 9. (*a*) Measured and (*b*) calculated H-polarized transmission spectrum of a 27 μm-long waveguide directed along Γ-K covering the spectral range of the H-bandgap of the surrounding perfect photonic crystal. Only the *even* waveguide modes contribute to the transmission as the incoming plane wave cannot be coupled to the *odd* waveguide modes. The small stopgap at a frequency of 0.45 c/a is caused by the anticrossing of two even waveguide modes.

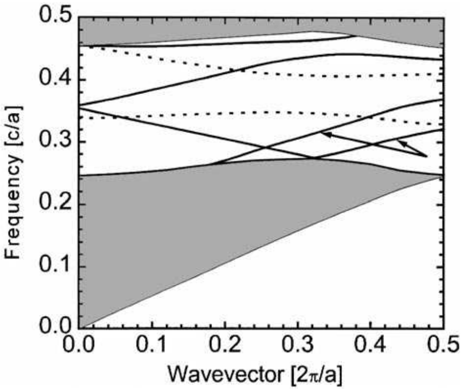

Figure 10. Computed H-polarized bandstructure of the waveguide oriented along Γ-K. Solid and dotted curves correspond to even and odd modes, respectively. The two bands which are labelled with arrows appear due to the overetched pores on either side of the waveguide. The shaded areas correspond to the modes available in the adjacent perfect crystal regions.

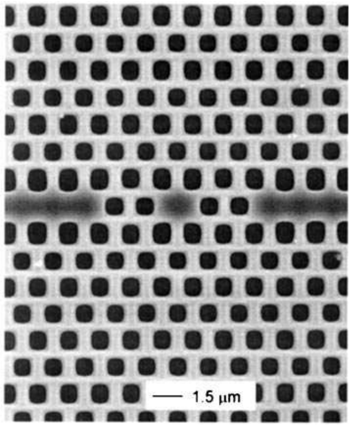

Figure 11. Top view of the photonic crystal region containing the waveguide–microresonator–waveguide structure. The r/a-ratio of the pores amounts to 0.433. The waveguides on the left and right serve to couple the light into the point defect (microresonator).

In addition to line defects point defects consisting of just one missing pore are also of special interest. Such a micro resonator-type defect also causes photonic states whose spectral positions lie in the range of the bandgap of the surrounding perfect photonic crystal. The lightfields belonging to these defect states are therefore confined to the very small volume of the point defect resulting in very high energy densities inside the defect volume. As the point defect can be considered as a microcavity surrounded by perfect reflecting walls, resonance peaks with very high Q-values are expected in the transmission spectra. To study this experimentally we fabricated a sample including a point defect which was placed between two line defects serving as waveguides for coupling light in and out [20]. Figure 11 shows a SEM image of the described sample with $r/a = 0.433$. Measuring transmission through this waveguide–microresonator–waveguide structure demands an optical source with a very narrow linewidth. Therefore, a continuous wave optical parametric oscillator (OPO) has been used which is tunable between 3.6 and 4 μm and delivers a laser beam of 100 kHz linewidth. For spatially resolved detection an uncoated tapered fluoride glass fibre mounted to a scanning nearfield optical microscope-head was applied and positioned precisely to the exit facet of the outcoupling photonic crystal waveguide. In the transmission spectrum two-point defect resonances at 3.616 and 3.843 μm could be observed (figure 12). Their spectral positions are in excellent agreement with the calculated values of 3.625 and 3.834 μm predicted by FDTD calculations taking into account the slightly widened pores surrounding the point defect. The measured point defect resonances exhibited Q values of 640 and 190, respectively. The differences to the theoretical predicted values of 1700, 750 could be caused by very small pore diameter variations (of the order of 1%) with the depth. A slight variation of the resonance frequency with pore depth and a scattering of light out of the plane of periodicity can be the consequences leading to a broadened averaged resonance peak. However, the reported high Q-values of this two-dimensional microresonator might already be sufficient for studying the modification of radiation properties of an emitter placed in such a point defect. Microcavities with even higher Q-values might be possible by increasing the number of pores to three or four which separate the point defect from the waveguides.

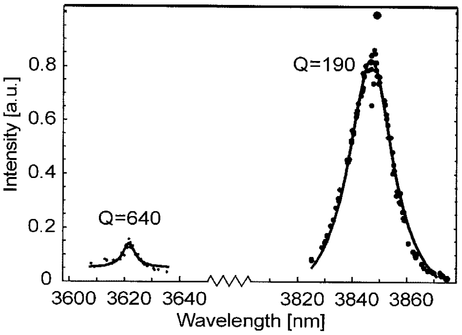

Figure 12. Measured monopole ($Q = 640$) and decapole resonances ($Q = 190$) of the point defect at wavelengths of 3.616 and 3.843 μm.

3. Technologically relevant structures

In the preceding paragraphs experiments were reported which demonstrate the properties of macroporous silicon for two-dimensional photonic crystals with bandgaps in the mid IR. Their high accuracy makes them a perfect model system to explore the concept of photonic crystals in the IR region. In addition to their physically interesting properties photonic crystals bear considerable potential for optical telecommunications (for instance, application of line defects for routing of light beams). For these applications photonic crystal waveguides have to work in a wavelength range between 1.3 and 1.5 μm so that they are compatible with the existing glass-fibre network. This fact requires photonic crystals with bandgaps in the corresponding spectral range. As is known from Maxwell's equations the spectral position of the bandgap scales linearly with the lattice constant of the photonic crystals. Therefore, structures with sub-micrometer dimensions are necessary. Although they should not show a novel physical behaviour, their fabrication is still an experimental challenge. We fabricated a triangular lattice with a pitch $a = 0.5$ μm and a r/a-ratio of 0.425. To check the spectral position of the first-order bandgap, reflection measurements were performed using an IR microscope connected to a FTIR spectrometer. The reflection for H- and E-polarized light incident in the Γ-M direction was measured separately. A gold mirror was used as a reference. Figure 13 shows a comparison of the measured reflection spectra with the bandstructure and with reflection calculations using a programme based on a transfer-matrix approach [21][6]. The grey-shaded spectral ranges represent the

---

[6] The program 'Translight' can be downloaded from http://www.elec.gla.ac.uk/~areynolds/software.html. It is based on the paper by Bell *et al* [21].

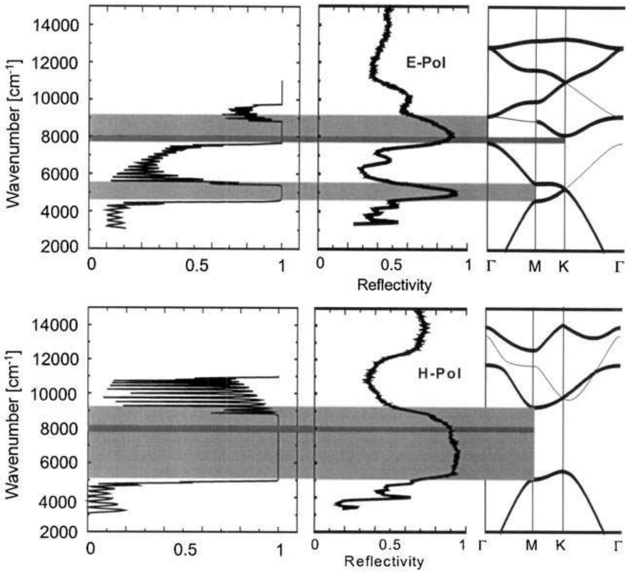

Figure 13. Reflectivity along Γ-M for a two-dimensional triangular macroporous silicon photonic crystal with a lattice constant of 0.5 μm for E-polarization (upper part) and H-polarization (lower part). Left, calculated reflectivity assuming a finite photonic crystal containing eight pores rows. The periodic Fabry–Perot resonances are caused by multiple reflections at the facets of the assumed thin bar. Middle, measured reflectivity of a semi-infinite photonic crystal. No resonances appear, as the second facet lies at infinity. Right, comparison with bandstructure. Thick bands contribute to transmission while for the thin bands the incident plane waves cannot couple. In addition to the bandgaps they also cause total reflection (grey-shaded regions). The dark-shaded range shows the complete bandgap around 8000 cm^{-1} (1.25 μm).

theoretically expected regions of high reflectivity stemming from the bandgaps. They correspond very well to the experimental results. The thick printed bands are transmission bands while the thin printed bands are bands in which a plane wave cannot couple into the photonic crystal slab. The reflection calculations were carried out assuming a finite bar of the photonic crystal containing eight layers. This finite thickness causes the Fabry–Perot interferences in the spectrum by multiple reflections at the front and back surface of the bar. However, in the experiment we investigated a semi-infinite photonic crystal. In this case the Fabry–Perot resonances are absent. Apart from this difference the calculated reflection curves agree very well with the measured ones and the spectral ranges of very high reflectivity caused by the bandgaps (ideal total reflection) coincide. Although the reflected light contained contributions from beams with an incidence angle of up to 30° (due to the focussing conditions of the microscope) this off-normal incidence has only a negligible effect. The incident light is bent by refraction towards the normal propagating with a much smaller angular deviation inside the photonic crystal. Additionally, the width and position of this first-order bandgap is not very sensitive for small angular deviations [22]. This is the reason why good agreement with the bandstructure along Γ-M and the calculation can be observed. From the calculated bandstructure a complete bandgap in the range 1.22–1.3 μm can be derived.

Together with the results of Rowson *et al* [23] who showed bandgaps at 1.5 μm this experiment proves that macroporous silicon structures can be fabricated and used as two-dimensional photonic crystals for the technologically interesting telecommunication wavelengths between 1.3 and 1.5 μm.

As was pointed out earlier the attenuation for light frequencies within the bandgap amounts to 10 dB per pore row. As Maxwell's equations scale with the structure size this relative property also remains unchanged for the downscaled structure. This enables a close packing of waveguides, as the separation of six to eight pore rows should be sufficient to avoid any cross-talk between neighbouring waveguides.

4. Tunability of photonic bandgaps

Small deviations of the fabricated experimental structures from the designed ones have a serious influence on their optical properties. In particular, the design of a microresonator (point defect) with a well defined resonance frequency in the near IR only allows fabrication tolerances in the sub-nanometre regime, a demand which currently cannot be fulfilled reproducibly. Additionally, for many applications, optical switches for example, one would like to shift the bandgap during operation. Therefore, tuning the optical properties during operation is a major point of interest.

One way to achieve this is to change the refractive index of at least one material inside the photonic crystal. This can be obtained by controlling the orientation of the optical anisotropy of one material incorporated in the photonic crystal [24].

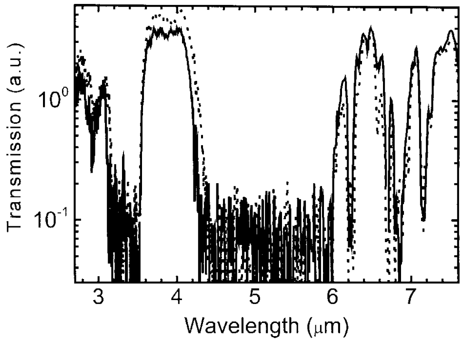

Figure 14. Shift in a bandedge caused by the thermally induced reorientation of an infiltrated liquid crystal: H-polarized transmission along Γ-K after infiltration of the liquid crystal E7. Solid curve, liquid crystal in its nematic phase (35 °C); dotted curve, liquid crystal in its isotropic phase (62 °C).

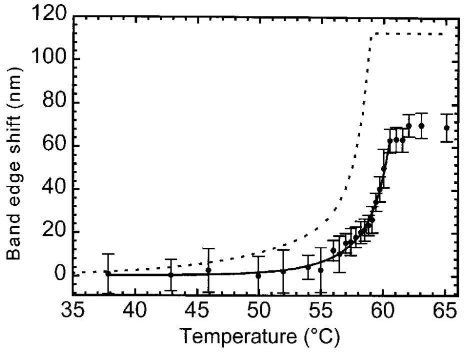

Figure 15. Temperature dependence of the bandedge shift caused by the temperature-induced phase transition of the infiltrated liquid crystal. Solid curve, fit to experimental data points; dashed curve, calculation assuming a simple axial alignment of the liquid crystal in the pores.

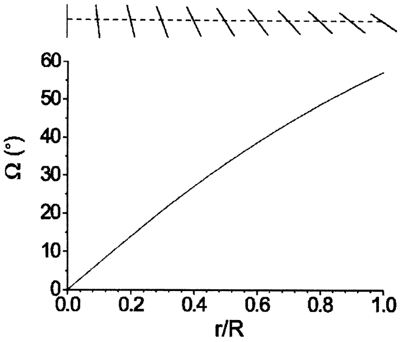

Figure 16. Alignment of the liquid crystal within a cylindrical pore in the case of ER configuration with a weak molecular anchoring strength of $W_\Theta = 1 \times 10^{-5}$ J m^{-2}. Bottom, radial dependence of the director angle Ω. Top, orientation of the director at discrete radial positions.

As proof of the latter we infiltrated a liquid crystal (E7 from EM Industries Inc.) into a two-dimensional triangular pore array with a pitch of 1.58 μm and observed the shift of a bandedge depending on the temperature. The liquid crystal E7 is in its nematic phase at room temperature but becomes isotropic at $T > 59$°C. The refractive index for light polarized along the director axis is $n_e = 1.69$ while it is only $n_0 = 1.49$ for perpendicular polarization exhibiting strong anisotropy.

The transmission of H-polarized light was measured along the Γ-K direction through a 200 μm-thick bar of the infiltrated photonic crystal. Figure 14 shows the transmission spectra obtained. At room temperature the first stopband of the H-polarization is observable in the range between 4.4 and 6 μm. Although a large bandgap for the H-polarization still exists, the complete bandgap, which is characteristic of the unfilled structure, is lost due to the lowered refractive-index contrast within the infiltrated crystal. Therefore the investigations were only carried out for H-polarization. When the structure is heated up, the upper band edge at 4.4 μm is red shifted while the lower bandedge exhibits no noticeable shift. At a temperature of 62°C the red shift saturates and the total shift amounts to $\Delta\lambda = 70$ nm as shown in figure 15. This corresponds to 3% of the bandgap width. The shift is caused by the change in orientation of the liquid-crystal molecules inside the pores. In a simplified model one can assume that all the liquid-crystal molecule directors line up parallel to the pore axis when the liquid crystal is in its nematic phase at room temperature. Then the H-polarized light sees the lower refractive index n_0 inside the pores. If the temperature is increased above 59°C a phase transition occurs and the liquid-crystal molecule directors are randomly oriented. The H-polarized light now reaches a refractive index inside the pores which is an average over all these orientations. According to this model a red shift of $\Delta\lambda = 113$ nm is expected which is considerable larger than that measured. However, the assumption of perfect axial alignment of all the directors is questionable. From free energy considerations the escaped-radial (ER) alignment (figure 16) is expected to be the thermodynamical stable configuration of the liquid-crystal molecules within the pores. In this case only the directors in the centre of the pore are axially aligned. The directors near the pore walls are inclined. The refractive-index change from this configuration to the isotropic phase is smaller and explains the smaller bandedge shift. Moreover, the lightfields of the modes at the higher bandedge ($\lambda = 4.4$ μm) are concentrated in the centre of the pores. They experience a strong refractive-index change caused by the phase transition as the initially axially-aligned directors in the pore centre switch to total random orientations. The field distribution of the modes at the lower bandedge are mainly concentrated in the silicon walls and, therefore, do not experience such a change in the refractive index so that the lower bandedge does not shift. Although the shifting or switching of a bandgap via temperature is not very practical, the present study confirms the possible tunability of photonic bandgaps using liquid crystals.

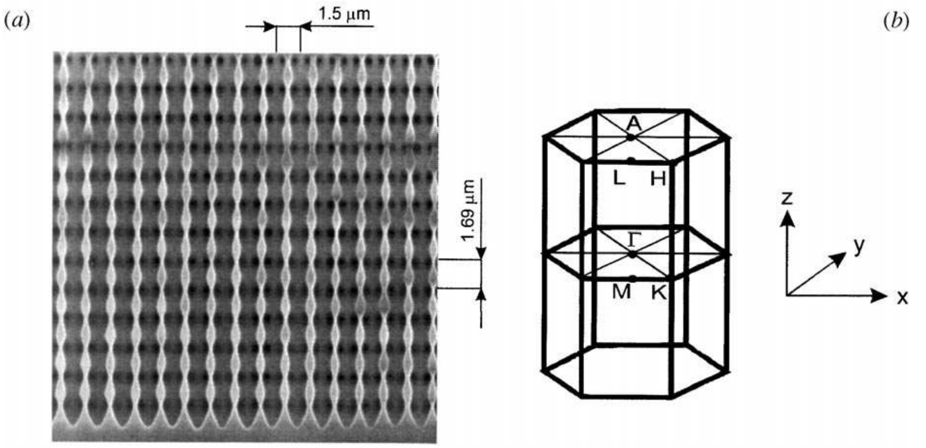

Figure 17. (*a*) SEM image showing a longitudinal section of the modulated pore structure. The variation in the pore diameter with depth can be modelled by a sinusoidal modulation $r = r_0 + \Delta r\ \sin(2\pi z/l_z)$ with $r_0 = 0.63\ \mu$m, $\Delta r = 0.08\ \mu$m and $l_z = 1.69\ \mu$m. (*b*) Hexagonal Brillouin zone showing the high-symmetry directions.

5. Three-dimensional photonic crystals based on macroporous silicon

Thus far, the main work based on macroporous silicon and photonic crystals concerned two-dimensional photonic crystals. Recently, however, attempts have been undertaken to use macroporous silicon for three-dimensional photonic crystals.

One approach for introducing a refractive-index variation in the third dimension is the modulation of the pore diameter with pore depth [25]. As described in the first paragraph of this review, the pore diameter of the macropores can be controlled during the fabrication process (photo-electrochemical etch process) by the intensity of the back illumination of the wafer. Strong illumination leads to high-etching currents and, therefore, wide pores while the opposite is valid for low illumination.

We now varied the illumination intensity periodically during the etch process applying a zig-zag profile. Figure 17(*a*) shows a SEM image of a longitudinal section of the sample. The pore diameter modulation can be well approximated by a sinusoidal dependence on the pore depth. The modulation period amounts to 1.69 μm and the porosity varies between 81 and 49% between the planes of wide- and narrow-pore diameters. The lattice constant a of the two-dimensional pore pattern is again 1.5 μm. The resulting three-dimensional photonic crystal has a hexagonal lattice and the corresponding Brillouin zone is also hexagonal (figure 17(*b*)). Note, that this is the first three-dimensional photonic crystal in the IR region which perfectly extends over more than 10 lattice periods. To investigate the optical properties of the structure introduced by the pore diameter modulation we performed transmission measurements along the pore axis which correspond to the Γ-A direction. The spectrum is shown in figure 18 and compared to a three-dimensional bandstructure calculation using the plane-wave method. For comparison with the experiment, the left side of the bandstructure shows the relevant dispersion relation along Γ-A. The stopgap in this direction caused by the periodic pore diameter modulation is indicated by a grey bar. This coincides well with the range of zero transmission between 1350 ($\lambda = 7.41\ \mu$m) and 1680 cm^{-1} ($\lambda = 5.95\ \mu$m) measured along the pores. Although the structure does not show a complete three-dimensional bandgap it has another distinct property: as it is not based on building blocks of a fixed shape (e.g. spheres or ellipsoids) the periodicity can be different for all directions. The modulation period along the pore axis (z-axis) can be independently controlled from the periodicity in the x–y-plane. Consequently, the dispersion relation along the pores can be adjusted nearly independently from the dispersion relation perpendicular to them.

Another approach to fabricating three-dimensional photonic crystals on the basis of macroporous silicon includes a two-step process [26]. In the first step a conventional two-dimensional array of straight pores is photo-electrochemically etched. Afterwards additional pores are drilled under oblique angles from the top using a focused ion beam (FIB). In this way a set of three different pore directions is established which cross each other depthwise. The fabricated structure is very similar to the well known Yablonovite structure for the microwave region. However, a complete three-dimensional bandgap is not yet shown since the angles between the three different pore sets have not been properly aligned. Although the depth of the structure is limited due to the FIB process, this method has the potential for the fabrication of a three-dimensional photonic crystal with a complete three-dimensional bandgap.

Another fabrication technique which should give a very similar result uses the photo-electrochemical etching of macropores on a (111)Si surface [27]. In contrast to the pore growth on a (100)Si surface in the case of a (111)Si surface the pores grow into ⟨113⟩ directions. As there are three equivalent ⟨113⟩ directions available from the (111) surface, three pores start to grow from each nucleation point

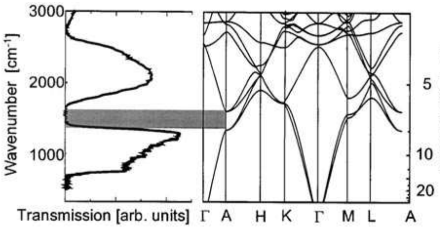

Figure 18. Transmission measured in the Γ-A direction (along the pore axis) and comparison with the calculated three-dimensional bandstructure. The grey bar indicates the stopgap for light propagation in this direction causing zero transmission.

at the surface. Bandstructure calculations for a corresponding structure show that the pores along the three ⟨113⟩ directions grow at suitable angles such that the structure should exhibit a three-dimensional complete photonic bandgap. Figure 19 shows an image of such a structure where the nucleation spots of the pores at the (111) surface are still randomly distributed. Therefore, this structure does not yet have the described long-range periodicity of crossing pores and exhibits no photonic bandgap. However, the crossing pores are clearly visible and the intended structure can be imagined.

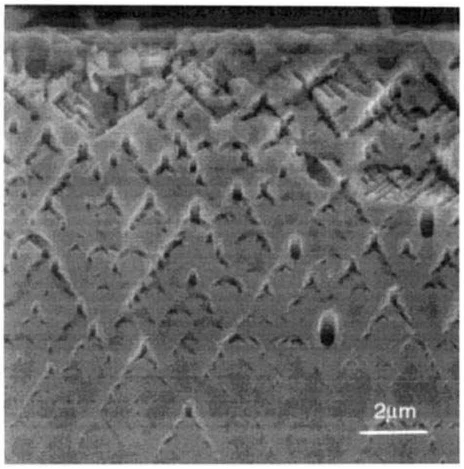

Figure 19. Crossing pores caused by the photo-electrochemical etching of a (111) n-type silicon surface. The nucleation spots of the pores at the (111) surface are random so that a strict periodic arrangement cannot yet be obtained.

6. Summary

In summary we have shown that macroporous silicon is a suitable material to fabricate ideal two-dimensional photonic crystals for the IR region. Due to the high-refractive-index contrast between silicon and air the bandgaps are large and for a triangular array of pores a complete bandgap for the light propagating in the plane of periodicity appears. Experimental investigations of such a structure for different porosities (r/a-values) confirms the calculated gap map and the maximum width of the complete bandgap of 16% for $r/a = 0.475$. The wide bandgap of the H-polarization causes a strong attenuation for light with frequencies within the gap. The corresponding field is exponentially damped and a damping constant of 10 dB per pore row could be experimentally determined. In addition to the bandgaps the long wavelength regime below the first bandgap was also investigated. Large birefringence was experimentally and theoretically studied and a maximum value of $\Delta n_{\text{eff}} = 0.366$ (difference between H- and E-polarization) was obtained which is by a factor of 43 larger than the birefringence of quartz. Due to the photolithographic prestructuring of the macroporous silicon, defects could intentionally be introduced. The transmission through a straight waveguide was investigated. After comparison of the experimental features with bandstructure calculations a single mode transmission in a spectral range with a bandwidth of 10% could be identified. Additionally, transmission measurements at a point defect have been performed. Two resonances with Q-values of 647 and 191 were found and comparison with theory reveals that they can be attributed to the monopol and decapol mode of the microresonator. To obtain bandgaps in the technologically interesting near-IR spectral region macroporous silicon two-dimensional photonic crystals with structure sizes of $a = 0.5\ \mu$m were fabricated. They exhibit bandgaps in the optical telecommunication window around $\lambda = 1.3\ \mu$m which was confirmed by reflection measurements.

Another issue, closely related to applications, is the tunability of photonic bandgaps. We demonstrated a red shift of an upper bandedge by 70 nm based on the refractive-index change due to the reorientation of liquid crystals infiltrated into the pores. The reorientation was initiated by the temperature change and corresponds to the phase transition of nematic → isotropic of the liquid crystal.

Finally, perfect extended three-dimensional photonic crystals based on macroporous silicon were presented. Transmission measurements on these three-dimensional photonic crystals with modulated pores showed good agreement with the full three-dimensional bandstructure calculations. Although these photonic crystals do not exhibit a complete three-dimensional bandgap the dispersion relation along the pores can almost independently be tuned compared to the dispersion relation perpendicular to it. In particular, one can imagine utilizing the mode structure of these photonic crystals to realize novel atom traps [28].

All these experiments show that macroporous silicon is an ideal material to study the properties of photonic crystals in the IR regime as well as for possible technological applications operating in this spectral range.

Acknowledgments

The authors gratefully acknowledge H Föll for helpful discussions and especially appreciate the fruitful cooperation with V Lehmann, P Villeneuve, M Agio, C Soukoulis and S John.

References

[1] Joannopoulos J D, Meade R D and Winn J N 1995 *Photonic Crystals* (Princeton, NJ: Princeton University Press)

[2] Johnson S G, Fan S, Villeneuve P R, Joannopoulos J D and Kolodziejski L A 1999 *Phys. Rev.* B **60** 5751

[3] Labilloy D, Benisty H, Weisbuch C, Krauss T F, De La Rue R M, Bardinal V, Houdré R, Oesterle U, Cassagne D and Jouanin C 1997 *Phys. Rev. Lett.* **79** 4147

[4] Grüning U, Lehmann V and Engelhardt C M 1995 *Appl. Phys. Lett.* **66** 3254

[5] Grüning U, Lehmann V, Ottow S and Busch K 1996 *Appl. Phys. Lett.* **68** 747

[6] Lau H W, Parker G J, Greef R and Hölling M 1995 *Appl. Phys. Lett.* **67** 1877

[7] Lehmann V and Föll H 1990 *J. Electrochem. Soc.* **137** 653

[8] Lehmann V 1993 *J. Electrochem. Soc.* **140** 2836

[9] Meade R D, Brommer K D, Rappe A M and Joannopoulos J D 1992 *Appl. Phys. Lett.* **61** 495

[10] Sakoda K 1995 *Phys. Rev.* B **52** 8992

[11] Robertson W M, Arjavalingam G, Meade R D, Brommer K D, Rappe A M and Joannopoulos J D 1992 *Appl. Phys. Lett.* **61** 495

[12] Sakoda K 1995 *Phys. Rev.* B **52** 7982

[13] Leonard S W, van Driel H M, Busch K, John S, Birner A, Li A-P, Müller F, Gösele U and Lehmann V 1999 *Appl. Phys. Lett.* **75** 3063

[14] Kirchner A, Busch K and Soukoulis C M 1998 *Phys. Rev.* B **57** 277

[15] Halevi P, Krokhin A A and Arriaga J 1999 *Appl. Phys. Lett.* **75** 2725

[16] Genereux F, Leonard S W, van Driel H M, Birner A and Gösele U 2001 *Phys. Rev.* B **63** 161101(R)

[17] Netti M C, Harris A, Baumberg J J, Whittaker D M, Charlton M B D, Zoorob M E and Parker G J 2001 *Phys. Rev. Lett.* **86** 1526

[18] Leonard S W, van Driel H M, Birner A, Gösele U and Villeneuve P R 2000 *Opt. Lett.* **25** 1550

[19] Benisty H, Olivier S, Rattier M and Weisbuch C 2001 *Photonic Crystals and Light Localization in the 21st Century* (New York: Kluwer Academic) pp 117–28

[20] Kramper P, Birner A, Agio M, Soukoulis C, Gösele U, Mlynek J and Sandoghdar V *Phys. Rev.* B to be published

[21] Bell P M, Pendry J B, Martin Moreno L and Ward A J 1995 *Comput. Phys. Commun.* **85** 306

[22] Rowson S, Chelnokov A, Cuisin C and Lourtioz J-M 1999 *J. Opt. A: Pure Appl. Opt.* **1** 483

[23] Rowson S, Chelnokov A and Lourtioz J-M 1999 *Electron. Lett.* **35** 753

[24] Busch K and John S 1999 *Phys. Rev. Lett.* **83** 967

[25] Schilling J, Müller F, Matthias S, Wehrspohn R B and Gösele U 2001 *Appl. Phys. Lett.* **78** 1180

[26] Chelnokov A, Wang K, Rowson S, Garoche P and Lourtioz J-M 2000 *Appl. Phys. Lett.* **77** 2943

[27] Christophersen M, Carstensen J, Feuerhake A and Föll H 2000 *Mater. Sci. Eng.* B **69–70** 194

[28] Toader O, John S and Busch K 2001 *Opt. Exp.* **8** 217

IEEE JOURNAL OF QUANTUM ELECTRONICS, VOL. 38, NO. 7, JULY 2002 805

Silicon-Based Photonic Crystal Slabs: Two Concepts

Cécile Jamois, Ralf B. Wehrspohn, Jörg Schilling, Frank Müller, Reinald Hillebrand, and Wolfram Hergert

***Abstract*—We compare theoretically two different concepts of vertical light confinement in two-dimensional (2-D) silicon photonic crystals. Light guidance obtained by variation of the refractive index in an SiO_2/Si/SiO_2 sandwich structure leads to a complete bandgap for all directions and polarizations with a gap–midgap ratio of about 8.5% and a bandgap for even modes only of about 27%. The complete bandgap is 50% smaller than for 2-D photonic crystals due to the lower confinement of light in the high-index material silicon and polarization mixing. Light guidance obtained by a vertical variation of the porosity, i.e., pore radius, leads under optimum conditions to a bandgap for even modes only, with a gap–midgap ratio of about 10%. The feasibility of such a structure is shown for macroporous silicon where the pore diameter can be varied with depth. In both cases, the optimum slab thickness can be approximated by classical waveguide optics, reducing the parameter space for optimization.**

***Index Terms*—Bandgap, band structures, claddings, confinement, core, field distributions, guided modes, photonic crystals, pore modulation, slabs.**

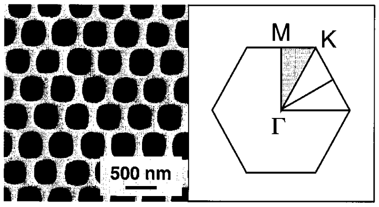

Fig. 1. Example of a PC consisting of macroporous silicon (scanning electron microscopy top view). The pitch of the hexagonal lattice is $a = 500$ nm, and the pores are 100 μm deep. On the right, the first Brillouin zone of the hexagonal lattice is shown. The position of the three high-symmetry points Γ, M and K is indicated.

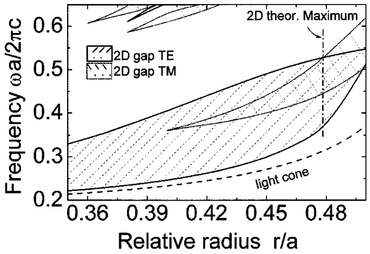

Fig. 2. 2-D gap map (normalized frequency $\omega a/2\pi c$ versus relative radius r/a) for a triangular lattice of infinite air holes in silicon (computed by Busch [6]). The position of the largest gap–midgap ratio is indicated. The first TM band (corresponding to the light line at the M point in macroporous silicon) is also shown (dashed line).

I. Silicon-Based Photonic Crystals (PCs)

Two-dimensional (2-D) silicon-based photonic crystals have been extensively studied, both theoretically and experimentally [1]–[3]. In these structures, the dielectric constant is periodic in one plane (usually defined as the xy plane) and extends infinitely in the third direction (z direction). Lattice types include quadratic, hexagonal, or graphite (honeycomb) lattices. It has turned out that, for air holes in a dielectric, the hexagonal lattice opens up the largest photonic bandgap [4]. For light propagating in the plane of periodicity of the 2-D PC, the polarizations decouple: either the electric field is aligned along the pores [E-polarization or transverse magnetic (TM)], or the magnetic field is in the direction of the pores [H-polarization, transverse electric (TE)]. However, ideal 2-D PCs extend infinitely in the z direction, a situation that cannot be realized experimentally. Nevertheless, 3-D numerical approximations show that a 2-D PC can be approximated by structures with aspect ratios (ratio between pore/rod length to pore/rod diameter) larger than 20 times the lattice constant a. Experimentally, a material exhibiting aspect ratios of 100–500 is macroporous silicon (Fig. 1). It has been recently shown that the optical properties of a bulk macroporous silicon PC as well as integrated defects can be well described by 2-D simulations [2], [5]. The variation of the photonic bandgap with pore radius for a hexagonal lattice of air pores in silicon is shown in Fig. 2 ($\varepsilon_{\mathrm{Si}} = 11.6$). A complete 2-D bandgap, i.e., a forbidden frequency range for all in-plane wavevectors and both polarizations, appears for pore radii $r > 0.4a$. The variation of the gap–midgap ratio of the complete bandgap (ratio between the gap width and midgap frequency) with the relative radius shows a narrow maximum; the largest gap–midgap ratio for this structure is 16.3% and is found for a pore radius $r = 0.478a$.

2-D PCs cannot, by definition, provide light confinement in the direction parallel to the pore axis. A way to avoid out-of plane losses is the use of PC *slabs*. These slab structures consist of a 2-D PC (core) surrounded by two layers of lower effective refractive index (claddings) that provide index guiding by total internal reflection in the direction normal to the plane of the crystal. Of course, in most applications of PC slabs in integrated optics, one also needs to introduce defects into the planar PC lattice, so that light is guided in all three dimensions: in the lateral plane due to the presence of 2-D PC defects, and in the direction parallel to the pore axis due to total internal refection caused by the effective index modulation. A prerequisite for leakage-free

Manuscript received September 18, 2001; revised March 5, 2002.

C. Jamois, R. B. Wehrspohn, J. Schilling, F. Müller, and R. Hillebrand are with the Max-Planck Institute of Microstructure Physics, D-06120 Halle, Germany (e-mail: jamois@mpi-halle.de; wehrspoh@mpi-halle.de; schill@mpi-halle.de; fmuel@mpi-halle.de; hi@mpi-halle.de).

W. Hergert is with the Department of Physics, Martin Luther University Halle-Wittenberg, D-06108 Halle, Germany (e-mail: hergert@physik.uni-halle.de).

Publisher Item Identifier S 0018-9197(02)05695-6.

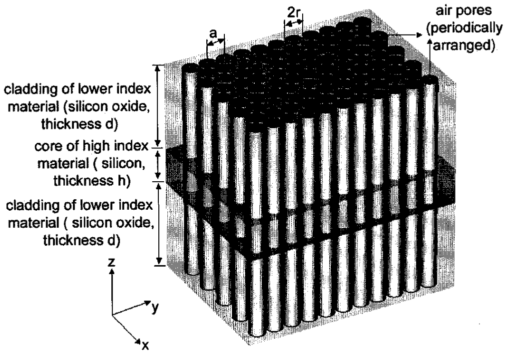

Fig. 3. Schematic diagram of a silicon PC slab consisting of a hexagonal lattice of air pores in a silicon core with two silicon oxide claddings.

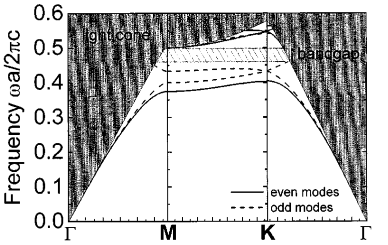

Fig. 4. Band structure of the PC slab presented in Fig. 3 for the optimum set of parameters $\varepsilon_{Si} = 11.6$, $\varepsilon_{\mathrm{ox}} = 2$, $h = 0.64a$, $d = 9a$, and $r = 0.46a$, leading to a complete photonic bandgap with an 8.5% gap–midgap ratio. The grey region overlaid on the diagram (light cone) is limited by the light line in silicon oxide and represents a continuum of radiation (i.e., nonguided) modes. Light confinement in the plane of the PC is only possible below the light line. With respect to the lateral xy plane of symmetry in the middle of the PC, guided modes of the crystal can be separated into even (solid lines) and odd (dashed lines) modes.

defect mode confinement in PCs is a large complete bandgap. It is the aim of this work to find optimum designs for bulk PC slabs based on silicon, leading to large complete bandgaps.

There are two realistic ways to achieve the effective index modulation required in PC slabs. The usual way is to use materials with different dielectric constants for core and cladding: for example, a possible structure is a 2-D PC in a sandwich structure consisting of a high-index semiconductor core with low-index oxide or air claddings. A different way to achieve an effective index modulation is to vary the pore diameter in the direction parallel to the pore axis. In this paper, we present and discuss the advantages and disadvantages of these two types of bulk slab structures in the framework of current silicon technology: a silicon slab with two silicon oxide claddings based on silicon-on-insulator (SOI) substrates [7], [8] or modulated pores in macroporous silicon [9].

II. PC SLAB WITH INDEX MODULATION

The first type of structure we are studying is a planar PC made out of a thin layer of high-index material surrounded by two claddings of lower index materials. This kind of structure is usually based on silicon or III–V compounds and has been largely studied in the last few years to build both passive and active optical devices [10]–[18]. A typical structure we are dealing with is presented in Fig. 3. It is composed of a thin silicon slab with two silicon oxide claddings. The thickness of the oxide claddings is fixed to 3 μm, since the commercially available SOI wafers we intend to use for future experimental realizations of the structures have a maximum embedded oxide thickness of $d = 3\ \mu$m (Soitec S.A.). The air pores are ordered in a hexagonal lattice and go through the whole structure.

The finite thickness of the PC slab leads to major differences in the band structure compared to the ideal 2-D case. First, the modes do not decouple anymore into TE and TM polarization. However, since the xy plane in the middle of the PC is a mirror plane of our structure, the modes can be labeled as even and odd modes. In the case of even (odd) modes, the magnetic field is even (odd) with respect to the xy plane of symmetry. Secondly, not all the modes existing in the PC slab are guided. Most of them couple with modes of the claddings and are either guided in the cladding or scattered out of the slab. This continuum of radiation states is usually called the light cone and is limited by the light line in the cladding. Thus, we have to calculate the light line—here for silicon oxide ($\varepsilon_{\mathrm{ox}} = 2.1$)—and overlay it with the band structure [10], [11]. Only the modes that lie below this boundary are guided, i.e., confined in the silicon slab.

Band structure calculations were performed using a block-iterative frequency-domain code (MIT package) [19], [20] on a computer with a 2-GHz Pentium IV processor and 2-Gb Rambus RAM. Due to the high-index contrast between core and cladding full 3-D band structure calculations are necessary to simulate the PC slab. Note that, for thick low-index contrast slabs like InP–GaInAsP or InGaAs–AlGaAS structures [18], it is possible to calculate the bandstructure by using 2-D numerical models, similar to macroporous silicon structures [21]. We checked for 3-D convergence of the results as a function of the structure discretization and compared it with 3-D plane-wave results. We determined that a minimum grid size of 64 points and a minimum subgrid size of 15 points are needed for the results to be reliable and in line with 3-D plane-wave expansion calculations.

We have varied the thickness of the silicon slab h/a and the pore radius r/a to obtain the largest possible bandgap for given values of $\varepsilon_{\mathrm{Si}} = 11.6$, $\varepsilon_{\mathrm{ox}} = 2.1$ and the cladding thickness $d = 3\ \mu$m. The results of the optimization yield a complete bandgap in the even and odd guided modes for $r/a > 0.42$ (Fig. 4). The largest gap–midgap ratio is 8.5% for the optimum set of parameters: $h = 0.64a$, $d = 9a$, and $r = 0.46a$, corresponding to $a = 730$ nm, $h = 470$ nm, $d = 3\ \mu$m, and $r = 335$ nm for a midgap frequency of 1.55 μm. For this set of parameters, the gap–midgap ratio for even modes is about 27%. A systematic study of the variations of the gap–midgap ratio with h/a and r/a allowed us to draw a 3-D gap map for our PC slab. Fig. 5 shows the two most interesting cuts through this gap map: the variations of the gap–midgap ratio with r/a for $h/a = 0.64$, and the variations of the gap–midgap ratio with h/a for $r/a = 0.46$. One can observe that the variation of the gap–midgap ratio

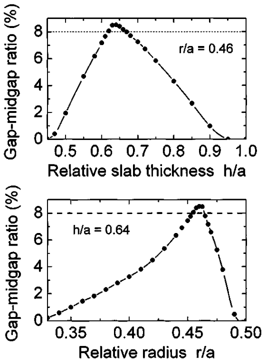

Fig. 5. Variations of the gap–midgap ratio with the relative core thickness (top) and the relative radius (bottom) for the PC presented in Fig. 3. The variations with h/a are determined at a constant radius $r = 0.46a$, and the variations with r/a are determined at a constant core thickness $h = 0.64a$.

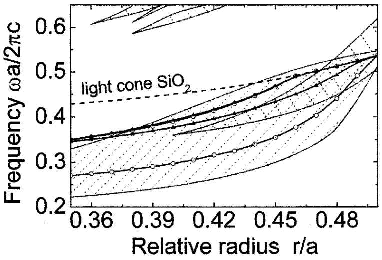

Fig. 6. Gap map of the PC slab presented in Fig. 3, for a relative core thickness $h/a = 0.64$. The even gap is limited by the two lower order even bands (see Fig. 4), which are represented by open circles. The odd gap is between the second and third bands, which are represented by black triangles. The light cone in silicon oxide is also shown (dashed line). For comparison, the gap map for a perfect 2-D PC in macroporous silicon is drawn in the background (gray lines).

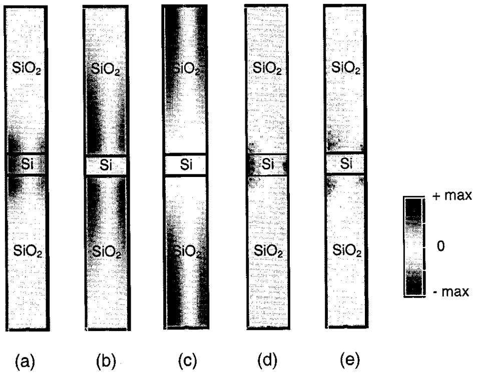

Fig. 7. Vertical cross section in a crystal unit cell of the electric field distribution for PC eigenmodes (z component), in the case of the structure presented in Fig. 3 with the optimized parameters $h = 0.64a$, $d = 9a$, and $r = 0.46a$. (a) M point, odd mode, band 1, (b) M point, even mode, band 2, (c) M point, odd mode, band 3, (d) K point, odd mode, band 2, and (e) K point, even mode, band 3. The black lines indicate the position of the silicon core.

with r/a is similar to that of perfect 2-D PCs. Indeed, a narrow maximum for a radius of $0.46a$ is observable, which is close to the optimum radius value of the ideal 2-D silicon PC (Fig. 2). However, we can see that the largest gap–midgap ratio obtained in the PC slab is about 50% smaller than in the case of the ideal 2-D PC. This originates from the lower confinement of light in the high-index material silicon since light penetrates into the oxide claddings. Additionally, polarization mixing due to the small height of the core occurs.

The variation of the gap–midgap ratio with h/a is different from the variations with r/a. We see a quite broad maximum, which indicates that the thickness of the slab is a less critical parameter. Indeed, in a range of about 20 nm around the optimum thickness value—470 nm at $\lambda_0 = 1.55\ \mu$m—the gap–midgap ratio is still larger than 8%—in the case of the pore radius, a variation of only 4 nm from the optimum value is necessary for the gap–midgap ratio to fall under 8%. This broad maximum will be an advantage for the future experimental realization of the PC slab. It is interesting to note that taking a planar waveguide with the effective refractive index of the different layers, we have found an optimum core thickness of 500 nm for a monomode regime at a wavelength of 1.55 μm

$$h_{\text{mono}} \le \frac{\lambda_0}{2\sqrt{n_2^2 - n_1^2}} = 500\ \text{nm for}\ \lambda_0 = 1.55\ \mu\text{m}. \qquad (1)$$

The effective refractive index values have been determined by taking ck/ω for the first band of the 2-D corresponding system ($n_1 = 1.1$ in the claddings and $n_2 = 1.9$ in the core). The maximum thickness of a monomode planar waveguide is very close to the calculated optimum thickness of the silicon layer of our PC slab (470 nm). Thus, this simple estimation gives a good approximation of the optimum thickness of the PC slab and helps reducing the parameter space for design optimization in further calculations.

The variations of the even and odd gap position for this optimum thickness ($h = 0.64a$) is shown in Fig. 6. The position of the SiO$_2$ light cone is also indicated. Comparison between the even (odd) dielectric band that is mainly TE-polarized (TM) with the TE (TM) dielectric band of the ideal 2-D PC shows a shift of the dielectric band of the PC slab to higher frequencies. Indeed, in the case of PC slabs, a part of the field energy penetrates into the claddings where it decays exponentially. Since the fields of the dielectric bands are mostly located in the dielectric and since the claddings have a lower refractive index than silicon, the energy of the fields for these bands is higher than in the corresponding ideal 2-D silicon PC.

It is more difficult to explain the position of the air bands. Indeed, they show a stronger polarization mixing of TE and TM, so a direct comparison with the 2-D gap map is not possible.

Fig. 7 shows some electric field distributions for even and odd modes at the M and K points of the first Brillouin zone. Comparing these distributions with the band structure presented in Fig. 4 verifies that for cases (a), (d) and (e) the modes lying

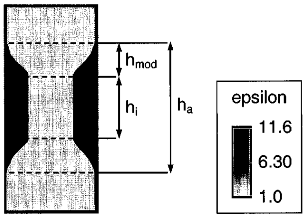

Fig. 8. Vertical section of the computer-generated dielectric model used to simulate modulated air pores in macroporous silicon. The continuous pore radius modulation is represented by an ellipsoid slice with thickness h_{mod} inserted between two cylinders.

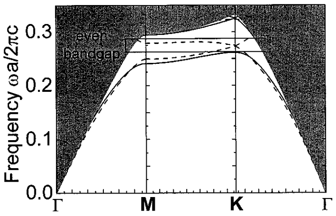

Fig. 9. Band structure of the PC slab with modulated pore radius in macroporous silicon for the optimum set of parameters $h_i = 0.81a$, $h_a = 1.39a$, $d = 12a$, $r_i = 0.38a$, and $r_a = 0.48a$. Solid lines: even modes, dashed lines: odd modes. For this optimum design an even bandgap occurs with a gap–midgap ratio of 10%.

below the light line are confined in the plane of the PC. In contrast, distribution (c) confirms that modes lying in the light cone may be not guided.

Note that the second-band even mode at the M point in (b) lies very close to the light cone but is still confined. It is the upper boundary of the complete bandgap. This mode extends about 2.5 μm into the claddings. Thus, the large cladding thickness of $d = 3$ μm is a prerequisite for a large bandgap.

III. PC SLAB WITH POROSITY MODULATION

The second type of planar PC consists of a structure where the effective index contrast necessary for in-plane confinement is obtained by modulation of the pore radius. In the core, the pore radius is smaller, and thus the effective refractive index is higher.

From experiments with macroporous silicon, it is known that the transition between different pore radii is sinusoidal [9]. In our simulations, the continuous radius modulation is approximated by an ellipsoid slice inserted between two cylinders (Fig. 8). We have done 3-D band structure calculations using the MIT package. For the discretization of the structure, the same parameters as in Section II (grid and sub-grid) have been used.

A first estimate for the design comes from the light line of macroporous silicon. This light line has been calculated and is shown in Fig. 2. It can be seen that the light line is very low, so that we have to choose a large pore diameter in the claddings and a small pore diameter in the core if we want the light line to be sufficiently high above the low-order bands. However, it can be already seen from Fig. 2 that a complete bandgap will not be obtained, thus we focus our attention on the even bandgap. Due to the even modes not being purely TE-polarized in such planar structures, the introduction of defects into the lattice will lead to leaky modes. This is an important disadvantage of this second type of PC slab compared to the silicon slab with oxide claddings having a complete bandgap.

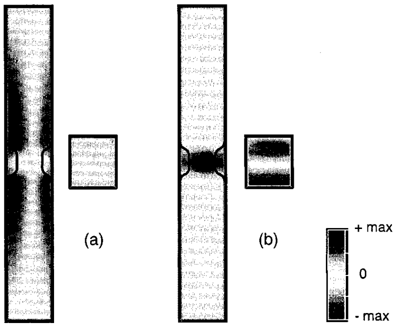

Fig. 10. Side-view and horizontal cross section in a crystal unit cell of the (a) electric and (b) magnetic field distribution for the PC slab of modulated air pores in silicon with the optimized parameters $h_i = 0.81a$, $h_a = 1.39a$, $d = 12a$, $r_i = 0.38a$, and $r_a = 0.48a$. The mode shown is the second-order even mode at the M point (z component). The black lines indicate the pore profile.

An initial guess from Fig. 2 is a radius r_i of $0.38a$ in the core and r_a of $0.48a$ in the claddings. Again, we approximate the optimum core thickness using the planar waveguide model [see (1)]. The effective refractive index for TE-like modes is about 2.2 for $r/a = 0.38$ and 1.4 for $r/a = 0.48$ that leads to a thickness of $1.2a$. A further optimization of this thickness for the two chosen radius values leads to an even bandgap of 10% for an internal core thickness $h_i = 0.81a$ and a total pore modulation $h_a = 1.39a$ (Fig. 9). Since the optimum thickness of the planar waveguide lies between the optimized heights h_i and h_a, we can maintain that this result is again in good agreement with the planar waveguide approximation [see (1)].

Fig. 10 shows field distributions for the second-order even mode at the M point for the optimized structure. This state lies slightly above the upper limit of the even bandgap. As in the case of the PC slab with oxide claddings, we confirm that this state is still well confined although it lies close to the light line. Furthermore, this figure highlights the polarization mixing that occurs in finite 2-D PCs: indeed, if the even mode we are considering was purely TE-polarized, the z-component of its electric field should be equal to zero, but this is not the case here.

It is interesting to note that the experimental realization of such a structure is possible. Indeed, we have already realized a 3-D PC of modulated air pores in silicon having parameters close to those of our designed slab structure, as presented in [2], [9]. Furthermore, preliminary experiments show that it is possible to achieve a pore modulation with $h_a = 1.4a$ and $\Delta r/a = 0.1$ in macroporous silicon (Fig. 11).

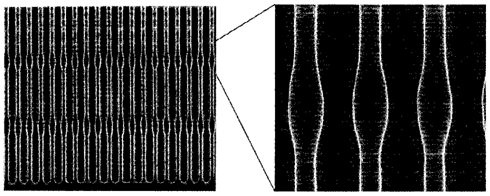

Fig. 11. Graded-index, embedded waveguides in macroporous silicon (SEM side view). The lattice constant is 4.2 μm, and the pore radius is 3 μm in the claddings and 2 μm in the core. Multiple parallel waveguides are shown.

IV. CONCLUSION

Two different concepts of vertical light confinement in 2-D silicon PCs have been analyzed. Light guidance obtained by variation of the refractive index in an SiO_2/Si/SiO_2 sandwich structure leads to a bandgap for all directions and both polarizations with a gap–midgap ratio of about 8.5%, and 27% considering even modes only. This is 50% smaller than that for 2-D PCs due to the lower confinement of light in the high-index material silicon and polarization mixing. Light guidance obtained by a vertical variation of the porosity, i.e., pore radius, leads under optimum conditions to a bandgap for even modes only with a gap–midgap ratio of about 10%. The feasibility of such a structure has been shown for macroporous silicon where the pore diameter can be varied with depth. However, because of the polarization mixing that occurs in planar PCs, it is preferable to have structures exhibiting a complete bandgap as we intend to introduce defects into the lattice in the future. The difference between these two concepts can be explained by the fact that the changes of the effective refractive index of the cladding layer are more sensitive to the matrix material than to the pore radius. In both cases, the optimum slab thickness can be approximated by classical waveguide optics, thus reducing the parameter space for optimization.

ACKNOWLEDGMENT

The authors are very grateful to the MIT *ab initio* group for allowing the use of their computation package, and to K. Busch for the calculation of the gap map of perfect 2-D PCs in macroporous silicon.

REFERENCES

[1] A. Birner *et al.*, “Silicon-based photonic crystals,” *Adv. Mater.*, vol. 13, pp. 377–388, Mar. 2001.

[2] J. Schilling *et al.*, “A model system for 2D and 3D photonic crystals: Macroporous silicon,” *J. Opt. A: Pure Appl. Opt.*, vol. 3, pp. S121–S132, Oct. 2001.

[3] H. W. Lau *et al.*, “High aspect ratio submicron silicon pillars fabricated by photoassisted electrochemical etching and oxidation,” *Appl. Phys. Lett.*, vol. 67, pp. 1877–1879, Sept. 1995.

[4] R. D. Meade *et al.*, “Existence of a photonic band gap in two dimensions,” *Appl. Phys. Lett.*, vol. 61, pp. 495–497, July 1992.

[5] U. Grüning *et al.*, “Two-dimensional infrared photonic bandgap structure based on porous silicon,” *Appl. Phys. Lett.*, vol. 66, pp. 3254–3256, June 1995.

[6] A. Birner *et al.*, “Transmission of a microcavity structure in a two-dimensional photonic crystal based on macroporous silicon,” *Mater. Sci. Semicon. Process.*, vol. 3, pp. 487–491, 2000.

[7] Baba *et al.*, “Light propagation characteristics of defect waveguides in a photonic crystal slab,” in *Photonic Crystals and Light Localization in the 21st Century*. ser. C, C. M. Soukoulis , Ed. Dordrecht, The Netherlands: Kluwer, 2001, vol. 563, NATO Science Series, pp. 105–116.

[8] M. Loncar *et al.*, “Waveguiding in planar photonic crystals,” *Appl. Phys. Lett.*, vol. 77, pp. 1937–1939, Sept. 2000.

[9] J. Schilling *et al.*, “Three-dimensional photonic crystals based on macroporous silicon with modulated pore diameter,” *Appl. Phys. Lett.*, vol. 78, pp. 1180–1182, Feb. 2001.

[10] S. G. Johnson *et al.*, “Guided modes in photonic crystals slabs,” *Phys. Rev. B*, vol. 60, pp. 5751–5758, Aug. 1999.

[11] M. Loncar *et al.*, “Design and fabrication of silicon photonic crystal optical waveguides,” *J. Lightwave Technol.*, vol. 18, pp. 1402–1411, Oct. 2000.

[12] H. Benisty *et al.*, “Radiation losses of waveguide-based two-dimensional photonic crystals: Positive role of the substrate,” *Appl. Phys. Lett.*, vol. 76, pp. 532–534, Jan. 2000.

[13] I. El-Kady *et al.*, “Dielectric waveguides in two-dimensional photonic bandgap materials,” *J. Lightwave Technol.*, vol. 17, pp. 2042–2049, Nov. 1999.

[14] M. Tokushima *et al.*, “Lightwave propagation through a 120° sharply bent single-line defect photonic crystal waveguide,” *Appl. Phys. Lett.*, vol. 76, pp. 952–954, Feb. 2000.

[15] E. Chow *et al.*, “Three-dimensional control of light in a two-dimensional photonic crystal slab,” *Nature*, vol. 407, pp. 983–986, Oct. 2000.

[16] O. Painter *et al.*, “Two-dimensional photonic bandgap defect mode laser,” *Science*, vol. 284, pp. 1819–1821, June 1999.

[17] A. Talneau *et al.*, “Quantitative measurement of low propagation losses at 1.55 μm on planar photonic crystal waveguides,” *Opt. Lett.*, vol. 26, pp. 1259–1261, Aug. 2001.

[18] T. D. Happ *et al.*, “Two-dimensional photonic crystal laser mirrors,” *Semicond. Sci. Technol.*, vol. 16, pp. 227–232, Apr. 2001.

[19] S. G. Johnson *et al.*, “Bloch-iterative frequency-domain methods for Maxwell’s equations in a planewave basis,” *Opt. Express*, vol. 8, pp. 173–190, Jan. 2001.

[20] S. G. Johnson. MIT photonic-bands. [Online]. Available: http://ab-initio.mit.edu/mpb.

[21] Weisbuch *et al.*, “3D control of light in waveguide-based two-dimensional photonic crystals,” *IEICE Trans. Commun.*, vol. E84-B, pp. 1286–1294, May 2001.

Cécile Jamois was born in Rennes, France, in 1977. She studied physical engineering at the Institut National des Sciences Appliquées, Rennes, France, and at the Technical University of Aachen, Aachen, Germany, receiving her diploma degree in 2000. She is currently working toward the Ph.D. degree at the Max-Planck-Institute of Microstructure Physics, Halle, Germany.

She works on the design development and research of silicon-based photonic crystal slabs.

Ralf B. Wehrspohn was born in Lübeck, Germany, in 1970. He received the diploma degree in physics from the University of Oldenburg, Oldenberg, Germany, in 1995, and the Ph.D. degree from Ecole Polytechnique, France. His doctoral work concerned thin-film technology and electrochemistry.

In 1998 he joined the Philips Research Laboratories in Redhill, U.K., to work on thin-film transistors for AMLCD. Since the end of 1999 he has been responsible for the activities on photonic crystals and self-ordered porous materials at the Max-Planck-Institute of Microstructure Physics, Halle, Germany.

Jörg Schilling was born in Halle, Germany, in 1973. He studied physics at the Martin-Luther-University Halle-Wittenberg, Halle, Germany, and at the Heriott-Watt-University, Edinburgh, Scotland. In 1999 he received his diploma degree. He is currently working toward the Ph.D. degree at the Max-Planck-Institute of Microstructure Physics, Halle, Germany.

He works on the fabrication and investigation of two- and three-dimensional photonic crystals on the basis of macroporous silicon. His research interests include photonic crystals and X-ray reflectivity of thin films.

Frank Müller was born in Reutlingen, Germany, in 1960. He received the diploma degree in physics and the Ph.D. degree from the Technical University of Munich, Munich, Germany, in 1988 and 1993, respectively. His doctoral work concerned IR spectroscopy on microporous silicon and two-dimensional electron gas systems.

In 1993, he joined the Max-Planck-Institute of Microstructure Physics, Halle, Germany. His research topics are porous materials, photonic crystals and self-ordered materials.

Reinald Hillebrand was born in Worbis, Germany, in 1952. He received the Ph.D. degree in physics from the Martin-Luther-University Halle-Wittenberg, Halle, Germany, in 1987. His doctoral work concerned computer simulations of high-resolution electron microscope images as well as image processing.

Since 1992, he has been with the Max-Planck-Institute of Microstructure Physics, Halle, Germany, working on applications of fuzzy logic and neural networks for the interpretation of HREM micrographs. In 1996, he specialized his theoretical research activities in the field of photonic crystals.

Wolfram Hergert was born in Mügeln, Germany, in 1954. He received the diploma degree in physics and the Ph.D. degree from the University of Halle-Wittenberg, Halle, Germany, in 1977 and 1982, respectively. His doctoral work concerned electron theory of metals.

After working on electronic and magnetic properties of low-dimensional systems he joined Nagoya University, Nagoya, Japan, in 1994, and then returned the University of Halle-Wittenberg, where he is currently Professor of Computational Physics.

PHYSICAL REVIEW B **66**, 1211XX(R) (2002)

Ultrafast band-edge tuning of a two-dimensional silicon photonic crystal via free-carrier injection

S. W. Leonard* and H. M. van Driel
Department of Physics, University of Toronto, 60 Saint George Street, Toronto, Ontario M5S 1A7, Canada

J. Schilling and R. B. Wehrspohn
Max-Planck-Institute of Microstructure Physics, Weinberg 2, D-06120 Halle, Germany

(Received 1 August 2002)

Ultrafast tuning of the band edge of a two-dimensional silicon/air photonic crystal is demonstrated near a wavelength of 1.9 μm. Changes in the silicon refractive index are optically induced by injecting free carriers with 800 nm, 300 fs pulses. The rise time of the shift occurs on the time scale of the pulse width apart from a small component associated with carrier cooling; the recovery time is related to electron-hole recombination. The band edge is observed to shift linearly with pump beam fluence, with a shift in excess of 30 nm for a pump beam fluence of 2 mJ cm^{-2}. A nonuniform spectral shift is attributed to finite pump beam absorption depth effects.

DOI: 10.1103/PhysRevB.66.1211XX PACS number(s): 42.70.Qs, 42.65.Re, 42.79.Ta

Photonic crystals are periodic dielectric materials which continue to generate considerable interest because of their ability to offer novel ways to control the flow of light.[1–6] This new class of optical materials has led to the demonstration of interesting physical phenomena such as novel waveguiding effects,[7,8] superprism effects,[9] and control over spontaneous emission rates.[10] There is clearly a great potential for a new generation of passive and active optical components including new types of integrated optical circuits.

Many of the unusual properties of photonic crystals are based on the existence of a partial or complete photonic band gap, a natural consequence of the material's underlying periodicity. The range of physical phenomena or applications of photonic crystals could be enlarged in scope if these band gaps, or indeed, other characteristics of photonic crystals, could be tuned on very short time scales. In the past, studies of tunable photonic crystals have focused primarily on electro and thermooptic band-edge tuning via infiltrated liquid crystals.[11–14] Unfortunately, the molecular reorientation processes responsible for changes in the refractive index of thermotropic liquid crystals typically occur on time scales ranging from milliseconds to seconds, strictly prohibiting rapid band-edge tuning.

Much faster tunability can only be achieved using electronic processes. Ultrafast changes in the refractive index can occur via nonresonant processes such as the optical Kerr effect, or resonant processes in which free electrons and holes[15] are created. The former effect can induce index changes which follow the light pulse, but requires high light intensities. The latter process requires substantially lower pump intensity and can still lead to induced changes limited by the pulse width. Relaxation should be limited by the carrier recombination time, which can be as short as a picosecond in suitably designed materials.[16,17] Recently, Halevi and Ramos-Mendieta[18] have theoretically shown how thermally activated carriers can tune two-dimensional photonic crystals fabricated with a narrow gap semiconductor (InSb). Susa[19] has also theoretically studied how the continuous optical injection of free carriers can shift the band edge of a two-dimensional photonic crystal for moderate pumping intensities. Experimentally, free carriers generated by two-photon absorption have been used to change the refractive index and transmission properties of a Si/SiO$_2$ dielectric stack (1D photonic crystal).[20] However, since the induced transmission changes were quite small ($<0.5\%$) and were measured only at one wavelength, it was not possible to offer many details about the temporal or spectral characteristics of the induced changes. Also, Chelnikov *et al.*[21] were able to show how free carriers could also control defect mode absorption in a 3D silicon crystal with a photonic gap in the submillimeter range near 250 GHz. Hence, while some preliminary results have been given, very little is known about how optical beams can be used to alter the optical properties of high-dimensional (2D or 3D) photonic crystals, and their band gaps, in particular, in the near infrared region of the spectrum where most applications would be expected to arise.

Here we report the demonstration of ultrafast photonic band-edge tuning in a two-dimensional photonic crystal in the near infrared.[22] Optically injected free carriers are used to induce a large >30-nm band-edge shift on femtosecond time scales. This is done in macroporous silicon photonic crystals, fabricated using the techniques reported in Refs. 23–25. The samples have a triangular lattice of air pores in silicon, with a pitch of 500 nm and a pore radius of 206 nm. The pores extend 100 μm in depth and the sample is cleaved perpendicular to the so-called Γ-M direction, as shown in Fig. 1. For this direction, a stop gap occurs from 1.9 to 2.3 μm; this gap is the focus of this report.

The injection of electron-hole pairs in a semiconductor is known to alter both the refractive index and absorption coefficient via a Drude contribution to the dielectric function.[15] In the absence of significant absorption, the dielectric function can be described by $\epsilon(\omega)=\epsilon_b-\omega_p^2/\omega^2$, where $\omega_p=(Ne^2/\epsilon_0 m^*)^{1/2}$ is the plasma frequency, N is the density of electron-hole pairs, ϵ_b is the dielectric constant of quiescent silicon, m^* is the reduced effective mass and ω is the probe frequency. For our experiments, in which probe light with a wavelength near 1.9 μm is used and carrier densities are less than 2×10^{19} cm^{-3}, the imaginary terms in the dielectric function arising from free-carrier absorption and

0163-1829/2002/66(12)/1211XX(4)/$20.00

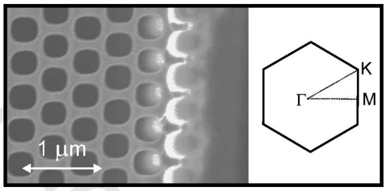

FIG. 1. Scanning electron microscope image of two-dimensional photonic crystal with lattice pitch of 500 nm. The sample has a height of 100 μm and a radius to pitch ratio of $r/a=0.411$. Inset, first Brillouin zone of triangular lattice.

intervalence-band absorption are very small.[26]

To illustrate the effect of free carriers on the properties of our photonic crystal, we calculated the dependence of the photonic band structure on the plasma frequency. The Drude form of the dielectric function allows a plane-wave expansion of Maxwell's equations to be cast in the form of a standard eigenvalue equation.[29] We performed calculations for our structure with plasma frequencies in the range $0<\omega_p a/2\pi c<1$ and found that 400 plane waves provided sufficient convergence.

The photonic band structure for the **E**- and **H**-polarized bands (electric-field polarized parallel and perpendicular to pore axis, respectively) and the dependence of the band-edge frequencies on the plasma frequency is shown in Fig. 2. All band-edge frequencies are blue shifted with increasing plasma frequency. The magnitude of the band-edge shift depends on both the mode frequency and the concentration of the mode energy in the silicon. The two-dimensional photonic band gap near 1.4 μm (indicated by the dashed line in Fig. 2) closes completely for plasma frequencies greater than $\omega_p=0.57\times 2\pi c/a$ (corresponding to $N=2.3\times 10^{20}$ cm^{-3} for our material).

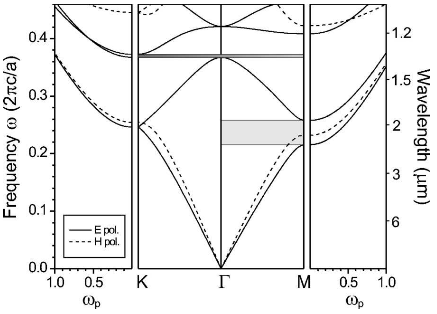

FIG. 2. Band structure of two-dimensional photonic crystal and dependence of band-edge frequencies on the plasma frequency ω_p, assuming a lossless dielectric function. The radius to pitch ratio is 0.411 and the wavelength scale is calculated assuming a pitch of 500 nm. The plasma frequency is given in units of $2\pi c/a$. Also shown are the complete two-dimensional band gap (narrow rectangle) and the stop band investigated in the experiment (wide rectangle).

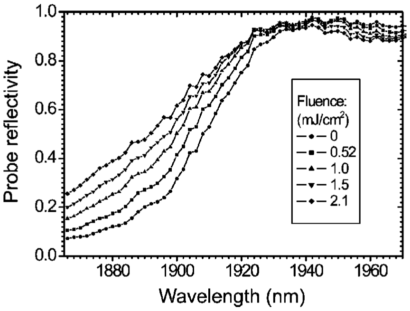

FIG. 3. **E**-polarized reflectivity of photonic crystal in Γ-M direction in vicinity of high-frequency fundamental band edge, and its dependence on pump fluence.

To observe the effects of carriers on the photonic band structure, we performed ultrafast pump and probe experiments using an optical parametric amplifier system pumped by a 800 nm, Ti:sapphire regenerative amplifier with a pulse repetition rate of 250 kHz. The system was configured to produce collinearly propagating **E**-polarized probe pulses near 1.9 μm (resonant with the high-frequency side of the first band gap) and **H**-polarized pump pulses at 800 nm, each with a width of approximately 300 fs. The probe was focused to a spot size of 30 μm, within the 90-μm spot size of the pump beam. The reflectivity spectrum was measured with a monochromator and a pyroelectric detector. A variable delay in the pump path allowed for the probe reflectivity to be measured as a function of time delay.

The probe reflection spectrum and its dependence on the pump pulse fluence is shown in Fig. 3 (measured with the probe delayed 13.5 ps from the pump, well beyond initial reflectivity transients). The unpumped sample reflectivity has a maximum value of 0.97 in the band gap, indicating high surface quality. The spectra are clearly blue shifted with increasing pump fluence, consistent with the Drude model discussed above. A maximum shift of 31 ± 1 nm is observed for a pump fluence of 2.1 ± 0.4 mJ cm^{-2}. This shift spans nearly 10% of the unpumped crystal stop band. The steepness of the band-edge facilitates the observation of large differential reflectivities, in excess of 250% for the maximum pump fluence, although this steepness changes with fluence because of spatial inhomogeneity in the plasma with depth (see below). The reflectivity within the stop gap remains above 0.90 at the maximum pump fluence, indicating that absorption has a negligible effect on reflectivity.

The temporal evolution of the band-edge shift was observed by measuring the reflectivity of the photonic crystal while varying the delay between the pump and the probe pulses. The observed dependence is shown in Fig. 4, where the differential reflectivity is plotted as function of the probe delay for a pump pulse fluence of 1.3 mJ cm^{-2} at a probe wavelength of $\lambda=1900$ nm. The differential reflectivity increases with a rise time of approximately 400 fs, consistent with pump and probe pulse widths. There is also a residual rise of the reflectivity which occurs on a time scale of 2–3

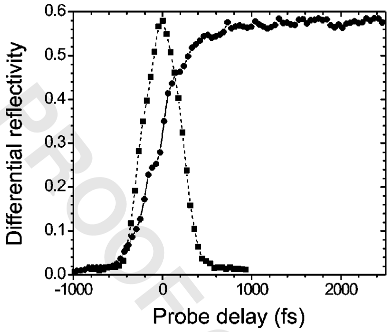

FIG. 4. Dependence of differential reflectivity ($\Delta R/R$) on probe delay for $\lambda=1900$ nm and a pump fluence of 1.3 mJ cm^{-2} (solid). Also plotted is pump and probe cross correlation (dashed, arbitrary units).

ps; this is attributed to carrier cooling effects. As the carriers cool, their effective mass decreases, raising the Drude contribution to the dielectric constant and hence the reflectivity. The subsequent plateau was observed to be constant over the 70-ps delay range of the experiment. The constant plateau is consistent with the >1 ns expected carrier recombination lifetime of bulk silicon, governed by Auger recombination[30,31] and surface recombination. The recombination lifetime can be reduced to approximately a picosecond via the introduction of radiation-induced defects or other nonradiative traps (e.g., as was done with other materials using ion implantation of oxygen in silicon on sapphire[16] and low-temperature grown[17] GaAs).

The observed dependence of the band-edge shift on the pump fluence fits very well with the linear behavior predicted by the plane-wave model. By fitting the maximum observed shift with the calculated shift, we obtained a relationship between the measured pump fluence and the excited carrier density. The inferred density fell in the range $(0.2<N<1.9)\times 10^{19}$ cm^{-3} for the pump fluences used in the experiment. Using the fitted relationship between the density and the pump fluence, the effective pump absorption depth can be calculated via the relation $N=F(1-R)/(E_p l)$, where F is the pump fluence, R is the pump reflectivity (measured to be 0.56), E_p is the pump photon energy, and l is the effective pump absorption depth. This relation gives $l=2.0\pm 0.4$ μm, which is five times smaller than that of bulk silicon.[33] The shallower absorption depth is attributed to a lower group velocity of the photonic band at 800 nm compared to that of bulk Si. The pump energy is therefore absorbed within approximately three crystal rows (one crystal row in the Γ-M direction has a length of $\sqrt{3}a=866$ nm), leading to a carrier density that is spatially inhomogeneous. We note that this depth could be extended by pumping with a wavelength closer to the electronic band edge of silicon, where the pump absorption depth is much larger.

The spatially inhomogeneous plasma, and the resulting depth dependence of the photonic band edge, accounts for important features of the reflectivity spectrum. When the crystal is not pumped, light with a wavelength below approximately 1880 nm (significantly below the band edge in Fig. 3) is partially reflected via the impedance mismatch at the crystal surface. Although most of the light couples to a propagating mode and probes the entire crystal, the reflected light only probes the surface layer of the crystal. However, when the wavelength is inside the stop band ($\lambda \gtrsim 1940$ nm), all of the light is reflected due to the coherent superposition of an infinite number of backscattered waves from deep within the crystal. Therefore, as the wavelength increases toward the band edge, the reflection mechanism changes from impedance mismatch to Bragg scattering, and the *reflected* light probes deeper regions of the crystal.

The consequence for our inhomogeneously pumped crystal is that the short-wavelength reflectivity probes the highly pumped surface region, resulting in a large spectral shift. However, as the wavelength increases and crosses the blue shifted band edge of the pumped crystal, the reflected light penetrates deeper into the crystal. In fact, some of the deeply penetrating waves couple to the propagating modes of the weakly pumped part of the crystal, resulting in a lower reflectivity and a smaller shift. This effect is clearly seen in Fig. 3, where the shift is large for short wavelengths but decreases as the wavelength increases toward the band edge. This observation validates measuring the blue shift near the bottom of the peak, where the efficiently pumped surface layers are being probed. The qualitative explanation given above was theoretically verified using a one-dimensional transfer-matrix model of the inhomogeneously pumped photonic crystal. The results, to be presented elsewhere, correctly reproduce the observed spectral shape for an absorption depth of three layers, confirming our model.

In summary, we have demonstrated ultrafast all-optical tuning of the band gap of a silicon photonic crystal using free-carrier injection. Our results indicate that optical free-carrier injection offers a practical means of controlling the band edges and photon densities of states on ultrafast time scales. The use of free carriers to control the properties of photonic crystals clearly presents many exciting opportunities for ultrafast all-optical switching in the near future.

We thank Serguei Grabtchak and Jessica Mondia for useful discussions and S. Matthias, F. Müller, and A. Birner for technical assistance. Two of the authors (S.W.L. and H.V.D.) gratefully acknowledge the financial support of the Natural Sciences and Engineering Research Council of Canada and Photonics Research Ontario.

---

*Present address: Photonami Inc., 50 Mural St. Unit 10-11, Richmond Hill, Ontario L4B 1E4, Canada.

[1] E. Yablonovitch, Phys. Rev. Lett. **58**, 2059 (1987).
[2] S. John, Phys. Rev. Lett. **58**, 2486 (1987).
[3] *Photonic crystals and light localization in the 21st century*, edited by C. Soukoulis (Kluwer Academic Publishers, Boston, 2001).
[4] J. D. Joannopoulos, R. D. Meade, and J. N. Winn, *Photonic Crystals: Molding the Flow of Light* (Princeton University Press,

Princeton, 1995).

[5] S. Noda, A. Chutinan, and M. Imada, Nature (London) **407**, 608 (2000).

[6] A. Blanco *et al.*, Nature (London) **405**, 437 (2000).

[7] E. Chow *et al.*, Opt. Lett. **26**, 286 (2001).

[8] R.F. Cregan *et al.*, Science **285**, 1537 (1999).

[9] H. Kosaka *et al.*, Phys. Rev. B **58**, R10096 (1998).

[10] H.P. Schriemer *et al.*, Phys. Rev. A **63**, 011801(R) (2001).

[11] K. Busch and S. John, Phys. Rev. Lett. **83**, 967 (1999).

[12] K. Yoshino *et al.*, Jpn. J. Appl. Phys., Part 1 **38**, L961 (1999).

[13] S.W. Leonard *et al.*, Phys. Rev. B **61**, R2389 (2000).

[14] D. Kang *et al.*, Phys. Rev. Lett. **86**, 4052 (2001).

[15] M.I. Gallant and H.M. van Driel, Phys. Rev. B **26**, 2133 (1982).

[16] F.E. Doany, D. Grischkowsky, and C.-C. Chi, Appl. Phys. Lett. **50**, 460 (1987).

[17] F.W. Smith *et al.*, Appl. Phys. Lett. **54**, 890 (1989).

[18] P. Halevi and F. Ramos-Mendieta, Phys. Rev. Lett. **85**, 1875 (2000).

[19] S. Susa, Jpn. J. Appl. Phys., Part 1 **39**, 6288 (2000).

[20] A. Haché and M. Bourgeois, Appl. Phys. Lett. **77**, 4089 (2000).

[21] A. Chelnikov *et al.*, Electron. Lett. **34**, 1965 (1998).

[22] H. M. van Driel *et al.*, MRS Symp. Proc. 722 L3. 1 (2002).

[23] U. Grüning *et al.*, Appl. Phys. Lett. **68**, 747 (1996).

[24] A. Birner *et al.*, Adv. Mater. **13**, 377 (2001).

[25] J. Schilling *et al.*, Opt. Mater. **17**, 7 (2001).

[26] Using an effective mass[27] of $m^*=0.16m_0$ (where m_0 is the electron mass), a momentum relaxation time of $\tau\sim100$ fs, and an intervalence band cross section[28] of 10^{-17} cm^2, the magnitude of the free-carrier induced imaginary term[15] in the dielectric function is approximately an order of magnitude smaller than that of the real term.

[27] O. Madelung, *Semiconductors-Basic Data* (Springer, New York, 1996), p. 11.

[28] L.M. Lambert, Phys. Status Solidi A **11**, 461 (1972).

[29] V. Kuzmiak, A.A. Maradudin, and F. Pincemin, Phys. Rev. B **50**, 16 835 (1994).

[30] A. Haug and W. Schmid, Solid-State Electron. **25**, 665 (1982).

[31] Using an Auger coefficient of 1.9×10^{-31} for silicon,[32] the minimum recombination lifetime (corresponding the maximum density of 2.0×10^{19} cm^{-3}) is predicted to be approximately 13 ns, consistent with the observed time-independent plateau in the picosecond regime.

[32] J. Dziewior and W. Schmid, Appl. Phys. Lett. **31**, 346 (1977).

[33] W.C. Dash and R. Newton, Phys. Rev. **99**, 1151 (1955).

Mat. Res. Soc. Symp. Proc. Vol. 722 © 2002 Materials Research Society

Large-area porous alumina photonic crystals via imprint method

J. Choi, J. Schilling, K. Nielsch, R. Hillebrand, M. Reiche, R. B. Wehrspohn,
U. Gösele

Max–Planck–Institute of Microstructure Physics, Weinberg 2, 06120 Halle, Germany

Abstract

A perfect 2D porous alumina photonic crystal with 500 nm interpore distance was fabricated on an area of 4 cm^2 via imprint methods and subsequent electrochemical anodization. A 4' ' imprint stamp consisting of a convex pyramid array was obtained by modern VLSI processing using *DUV*-lithography, anisotropic etching, *LPCVD* Si_3N_4 deposition and wafer bonding. The optical properties of the porous alumina photonic crystal were measured with an infrared microscope in Γ-M direction. For both polarizations, a bandgap is observed at around 1 µm for $r/a = 0.42$. A reflectivity of almost unity for E-polarization in the region of the bandgap is a sign of the high quality of the structure, indicating almost no scattering losses. These experimental results could be correlated very well to the bandstructure as well as reflectivity calculations assuming a dielectric constant of $\varepsilon = 2.0$ for the anodized alumina.

Introduction

Periodic dielectric materials allowing to control the flow of light are classified as photonic crystals (PCs)[1]. After the concept of PCs was theoretically proposed, numerous papers have been published focusing on the near-IR spectral range. For extending this concept to the range of visible frequencies, new materials which are transparent in the visible and allow nano-structuring are required. Nowadays, 3-dimensional inverse opal structures [2], microperiodic polymeric structures via holographic lithography [3] and autocloning technique stacking alternatively two different materials on substrate with groove [4] are attractive to fabricate photonic crystals for visible ranges.

Due to their low absorption coefficient, excellent thermal stability and easy handling, porous alumina structures could be potential materials for photonic crystals. However, since a perfect arrangement of porous alumina channels is required for 2-D PCs, only few studies on porous alumina photonic crystals exist [5-7]. To fabricate mono-domain porous alumina structures, a method to pre-pattern the surface of aluminum before conventional anodization is a prerequisite. So far, three kinds of methods for pre-structuring have been developed: one is imprint by a dot-like stamp [8], another is e-beam lithography [9], and the other is 2-step imprint by commercial gratings [7]. For mass products in the future, imprint methods are considered to be more suitable than the e-beam lithography. However, the stamps, which have been developed for imprinting up to now, allow only small imprint areas.

Here, we will introduce a novel 4″ imprint stamp consisting of regular arrays of Si_3N_4 pyramids obtained by standard silicon processing techniques and discuss porous alumina photonic crystals as one of the possible applications.

Fabrication of a novel 4" imprint stamp.

For the imprint master stamp, a 4″ silicon wafer (100) was used as starting material. A 2D hexagonal array with a period of 500 nm on the silicon wafer was patterned by deep-*UV* lithography (248 nm). Afterward, the pattern was dipped in KOH for anisotropic etching, resulting in inversed pyramids in the silicon wafer. A replica of the Si inversed pyramids was obtained by *CVD*-deposition of Si_3N_4 layer on top of the patterned silicon. Another silicon substrate was bonded on top of the Si_3N_4 layer so that the Si_3N_4 was sandwiched between two silicon substrates. Subsequently, the initially patterned silicon substrate was removed by grinding and spin-etching. The pyramid of the master stamp with a height of about 260 nm and a lattice constant of 500 nm are shown in figures 1 (a) and (b).

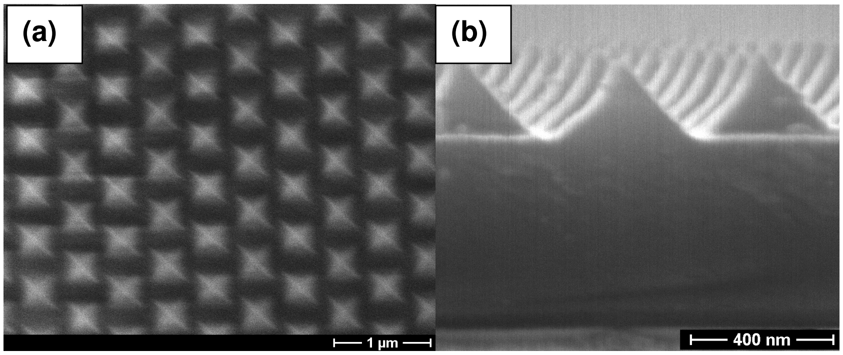

Figure 1 SEM images of a novel imprint stamp consisting of pyramids with 500 nm lattice constant and 260 nm height. (a) top view and (b) side view

The pyramidal shape of the master is very suitable to press it on electropolished aluminum surface. Typically, a pressure for indentation as low as $5kN/cm^2$ is used, which is 50 times lower than the dot-like stamp fabricated by Masuda's group [5, 10]. In figure 2, we can see inverse pyramidal holes in the aluminum surface after indentation. It indicates good pattern transfers from master stamp onto aluminum surface. The depths of the holes formed by imprinting with different pressures have been investigated by AFM depth analysis as shown in Fig. 3. In fact, a pre-patterned hole with the depth of 20 nm is sufficient to guide the position of a pore formed by subsequent anodization. From the *AFM* analysis, it can be observed that the surface roughness of pre-patterned area is much lower than that of just electropolished area. It could effectively lead to a perfect arrangement of pores at the beginning of pore formation.

Anodization of pre-patterned aluminum

The interpore distance of porous alumina is strongly influenced by the anodizing potential with a proportionality constant of around 2.5 nm/V [11]. For example, 500 nm periodic porous structures can be fabricated at 195V. Therefore, a pre-patterned aluminum with 500 nm interpore distance was subsequently anodized

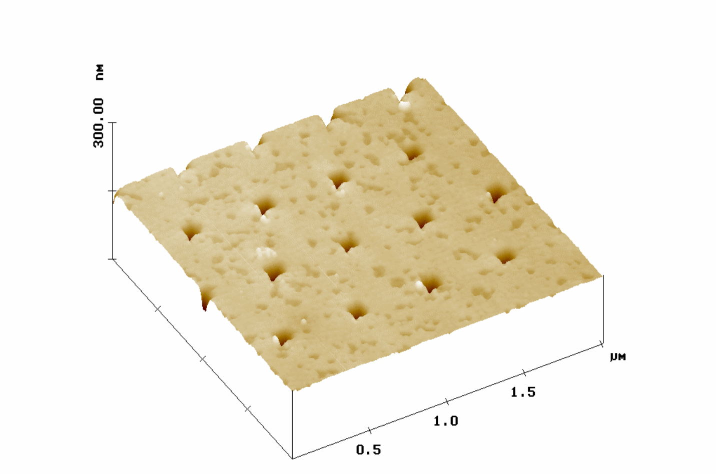

Figure 2 AFM image of inverse pyramidal holes in the surface of electropolished aluminum after imprint under 5 kN/cm^2.

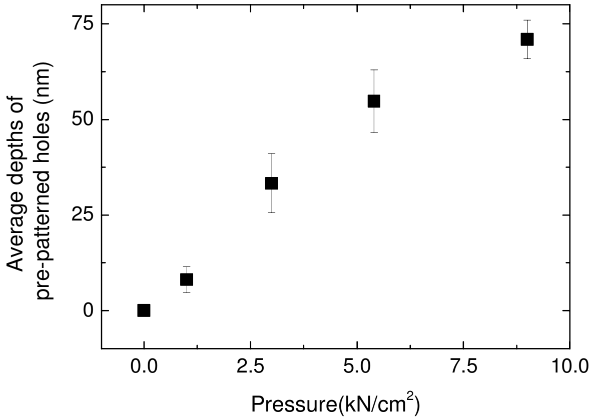

Figure 3 The relationship between imprint pressure and average depths of pre-patterned holes in the surface of aluminum.

in 1 wt% phosphoric acid at 195 V for 16h. The rate of growth of pore channels in phosphoric acid at 195 V is approximately 5 ~ 7 µm/h. In figures 4 (a) and (b), we can see perfectly arranged pores and straight pore-channels, respectively. In principle, a mono-domain of porous alumina with 4 cm^2-scale can be fabricated by our imprint method. In addition, notice that the inversed pyramidal holes shown in figure 2 change to a circular shape shown in figure 4 during the anodization. This means that the pore shape after anodization is independent of pre-pattern shape on the surface. Note that the pore shape can be control by the pre-patterning lattice such as rectangular and honeycomb [12].

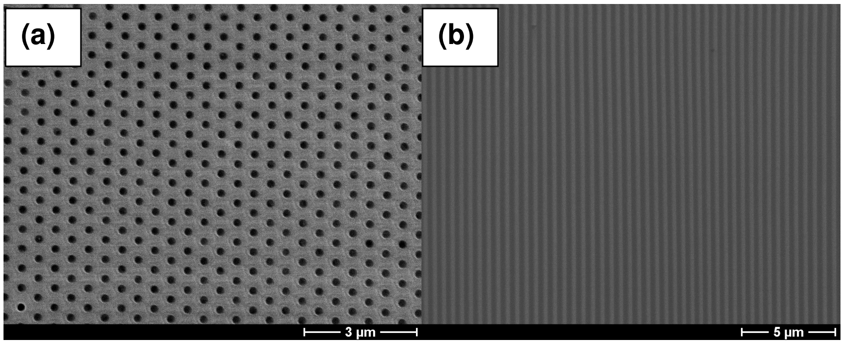

Figure 4 SEM images of a mono-domain porous alumina fabricated by anodization of pre-patterned aluminum. (a) top view and (b) side view

Optical characterization of porous alumina

For the optical characterization, the reflectivity of the porous alumina structure with r/a = 0.42 (radius / interpore distance) is measured along Γ-M direction with a FT-IR microscope. In figs. 5 (a) and (b), we compare the measured reflectivity (solid lines) and the theoretical calculation (dot lines) computed by the transfer-matrix method [13]. For both E- and H- polarization, the band-gap positions observed in the measurement are in good agreement with calculations assuming $\varepsilon = 2.0$. In addition, almost 100% reflectivity for E-polarization in the band gap is observed, indicating very low losses and high quality structures. The slightly stronger angular dependence of the H-polarization may lead to the lower reflectivity, since the IR-objective has an angular aperture of 30°.

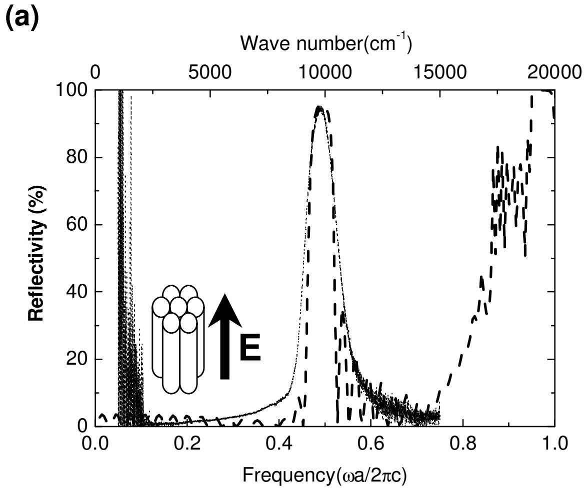

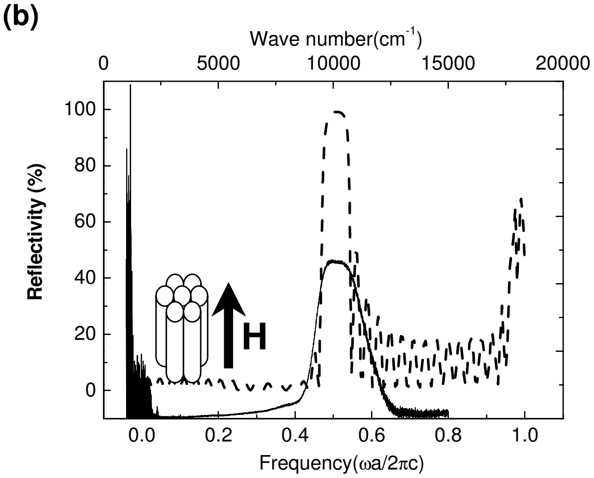

Figure 5 Reflectivity measured by FT-IR microscope (solid lines) and calculation computed by transfer matrix method assuming ε = 2.0 and 8 layers (dot lines). (a) E- polarization and (b) H- polarization.

The bandstructure of porous alumina with r/a = 0.42 is calculated by plane-wave method (figure 6). In Γ-M direction, a bandgap exists at the normalized frequency of around 0.5 in very good agreement with the experimental results and the computations of figure 5.

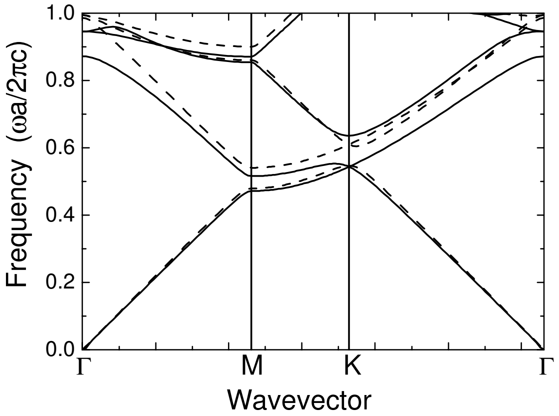

Figure 6 Bandstructure of porous alumina photonic crystals calculated by plane wave method assuming ε =2.0 when r/a = 0.42. Dash lines correspond to TE (H) polarization and solid lines to TM (E) polarization.

Conclusion

A novel 4" imprint stamp consisting of a pyramid array having a 500 nm lattice constant and 260 nm height was developed via VLSI processing. 2D porous alumina photonic crystals with 500 nm interpore distance were fabricated via imprint methods. For r/a = 0.42, a bandgap was observed at around 1 µm which was in good agreement with theoretical calculation assuming a dielectric constant of $\varepsilon = 2.0$.
In the case of E-polarization, a reflectivity of almost unity was observed, indicating almost no scattering losses and high quality structures.

Acknowledgements

The authors would like to acknowledge C. Jamois for technical assistance.

References

[1] J. D. Joannopoulos, R. D. Meade and J. N. Winn, *Photonic Crystals* (Princeton, NJ: Princeton University Press 1995).
[2] JEGJ Wijnhoven, W.L. Vos**,** Science **281**, 802 (1998).
[3] M. Campbell, D. N. Sharp, M.T. Harrison, R. G. Denning, A. J. Turberfield, Nature **404**, 53(2000).
[4] T. Sato, K. Miura, N. Ishino, Y. Ohtera, T. Tamamura, S. Kawakami S, Opt. Quant. Electron. **34**, 63(2002).
[5] H. Masuda, M. Ohya, H. Asoh, M. Nakao, M. Nohtomi, and T. Tamamura, Jpn. J. Appl. Phys. **38**, L1403 (1999).
[6] H. Masuda, M. Ohya, K. Nishio, H. Asoh, M. Nakao, M. Nohtomi, A. Yokoo and T. Tamamura, Jpn. J. Appl. Phys. **39**, L1039 (2000).
[7] I. Mikulskas, S. Juodkazis, R. Tomašiūnas, and J. G. Dumas, Adv. Mater. **13**, 1574 (2001).
[8] S. Pang, T. Tamamura, M. Nakao, A. Ozawa, and H. Masuda, J. Vac. Sci. Technol. B **16**, 1145 (1998).
[9] A.-P. Li, F. Müller, and U. Gösele, Electrochem. Solid-State Lett. **3,** 131 (2000).
[10] H. Asoh, K. Nishio, M. Nakao, T. Tamamura, H. Masuda, J. Electrochem. Soc. **148**, B152 (2001).
[11] R.B. Wehrspohn, A.P. Li, K. Nielsch, F. Müller, W. Erfurth and U. Gösele, in Oxide Films, K.R. Hebert, R.S. Lillard, B.R. Mac Dougall eds., **PV-2000-4**, Electrochemical Society, Pennington, 271, (2000).
[12] Masuda H. Asoh H. Watanabe M. Nishio K. Nakao M. Tamamura T. Adv. Mater. **13**, 189(2001).
[13] Translight package, A.L. Reynolds, University of Glasgow (http://userweb.elec.gla.ac.uk/a/areynolds/)

APPLIED PHYSICS LETTERS VOLUME 78, NUMBER 9 26 FEBRUARY 2001

Three-dimensional photonic crystals based on macroporous silicon with modulated pore diameter

J. Schilling,[a] F. Müller, S. Matthias, R. B. Wehrspohn, and U. Gösele
Max-Planck-Institut für Mikrostrukturphysik, Weinberg 2, D-06120 Halle, Germany

K. Busch
Institut für Theorie der Kondensierten Materie, Universität Karlsruhe, P. O. Box 6980, 76128 Karlsruhe, Germany

(Received 17 October 2000; accepted for publication 8 January 2001)

We report on the fabrication and optical characterization of a three-dimensional (3D) photonic crystal on the basis of macroporous silicon. The structure consists of a 2D array of air pores in silicon whose diameter is varied (modulated) periodically with depth. The bandstructure of the resulting 3D hexagonal photonic crystal is calculated and compared with transmission measurements. The described structure allows to adjust the dispersion relation along the pore axis almost independently from the dispersion relation in the plane perpendicular to the pore axis. © *2001 American Institute of Physics.* [DOI: 10.1063/1.1351533]

In the last decade photonic crystals have gained considerable interest because of their possibility to mold the flow of light.[1] Especially the localization of light in defects was investigated theoretically and experimentally. Most of this work was done with two-dimensional (2D) photonic crystals because of their ease of fabrication and introduction of defects compared to 3D photonic crystals. However 2D photonic crystals can only be used to localize light in two dimensions whereas for a complete localization of light 3D photonic crystals are required.

Here we present the fabrication of a 3D photonic crystal for infrared (IR) frequencies using macroporous silicon typically applied for the fabrication of 2D photonic crystals.[2–4] The structure consists of a 2D ordered array of air pores which were etched into a silicon wafer. Due to the fabrication process macropores with high aspect ratios (ratio between pore depth and pore diameter) of 100 and more can be achieved. For specific types of lattices such as triangular or honeycomb lattices, a complete 2D photonic band gap in the IR can be observed. However, as the structure only exhibits 2D periodicity of the refractive index it is an optically isotropic material in the direction along the pore axes. To obtain a 3D photonic crystal a periodic index variation along the pores has to be achieved. This may be realized through a periodic variation of the pore diameter with pore depth.

Our samples are fabricated using a lithographic prestructuring process. In the first step the initiation spots for the pores are defined photolithographically on the (100)-oriented *n*-type silicon wafer representing a triangular pattern. Subsequent alkaline etching forms etch pits which serve as pore nuclei. The macropores are obtained by applying a photoelectrochemical etch process.[5,6] In order to enable electrochemical dissolution of *n*-type silicon in HF, electronic holes have to be generated by light absorption. For this purpose the sample is inserted in an etch cell with its front side exposed to aqueous HF while the back side is illuminated. The sample is anodically biased via a transparent back side ohmic contact and the cathode is formed by a platinum wire immersed in the HF solution. The photogenerated holes diffuse from the wafer back side to the etch front and are consumed by the etch process at the pore tips. This promotes dissolution of the silicon almost exclusively at the pore tips leading to further pore growth perpendicular to the (100) surface. The etch velocity is determined by the local current density j_{PS} at the pore tips and depends on temperature and HF concentration at the pore tips. Increasing the illumination of the sample causes a higher hole generation rate. This results in an increased total current density j which flows over the whole sample. As the local current density j_{PS} at the pore tips remains fixed, the increased total current density j leads to a larger pore cross section and a bigger pore diameter. For our triangular lattice the porosity p of the sample can thus be calculated through

$$p=\frac{A_{\mathrm{pore}}}{A_{\mathrm{unit\ cell}}}=\frac{2\pi}{\sqrt{3}}\left(\frac{r}{a}\right)^2=\frac{j}{j_{\mathrm{PS}}}. \qquad (1)$$

Here, A_{pore} and $A_{\mathrm{unit\ cell}}$ are the pore cross section and the area of the unit cell, whereas r and a are the pore radius and the pitch, respectively. The pore radius is solely determined by the etch current j, which itself is controlled by the illumination. The pore pattern and the pitch of the pore array are, on the other hand, defined by the initial lithographic prestructuring. However, the pitch should be in the range of a few times the depletion width.[5]

To achieve a periodic variation of the pore diameter with pore depth, the illumination intensity (and with that the etch current) is varied periodically while the pores grow into the substrate. However, to obtain a uniform period of this pore diameter modulation, changes of the etch velocity during the etch process have to be considered. For instance the transport of precursors and reaction products inside the pores is governed by diffusion and results in a decrease of the HF concentration towards the pore tips. This causes a decreasing etch velocity with increasing pore depth. Therefore, to keep

---

[a] Electronic mail: schill@mpi-halle.de

0003-6951/2001/78(9)/1180/3/$18.00

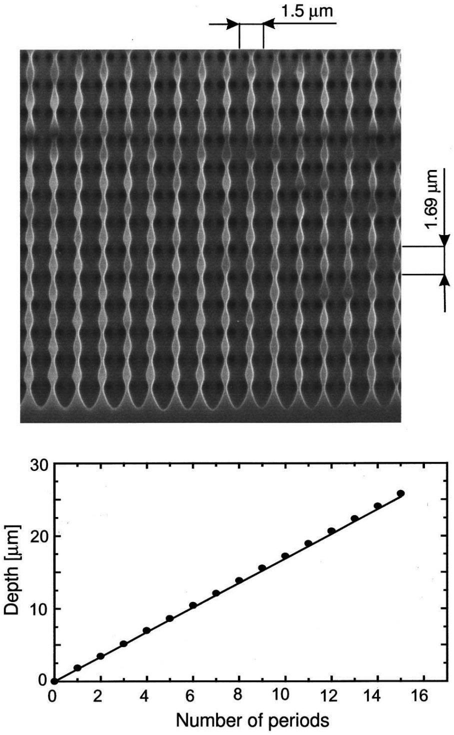

FIG. 1. (a) SEM image showing a longitudinal section of the modulated pore structure. (b) Position of the pore diameter maxima along the pore axis: • derived from SEM image; (—) linear fit.

the modulation period constant, the etching time of a period has to be adjusted with increasing pore depth. The whole etch process is *in situ* monitored by a computer which allows to control the illumination intensity in the prescribed way.

Figure 1(a) shows an example of a resulting structure. The substrate was *n*-type Si with a resistivity of 0.5 Ωcm. The macropores were arranged in a triangular lattice with a pitch of $a = 1.5\,\mu$m and were fabricated using the following etch parameters: $c_{HF} = 4$ wt %; $T = 17\,°$C; $U = 1.5$ V. The illumination of the wafer back side was modulated applying a zig-zag profile corresponding to a periodic length of $l_Z = 1.76\,\mu$m. Although the measured etch current exactly follows this profile, the etched pore profile shows a much smoother shape. The sharp minima and maxima of the current profile are smeared out. To check the uniformity of the modulation period, the positions of the pore diameter maxima along the pore axis are presented in Fig. 1(b). They can be fit very well by a line revealing an equidistant modulation period over the whole pore depth of 28.8 μm representing 17 periods. From the gradient of the curve a modulation period of $l_z = 1.69\,\mu$m was derived which is slightly reduced compared to the intended one (1.76 μm). A more detailed discussion on modulation shape and length can be found in Ref. 7.

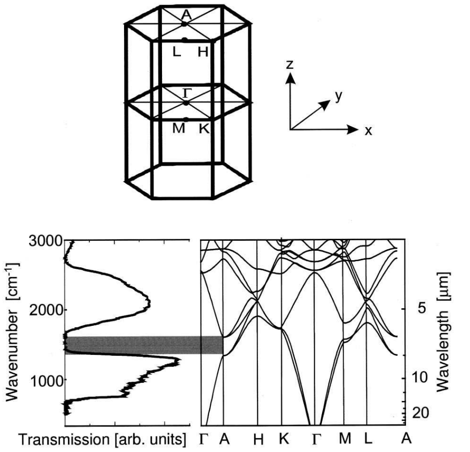

FIG. 2. (a) Hexagonal brillioun zone. (b) Transmission along Γ–A. (c) Calculated 3D band structure. The gray bar indicates the band gap in Γ–A direction and the corresponding spectral region of low transmission.

The modulated-pore array, shown in Fig. 1(a) exhibits a 3D periodic variation of the refractive index and thus forms a 3D photonic crystal with a hexagonal lattice. The hexagonal Brillioun zone is shown in Fig. 2(a). The corresponding photonic bandstructure [Fig. 2(c)] was calculated using a plane wave method with 673 plane waves. The variation of the pore radius was approximated by a sinusoidal modulation

$$r = r_0 + \Delta r \sin(2\pi z/l_z). \tag{2}$$

The parameters $r_0 = 0.63\,\mu$m ($r_0/a = 0.42$), $\Delta r = 0.08\,\mu$m ($\Delta r/a = 0.053$), $l_z = 1.69\,\mu$m ($l_z/a = 1.13$) were derived from the scanning electron microscopy (SEM) images. This results in a variation of the porosity between 81% and 49%. The convergence of the computation has been estimated to be better than 1%.

Wave vectors in the Γ–K–M plane correspond to waves travelling in the $x-y$ plane perpendicular to the pore axis. These directions correspond to the well investigated in-plane propagation in triangular 2D photonic crystals.[3,4,8] In the de-

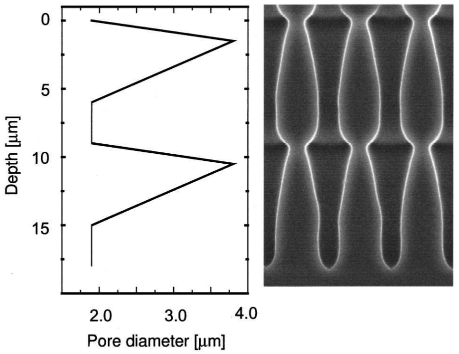

FIG. 3. (a) Two periods of the designed sawtooth-like profile (illumination modulation); (b) SEM image of the corresponding etched asymmetric pore profile.

scribed modulated structures these waves see the lateral periodicity of the 2D pore pattern and therefore the band structure for the paths Γ–M and Γ–K shows similarity with the bandstructure of a triangular 2D photonic crystal. On the contrary the path Γ–A corresponds to waves with wave vectors parallel to the pore axis. Their dispersion relation is governed by the periodic modulation of the pore diameter along the pore axis (z axis). It causes a stopgap in the Γ–A direction which can be noticed between 1350 cm^{-1} ($\lambda = 7.41\,\mu\mathrm{m}$) and 1680 cm^{-1} ($\lambda = 5.95\,\mu\mathrm{m}$) in the 3D band structure. The transmission along Γ–A was measured using a Fourier transform infrared spectrometer equipped with a glowbar, a KBr beamsplitter and a mercury cadmium telluride detector. The measured spectrum is shown in Fig. 2(b). Indeed around a wave number of 1500 cm^{-1} ($\lambda = 6.66\,\mu\mathrm{m}$) a distinct drop of the transmission can be observed. This agrees well with the theoretically predicted band gap in this region indicated by the gray shaded bar in Figs. 2(b) and 2(c).

As the modulation period is too long compared to the interpore distance of the pores, the band gap along Γ–A does not overlap with band gaps in other directions (e.g., in the Γ–M direction) and the investigated sample does not exhibit a complete 3D band gap. It is also questionable if an adjustment of the modulation period would give a complete 3D band gap. For this, band gaps in the oblique Γ–H and Γ–L directions are also necessary which have to overlap with the band gap along Γ–A and with a band gap in the Γ–K–M plane.

Nevertheless the described structure has another distinct property: The modulation period along the pore axis (z axis) can be independently controlled from the periodicity perpendicular to it ($x-y$ plane). The band gap along the pores can easily be tuned by the adjustment of the modulation period and with this also the whole band structure along Γ–A is shifted. The dispersion relation along the z axis can thus be adjusted compared with the dispersion relation in the $x-y$ plane simply by the right choice of the modulation period.

Additionally, the shape of the pore diameter modulation represents a further degree of freedom. Besides the already presented symmetric sinusoidal modulation profile, other profiles could be achieved by controlling the illumination during the etch process in a different way. By application of a sawtooth-like illumination profile [Fig. 3(a)] the asymmetric pore diameter modulation shown in Fig. 3(b) was obtained.[9] Such asymmetric profiles reduce the symmetry of the hexagonal lattice. The reduced symmetry influences the photonic band structure of the 3D crystal and is a topic of current theoretical investigations.

In conclusion we presented a method for the fabrication of 3D photonic crystals on the basis of macroporous silicon by modulation of the pore diameter. By adjustment of the modulation period the dispersion relation along the pore axis can be controlled nearly independently from the dispersion relation in the plane perpendicular to it.

One author (K.B.) acknowledges the financial support of the Deutsche Forschungsgemeinschaft under Bu 1107/2-1 (Emmy-Noether program).

[1] J. D. Joannopoulos, R. D. Meade, and J. N. Winn, *Photonic Crystals* (Princeton University Press, Princeton, New Jersey, 1995).
[2] U. Grüning, V. Lehmann, and C. M. Engelhardt, Appl. Phys. Lett. **66**, 3254 (1995).
[3] A. Birner, U. Grüning, S. Ottow, A. Schneider, F. Müller, V. Lehmann, H. Föll, and U. Gösele, Phys. Status Solidi A **165**, 111 (1998).
[4] S. Rowson, A. Chelnokov, C. Cuisin, and J.-M. Lourtioz, IEE Proc.-J: Optoelectron. **145**, 403 (1998).
[5] V. Lehmann, J. Electrochem. Soc. **140**, 2836 (1993).
[6] V. Lehmann and H. Föll, J. Electrochem. Soc. **137**, 653 (1990).
[7] F. Müller, A. Birner, J. Schilling, U. Gösele, Ch. Kettner, and P. Hänggi, Phys. Status Solidi A **182**, 585 (2000).
[8] J. Schilling, A. Birner, F. Müller, R. B. Wehrspohn, R. Hillebrand, U. Gösele, K. Busch, S. John, S. W. Leonard, and H. M. van Driel, Opt. Mater. (to be published).
[9] F. Müller, A. Birner, J. Schilling, R. B. Wehrspohn, and U. Gösele, Adv. Solid State Phys. **40**, 545 (2000).

Mat. Res. Soc. Symp. Proc. Vol. 722 © 2002 Materials Research Society

Dispersion relation of 3D photonic crystals based on macroporous silicon

J. Schilling, F. Müller, R.B. Wehrspohn, U. Gösele, K. Busch[1]
Max-Planck Institute of Microstructure Physics, Weinberg 2, 06120 Halle, Germany
[1] Institut für Theorie der Kondensierten Materie, Universität Karlsruhe, P.O. Box 6980,76128 Karlsruhe, Germany

ABSTRACT

Extended 3D photonic crystals based on macroporous silicon are prepared by applying a periodic variation of the illumination during photoelectrochemical etching. If the lateral pore arrangement is 2D hexagonal, the resulting structure exhibits a simple 3D hexagonal symmetry. The dispersion relation along the pore axis is investigated by optical transmission measurements. Photonic band gaps originating from the pore diameter modulation are observed and the group velocities of the photonic bands are determined by analyzing the Fabry-Perot resonances. Furthermore, angular resolved transmission measurements show a spectral region of omnidirectional total reflectivity.

INTRODUCTION

2D macroporous silicon photonic crystals have been extensively studied in the last seven years since the the pioneering work of Lehmann and Grüning [1,2]. A recent review is given by Schilling et al. [3]. The concept to obtain 3D photonic crystal by pore diameter modulation has already been predicted seven years ago [4], but just recently we have shown the first realizations of these 3D photonic crystals [5]. In the following we are going to analyze the optical properties in detail.

FABRICATION OF THE 3D PHOTONIC CRYSTALS

The fabrication of 2D macroporous silicon photonic crystal is described in Refs. 1-4. The pattern and the pitch of the 2D pore array are defined by lithographic prestructuring. The pore radius is determined by the etch current and can therefore be controlled by the backside illumination. Increasing the illumination of the sample causes a higher hole generation rate. This results in an increased total current density j leading to a higher porosity and a larger radius of the pores. To achieve a periodic variation of the pore diameter with pore depth, the illumination intensity and thus the etch current is varied periodically during pore growth. Figure 1 shows examples of resulting structures. The macropores are initially arranged in a 2D hexagonal lattice with a pitch of $a = 1.5$ µm (figure 1e). The etch parameters are: $c_{HF} = 4$ wt%; $T = 17$°C; $U = 1.5$ V. The illumination of the wafer backside was modulated applying zig-zag profiles with different periods. Shorter modulation periods of the illumination lead to shorter periods of the pore diameter modulation. Although the measured etch current exactly follows the intended zig-zag profile, the etched pore profiles show a slightly smoother shape. Especially for the shortest shown modulation period the minima and maxima of the zig-zag current profile are smeared out and the amplitude of the pore diameter modulation is reduced.

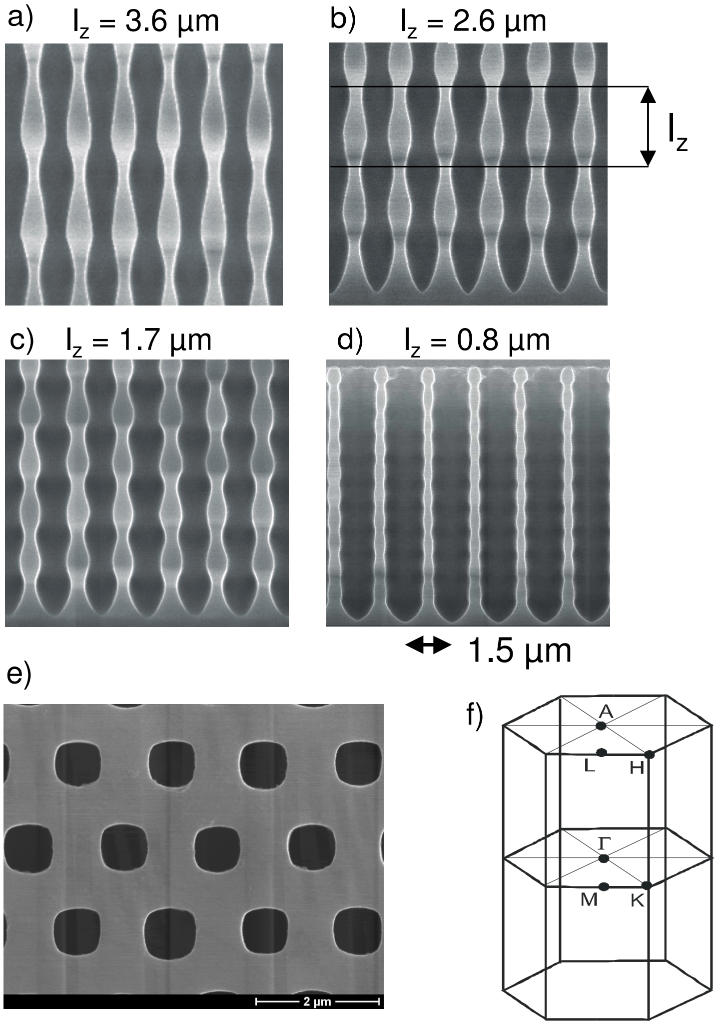

Figure 1. a)-d) SEM-images of cross sections of four different samples with different modulation periods l_z. e) Top view revealing the 2D hexagonal (triangular) ordering of the pores and the pore shape. f) 3D hexagonal Brillouin zone of the resulting simple 3D hexagonal photonic crystal assuming circular pores.

OPTICAL PROPERTIES

Assuming a circular pore cross section and a sinusoidal modulation of the pore radius r with $r=r_0+\Delta r \sin(2\pi z/l_z)$, the structure possesses a simple 3D hexagonal symmetry. The first Brillouin zone is shown in figure 1f. However, thorough analysis of figure 1e suggests that the pore form is not perfectly round but resembles more like squares with rounded edges. This squareness leads to a reduction of symmetry of the photonic crystal and a splitting of originally degenerate photonic bands [6]. Nevertheless, for the sake of simplicity, we assume in the following that the pores are circular which is a good approximation of the complete analysis [6].

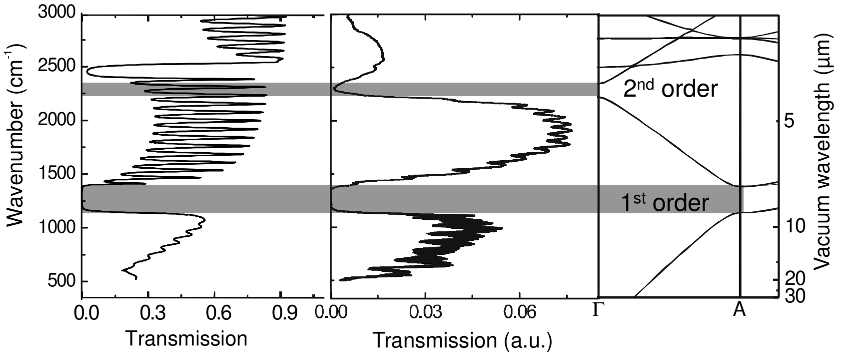

Figure 2. Transmission along pore axis (Γ-A direction) for a structure with a = 1.5µm, l_z = 2µm, r_0 = 0.62 µm, Δr = 0.09 µm . Left: calculation applying a 1D effective refractive index model: centre: transmission measurement: right: section of 3D band structure calculation.

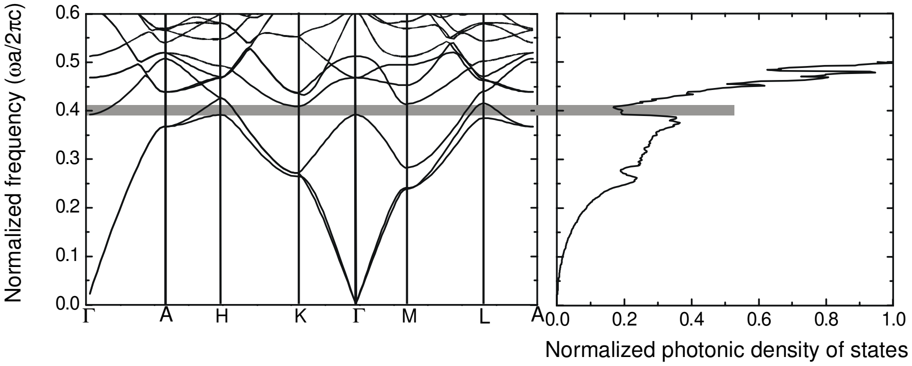

Figure 3. Left: 3D band structure for a modulated pore structure with l_z/a = 0.55, r/a = 0.42 and $\Delta r/a$ = 0.06. Right: normalised density of photonic states.

The dispersion relation for light propagating along the pore axis (Γ-A direction) is governed by the modulation period of the pore diameter. Therefore, optical transmission measurements with normal incidence were performed (figure 2, centre). Two spectral regions of vanishing transmission are observed as indicated by the gray bars. These regions are in good agreement with the first and second order bandgaps in the Γ-A section of the 3D band structure. The transmission along the pore axis can also be calculated approximating the structure by a 1D model. The structure was divided into several thin layers stacked in z-direction. For each of these layers an effective refractive index is calculated applying the Maxwell-Garnet formula. The transmission for this model is analytically calculated by the transfer matrix method (figure 2 left). The spectral range of the vanishing transmission around 1250cm^{-1} coincides very well with the first order band gap observed in the 3D calculation and in the transmission measurement. However, the second order bandgap at 2250cm^{-1} is shifted to higher frequencies in the 1D transmission calculation. This indicates that at higher frequencies the Maxwell-Garnet formula fails. The lateral periodicity of the refractive index in the xy-plane can no longer be neglected. To investigate if the structure might exhibit a complete 3D photonic bandgap, the band structure for a photonic crystal with the parameters $l_z/a = 0.55$, $r/a = 0.42$ and $\Delta r/a = 0.06$ was calculated (figure 3). In this case, the bandgap in the Γ-M-K-plane overlaps with the first order gap at the A-point. However, a complete 3D band gap does not exist since near the H and L points, as well as at the Γ-point photonic bands cross this spectral region. Even widening of the pores to $r/a > 0.5$ at places with maximum pore radius would not yield a complete 3D photonic bandgap. Nevertheless, a reduction of the photonic density of states by 50 % is theoretically possible (figure 3).

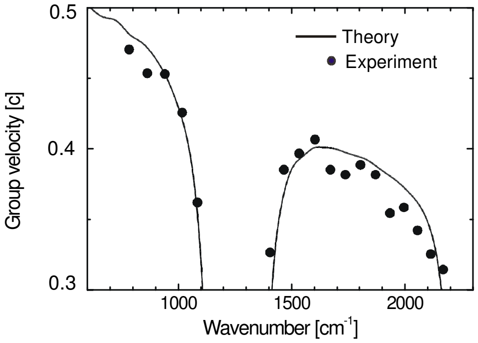

Fig. 4: Comparison of the experimentally determined group velocity with that obtained from 3D band structure calculations for the structure from Fig. 2.

Besides the position of the band gaps, the transmission measurements along the pore axis contain also information about the dispersion relation of the photonic bands in the Γ-A direction. Below and above the first order bandgap, the transmission curves exhibits pronounced oscillations (figure 2). These are Fabry-Perot resonances, which are caused by multiple reflections of the light between the surface air/photonic crystal and the interface photonic crystal/ bulk silicon substrate. The spacing between neighboring Fabry-Perot resonances in the k-space $\Delta k_{\max}^{phot.cryst}$ and in the frequency space $\Delta\omega_{\max}$ of the photonic crystal read

$$\Delta k_{\max}^{phot.cryst} = \frac{\pi}{d} \; ; \Delta\omega_{\max} \approx \frac{\partial\omega}{\partial k} \Delta k_{\max}^{phot.cryst} \tag{1}$$

where d describes the pore depth or the thickness of the photonic crystal. Merging these two relations, the dispersion relation in Γ-A direction of the photonic bands can be obtained purely from the experimentally determined values $\Delta\omega_{max}$ and d. The group velocity v_g along Γ-A is the derivative of ω with respect to $k_{\Gamma-A}$

$$v_g = \frac{\partial\omega}{\partial k_{\Gamma-A}} \approx \Delta\omega_{\max} \frac{d}{\pi} \tag{2}$$

Figure 4 shows a comparison of the experimentally determined and the calculated group velocities. The latter one has been obtained by taking the derivative $\partial\omega / \partial k$ of the photonic bands in the band structure in figure 2. Good agreement between theory and experiment is observed. The group velocity decreases near the first order photonic band gap around 1250 cm^{-1}, as expected. Further optical properties of this 3D photonic crystal can be revealed performing angular resolved transmission measurements. To select those modes of the photonic crystal which can couple to outside radiation incident from the top surface (Γ-A surface), the light cone has to be considered. The light cone corresponds to an angle of incidence of $\alpha = 90°$ from the Γ-A direction (dashed oblique lines in figure 5). All modes of the photonic band structure which lie below the light cone in the gray shaded area are "bound" modes. They can not be excited by radiation incident from the Γ-A surface under any angle. Only the white part of the band structure is of interest. Thorough inspection reveals a spectral range (indicated by the horizontal dashed bar) with no photonic bands in the white region. No photonic crystal modes are available which could be excited by incident radiation. All the radiation incident to the top Γ-A surface with frequencies in this range should therefore be totally reflected. This is called omnidirectional total reflection [7]. To verify this experimentally, transmission measurements were performed for angles of incidence $\alpha = 0°$ and $\alpha = 70°$. The sample was tilted towards the Γ-M and the Γ-K direction and s- and p-polarization were separately measured. Figure 6 shows exemplarily the transmission for a tilt towards the Γ-M direction. In the range 1300 $cm^{-1} < \omega < 1380$ cm^{-1} all transmission spectra show vanishing transmission corresponding to total reflection. This spectral region represents the overlap of the band gaps for the radiation incident under $\alpha = 0°$ and $\alpha = 70°$. It agrees very well with the horizontal dashed bar indicating the spectral range of omnidirectional total reflection. Strictly speaking these experimental results confirm only total reflection for incidence angles $0° < \alpha < 70°$. However, the transmission curves for grazing incidence ($\alpha = 90°$) will not differ significantly from the ones with $\alpha = 70°$ as can be seen from the intersections of the incidence lines for $\alpha = 90°$ (light cone) and $\alpha = 70°$ with the second photonic band. Compared to the intersection of the incidence line for $\alpha = 70°$ with the second band, there is a shift of 1.6% to lower frequencies. Taking this small shift into account, a region of omnidirectional total reflection between 1321 $cm^{-1} < \omega < 1380$ cm^{-1} with a spectral width of $\Delta\omega/\omega = 4.4\%$ has been determined experimentally.

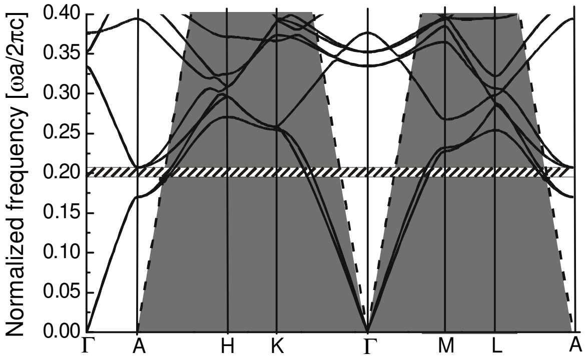

Figure 5. 3D band structure for a structure with $l_z/a = 1.33$, r/a = 0.42 and $\Delta r/a = 0.06$.The oblique dashed lines represent the light cone. The gray shaded area below contains the photonic modes bound to the photonic crystal. They can not couple to the incident radiation. The horizontal dashed bar indicates the spectral range of omnidirectional total reflection.

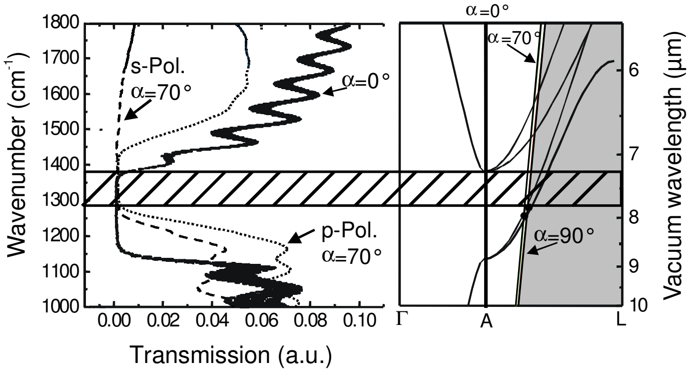

Figure 6. Comparison of angular dependent transmission measurements with band structure. The incident beam was tilted towards the Γ-M direction. The spectral region of omnidirectional total reflection is indicated by the horizontal dashed bar. It is derived from the band structure on the right and corresponds very well with the range of zero transmission for all experimental transmission curves

CONCLUSION

3D photonic crystals based on macroporous silicon have been fabricated by periodical variation of the pore diameter with the pore depth. This was achieved by periodic modulation of the illumination intensity during the photoelectrochemical pore etching process. Transmission measurements along the pore axis revealed photonic bandgaps which originate from the pore diameter modulation. By analysis of the Fabry-Perot resonances in the transmission curves the group velocity along the Γ-A direction for the lower bands could be determined. Angular resolved transmission measurements show that the modulated pore structure act as omnidirectional reflector in very good agreement with theory.

The authors acknowledge the financial support by the DFG in the framework of the focused program on photonic crystals (SPP 1113).

REFERENCES

[1] U. Grüning, V. Lehmann, and C.M. Engelhardt, *Appl. Phys. Lett.* **66**, 3254 (1995).
[2] U. Gruning, V. Lehmann, S. Ottow, and K. Busch, *Appl. Phys. Lett.* **68**, 747 (1996).
[3] J. Schilling et al., *J. Opt. A: Pure Appl. Opt*. **3**, 121 (2001).
[4] H.W. Lau, G.J. Parker, R.Greef, and M. Hölling, *Appl. Phys. Lett*. **67**, 1877 (1995).
[5] J. Schilling, F. Müller, S. Matthias, R.B. Wehrspohn, U. Gösele, and K. Busch, *Appl. Phys. Lett.* **78,** 1180 (2001).
[6] J. Schilling, unpublished results (2002).
[7] C. Chigrin, A. Lavrinenko, D.A. Yarotsky, and S. Gaponenko, *J. Lightwave Techn*. **17**, 2018 (1999)

APPLIED PHYSICS LETTERS VOLUME 79, NUMBER 9 27 AUGUST 2001

Hexagonally ordered 100 nm period nickel nanowire arrays

K. Nielsch,[a] R. B. Wehrspohn, J. Barthel, J. Kirschner, and U. Gösele
Max-Planck-Institute of Microstructure Physics, Weinberg 2, 06120 Halle, Germany

S. F. Fischer and H. Kronmüller
Max-Planck-Institute of Metal Research, Heisenbergstrasse 1, 70569 Stuttgart, Germany

(Received 9 November 2000; accepted for publication 6 July 2001)

The magnetic behavior of 100 nm period arrays of Ni nanowires embedded in a highly ordered alumina pore matrix were characterized by magnetometry and magnetic force microscopy. Reducing the diameter of the nanowires from 55 to 30 nm while keeping the interwire distance constant leads to increasing coercive fields from 600 to 1200 Oe and to increasing remanence from 30% to 100%. The domain structure of the arrays exhibits in the demagnetized state a labyrith-like pattern. These results show that stray field interactions of single domain nanowires are entirely dependent on the nanowire diameter. © *2001 American Institute of Physics.* [DOI: 10.1063/1.1399006]

Since 1991, the increase in storage density for commercially available hard disks has been 60% per year. Nowadays, hard disks with an areal density of about 10 Gbit/in.[2] are commercially available, and a number of companies have demonstrated densities ranging up to 50 Gbit/in.[2] in their laboratories. If the increase in areal density continues, the predicted superparamagnetic limit of about 70 Gbit/in.[2] might be reached for products in a few years.[1] One approach to extend this limit is via patterned perpendicular media,[2–5] in which one bit of information corresponds to one single domain nanosized particle, a so-called nanomagnet. Since each bit would be composed of a single high-aspect particle, the areal density of these patterned media can, in principle, be much more than one order of magnitude higher than in conventional longitudinal media. For example, an areal density of about 300 Gbit/in.[2] can be achieved by a hexagonally arranged array of nanomagnets with a lattice constant of about 50 nm.

One promising technique with which to obtain nanomagnet arrays is based on hexagonally arranged porous alumina templates.[6–12] Since 1981 there have been numerous publications about ferromagnetic-material-filled unarranged porous alumina templates.[6–11] These structures have large pore diameter size distributions and interpore distances and the degree of filling of the pores is not specified. Based on an approach by Masuda and Fukuda,[13] we have shown that ordered porous alumina arrays with a sharply defined pore diameter can be obtained by a two-step electrochemical anodization aluminum process.[14,15] The degree of self-ordering is polydomain with a typical domain size of a few microns. The interpore distance ($D_{\mathrm{int}}=50-500\,\mathrm{nm}$), the pore diameter ($0.3\times D_{\mathrm{int}}<D_p<D_{\mathrm{int}}$) and the length (0.2–200 μm) can be varied over a wide range.[13–15] Using pulsed electrodeposition, we homogeneously filled Ni and Co into porous alumina templates[12] (Fig. 1). Ferromagnetic nanowires (light) are embedded into the porous alumina matrix (dark). Nearly 100% pore filling was obtained for all samples.[12] The nanowires consist of nanocrystallites of between 20 and 100 nm which have a mostly tetrahedral shape, a face-centered-cubic (fcc) lattice, and preferential ⟨110⟩ orientation perpendicular to the nanowire axis as determined by high-resolution transmission electron microscopy.

The field dependent magnetization hysteresis was measured for three Ni-filled samples at room temperature by a superconducting quantum interference device (SQUID) magnetometer. Figure 2 shows the hysteresis loops of hexagonally ordered Ni nanowire arrays with a pitch of 100 nm, a nanowire length of 1 μm, and pore diameters of about $D_p=55\,\mathrm{nm}$ (sample A), 40 nm (sample B), and 30 nm (sample C). The external field was applied parallel (‖) and perpendicular (⊥) to the long axes of the nanowires. The hysteresis for sample A measured in the ‖ direction shows a coercive field of $H_C^{\parallel}\approx 600\,\mathrm{Oe}$ and squareness of about 30% [Fig. 2(a)]. For the ⊥ direction the hysteresis shows a low coercive field of $H_C^{\perp}\approx 100\,\mathrm{Oe}$. The hysteresis for both directions exhibits similar saturation fields ($H_s^{\parallel}\approx 4000\,\mathrm{Oe}$). Therefore, this sample does not have a preferential magnetic orientation. In contrast, sample B exhibits increased coercive fields of about $H_C^{\parallel}=1000\,\mathrm{Oe}$ and improved magnetic hardness (≈80% squareness). This sample has a preferential magnetic orientation along the wire axis ($H_S^{\parallel}\approx 3200$, $H_S^{\perp}\approx 5500\,\mathrm{Oe}$, and $H_C^{\parallel}\gg H_C^{\perp}$). With sample C($D_p=30\,\mathrm{nm}$) squareness of 98% and the highest coercive field $H_C^{\parallel}=1200\,\mathrm{Oe}$ [Fig. 2(c)], which is the highest reported coercivity for a high-density

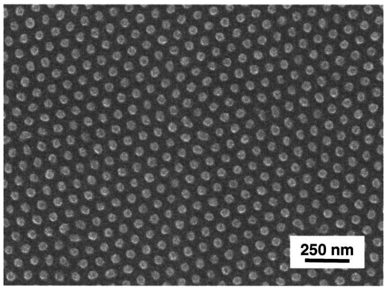

FIG. 1. Top-view scanning electron micrograph of a Ni-filled alumina membrane (sample B) with a pitch of 100 nm and $D_p\approx 40\,\mathrm{nm}$.

---

[a] Electronic mail: elch@mpi-halle.de

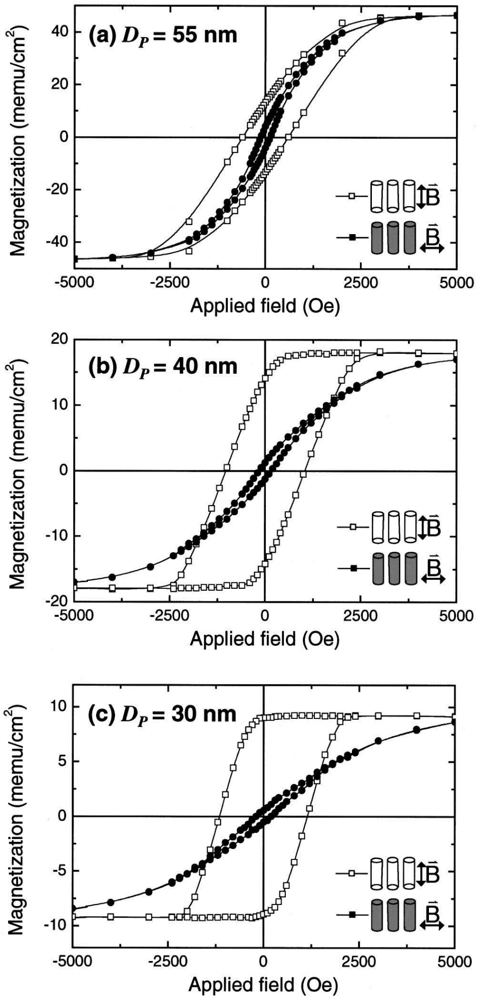

FIG. 2. SQUID hysteresis loops for hexagonally ordered Ni nanowire arrays with a pitch of 100 nm and pore diameters of $D_p \approx 55$ (a), ≈ 40 (b), and ≈ 30 nm (c).

($D_{\mathrm{int}} \leqslant 100$ nm) Ni nanowire array,[3–6,11] were obtained. Samples B and C have a similar magnetic anisotropy. In the following, the bulk value of the saturation magnetization $M_S = 484$ emu/cm^3 is used. By determining the absolute amount of nickel in the pores by atom absorption spectroscopy and relating it to the absolute magnetization by SQUID magnetometry, we obtain $M_S = 480 \pm 25$ emu/cm^3.

The magnetic anisotropy of an array of thin magnetic wires results from the interplay of a series of effective fields. In the case of a single domain wire, which is expected for Ni with diameters smaller than 55 nm,[16] we have to consider three contributions: (1) the macroscopic demagnetization field due to the average magnetic charges of the wires at the surface. For Ni and the geometry of the hexagonal pore structure the average derived demagnetization field ($-4\pi M_S P$; $P \cong$ porosity of the template structure) is about -1750 Oe for 55 nm pores, -920 Oe for 40 nm pores, and -520 Oe for 30 nm pores. (2) The form effect of the individual wire if magnetized parallel to the pore axis is of the order of $2\pi M_S = 3200$ Oe. (3) A third contribution results from the magnetocrystalline anisotropy energy, given by $(-)4K_1/3M_S \cong 120$ Oe for Ni with K_1 the magnetocrystalline anisotropy.

Reducing the pore diameter from 55 to 30 nm while keeping the interpore distance constant, the remanence increases up to nearly 100% and the coercive field shifts towards 1200 Oe. Sample B with $D_p = 40$ nm and sample C with $D_p = 30$ nm are single domain wires, which are preferentially magnetized in the $\|$-direction because the form effect of 3200 Oe easily overcomes the crystal field of 120 Oe. The theoretical effective coercive field of a single infinitely extended cylinder magnetized parallel to the $\langle 111 \rangle$ easy direction of the Ni cylinder axis for homogeneous rotation is given by $H_c^{\|} = 4K_1/3M_s + 2\pi M_s$. This holds if the cylinder diameter is smaller than the critical diameter D_{crit} for the curling process,[17] $D_p \leqslant D_{\mathrm{crit}} = 3.68\sqrt{A/\pi M_S^2}$ ($A = 8.6 \times 10^{-7}$ erg/cm for Ni) yielding for Ni $D_{\mathrm{crit}} = 40$ nm. Therefore, the curling mode is not an appropriate description for the magnetization of samples *B* and *C*. In addition, the demagnetizing field, $4\pi M_s P$, of the arrays has to be taken into account. By neglecting the magnetocrystalline anisotropy, one obtains $H_C^{\|} = 2\pi M_s(1-2P)$ which is for $D_p = 40$ nm $\rightarrow H_C^{\|} = 2100$ Oe and for $D_p = 30$ nm $\rightarrow H_C^{\|} = 2500$ Oe. The measured smaller coercive fields of ≈ 1000 and ≈ 1200 Oe indicate that the Stoner–Wohlfarth approximation of the switching fields is not valid. Holz[18,19] showed that at the wire ends a butterfly-type arrangement of magnetization exists which reduces the switching field considerably. Recently, it was shown by computer simulation[20,21] that for an aspect ratio of 20:1 and $D_p \approx 40$ nm the nucleation field is reduced by about a factor of 2 which agrees rather well with the results for the 40 nm wires. Experimental results obtained for isolated wires also agree reasonably well with the computer simulation.[22] In the case of an array of nanowires, in addition, collective demagnetization modes have to be taken into account which leads to a further decrease of the switching field.[23] The micromagnetic modeling reported by Hertel[23] results in coercive fields of 1400 Oe for a single Ni wire and about 1100 Oe and remanence of 100% for a hexagonal 100 nm period Ni wire array composed of 16 nanowires with diameters of about 40 nm. These values are in good agreement with our data.[23]

The observed squareness of less than 100% for sample B might result from imperfections of the polydomain pore array. The demagnetization field can locally overcome the switching field of an individual magnetic wire. These single nanomagnets will reverse their magnetic polarization to achieve a lower energetic state and to reduce their demagnetization field. This is observed for $D_p = 40$ nm (sample B), where approximately 10% of the nickel columns switch their magnetic polarization into the opposite direction after the whole sample has been magnetized along the wire axis when the applied field is zero.

In contrast, the same templates filled with cobalt exhibit

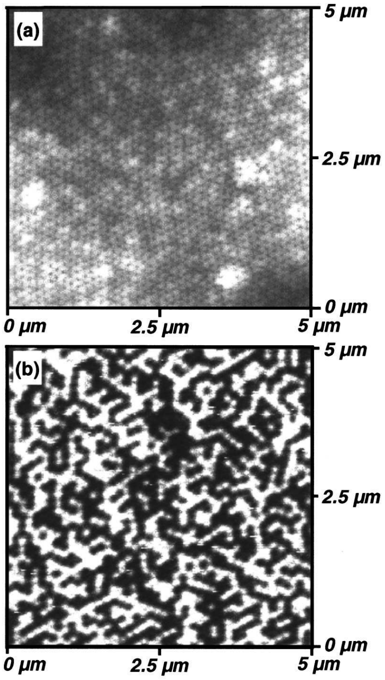

FIG. 3. Topographic image of a highly ordered alumina template with a pitch of 100 nm filled with $D_p \approx 40$ nm Ni nanowires (a). The corresponding MFM image (b) of the sample in the demagnetized state, showing the pillars magnetized alternately "upward" (light) and "downward" (dark).

low coercive fields ($H_C^{\|} < 500$ Oe) and high saturation fields ($H_S^{\|} > 5000$ Oe).[24] Like Metzger *et al.*,[25] we observe a strong interaction between the nanowires and a preferential magnetocrystalline anisotropy perpendicular to the wire axis. As long as the crystalline orientation cannot be controlled, Co is not a suitable candidate for perpendicular storage media, in line with Ref. 25.

A magnetic force microscopy (MFM) image of sample B in the demagnetized state and the corresponding topography are shown in Fig. 3. Dark spots in Fig. 3(b) indicate magnetization pointing upward and bright spots indicate magnetization pointing downward. Upward magnetization may be interpreted as the binary "1" and downward magnetization as the binary "0." It can be deduced from the image that the Ni pillars are single domain nanomagnets aligned perpendicular to the surface. The patterned domain structure is due to antiferromagnetic alignment of the pillars influenced by the weak magnetic interaction between these nanomagnets. The labyrinth pattern [Fig. 3(b)] of the domain structure is characteristic of a hexagonally arranged single domain magnetic particle with perpendicular magnetic orientation in the demagnetized state. In the case of a quadratic lattice, each of the four nearest neighbors will be aligned antiparallel and the domain structure exhibits a checkerboard pattern.[5] In the hexagonal lattice, two of the six nearest neighbors will align their magnetization parallel and four will be magnetized antiparallel if the stray field has only nearest neighbor interaction. In Fig. 3, we observe that, on average, 2.5 nanomagnets are aligned parallel and 3.5 are magnetized antiparallel. We suppose that stray field interaction is extended over several interpores due to the high aspect ratio of the magnetic nanowires.

In conclusion, the bulk magnetic properties of Ni nanowires arranged in a hexagonal pattern with a pitch of 100 nm were studied by SQUID magnetometry. Reducing the diameter of magnetic columns from $D_p = 55$ to 30 nm improves the hardness of the magnetic hysteresis and raises the coercivity from 600 up to 1200 Oe. This is due to a reduction in macroscopic interactions between the nanomagnets and enhancement of the switching field of the individual nanowire. The domain structure of highly ordered arrays of Ni columns is labyrinth like. Each magnetic pillar is a single domain magnetic particle, magnetized perpendicular to the template surface. Due to the fact that 100% squareness and low stray field interactions were detected for the sample with $D_p \approx 30$ nm, we expect that for this sample each Ni nanowire is able to be switched independently to the magnetization of its nearest neighbors and store one bit of information.

The authors would like to thank Dr. R. Hertel for fruitful discussions concerning magnetic modeling.

[1] D. Weller and A. Moser, IEEE Trans. Magn. **35**, 4423 (1999).
[2] R. O'Barr, S. Y. Yamamoto, S. Schultz, W. Xu, and A. Scherer, J. Appl. Phys. **81**, 4730 (1997).
[3] S. Y. Chou, M. S. Wei, P. R. Krauss, and P. B. Fischer, J. Appl. Phys. **76**, 6673 (1994).
[4] C. A. Ross, H. I. Smith, T. A. Savas, M. Schattenberg, M. Farhoud, M. Hwang, M. Walsh, M. C. Abraham, and R. J. Ram, J. Vac. Sci. Technol. B **17**, 3168 (1999).
[5] M. Hwang, M. C. Abraham, T. A. Savas, H. I. Smith, R. J. Ram, and C. A. Ross, J. Appl. Phys. **87**, 5108 (2000).
[6] M. P. Kaneko, IEEE Trans. Magn. **MAG-17**, 1468 (1981).
[7] M. Shiraki, Y. Wakui, T. Tokushima, and N. Tsuya, IEEE Trans. Magn. **MAG-21**, 1465 (1985).
[8] D. AlMawlawi, N. Coombs, and M. Moskovits, J. Appl. Phys. **69**, 5150 (1991).
[9] L. Feiyue, R. M. Metzger, and W. D. Doyle, IEEE Trans. Magn. **33**, 3715 (1997).
[10] G. J. Strijkers, J. H. J. Dalderop, M. A. A. Broeksteeg, H. J. M. Swagten, and W. J. M. de Jonge, J. Appl. Phys. **86**, 5141 (1999).
[11] H. Zeng, M. Zheng, R. Skomski, D. J. Sellmyer, Y. Liu, L. Menon, and S. Bandyopadhyay, J. Appl. Phys. **87**, 4718 (2000).
[12] K. Nielsch, F. Müller, A. P. Li, and U. Gösele, Adv. Mater. **12**, 582 (2000).
[13] H. Masuda and K. Fukuda, Science **268**, 1466 (1995).
[14] A. P. Li, F. Müller, A. Birner, K. Nielsch, and U. Gösele, J. Appl. Phys. **84**, 6023 (1998).
[15] A. P. Li, F. Müller, and U. Gösele, Electrochem. Soc. Lett. **3**, 131 (2000).
[16] *Supermagnets, Hardmagnetic Materials*, edited by G. J. Long and F. Grandjean (Kluwer Academic, Dordrecht, 1991), pp. 461–498.
[17] A. Aharoni and S. Shtrikman, Phys. Rev. **109**, 1522 (1958).
[18] A. Holz, Z. Angew. Phys. **23**, 170 (1967).
[19] A. Holz, Phys. Status Solidi **26**, 751 (1968).
[20] C. Seberino and H. N. Bertram, IEEE Trans. Magn. **33**, 3055 (1997).
[21] H. Suhl and H. N. Bertram, J. Appl. Phys. **82**, 6128 (1997).
[22] R. O'Barr and S. Schultz, MMM'96, Atlanta, 1996.
[23] R. Hertel, J. Magn. Magn. Mater. (in press).
[24] K. Nielsch, F. Müller, R. B. Wehrspohn, U. Gösele, S. F. Fischer, and H. Kronmüller, *Proceedings of the Electrochemical Society*, Series PV 2000-8 (The Electrochemical Society, Pennington, NJ, 2000).
[25] R. M. Metzger, V. V. Konovalov, M. Sun, T. Xu, G. Zangari, B. Xu, M. Benakli, and W. D. Doyle, IEEE Trans. Magn. **36**, 30 (2000).

VOLUME 89, NUMBER 2 PHYSICAL REVIEW LETTERS 8 JULY 2002

Spin-Wave Quantization in Ferromagnetic Nickel Nanowires

Z. K. Wang, M. H. Kuok,* and S. C. Ng
Department of Physics, National University of Singapore, Singapore 117542, Republic of Singapore

D. J. Lockwood
Institute for Microstructural Sciences, National Research Council, Ottawa, K1A 0R6, Canada

M. G. Cottam
Department of Physics and Astronomy, University of Western Ontario, London, Ontario N6A 3K7, Canada

K. Nielsch, R. B. Wehrspohn, and U. Gösele
Max-Planck-Institute of Microstructure Physics, Weinberg 2, D-06120 Halle, Germany
(Received 31 January 2002; published 19 June 2002)

The dynamical properties of uniform two-dimensional arrays of nickel nanowires have been investigated by inelastic light scattering. Multiple spin waves are observed that are in accordance with dipole-exchange theory predictions for the quantization of bulk spin waves. This first study of the spin-wave dynamics in ferromagnetic nanowire arrays reveals strong mode quantization effects and indications of a subtle magnetic interplay between nanowires. The results show that it is important to take proper account of these effects for the fundamental physics and future technological developments of magnetic nanowires.

DOI: 10.1103/PhysRevLett.89.027201 PACS numbers: 75.10.Jm, 75.30.Ds, 75.75.+a, 78.35.+c

Regular arrays of magnetic submicrometer-size dots and wires are currently attracting great interest due to their interesting physics and potential applications in magnetic sensors and memory devices [1,2], and their static properties have been studied extensively [3–7]. Their dynamical properties are of fundamental importance in evaluating the time scale of the magnetization reversal process, which governs the writing time in magnetic storage devices [8–10]. The low-energy magnetic excitations or spin waves (SWs) that define the time scale are best investigated via Brillouin (inelastic) light scattering (BLS) [11]. Only surface SWs have been observed so far by BLS in deep-etched micron-size magnetic circular dots and rectangular wires [12–15]. Here we employ BLS to study SWs in highly ordered arrays of ferromagnetic nickel nanowires, fabricated by self-assembly in Al_2O_3 templates following Nielsch *et al.* [16,17], and analyze the results by adapting a recent dipole-exchange theory for cylindrical nanowires [18]. Our novel results reveal three SWs whose frequencies sharply increase with decreasing diameter. The theory shows that these modes are caused by the radial quantization of bulk SWs. Besides its fundamental significance for the physics of nanomagnets, such quantization and also interwire coupling are factors that will strongly influence nanomagnetic device performance.

The two-dimensional arrays of nickel nanowires were prepared in the following way. Hexagonally ordered porous Al_2O_3 templates were first fabricated on aluminum substrates using a two-step electrochemical anodization process [19]. By means of pulsed electrodeposition, the resulting high-aspect-ratio porous alumina templates were homogeneously filled with nickel [16]. Scanning electron micrographs of the nanowire structures [17] revealed that they have a length of about 1 μm and a periodic wire spacing of 100 nm, with respective nanowire diameters of 30, 40, and 55 nm. Samples of nanowires with a 25 nm diameter and interwire separation of 65 nm were also obtained. Using superconducting quantum interference device magnetometry [17], the saturation magnetization, M_s, of the nickel nanowires was found to be 0.0480 T.

Brillouin spectra at room temperature were recorded in the 180° backscattering geometry using a (3 + 3)-pass tandem Fabry-Pérot interferometer equipped with a silicon avalanche diode detector, and the 514.5 nm line of an argon-ion laser. The laser light was incident on the top surface of each alumina membrane such that the surface normal, which is parallel to the symmetry axes of the nanowires, lies in the scattering plane. Measurements were made in *p-s* polarization configurations, with a typical data acquisition time of 8 h. Figure 1 shows a typical *p-s* polarized anti-Stokes Brillouin spectrum (which is similar to the Stokes spectrum) in zero applied field, recorded at an incident angle of 45°, of a 30 nm diameter nickel nanowire sample, which features three Brillouin peaks. Since they appear symmetrically, in the respective Stokes and anti-Stokes spectra, about the elastic peak and their positions shift on application of a magnetic field (see inset of Fig. 1), they are attributed to bulk SWs. The spectral peaks were fitted with a Lorentzian function, as shown in Fig. 1, and the variation of the fitted SW frequencies with the nanowire radius is displayed in Fig. 2. The inset of Fig. 1 shows the variation of the SW frequencies when a magnetic field is applied transverse to the axis of the nanowires. This field causes a canting of the magnetization

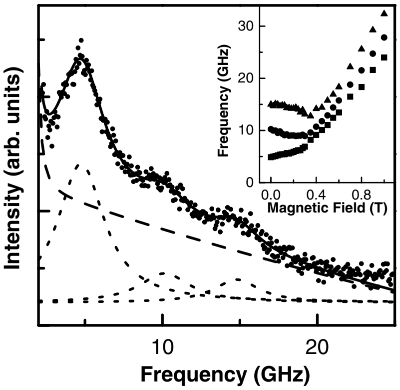

FIG. 1. Brillouin anti-Stokes spectrum of the 30 nm diameter nickel nanowire sample in zero applied magnetic field. Experimental data are denoted by dots. The peaks are due to the three bulk spin waves. The spectrum is fitted with Lorentzian functions (dotted curves) and a background (dashed curve); the full fitted spectrum is shown as a solid curve. The inset shows the bulk spin-wave frequencies versus applied magnetic field for the same sample.

direction, which acquires a component in the transverse direction (for which the demagnetizing field is $2\pi M_s \approx 0.30$ T). It is noticeable that there is a different behavior for the SW frequencies above and below this approximate field value.

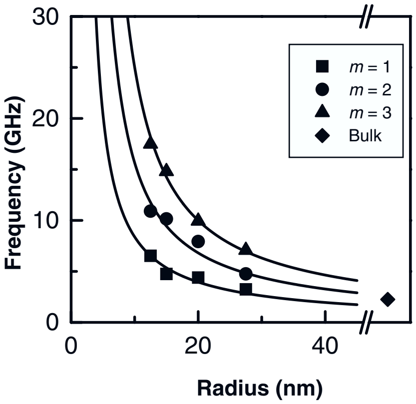

FIG. 2. Variation of bulk spin-wave frequencies with nanowire radius in zero applied magnetic field. The experimental data points, for each radius, correspond to the three values of the azimuthal quantum number m. The solid curves represent the respective best fits of the experimental data with Eq. (4). The diamond denotes the frequency of the bulk spin wave for bulk nickel [20].

The theory of Arias and Mills [18] was formulated for dipole-exchange SW excitations in ferromagnetic nanowires of circular cross section, where the magnetization is parallel to the axis of the wire. In this theory the general form of the magnetic scalar potential within the nanowire, as obtained from the Bloch equation of motion with dipole field terms and exchange terms included, can be expressed in cylindrical coordinates as

$$\Phi_M(r,\phi,z) = J_m(qr)\exp(im\phi)\exp(ikz). \quad (1)$$

Here k is the component of the SW wave vector along the z direction (parallel to the axis of a nanowire), and $J_m(qr)$ is a Bessel function of order m $(= 1, 2, 3, \ldots)$. The complex variable q is found from the roots of a sixth-order polynomial [18]. In the case of zero applied magnetic field, we find that this can be factorized as

$$(q^2 + k^2)[Dq^2(Dq^2 + 4\pi M_s + 2Dk^2) + (Dk^2)^2 - \omega^2] = 0, \quad (2)$$

where D is the exchange stiffness, M_s is the saturation magnetization, and ω is the SW frequency. The bulk standing modes of the nanowires correspond to real values of q (which has the role of a SW radial wave vector component) and thus correspond to SW frequencies that are given by

$$\omega = [Dq^2(Dq^2 + 4\pi M_s + 2Dk^2) + (Dk^2)^2]^{1/2}. \quad (3)$$

The full theory [18] requires taking into account numerically the "mixing" of the bulk SWs with the surface SWs, which correspond to imaginary values of q, together with boundary conditions. Here we modify this approach to obtain an approximate analytic theory applicable for small and large pinning [11], for which the radial function $J_m(qr)$ will have antinodes and nodes, respectively, at $r = R$ (the radius of a nanowire). Denoting $a_m = q_m R$, the lowest three values are $a_1 = 1.84$, $a_2 = 3.05$, and $a_3 = 4.20$ for $m = 1$, 2, and 3, respectively, in the case of small pinning. The corresponding numbers for large pinning are $a_1 = 3.83$, $a_2 = 5.14$, and $a_3 = 6.38$.

The expression for ω can be further simplified if $k^2 \ll (a_m/R)^2$ (see discussion below):

$$\omega = \left\{D\left(\frac{a_m}{R}\right)^2\left[D\left(\frac{a_m}{R}\right)^2 + 4\pi M_s\right]\right\}^{1/2}. \quad (4)$$

The above equation is used to fit our results with D as a parameter and M_s fixed at the measured value of 0.0480 T [17]. Figure 2 shows that the fit thus obtained is good, in the case of small pinning, and yields $D = 3.13 \times 10^{-14}$ T cm^2, which is some 11 times smaller than that obtained by Sandercock and Wettling [20] in a BLS study of SWs in bulk nickel. The reason for this discrepancy may be associated with the different sample geometry and direction of the SW wave vector (compared to Ref. [20]) or, more likely, due to the long-range dipolar fields of the surrounding nanowires in the array. The fit to the experimental data is poor for large pinning, thus implying that the surface anisotropies in the nanowire samples are small.

Our $k = 0.041\ \mathrm{nm}^{-1}$ and therefore $k^2 = 1.6 \times 10^{-3}\ \mathrm{nm}^{-2}$. Now $(a_m/R)^2$ ranges from 4.48×10^{-3} to $0.11\ \mathrm{nm}^{-2}$ and therefore $k^2 \ll (a_m/R)^2$, thus justifying our use of Eq. (4). A measure of the relative importance of the exchange to dipolar coupling on a SW at wave number k is given by $\rho \equiv (Dk^2/4\pi M_s)^{1/2}$ (see, e.g., Ref. [21]). In the case of our nickel nanowires $\rho = 0.093$, which is small, but not sufficiently small that exchange effects may be neglected. Another measure is the exchange length, defined as ρ/k, which has the value of 2.27 nm for the nickel nanowires. The range of radii R studied, 12.5 to 27.5 nm, is larger than the exchange length, but not by a very large factor. This clearly indicates that a dipole-exchange theory [18] is necessary for the analysis of SWs in small-size nickel nanowires, and that the earlier magnetostatic theories [21,22] are inadequate because exchange effects are ignored.

In conclusion, we report the first observation by BLS of multiple SWs in uniform arrays of nickel nanowires. Our analysis, on the basis of a dipole-exchange theory, indicates that the discrete modes observed are a consequence of the quantization of bulk SWs due to confinement by the small cross section of the nanowires. Previously, BLS has only been employed to study surface SW confinement in surfaces patterned with micrometer-size magnetic platelets and strips [12]. By contrast, interesting new bulk effects arise in the present case due to the extremely anisotropic geometry of the long nanometer-size cylinders. Such a geometry is envisaged for the next generation of perpendicular magnetic storage media based on metallic nanowire arrays. Besides the spin reversal dynamics in single magnetic nanowires, the interactions between the nanowires indirectly evidenced here are also of great importance at high packing density. Future developments in quantum nanomagnetic data storage technology will depend on a detailed understanding of the physical nature and magnitude of intra- and interwire magnetic interactions.

This project is funded in part by the National University of Singapore and NSERC (of Canada).

---

*Corresponding author.
Email address: phykmh@nus.edu.sg

[1] T. Aign *et al.,* Phys. Rev. Lett. **81**, 5656 (1998).
[2] M. Todorovic, S. Schultz, J. Wong, and A. Scherer, Appl. Phys. Lett. **74**, 2516 (1999).
[3] T. M. Whitney, J. S. Jiang, P. C. Searson, and C. L. Chien, Science **261**, 1316 (1993).
[4] T. Thurn-Albrecht *et al.,* Science **290**, 2126 (2000).
[5] T. Shinjo *et al.,* Science **289**, 930 (2000).
[6] V. F. Puntes, K. M. Krishnan, and A. P. Alivisatos, Science **291**, 2115 (2001).
[7] O. Pietzsch, A. Kubetzka, M. Bode, and R. Wiesendanger, Science **292**, 2053 (2001).
[8] U. Ebels *et al.,* Phys. Rev. B **64**, 144421 (2001).
[9] A. Encinas-Oropesa *et al.,* Phys. Rev. B **63**, 104415 (2001).
[10] M. R. Freeman and B. C. Choi, Science **294**, 1484 (2001).
[11] M. G. Cottam and D. J. Lockwood, *Light Scattering in Magnetic Solids* (Wiley, New York, 1986).
[12] S. O. Demokritov, B. Hillebrands, and A. N. Slavin, Phys. Rep. **348**, 441 (2001).
[13] J. Jorzick *et al.,* Appl. Phys. Lett. **75**, 3859 (1999).
[14] C. Mathieu *et al.,* Phys. Rev. Lett. **81**, 3968 (1998).
[15] J. Jorzick *et al.,* Phys. Rev. B **60**, 15 194 (1999).
[16] K. Nielsch, F. Müller, A. P. Li, and U. Gösele, Adv. Mater. **12**, 582 (2000).
[17] K. Nielsch *et al.,* Appl. Phys. Lett. **79**, 1360 (2001).
[18] R. Arias and D. L. Mills, Phys. Rev. B **63**, 134439 (2001).
[19] A. P. Li *et al.,* Adv. Mater. **11**, 483 (1999).
[20] J. R. Sandercock and W. Wettling, J. Appl. Phys. **50**, 7784 (1979).
[21] T. Wolfram and T. E. DeWames, Prog. Surf. Sci. **2**, 233 (1972).
[22] T. M. Sharon and A. A. Maradudin, J. Phys. Chem. Solids **38**, 977 (1977).

Lebenslauf

Name	Dr. rer. nat. Ralf Boris Wehrspohn
Adresse	Kleine Ulrichstr. 24a, 06108 Halle
Geburtsdatum	17. August 1970
Geburtsort	Lübeck, Schleswig-Holstein
Status	verheiratet, drei Kinder
September 2002	Antrag auf Eröffnung eines Habilitationsverfahrens an der Martin-Luther-Universität Halle-Wittenberg, Math.-Naturw.-Techn. Fakultät
seit Okt. 1999	Wissenschaftlicher Mitarbeiter am Max-Planck-Institut für Mikrostrukturphysik in Halle; Leitung der Gruppe Poröse Materialen / Photonische Kristalle
1.1.98 - 30.9.99	Wissenschaftlicher Mitarbeiter bei Philips Research Laboratories, Redhill, England.
1.7.97.- 31.12.97	Post-Doc an der École Polytechnique, Palaiseau, Frankreich.
1.9.95-27.6.97	Europäische Doktorarbeit, angefertigt an der Universität Oldenburg und der Ecole Polytechnique, Frankreich; Titel: *Porous amorphous silicon - pore formation and photoluminscent properties*; Disputation bestanden mit sehr gut (27.6.97)
1.10.90-29.8.95	Physikstudium an der Carl-von-Ossietzky-Universität Oldenburg; abgeschlossen mit Diplom in Physik.
1.8.75-30.6.89	Schulausbildung, abgeschlossen mit Abitur am Gymnasium in Buchholz i.d.N

Eidesstattliche Erklärung

Ich erkläre, dass meine Habilitationsschrift selbstständig und ohne fremde Hilfe verfasst, andere als die angegebenen Quellen und Hilfsmittel nicht benutzt und die den benutzten Werken wörtlich oder inhaltlich entnommenen Stellen als solche kenntlich gemacht wurden.

Dr. rer. nat. Ralf Boris Wehrspohn

Halle (Saale), im September 2002